



UNIVERSITÀ DEGLI STUDI DI TRENTO

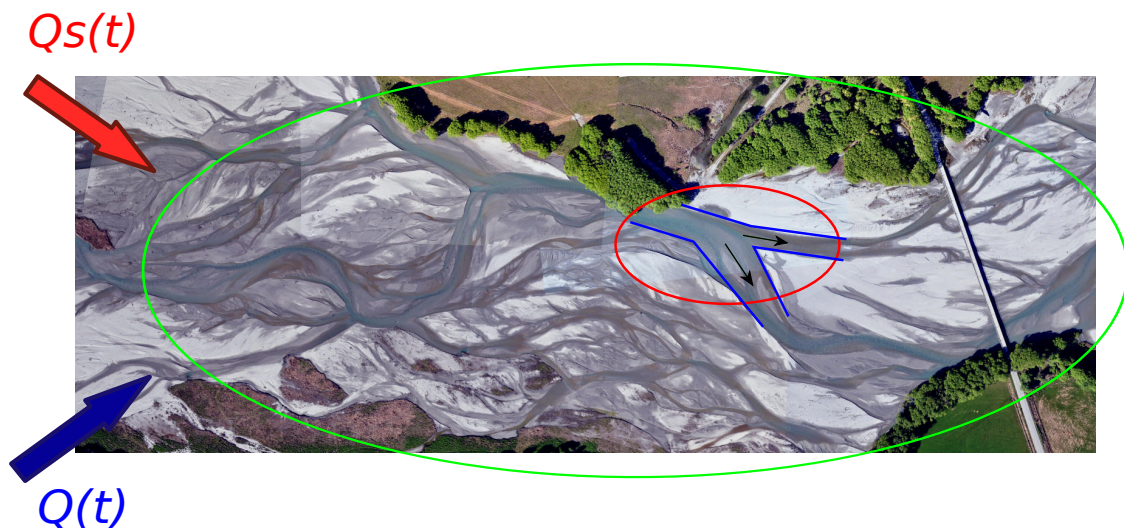


QUEEN MARY
UNIVERSITY OF LONDON

Erasmus Mundus Joint Doctorate School in Science for
Management of Rivers and their Tidal System

Marco Redolfi

Sediment transport and morphology of braided rivers: steady and unsteady regime



October 2014

Doctoral thesis in Science for Management of Rivers and their Tidal System,

Cycle: 1

Primary Institution:

Department of Civil, Environmental and Mechanical Engineering, University of Trento, Trento, Italy

Secondary Institution:

School of Geography, Queen Mary University, London, UK

Associate partner: Leibnitz-Institute für Gewässerökologie und Binnenfischerei (IGB), Berlin

Supervisors:

Marco Tubino, University of Trento

James Brasington, Queen Mary University of London

Academic year 2014/2015



Erasmus Mundus
Joint Doctorate Programme



**SMART - Science for Management of
Rivers and their Tidal systems**

The SMART Joint Doctorate Programme

Research for this thesis was conducted with the support of the Erasmus Mundus Programme ¹, within the framework of the Erasmus Mundus Joint Doctorate (EMJD) SMART (Science for Management of Rivers and their Tidal systems). EMJDs aim to foster cooperation between higher education institutions and academic staff in Europe and third countries with a view to creating centres of excellence and providing a highly skilled 21st century workforce enabled to lead social, cultural and economic developments. All EMJDs involve mandatory mobility between the universities in the consortia and lead to the award of recognised joint, double or multiple degrees. The SMART programme represents a collaboration among the University of Trento, Queen Mary University of London, and Freie Universität Berlin. Each doctoral candidate within the SMART programme has conformed to the following during their 3 years of study:

- (i) Supervision by a minimum of two supervisors in two institutions (their primary and secondary institutions).
- (ii) Study for a minimum period of 6 months at their secondary institution.
- (iii) Successful completion of a minimum of 30 ECTS of taught courses.
- (iv) Collaboration with an associate partner to develop a particular component / application of their research that is of mutual interest.
- (v) Submission of a thesis within 3 years of commencing the programme.

¹ This project has been funded with support from the European Commission. This publication reflects the views only of the author, and the Commission cannot be held responsible for any use which may be made of the information contained therein.

This page is intentionally left blank

Abstract

Braided rivers are complex, fascinating fluvial pattern, which represent the natural state of many gravel and sand bed rivers. Both natural and human causes may force a change in the boundary conditions, and consequently impact the river functionality. Detailed knowledge on the consequent morphological response is important in order to define management strategies which combine different needs, from protection of human activities and infrastructures to preservation of the ecological and biological richness.

During the last decades, research has made significant advance to the description of this complex system, thanks to flume investigations, development of new survey techniques and, to a lesser extent, numerical and analytical solutions of mathematical models (e.g. Ashmore, 2013).

Despite that, many relevant questions, concerning the braided morphodynamics at different spatial and temporal scales (from the unit process scale, to the reach scale, and eventually to the catchment scale) remain unanswered. For example, quantitative analysis of the morphological response to varying external controls still requires investigation and needs the definition of suitable, stage-independent braiding indicators. In addition, the morphodynamics of the fundamental processes, such as bifurcations, also needs further analysis of the driving mechanisms.

General aim of the present study is to develop new methods to exploit, in an integrated way, the potential of the new possibilities offered by advanced monitoring techniques, laboratory models, numerical schemes and analytical solutions. The final goal is to fill some gaps in the present knowledge, which could ultimately provide scientific support to river management policies.

We adopted analytical perturbation approaches to solve the two-dimensional shallow water model; we performed laboratory simulations on a large, mobile-bed flume; we analysed existing topographic measurements from *LiDAR* and Terrestrial Laser scanning Devices; and we simulated numerically the river hydrodynamics. Within each of the six, independent, research chapters, we interconnected results from the different approaches and methodologies, in order to take advantage of their potential.

Summarising, the more relevant and novel outcomes of the present work can be listed as follows:

- (i) We explored the morphological changes during a sequence of flood events in a natural braided river (Rees River, NZ) and we proposed a morphological method to assess the sediment transport rate. In particular we propose a semi-automatic method for estimating the particles path-length (Ashmore and Church, 1998) on the basis of the size of the deposition patches, which can be identified on the basis of *DEM* of differences. Comparison with results of numerical simulation confirmed that such an approach can reproduce the response of the bedload rate to floods of different duration and magnitude.
- (ii) We developed a new indicator of the reach-scale morphology and, on the basis of existing laboratory experiments, we explored its dependence, under regime conditions, to the controlling factors: slope, discharge, confinement width, grain size. In spite of its synthetic nature, this simple indicator embeds the information needed to estimate the variability of the Shield stress throughout the braided network, and consequently enables to assess the transport-rate and its variation with the driving discharge.
- (iii) We investigated, through flume experiments, the effect of the flow unsteadiness on the sediment transport in a braided river. This is possible only by following a statistical approach based on multiple repetitions of the same flow hydrograph. Results revealed that for confined network an hysteresis of the bedload response occurs, which leads to higher sediment transport during increasing flow, whereas relatively unconfined networks always show quasi-equilibrium transport rates.
- (iv) A second set of laboratory experiments provided information on the morphodynamics of a braided network subject to variations of the sediment supply. We proposed a simple diffusive model to quantify the evolution of the one-dimensional bed elevation profile. Such simple approach, albeit having a limited range of practical applications, represents the first attempt to quantify this process and enables to study the relevant temporal and spatial scales of the phenomenon.
- (v) We solved analytically the two-dimensional morphodynamic model for a gravel-bed river bifurcation. This furnishes a rigorous proof to the idea proposed by Bertoldi and Tubino (2007) to interpret the morphological response of bifurcation in light of the theory of the morphodynamic influence. The analytical approach enables to investigate the fundamental mechanics which leads to balance, and unbalance, configurations and, from a more practical point of view, allows for a better prediction of the instability point than the existing 1D models (e.g. Bolla Pittaluga et al., 2003).

Contents

1	Introduction	1
1.1	The braided rivers	1
1.2	Braided rivers morphodynamics and predictions	3
1.3	The fundamental unit processes	6
1.3.1	Bifurcations	6
1.3.2	Confluences	6
1.3.3	Bars	7
1.4	The sediment transport	8
1.5	Aims and methods of the present study	10
1.5.1	The study rivers	12
1.5.2	The experimental setup	15
1.6	Outline of the thesis	16
2	Morphological changes and sediment transport: The Rees River (New Zealand)	21
2.1	Introduction	21
2.2	The study site	23
2.3	Data collection	23
2.3.1	Topographic data	23
2.3.2	Hydrological and sediment transport data	24
2.4	Methods	26
2.4.1	Data manipulation	26
2.4.2	The path length method	28
2.4.3	Numerical simulations	31
2.5	Results	35
2.5.1	Analysis of deposition and scour volumes	35
2.5.2	Characteristic length and sediment transport	36
2.6	Discussion	47
2.6.1	Relationship between patches size and path length	47
2.6.2	Volume compensation and temporal resolution	49
2.6.3	Effect of the volume compensation on the transport estimate	52

2.6.4	Effect of the confidence interval	54
2.7	Conclusions	55
2.8	List of symbols and acronyms	58
2.9	Appendixes	59
2.9.1	Distributions of the morphological variations	59
2.9.2	Comparison between different methods	59
2.9.3	Some considerations about the reach extent	62
2.9.4	Analysis of channels movements	65
2.9.5	Path-length approach in the case of significant compen- sation	67
3	Distribution of elevation and sediment transport	71
3.1	Introduction	71
3.2	The method	73
3.2.1	Definition and scaling	73
3.2.2	Flume experiments data	76
3.3	Results	77
3.4	Elevation distribution and sediment transport	86
3.4.1	Introduction	86
3.4.2	A reach-scale bedload estimator	88
3.4.3	Results	90
3.4.4	Discussion	94
3.5	Conclusions	101
3.6	List of symbols and acronyms	102
3.7	Appendix	103
3.7.1	Averaging length and spatial scales of braiding	103
3.7.2	Sensitivity of the coefficient α to the curve extension . . .	109
4	Sediment transport and discharge unsteadiness: a laboratory study	111
4.1	Introduction	111
4.2	Background	112
4.2.1	Example: the role of the unsteadiness in alternate mi- grating bars morphology	113
4.2.2	Variability of sediment transport rate: a fundamental problem	119
4.3	Method	120
4.3.1	Experimental set-up	121
4.4	Results	127
4.5	Discussion	134
4.6	Conclusions	139
4.7	List of symbols	140
4.8	Appendices	142

4.8.1	Equilibrium response of braided network with different confinement width	142
4.8.2	Analysis of active and dry area during the experiment W1	143
5	A diffusive 1D model for the morphological response to varying sediment supply	149
5.1	Introduction	149
5.1.1	The diffusive model	151
5.1.2	The hyperbolic model	154
5.1.3	Laboratory experiments	157
5.1.4	Experimental results	158
5.2	Discussion	161
5.3	Conclusions	163
5.4	List of symbols and acronyms	164
5.5	Appendix	166
5.5.1	1D models for single-thread rivers	166
5.5.2	Solution of the diffusive model	168
5.5.3	Solution of the linear hyperbolic model	169
5.5.4	Analysis of the hyperbolic model	171
5.5.5	A statistical approach	173
6	Analytical solution for a small obstacle in a gravel-bed channel	179
6.1	Introduction	179
6.2	Formulation of the model	180
6.3	The perturbation approach	184
6.3.1	General solution for the straight channel A and B	185
6.3.2	General solution for the central channel Obst	188
6.3.3	The matching condition	191
6.3.4	Matching of the one-dimensional ($m = 0$) component	194
6.3.5	Matching of the two-dimensional ($m \geq 1$) components	195
6.4	Results	196
6.5	Discussion	199
6.5.1	The effect of the secondary currents	201
6.5.2	The role of the boundary conditions	202
6.6	Conclusions	206
6.7	Appendix: Eigenstructure of the linear, coupled, time-dependent problem	208
6.7.1	Appendix 2: Numerical modelling	212
6.7.2	List of symbols and acronyms	216
7	Perturbative solution of the 2D model for gravel-bed river bifurcations	221
7.1	Introduction	221

7.2	Gravel bed rivers bifurcations and morphodynamic influence . . .	223
7.2.1	The theory of the morphodynamic influence	223
7.2.2	Channel bifurcations: simplified modelling and morpho- dynamic influence	224
7.3	Formulation of the problem	227
7.3.1	The two-dimensional model	229
7.3.2	Perturbation approach	231
7.3.3	The steady linear solution	232
7.3.4	Linear solution for the small-angle divergent bifurcation .	235
7.3.5	Morphodynamic influence and its relation to the eigen- values of the linear system	236
7.4	Free steady solution for a channel bifurcation	237
7.4.1	Solution for the downstream branches	239
7.4.2	Solution for the main channel	240
7.4.3	The matching procedure	241
7.4.4	Solution for the small-angle bifurcation	243
7.5	Results	245
7.5.1	Example: first $N = 1$ approximation	245
7.5.2	The complete solution	246
7.5.3	Comparison with numerical results and laboratory exper- iments	247
7.5.4	The small-angle bifurcation	248
7.6	Discussion	253
7.7	Conclusions	254
7.8	List of symbols and acronyms	255
7.9	Appendixes	257
7.9.1	The matching procedure	257
7.9.2	Stationary $1D$ solutions	261
7.9.3	The role of the secondary currents	264

List of Figures

1.1	Picture of the River Rakaia (New Zealand, $43^{\circ}21' S$, $171^{\circ}27' E$). Courtesy of Bill Irwin (www.billirwinarts.com).	3
1.2	Example of braided rivers of different scales. a) Brahmaputra river (Bagladesh-India $25^{\circ}53' N$, $89^{\circ}54' E$), from <i>Google Earth, Digital Globe (2014)</i> ; b) Sunwapta river (Alberta, Canada), from Bertoldi (2005) c) Flume experiment (Trento, Italy); flow is from the top to the bottom.	5
1.3	Bifurcation of the River Sunwapta (Alberta, Canada). From Bertoldi (2005). Flow is from left to right.	6
1.4	Example of sediment transport measured during one of our long-term experiments. A filtering algorithm which removes the frequency components faster than $1 h$ and $5 h$ (red and blue lines respectively) has been applied.	9
1.5	Location of the study reach of the Rees River (Otago, New Zealand).	13
1.6	Aerial view of the study reach of the River Rees. Flow is from left to right.	13
1.7	Image of the River Tagliamento from Monte Ragogna in the upstream direction. From www.comitato-arca.it	15
1.8	Picture of the River Sunwapta (Alberta, CA). Flow is towards the camera. From Bertoldi (2005).	16
1.9	Photograph of the Trento's flume; from Welber (2013). Flow is towards the camera.	17
1.10	Sketch of the Trento's flume. Upper part: longitudinal section; lower part: planimetric view. Based on the Welber (2013).	17
1.11	Representation of the main perspectives we adopted for the analysis of a braided reach.	19
1.12	Schematic description of the thesis structure. Letters refers to the three main parts: 1) Study of the reach-scale morphodynamics; 2) Effect of the variation through time of water and sediment supply; 3) Analysis of fundamental unit processes.	20

2.1	Estimated discharge during the study periods. Numbers and relative segments indicates the duration of the morphological surveys.	25
2.2	<i>DEM</i> of difference during the more intense flood event. Flow from left to right.	25
2.3	Map of the estimated error $\sigma(x, y)$ for the first (00) survey. Values in $[m]$.	27
2.4	Sketch of the movement of volumes for the Ashmore and Church (1998) method. The dashed lines represent the limits of the study reach.	29
2.5	Example: deposition and erosion patches (blue and red areas respectively) and relative ellipses. In this example the patches having $A < 100 m^2$ are excluded from the analysis (yellow colour for erosion, cyan for deposition).	30
2.6	Hypsometric curves of the bottom elevation of the different surveys after removing a constant slope $S = 0.574 \%$. Only the area common between the different <i>DEMs</i> has been considered.	32
2.7	Example: water depth (in $[m]$) predicted by the numerical model for $Q = 120 m^3s^{-1}$.	33
2.8	Sediment rate curve resulting from the numerical model. The topography of <i>dem 08</i> has been considered.	34
2.9	Scour and deposition volumes (upper panel), active areas (central panel) and mean variation of elevation in the active areas (lower panel) for the different events.	36
2.10	Histograms of the bed level changes. Each bar represents the extension of the area that experienced the elavation change $\Delta\eta$. The red line on the lower panel represents the best-fitting Gaussian distribution.	37
2.11	Correlation between erosion volumes and the different parameters adopted in order to quantify the intensity of the storm event. <i>Vol</i> represents the volume of water exceeding the threshold $Q_{cr} = 30 m^3s^{-1}$.	37
2.12	Cumulative (and normalised) spectral density of the cross-section averaged profiles for the different events. The total (sum of erosion and deposition across the section) volume has been considered.	38
2.13	Cumulative frequency distribution of the weighted major axis length of erosion and deposition patches.	39
2.14	Analysis of size of the scour (yellow bar) and deposition (red bar) patches. Upper panel: mean area. Central panel: mean length of the semi-major axes of the ellipse having the same second-order moments. Lower panel: mean length of the semi-major axes.	40
2.15	Schematic representation of the relation between the average transport and the estimation based on patches length and erosion volume.	42

2.16	Example of variation of the bedload along a streamline. Results from numerical model with $Q = 323 \text{ m}^3\text{s}^{-1}$	42
2.17	Correlation between the estimated volume of bedload transport and the different metrics considered in order to quantify the intensity of the storm events. <i>Int</i> indicates the temporal integral normalised with the larger value, <i>Vol</i> represents the volume of water exceeding the threshold $Q_{cr} = 30 \text{ m}^3/\text{s}$	44
2.18	Reach-averaged sediment transport, computed from the numerical model and using our approach (considering scour patches). Upper panels: Wong and Parker (2006b) (Eq.2.14). Lower panel: Parker (1990). Two different values of the critical discharge have been considered, the regression refers to $Q_{cr} = 40 \text{ m}^3\text{s}^{-1}$; porosity is fixed to $p = 0.3$	45
2.19	Path length computed from the numerical model and using the present approach (considering scour patches). Upper panels: Wong and Parker (2006b) (Eq.2.14). Lower panel: Parker (1990); two different values of the critical discharge have been considered, the regression refers to $Q_{cr} = 40 \text{ m}^3\text{s}^{-1}$; porosity is fixed to $p = 0.3$	46
2.20	Comparison (in terms of global erosion and deposition volumes) between the the difference between two <i>DEMs</i> and the sum of the differences with an intermediate <i>DEM</i>	50
2.21	Volume of scour/deposition for the entire period 00-10 estimated by using a different number of <i>DEMs</i> , from two (first and last only) to eight (sum of seven differences between intermediate <i>DEMs</i>).	51
2.22	Path length as a function of the measurement interval Δt consequent to the formula proposed by Lindsay and Ashmore (2002).	53
2.23	Transport length L^{tot} for the entire period 00-10, estimated by using a different number of intermediate <i>DEMs</i>	54
2.24	Transport volume for the entire period 00-10, estimated through a different number of intermediate <i>DEMs</i>	54
2.25	Comparison between weighted length of scour and deposition patches computed with different confidence intervals. The central panel represents the result of figure 2.14.	56
2.26	Distribution elevation of the scour (upper panel) and erosion (lower panel) volumes. The elevation refers to the antecedent topography.	60
2.27	Longitudinal integral of the scour volumes as a function of the transverse coordinate y for the different storm events. A 10 <i>m</i> window average has been adopted to filter the signals.	61
2.28	Longitudinal profile of the laterally integrated net volume for different storm events. A 100 <i>m</i> window average has been adopted to filter the signals.	61

2.29	Comparison between the mean area computed without any threshold and the mean area obtained <i>a)</i> after excluding patches with $A < 10 \text{ m}^2$ (left panels); <i>b)</i> after applying the filtering algorithm (right panels). Upper panels: deposition patches, lower panels: scour patches.	64
2.30	Comparison between the mean semi-major length computed without threshold and the one obtained <i>a)</i> after excluding patches with $A < 10 \text{ m}^2$ (left panels); <i>b)</i> after applying the filtering algorithm (right panels). Upper panels: deposition patches, lower panels: scour patches.	64
2.31	Comparison between the weighted mean of the semi-major axes computed with the three methods. Upper panels: deposition patches, lower panel: scour patches. Dashed line represent the 1 : 1 relation.	65
2.32	Erosion volume per unit length computed on windows of different lengths.	66
2.33	Map of the wet area during survey 00 (red area) and 01 (blue area). The common area is depicted in green, the black line represent the extension of the survey.	67
2.34	Example of manual channel recognition for a portion of the braidplain (survey 09, Williams et al., 2013b)).	68
2.35	Changes of wetted area between different events. Upper panel: wetted area in common. Lower panel: common area divided by the total wetted area of the two surveys.	68
2.36	Example of the three different definitions of the erosion volumes at a given location. The time evolution is the result of a simple random process.	69
2.37	Volumes of erosion V_e^T and \tilde{V}_e^T for the entire period 00-10.	70
3.1	Definition of the $b(D)$ curve for each cross-section. b_s is the cumulative length of the blue segments. By repeating the procedure for each section of a braided river reach we obtain the averaged $b(D)$ curve.	74
3.2	Definition of the Average section (right side) on the basis of the $b(D)$ curves and distinction in different shapes on the basis of the coefficient α , following Toffolon and Crosato (2007).	75
3.3	$b(D)$ curves of the TN1 and TN2 experiments. The square marker at the end of each curve indicates the formative condition as defined by the simple uniform flow model of section 3.4. Different colours represent different slopes.	79

3.4	Mean variation of elevation across the section, as a function of the discharge, for TN1 and TN2 experiments. Left panel: difference between the highest and lowest point of the section; right panel: standard deviation of $\eta(y)$	79
3.5	Coefficient of the power law which best fitting the TN1 (circular markers) and TN2 (squared markers). Different colours represent different slopes.	80
3.6	$b(D)$ curves of river Sunwapta (left panel) and Rees (right panel). The dashed line represents the best fitting of the power law $b = kD^\alpha$	81
3.7	$b(D)$ curves for different areas of the study reach. The black squares represent the estimated width with $Q = 1000 \text{ m}^3\text{s}^{-1}$. . .	83
3.8	Exponent of the $b(D)$ curves as a function of the specific discharge for the Sunwapta River and for the different sub-reaches of the Tagliamento River. A representative discharge $Q = 1000 \text{ m}^3\text{s}^{-1}$ was adopted. The labels refers to the sub-areas of figure 3.7a. . .	84
3.9	$b(D)$ curves of the TN3 experiments with $Q = 2.0 \text{ ls}^{-1}$. Different colours indicates a different confinement width W ; The square marker at the end of each curve indicates the formative conditions as defined by the simple uniform flow model defined in section 3.4.	85
3.10	Exponent of the power law which is best fitting the $b(D)$ curves of TN3 experiments, as a function of the dimensionless specific water discharge. Colours indicate different Q , the cyan points refer to transition networks, for which a power-law interpolation may be inappropriate.	86
3.11	Exponent of the power law which is best fitting the $b(D)$ curves of TN1, TN2, TN3 experiments as a function of the dimensionless specific water discharge.	87
3.12	Exponent of the power law which is best fitting the $b(D)$ curves of TN1, TN2, TN3 experiments as a function of the total dimensionless discharge.	88
3.13	Map of the Shields stress of the Rees River from the hydrodynamic model with $Q = 323 \text{ m}^3\text{s}^{-1}$. Only areas with $\theta > 0.038$ are represented. Flow is from left to right; axes are not to scale. .	90
3.14	Cumulative Shields stress distributions of the Rees River reach from the shallow water model (blue lines) and from the <i>Average section</i> method (red lines), with discharge $Q = 323 \text{ m}^3\text{s}^{-1}$ (continuous lines) and $Q = 200 \text{ m}^3\text{s}^{-1}$ (dashed plots). b indicates the area divided by the reach length; the θ axis has been reversed in order to easily recognise the <i>Average section</i> profile.	91

3.15	Comparison between TN1 laboratory observations, the (Bertoldi et al., 2009a) (black circles) method and the <i>Average section</i> method (magenta squares) in terms of average solid discharge. The logarithmic formula (Eq.3.12) has been adopted for the hydraulic resistance. Different filling colours represent different flume slopes.	93
3.16	Comparison between TN3 laboratory observations, the <i>Average section</i> method and the estimation based on cross-section averaged parameters. The Parker (1990) formula has been adopted for bedload transport, the Engelund formula (Eq.3.12) for the hydraulic resistance. Different colours indicates different discharges.	94
3.17	Comparison between at-a-station response of the numerical model and of the <i>Average section</i> method.	95
3.18	Measurements of inundated areas at <i>Cornino</i> and <i>Flalogna</i> sub-reaches (green and red points respectively), from Welber et al. (2012), and estimations using the analytic solution. $S = 0.35\%$, $d_s = 4\text{ cm}$ are adopted as parameters.	95
3.19	Test sections adopted for the analysis of the model response. For a given α the green curve represents the reference section, whose bankfull conditions (square marker) correspond to a discharge Q_0 and a maximum depth D_0 . The red and blue curves indicate wider and narrow sections characterised by the same bankfull depth.	98
3.20	Wetted width as function of the water discharge, for distinct values of the exponent α and the coefficient k of the <i>Average section</i> . The black markers correspond to average Shields stress $\bar{\theta} = 0.06$; slope is $S = 0.5\%$	99
3.21	Sediment flux curves for distinct values of the exponent α and the coefficient k of the <i>Average section</i> . The black markers correspond to a value of the average Shields stress $\bar{\theta} = 0.06$. The Meyer-Peter and Müller (1948) transport formula and a slope $S = 0.5\%$ is adopted; δ indicates the exponent of the power-law which fits the curves.	100
3.22	Average section of the TN3 experiments, computed on different windows of length L placed at the downstream portion of the flume. Different panel refers to different runs.	104
3.23	Average section of the run 5 of the TN3 experiments, computed by positioning the windows in order to avoid overlapping (except for the bigger window $L = 20\text{ m}$ which overlaps all the others). .	105
3.24	Longitudinal profiles of $b(D^* = 15)$ of the TN2 experiments. The vertical dashed lines separate different runs.	105

3.25	Londinal profiles of wetted width of the TN2 experiments according to the Bertoldi et al. (2009a) method. The vertical dashed lines separate different runs.	105
3.26	Fourier spectrum of the $b(x)$ signal. Upper panel: single components, lower panel: cumulative energy content.	106
3.27	Map of the (normalised) continuous wavelet transform of the $b(x)$ signals of the TN3 experiments. The Morlet scaling function has been adopted; the vertical dashed lines separate different runs.	107
3.28	Cumulative spectrum of TN1 and TN3 experiments.	108
3.29	Path length of the TN3 experiments, computed through the inverse application of the Ashmore and Church (1998) method.	109
3.30	Variability of the coefficient α with the maximum D adopted as a limit of the curves. Only a single run for each slope (the one with lower Q) of the TN1 and TN2 experiments is considered. The dashed line correspond to D_{form} , which is the value adopted in the previous analyses.	110
4.1	Example of hysteresis of the transport rate curve due to flow unsteadiness. The red curve shows the response in equilibrium (i.e. constant discharge through time) conditions. Clockwise hysteresis indicates an advance (i.e. negative lag) of the sediment transport with respect to the water discharge.	115
4.2	Height of the alternate bars predicted by the Tubino (1991) theory for a channel subject to periodic variations of the water discharge between two constant values. HI and LO indicate the high and low flow phases respectively; the dashed line represent the equilibrium amplitude of the alternate bars; time is relative to the timescale of the bar growth.	117
4.3	Bedload transport of a channel subject to periodic variations of the water discharge between two constant values, according to the result of figure 4.2 and to the transport estimation of Eq. 4.6. HI and LO indicate the high and low flow phases respectively; the dashed line represent the equilibrium transport rate; Time is relative to the timescale of the bar growth.	118
4.4	Time averaged sediment output measured during the constant-discharge run W3 EQ2.5 RW. Two different cut-off periods (1 h and 5 h) have been adopted to filter out high-frequency oscillations.	121
4.5	Picture of the flume during experiment W1 ($W = 1 m$). Flow is from the camera, discharge is $Q = 2.0 l/s$	123
4.6	Hydrodraph adopted during experiment W1. The red points represent the instants of the manual surveys of wetted and active widths.	124

4.7	Picture of the flume during W3 C5 ($W = 2.9\text{ m}$). Flow is from the camera, discharge is $Q = 1.5\text{ l/s}$	125
4.8	Liquid discharge during experiment W3. The vertical dashed lines indicate interruptions of the flow needed for the laser scanning. The whole sequence was repeated three times (plus three additional cycles), for a total of 24 cycles and 6 scans.	126
4.9	Morphology at the end of the end of the W3 1.5 RW. Axes are not to scale (2 : 1 aspect ratio). Elevations in $[cm]$ with respect to the initial slope.	127
4.10	Example: variability of the bedload during the first three cycles of experiment W1. The dashed line shows the liquid discharge.	128
4.11	Statistics of the bedload during experiment W1. A 20 <i>min</i> moving average filter has been applied. The dashed line shows the liquid discharge.	129
4.12	Solid discharge during the 24 cycles of the run W3, after a 20 <i>min</i> moving window averaging. The dashed line shows the liquid discharge.	129
4.13	Mean solid discharge of the 21 cycles of the experiment W1. A 20 <i>min</i> moving average filter has been applied. The blue dashed line shows the liquid discharge; the red and magenta lines indicates the equilibrium values measured during equilibrium runs.	130
4.14	Analysis of transport during experiment W1. The error bars indicate the standard deviation between the 21 cycles.	131
4.15	Probability that the difference between equilibrium and within-cycle transport rate is zero, as a function of the uncertainty in the knowledge of equilibrium bedload. The dashed line represent a 5% threshold; when the curves are below this line we can assume a statistically significant difference.	132
4.16	Mean solid discharge of the 24 cycles of experiment W3. A 20 <i>min</i> moving average filter has been applied. The blue dashed line shows the liquid discharge; the red and magenta lines indicates the equilibrium values measured during equilibrium runs.	133
4.17	Analysis of transport during experiment W3. The error bars indicate the standard deviation of the average.	133
4.18	Average section during W3 experiment. Cx indicates the topography measured during the x -th cycle.	135
4.19	Average section during different constant discharge runs, both in the confined (W1 series) and unconfined (W3 experiment) case.	136
4.20	Distribution of elevation during different equilibrium runs of the W1 (confined) experiment. Arrows indicate the changes of the equilibrium distribution with increasing discharge.	137
4.21	Average during the high flow phase of the different cycles. The green line indicates the linear trend.	139

4.22	Solid discharge during equilibrium runs in different conditions of discharge and flume width (TN3 (Garcia Lugo, 2014) and present experiments). Different colours correspond to different discharges. the black line represents the log-linear fitting.	143
4.23	Mean active (asterisk marker) and wetted (square markers) width during equilibrium run in different conditions of discharge and flume width. Red points: TN3 experiments (Garcia Lugo, 2014), blue points: present (RW) experiments.	144
4.24	Spatial and ensemble average of the active and wetted width during the cycle. Red and green colours indicated high and low discharge respectively.	145
4.25	Ensemble mean of the wetted width at different locations. Error bars indicate the standard deviation of the single ($6 \times 4 = 24$) measurements.	147
4.26	Ensemble mean of the active width at different locations. Error bars indicate the standard deviation of the single ($6 \times 4 = 24$) measurements.	147
4.27	Difference of wetted and active width between sections 10 and 11, repeatedly measured during the high flow phase of different cycles.	148
5.1	Comparison between the linear and the nonlinear solution (continuous and dashed lines respectively) after a 30 % reduction of the sediment supply from an initial condition $S_0 = 1\%$. An exponent $\gamma = 1.6$ has been adopted.	153
5.2	Comparison between the linear and the nonlinear solution (continuous and dashed lines respectively) after a reduction of the sediment supply which will produce the same long-term profile of figure 5.1 for the case of a single-thread channel. The Parker (1990) transport formula with an initial Shields stress $\theta_0 = 0.06$ has been adopted.	154
5.3	Evolution of the bottom level profile according to the hyperbolic model. Continuous line: $T_M^* = 0$, dashed line: $T_M^* = 0.05$	157
5.4	Variation in time of the bottom elevation during <i>Run 1</i> for several sections located at distance x from the inlet of the flume.	159
5.5	Bed level profiles during <i>Run 1</i> and analytical solution of the linear model (dashed lines).	160
5.6	Map of the initial part of the flume after 50 h and 115 h of the degradation phase. Elevation (in [cm]) is relative to the local linear trend.	160
5.7	Map of the initial part of the flume during the equilibrium (upper panel) and aggradation (lower 3 panels) phases. Elevation (in [cm]) is relative to the local linear trend.	161

5.8	Bed level profiles during <i>Run 2</i> and analytical solution of the linear model.	162
5.9	Evolution of the bottom level profile according to the diffusive model. Upper panel: finite domain; lower panel: infinite domain	172
5.10	Evolution of the bottom level profile according to the diffusive model in the case of a sudden bed level lowering at the downstream boundary.	173
5.11	Evolution of the bottom level profile according to the hyperbolic model in the case of semi-infinite domain. Upper panel: positive unsteady effect. Lower panel: negative unsteady effect. Continuous line: $T_M^* = 0$; dashed line: $T_M^* = 1 \cdot 10^{-2} a^*$	174
5.12	Evolution of the bottom level profile according to the volume-storage model in the case of semi-infinite domain. A unitary negative variation of $\Delta qs^*/ b^*$ is considered Upper panel: evolution at the unitary scale, at which the diffusion and the storage processes have the same magnitude. Lower panel: solution on a larger scale, for which the importance of the diffusion is smaller.	175
5.13	Variation through time of the solid discharge at $x = L$ in a semi-infinite channel for an instantaneous unitary variation of the input solid discharge Δqs^*	177
6.1	Sketch of the planimetric configuration.	180
6.2	Sketch of the notation. The dashed magenta line represents the obstacle at $x = 0$	181
6.3	Eigenvalues λ_j for the first ($m = 1$) mode. $d_s = 0.05$, $\theta_0 = 0.1$, $r = 0.5$ are adopted as parameters of the basic flow.	187
6.4	Structure of the solution for upstream and downstream semi-infinite channels in super and sub-resonant cases; the red line represent the section at which the boundary condition is applied.	187
6.5	Bottom elevation map for the sub-resonant case. The length of the obstacle (small magenta bump on the left bank) is $L = 10$. $\beta = 15.7$, $\theta_0 = 0.1$, $d_s = 0.02$, $r = 0.5$, the Meyer-Peter and Müller (1948) bedload formula are adopted as parameters, which give $\beta_R = 15.80$	197
6.6	Bottom elevation map for the super-resonant case. The length of the obstacle (small magenta bump on the left bank) is $L = 10$. $\beta = 15.9$, $\theta_0 = 0.1$, $d_s = 0.02$, $r = 0.5$, the Meyer-Peter and Müller (1948) bedload formula are adopted as parameters, which give $\beta_R = 15.80$	197

6.7	Longitudinal profiles at the left bank ($y = 1$) for the first $N = 10$ Fourier components of the analytical solution. The parameters of the basic flow are $\theta_0 = 0.1$, $d_s = 0.02$, $r = 0.5$ which leads to $\beta_R = 15.8$; the length of the obstacle is $L = 10$. $\Delta\eta$ represents the upstream scour produced by the $1D$ effects of the obstacle. .	198
6.8	Bottom elevation map for the sub-resonant case. Same parameters as in figure 6.5 but with a smaller aspect ratio ($\beta = 12.0$), which increases the damping rate of the downstream steady bars.	199
6.9	Bottom elevation map for the super-resonant case from the numerical experiments of Siviglia et al. (2013). Upper panel: sub-resonant ($\beta = 10.42$) case, lower panel: sub-resonant ($\beta = 16.72$) case. $\theta_0 = 0.1$, $d_s = 0.067$, $r = 0.3$ and the Wong and Parker (2006c) bedload formula have been adopted. The resonant point is $\beta_R = 13.28$	200
6.10	Bottom elevation map, for the symmetric obstacle under super-resonant conditions ($\beta = 28.0$, $\beta_R = 15.80$). The same parameters as in figures 6.5, 6.6 have been adopted.	200
6.11	Maps of bottom elevation without (left) and with (right) secondary currents. $\beta = 15.9$, $\theta_0 = 0.1$, $d_s = 0.02$, $r = 0.5$ are adopted as parameters; the first $N = 10$ Fourier components have been considered.	202
6.12	Intensity of the spiral flow τ_H/τ_0 for the $L = 2$ obstacle of figure 6.11c. Positive values indicates negative (left bending) curvature \mathcal{C} and consequently positive bottom velocities and stresses. . . .	203
6.13	Cross sectional profiles of the solution at $x = 0$ for a relatively short $L = 2$ obstacle. $\beta = 15.9$, $\theta_0 = 0.01$, $d_s = 0.02$, $r = 0.5$ are adopted as parameters; the first $N = 10$ Fourier components have been considered.	204
6.14	Bottom elevation map for the super-resonant case after imposing a sinusoidal perturbation of the transverse velocity at the upstream boundary. $L = 10$, $\beta = 15.9$, $\theta_0 = 0.1$, $d_s = 0.02$, $r = 0.5$, the Meyer-Peter and Müller (1948) bedload formula are adopted as parameters, while the amplitude of the upstream perturbation is of 0.1δ	206
6.15	Schematic picture of the boundary conditions required by both the steady and the time-dependent models. The arrows indicates the direction of propagation of the boundary information whereas flow is from left to right. $f(y)$ indicates a generic function of the transverse coordinate.	207

6.16	Spatial development of the amplitude of the complex-conjugate solution in super-resonant conditions according to the weakly non-linear theory of Seminara and Tubino (1992). $real(\lambda)$ represents the initial (linear growth rate); the initial amplitude has been arbitrary fixed to 0.1, whereas the asymptotic equilibrium $ A_e $ depends on the basic flow (different values are here represented by different colours).	207
6.17	Eigenvalues of the hyperbolic problem in the x -direction for different values of the hydrodynamic timescale T_w . $\theta_0 = 0.1$ are adopted as parameter; the dashed line represent the function $\lambda = -1 + Fr_0$	211
6.18	Eigenvalues of the hyperbolic problem for different hydrodynamic timescales T_w . The dashed lines have a unitary (± 1) slope.	213
6.19	Rectangular mesh adopted for thw numerical simulations. Only the obstacle region is here represented.	214
6.20	Steady bottom configuration of the <i>Sub 2</i> experiment.	219
7.1	Sketch of the two-cells model of Bolla Pittaluga et al. (2003). Arrows indicate sediment fluxes across the cells boundaries. . . .	226
7.2	Laboratory experiments Bertoldi and Tubino (2007) and numerical simulation of Siviglia et al. (2013), and theoretical curves of Bolla Pittaluga et al. (2003). The Manning resistance law, Parker (1990) transport formula and $r = 0.5$ have been adopted.	227
7.3	Geometrical configuration and notation.	228
7.4	Morphodynamic influence in the different branches when the main channel is in super-resonant conditions. Because upstream and downstream influence can occur simultaneously, the bifurcation node acts like a control section and can lead to an unbalanced solution.	242
7.5	Solution at $x = 0$ in super-resonant conditions according to the first $N = 1$ approximation. Continuous line: main channel; dashed line: secondary channels. The parameters of the basic flow are $d_s = 0.05$, $\theta = 0.08$, $r = 0.5$; the aspect ratio is $\beta = 16$. .	246
7.6	Example of bottom elevation obtained by considering $N = 50$ modes. Upper panel: super-resonant ($\beta = 15$) solution; lower panel: sub-resonant solution. $d_s = 0.05$, $\theta = 0.1$, $r = 0.5$, $\beta = 0.015$ are adopted as parameters, which leads to $\beta_R = 11.3$	247
7.7	Stability of flume and laboratory bifurcation (Bertoldi and Tubino, 2007; Siviglia et al., 2013) and distance between the aspect ratio β and the resonant value β_R , for different values of the Shields stress. The green, dashed line indicates the resonant conditions. .	249

7.8	Discharge ratio and inlet step of (Bertoldi and Tubino, 2007) and inlet step computed from the analytical model correspondent to the measured r_Q	249
7.9	Analytical solution for the diverging bifurcation. Elevations are expressed in $[m]$; $\theta_0 = 1.3$, $d_s = 2.52 \cdot 10^{-5}$, $\beta = 16$, $r = 0.5$, $C_0 = 12.5$, $B^* = 40 m$, $\alpha = 27.5^\circ$ are adopted as parameter, the first $N = 10$ harmonics have been considered. The angle adopted for these maps is not to scale.	251
7.10	Water surface and bottom elevation in a symmetric bifurcation, according to the numerical depth-averaged model of Edmonds and Slingerland (2008). The angle between distributaries is $2\alpha = 55^\circ$. $\beta \simeq 16$, $C \simeq 12.5$, $\theta \simeq 1.3$, $d_s = 2.5 \cdot 10^{-5}$ are the parameters of the main channel flow.	252
7.11	Example of the expansion of the first two modes in channel A as sum of N modes in the secondary channels.	262
7.12	Resonant aspect ratio as a function of the relative roughness and the Shields stress (for $r = 0.5$) with and without secondary currents (dashed and continuous lines respectively). The Parker (1990) transport formula has been adopted.	266
7.13	Bottom elevation $\eta_1\alpha$ of a diverging bifurcation similar to figure 7.9 but taking into account the secondary current. The colour scale is in $[m]$ and the contours interval is $0.33 m$	267
8.1	Braided reach of the River Rakaia (New Zealand, $43^\circ 34' S$, $171^\circ 45' E$); from <i>Google Earth, Digital Globe (2014)</i> . Flow is from left to right.	274

List of Tables

1.1	Grain size distribution of the reach (Williams et al., 2013b).	14
2.1	Most important parameters of the numerical simulations; the same values of Williams et al. (2013a) have been adopted.	31
2.2	Grain size classes adopted for the bedload estimation.	34
2.3	Estimated volume of the bedload transport for different storm events. $L = 2 \text{ km}$ and $p = 0.3$ are adopted as parameters.	41
2.5	Mean patches area, length and weighted length from the original method and after removing the smaller areas with the two mechanisms we propose. Both the results from the erosion and deposition map are reported.	63
3.1	Summary of the main features of the laboratory experiments.	77
3.2	Most important parameters of the numerical simulations.	90
3.3	Reach-averaged bedload from the <i>Average section</i> method and from <i>Delft3D</i> hydrodynamic simulations; two values of discharges and three different transport formulas have been tested.	92
4.1	Summary of the long-lasting, constant discharge runs of the W1 and W3 experiments.	123
4.2	Sediment transport rate from the equilibrium experiments of table 4.1. T_{skip} indicates the initial time needed for the development of the braided network, not considered in the computation of the averaged transport rate.	127
4.3	Mean, standard deviation and probability associated to each difference. In red we marked the cases for which the probability of the zero-mean hypothesis is $< 5\%$	132
4.4	Mean, standard deviation and probability associated to each difference. In red we marked the cases for which the probability of the zero-mean hypothesis is $< 5\%$	134
4.6	Mean, standard deviation and probability associated to each difference. In red we marked the cases for which the probability of the zero-mean hypothesis is $< 5\%$	146

4.7	Mean, standard deviation and probability associated to each difference. In red we marked the cases for which the probability of the zero-mean hypothesis is $< 5\%$	146
5.1	Main features of <i>Exp 1</i>	158
5.2	Main features of <i>Exp 2</i>	158
6.1	Most important settings of the numerical model.	215
6.2	Common parameters between the different experiments.	215
6.3	Hydraulic parameters of the different experiments.	216
7.1	Number of degrees of freedom (linearly independent solutions) for each channel, under sub and super-resonant conditions.	241
7.2	Range of the dimensionless parameters of the basic flow within the laboratory and numerical experiments of Bertoldi and Tubino (2007) and Siviglia et al. (2013) respectively.	248

Chapter 1

Introduction

Rivers represent a fundamental resource of water, energy, fishing, navigation and are recognised as an opportunity for sport and recreation activities. In addition they ensure more subtle but important functions, such as assimilation and dilution of pollutants, recycling of nutrients and recharge of groundwater resources. Rivers also represent an important ecosystem of high biodiversity, which sustain the life of a large variety of species.

Classic engineering has been mainly focused on the hydraulic protection against flooding risk and on the hydropower exploitation, often without much consideration about other aspect of the river functionality. Nonetheless, recent trend of river restoration and rehabilitation are based on a more comprehensive analysis of the fluvial system with more relevance of biological and ecological aspects. Such approach sometimes suggests intervention such as removal of some bank protections, re-opening or creation of secondary channels and mitigation of the hydropowering effect due to hydropower production (e.g. Klaassen et al., 2002).

The definition of sustainable and cost-effective intervention requires a deep knowledge of the river dynamics from many point of view: chemical, biological, ecological, hydrological, hydrodynamical, morphodynamical.

Different morphological patterns result depending on the flow regime, geological conditions, sediment availability and vegetation characteristics. Specifically, under conditions of relatively high stream power, coarse bed material and large sediment supply the multi-thread braided planform is likely to develop (e.g. Lane, 1957; Leopold and Wolman, 1957; Church, 2002).

1.1 The braided rivers

Braided rivers are characterised by complex and highly dynamics network of channels which develops on alluvial plains composed by gravel or sand.

A rigorous definition of braided rivers is not trivial; indeed there are multi-

1.1. *The braided rivers*

channel rivers which are usually not classified as braided (i.e. the so-called anastomosing pattern) or, on the other hand, braided rivers which under very high or very low flows show only a single wetted channel.

In addition, thresholds between channel patterns are often not sharp but a gradual transition from braided to different channel patterns is often observed (e.g. Gurnell et al., 2009). Additional terminology has been introduced to define the so-called wandering rivers which are defined by Desloges and Church (1989) as "irregularly sinuous channels, sometimes split about channel islands and in some places braided".

Murray and Paola (1994) defined the braiding phenomena as "the fundamental instability of laterally unconstrained free-surface flow over cohesionless beds" whereas according to Ashmore (2013) "Braided rivers have a distinctive alluvial morphology characterised by an unstable network of multiple channels separated by ephemeral bars".

From a morphodynamical perspective we could define as braided the rivers having complex and unpredictable dynamics due to the strong non-linear interaction between different processes (in-channel processes, bank erosion, bifurcations, avulsions, vegetation) which lead to a continuously-changing channel pattern.

This rapidly varying environment leads to much larger biological and ecological richness than other river patterns (e.g. Tockner et al., 2003, 2006)). The habitat diversity can be enhanced by secondary effects related to the morphological complexity such as the great variability of the temperature distributions (Tonolla et al., 2010) or the exchanges of groundwater at the local and at the reach scale (Doering et al., 2013).

Natural rivers are often populated by different species of riparian vegetation, which mutually interact with the morphodynamics, thus playing a fundamental role in the evolution of the river network (e.g. Tal and Paola, 2010; Coulthard, 2005; Bertoldi et al., 2011b,a).

These rivers are often heavily impacted by human activities which altered the functionality from both morphological and ecological point of view. In particular they are affected both by direct impacts, such as gravel mining, construction of embankments, channelisation and by variations at the catchment scale due to modifications of the land use, torrents regulations, construction of hydropower schemes and climate changes. For example Liebault et al. (2012) have shown a 53% decrease of the braided channel network French Alps during the last 200 years.

Many European rivers showed a large variety of physical, ecological, and environmental impacts due to anthropic pressure; in particular several braided rivers experienced a narrowing process, and in some cases a dramatic change of river pattern from multi-thread to single channel (e.g. Rinaldi et al., 2005; Gurnell et al., 2009).

Among the most significant stressors a key role is played by the sediment

1.2. Braided rivers morphodynamics and predictions



Figure 1.1: Picture of the River Rakaia (New Zealand, $43^{\circ}21' S$, $171^{\circ}27' E$). Courtesy of Bill Irwin (www.billirwinarts.com).

mining, which can lead to relevant incision both upstream and downstream the excavation site with consequent impacts on infrastructures, channel instability, water table lowering and sediment deficit in coastal zones (Rinaldi et al., 2005).

The more common practices carried out by agencies involved with river management about sediment mining are often very crude and poorly based upon scientific knowledge; therefore this problem requires a deeper understanding of the relevant processes (Rinaldi et al., 2005).

1.2 Braided rivers morphodynamics and predictions

The local properties of braided rivers (such as sediment transport or number of channels at a given section) show a strong spatial and temporal variability, which can not be predicted in detail for long times. This feature, typical of complex, non-linear systems, was clearly described by Paola (1996), who compared braiding phenomena with turbulence in fluids, which is a well-known complex phenomenon whose prediction is possible only from a statistical point of view.

For this reason it is often necessary to study the braided rivers morphodynamics through a statistical approach; for example it is possible to analyse how the reach-averaged or the time-averaged properties (width, total and active number of channels, sediment transport rate) depend upon the controlling conditions (slope, maximum available width, water and sediment supply, bed material).

Many laboratory and field studies have pursued those questions during the

1.2. Braided rivers morphodynamics and predictions

last decades (see Ashmore, 2013, for a comprehensive review).

The definition of reach-averaged quantities needs, first of all, to assess what is the length required for constructing a sufficiently robust statistics. Sampling criteria for braiding intensity indicate that a suitable reach length (needed to average out bar-scale variation in braiding) is at least ten times the channel width (Egozi and Ashmore, 2009). Behind this practical question there is a more conceptual problem concerning the length scale of the braided morphology.

Single-thread meandering rivers show a dominant length scale which is proportional to the channel width (e.g. Seminara and Tubino, 1992). Similarly, straight gravel-bed channels often develop migrating alternate bars (e.g. Ikeda, 1984; Lanzoni, 2000), whose wavelength is again scaling with the channel width.

The definition of a length scale of a braided river is more challenging, because of the coexistence of different spatial and temporal scales (Sapozhnikov and Fofoula-Georgiou, 1998). However, since braided channels are initiating from regular bars, it has been proposed (Ashmore, 2001) that the characteristic length scale is related to the pool-bar length; specifically laboratory and field observations (Hundey and Ashmore, 2009) suggest that the confluence-bifurcation length is $4 \div 5$ times the main channel width.

Evidences of internal scaling of the planimetric properties (e.g. Sapozhnikov and Fofoula-Georgiou, 1996; Lane, 2006) suggest that braided networks are self-similar fractals. However, it is not clear whether this similarity is exactly isotropic or if there is a degree of self-affinity (Sapozhnikov and Fofoula-Georgiou, 1998; Walsh and Hicks, 2002). The temporal scale of the channels kinematic is proportional to the square root of the length (Sapozhnikov and Fofoula-Georgiou, 1997), which correspond to the Froude scaling of the hydrodynamics and morphodynamics between rivers having different sizes.

The external scaling (i.e., similarity between rivers of different sizes, see figure 1.2) is implicit in the success of physical models of braiding in reproducing the morphodynamics of full-scale braided rivers (e.g. Hong and Davies, 1979). Specifically, Froude similarity has been proven to hold on a braided range of scales, from laboratory flume to large rivers (e.g. Young and Warburton, 1996).

The definition of the braiding richness requires the specification of suitable indexes. One of the most natural is the average number of channels (e.g. Egozi and Ashmore, 2008) across river sections. Only a subset of the total channels in a braided river are transporting bed material load and actively forming the braided pattern and river morphology; Bertoldi et al. (2009d) has shown the role of the dimensionless stream power in defining the active index, whereas the total number of channel appears to be more related to the dimensionless discharge. The ratio between active and total number index ranges from 0.3 to 0.8 depending on the stream power (Bertoldi et al., 2009d; Egozi and Ashmore, 2009), with a typical value around 0.4. Similarly Bertoldi et al. (2009d) suggested that the wetted width increases with discharge and the active width (i.e. the fraction of river width where sediment transport occurs) increases with the

1.2. Braided rivers morphodynamics and predictions

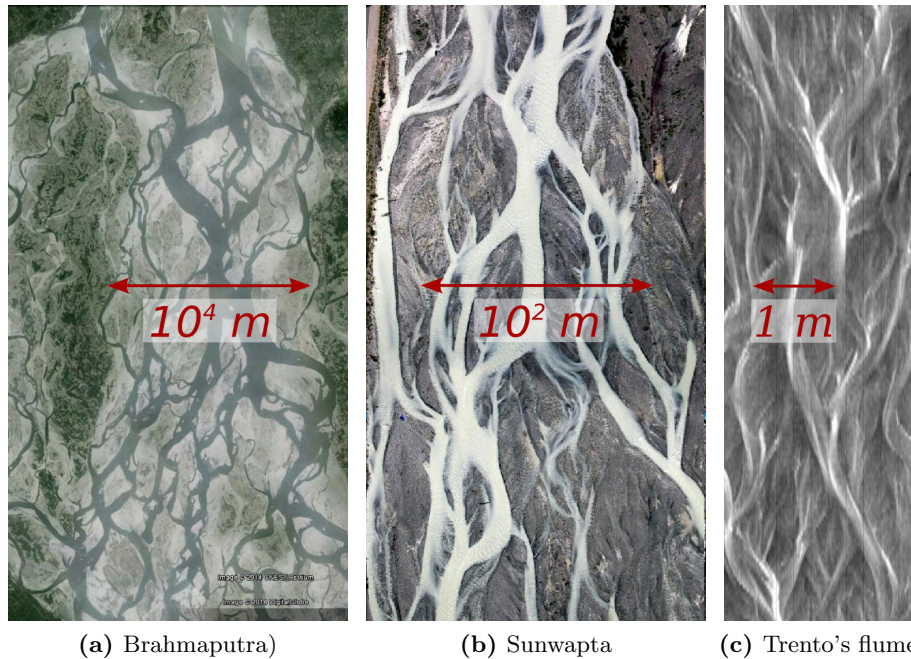


Figure 1.2: Example of braided rivers of different scales. a) Brahmaputra river (Bagladesh-India $25^{\circ}53' N$, $89^{\circ}54' E$), from *Google Earth, Digital Globe (2014)*; b) Sunwapta river (Alberta, Canada), from Bertoldi (2005) c) Flume experiment (Trento, Italy); flow is from the top to the bottom.

stream power.

Much less is known about the effect of the variation through time of the controlling conditions, namely water and sediment supply.

Egozi and Ashmore (2009) described the adjustment of channels, the change of braiding index and the associated temporal scales after stepwise increments of the liquid discharge; they found that the stable value was achieved via gradual increase of total braiding intensity while active braiding intensity adjusted very quickly to the increased flow.

Few studies investigated the morphological response of braided network to variations of the sediment availability; reducing the feed rate in a laboratory braided network, causes an incision of the main channel, in some cases, a transition to single-thread planform (Germanoski and Schumm, 1993; Marti and Bezzola, 2006; Madey et al., 2009; Pryor et al., 2011).

1.3. The fundamental unit processes



Figure 1.3: Bifurcation of the River Sunwapta (Alberta, Canada). From Bertoldi (2005). Flow is from left to right.

1.3 The fundamental unit processes

1.3.1 Bifurcations

Bifurcations represent a basic mechanism for developing and sustaining braided networks.

Theoretical approaches based on one-dimensional models, and equipped with a suitable description of the two and three-dimensional dynamics at the bifurcation (Wang et al., 1995; Bolla Pittaluga et al., 2003), as well as laboratory (Federici and Paola, 2003; Bertoldi and Tubino, 2007) and numerical experiments (Edmonds and Slingerland, 2008; Kleinhans et al., 2008; Siviglia et al., 2013), demonstrated that the aspect ratio (i.e. the width to depth ratio) is the key parameter controlling the distribution of water and sediment between the distributaries.

Specifically, it is clear that in gravel-bed channels small aspect ratios and relatively high Shields stresses lead to a stable, balanced configuration. Conversely, in a wide channel with low shear stress an instability often arises and produces an unbalanced configuration, with an uneven repartition of water and sediment fluxes between the distributaries. Such an unbalance condition is promoted by the process of bank erosion; indeed, as predicted by the theoretical model of Miori et al. (2006), this process tend to increase aspect ratio and a to decrease the Shields stress, which invariably leads to unbalanced bifurcations.

1.3.2 Confluences

Anabranch confluences and associated bars are fundamental in the braided river morphodynamics (Ashmore et al., 1992).

The dynamics of confluences has been extensively studied in the last decades

1.3. The fundamental unit processes

both in the field and in laboratory models. The morphological configuration depends upon the discharge ratio and the angle between the tributaries. Typically the flow convergence induces a double-helical circulation which drives the sediment towards the bank; this leads to a scour region with the characteristic spoon or trough shape (Ashmore, 2013). Because of the high relevance in engineering application many studies (e.g. Mosley, 1976; Ashmore and Parker, 1983; Best, 1986) have focused on the depth of the scour zone, which is typically $2 \div 3$ times the depth of the channels and decreases with the discharge ratio between the confluent branches (e.g. Best and Rhoads, 2008). Where the two currents join, a mixing interface develops and a shear layer occurs (Rhoads and Sukhodolov, 2008), whose intensity depends on the momentum differences between the incoming currents.

In the case of mobile banks the orientation of the downstream branch depends on the water and sediment supply of the tributary channels (Ashmore, 2013).

1.3.3 Bars

Migrating alternate bars are large-scale bed forms characterised by a sequence of steep consecutive diagonal fronts with deep pools at the downstream face and gentler riffles along the upstream face, whose height and wavelength scale with flow depth and channel width respectively (Lanzoni, 2000).

The formation of alternate bars in sand and gravel bed channels have been extensively studied through analytical theories, numerical simulation, laboratory models (e.g. Ikeda, 1984; Jaeggi, 1984; Colombini et al., 1987; Tubino et al., 1999; Lanzoni, 2000).

In particular, analytical theories have demonstrated that migrating alternate bars are the fundamental mechanism of instability of gravel bed channels and have identified the aspect ratio as the crucial parameters controlling this process; indeed for relatively narrow channels any small perturbation of the bottom is damped in time, whereas for aspect ratio higher than a critical threshold migrating bars develop. The length of these migrating bed waves is typically $7 \div 12$ times the width.

A second class is represented by the steady bars, also called forced bars because induced by channel curvature (Blondeaux and Seminara, 1985; Seminara and Tubino, 1992), variations of width (Repetto et al., 2002; Luchi et al., 2011), localised obstacles (Struiksmas and Crosato, 1989; Crosato et al., 2011). The wavelength, longer than for migrating bars, typically falls in the range of $15 \div 30$ times the channel width.

Laboratory experiments confirm the importance of bars in the initial development of braiding (Jang and Shimizu, 2005; Bertoldi and Tubino, 2005; Federici and Paola, 2003). Indeed, starting from a straight single-thread channel the development of alternate (mode 1), central (mode 2) or multiple (mode

1.4. *The sediment transport*

> 2) bars causes the development of a sinuous channel and ultimately the opening bifurcation and the formation of a braided network.

The actual development probably depends on the initial conditions. According to Bertoldi and Tubino (2005), starting from a narrow straight channel an initial widening due to the uniform bank erosion occurs. Once the critical aspect ratio for the formation of alternate bars (e.g. Colombini et al., 1987) a train of downstream migrating bars appears; this alternating bottom perturbation causes a deviation of the flow field, a nonuniform bank erosion and consequently leads to a regular sequence of bumps and, eventually, to a sinuous channel. At the same time the channel keeps widening until initial bifurcation develops via chute cutoff.

When the aspect ratio is relatively large the theories show the formation of central or multiple bars. Several works investigated the role of both migrating and steady bars on the development of braided rivers (e.g. Parker, 1976; Fredsoe, 1978; Paola, 2001; Crosato and Mosselmann, 2009), showing the role of the channel aspect ratio in determining the initial bar type and the number of channels.

1.4 The sediment transport

Direct measurements of bedload in natural braided rivers is very complicate, so that available data often have limited spatio-temporal extension and are typically measured during flood events of small magnitude.

Due to these difficulties, but also because of the possibility of a much higher control of the experimental conditions, the sediment transport in braided networks has been mainly investigated through laboratory-scale physical models. An exact dynamic similarity between the prototype and the reduced scale model is usually impossible to achieve; however, as reported by many studies (e.g. Young and Warburton, 1996; Warburton, 1996; Shvidchenko and Kopalani, 1998), a well designed laboratory model is able to reproduce in both qualitative and quantitative way the phenomena observed in the real-scale rivers.

Flume experiments have revealed an high variability of the solid transport over a broad range of temporal scales (e.g. Ashmore, 1988; Hoey and Sutherland, 1991); temporal fluctuations of the bed load (Ashmore, 2001) can be related to the frequent breakdown of an organised morphology (for instance due to chute cut-off or avulsion), with increased activity of the network during the high transport pulses (e.g. Ashmore, 1991).

Since the reach-averaged transport rate is usually well correlated with the total discharge, several empirical functions have been developed to predict average bedload rate from river discharge or stream power (Thompson, 1985; Davies, 1987; Ashmore, 1988; Young and Davies, 1990, 1991; Shvidchenko and Kopalani, 1998). However, it is not clear how this relationships depends on

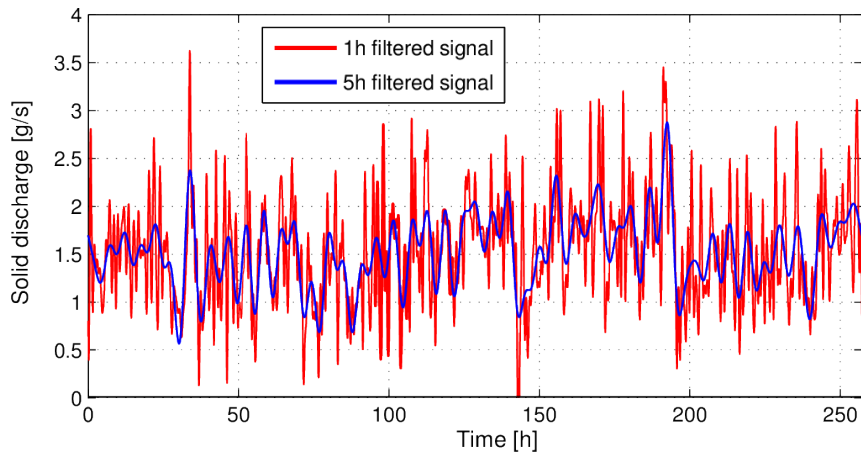


Figure 1.4: Example of sediment transport measured during one of our long-term experiments. A filtering algorithm which removes the frequency components faster than 1 h and 5 h (red and blue lines respectively) has been applied.

the experimental conditions and to what extent the coefficient obtained from the regression of experimental data are generally applicable.

After the first attempts to predict this flux through standard transport formulae (Carson and Griffith, 1987; Ashmore, 1988; Griffith, 1989) it became evident (Paola, 1996; Nicholas, 2000; Ferguson, 2003) the great importance of spatial variability of the hydraulic parameters, bottom morphology and grain size. Indeed the local transport intensity varies nonlinearly with the shear stress and consequently the reach-average bedload flux depends not only on the mean Shields stress but also on its spatial distribution across the section. This effect is particularly significant in braided networks, where the transport rate can be several times bigger than in the equivalent uniform, rectangular cross-section (Bertoldi et al., 2009a).

For this reason approaches based on the probability density function of the shear stress, and in particular on the Euler gamma function, have been introduced (Paola, 1996; Nicholas, 2000), whereas alternative methods have been proposed by Ferguson (2003); Bertoldi et al. (2009a).

An opportunity to estimate (a posteriori) the reach-averaged transport rate on the basis of repeated topographical surveys, is provided by the so-called morphological methods (Ashmore and Church, 1998), which can be divided in two categories, namely the budget method and the path-length method.

The first one is simply based on the net volume variation in a control volume, and therefore needs knowledge of the flux across one boundary condition; this problem can be solved by applying a bedload formula (e.g. Ham and Church, 2000) assuming zero flux at one boundary section (e.g. McLean, 1990; McLean and Church, 1999) or considering a non-negative flux throughout the reach (Ferguson et al., 1992; Goff and Ashmore, 1994).

1.5. *Aims and methods of the present study*

The path-length is defined as the travel distance of the sediment particles between the surveys; it is easy to prove (e.g. Einstein, 1937; Ashmore and Church, 1998) that the sediment transport can be calculated as the product between this path-length and the eroded (or deposited) volume. Neill (1971) applied this method for the case of meandering rivers; for the case of braided rivers a match-up of the erosion and deposition areas is often not possible so that an estimate of the mean travel distance should be inferred, for instance from pool-pool or bar-bar spacing. Evidence about the connection between morphological change and bed-load flux makes braided rivers a candidate for applying this path-length method (Ashmore, 2013); nevertheless a robust procedure to obtain this estimate from morphological data is still missing.

1.5 Aims and methods of the present study

General aim of the present work is to provide significant insight to the braided rivers morphodynamics and sediment transport, with particular reference to the effects due to the flow unsteadiness.

More specifically, we are interested in understanding how the river morphology and its dynamics depends on the different conditions (sediment substrate, discharge, slope, width, sediment supply) and what is the response of the system when these conditions are changing through time (as always the case in natural rivers).

Knowledge of this river morphodynamics and sediment transport is fundamental from the river management point of view. For instance it is important to know how river respond to: increasing confinement rate due to the construction of banks or levees; variations of the hydrological regime and sediment availability following dam construction, torrents regulation or variations of land use; changes of the vegetation pattern due to direct or indirect stresses; alterations caused by gravel mining.

As we have briefly seen within this introduction, a lot of work has been done to address these questions, and many of them have been, at least partially, answered. However several points are still unclear, unanswered or unexplored, so that additional effort is needed. New possibilities for further investigations are nowadays possible, thanks to the development of new technologies, which enable more powerful numerical computations, accurate large-scale measurement of braided morphology and increasing possibilities to share rich databases.

Aim of the *SMART* PhD programme is to strengthen the connection between different approaches for studying rivers and their tidal systems. Following this philosophy we try to take advantage, in an integrated way, different state of the art methods and available datasets, with the final aim to increase the scientific knowledge which supports river management policies.

Several approaches can be followed to investigate braided rivers morphodynamics and sediment transport changes in response to the external conditions.

1.5. *Aims and methods of the present study*

Most of existing studies are based either on field observations or on laboratory experiments.

Physical laboratory models, despite representing only an approximation of the processes (Young and Warburton, 1996; Paola et al., 2009) have revealed as a powerful tool for investigating the morphodynamical response to varying controls.

Field observations allows for a direct study of the braided network in its complexity and have recently received a great impulse, thanks to the development to new technologies which enable more accurate, extended and cost-effective surveys. Nevertheless some quantities, primarily the bedload transport, remain very difficult to measure in the field, so that at present no direct methods exist for a widespread survey of a complex and heterogeneous braided river.

More recently, the development of numerical models opened new possibilities for exploring the mechanisms which drive the braiding dynamics. Among this category, we can distinguish between approaches based on the shallow water schemes (usually two dimensional, e.g. Shimizu and Itakura, 1989; Jang and Shimizu, 2005) and methods based on reduced-complexity description, such the cellular automata models (e.g. Murray and Paola, 1994; Murray, 2003). Despite being still under development and having limited capability of quantitative description, they provide great opportunity to explore the fundamental processes and their non-linear mutual interactions.

Due to the complexity and nonlinearity of the braiding dynamics the possibility for analytical treatment of the governing equations is limited. However, as mentioned above, some specific processes such as bifurcations, alternate migrating bars, forced bar caused by channel curvature, have been successfully afforded with analytical solutions (e.g. Blondeaux and Seminara, 1985; Colombini et al., 1987; Zolezzi and Seminara, 2001; Repetto et al., 2002; Bolla Pittaluga et al., 2003; Luchi et al., 2011).

The complexity of the braided river morphodynamics suggests the best way to overcome the limitations of each specific method is to adopt an integrated approach, where different tools are combined in order to provide the information needed for a better understanding of the river processes.

For example analytical approaches, being limited to very specific problems, can not substitute laboratory investigation; nevertheless they allow for a complete control of the model outcome and a deeper understanding of the physical mechanisms. Similarly numerical models offers exceptional opportunity to obtain a description of the non-linear interaction among different processes and to obtain complete picture of the spatio-temporal variation of the relevant quantities.

At the same time we should not forget that models are by definition only a simplified representation of nature.

On the other hand, studying real rivers is difficult because of the large extension to survey, the relatively slow temporal evolution, the large number

1.5. Aims and methods of the present study

of involved processes (included biological components). Moreover the single elements are not independently acting but are strongly interacting, thus leading to a complex and largely unpredictable dynamical system.

Therefore we preferred not to focus on a single and specific method by to adopt a wider perspective, tackling the problem in different ways, namely

- field topographic measurements with recent techniques.
- statistical description of the braided river morphology at a reach scale;
- laboratory modelling of small-scale braided networks;
- numerical modelling of the braided river hydrodynamics;
- direct analytical solution of the depth-averaged shallow water model through perturbation approaches;

1.5.1 The study rivers

In order to exploring the properties of braided rivers and for the comparison with model results, we identified few field sites. This choice was principally based on two criteria: a) the availability of suitable, accurate and complete dataset; b) the selection of rivers having significantly different conditions in terms of width, slope and water discharge.

We chose three, well-known and studied, field sites, namely the Rees (New Zealand), the Tagliamento (Italy) and the Sunwapta (Canada) rivers.

The Rees River, New Zealand

The Rees River drains an area of 405 km^2 in the east side of Southern Alps, New Zealand. The catchment is characterised by rapid uplift (Beavan et al., 2010), erodible bedrock (Turnbull, 2000) and high annual precipitation (Henderson and Thompson, 1999) and consequently provides a significant bedload supply. Mean annual precipitation measured at Rees Valley Station (lower catchment) in the period $1988 \div 2011$ is 1462 mm (Williams et al., 2013b). The Rees is 41 km long and together with the adjacent Dart River, has formed a major delta which is prograding in the Lake Wakatipu (Wild et al., 2008).

The study reach has got an extension of $2.5 \times 0.8 \text{ km}$ and is located approximately 7 km upstream the lake. The coarse gravel deposits on the braidplain are approximately 17 m deep and underlain by lacustrine silts and clays (Williams et al., 2011). The median grain size measured in 28 sites throughout the reach is 19.9 mm , with d_{16} and d_{84} fractions of 10.4 mm and 35.2 mm respectively (table 1.1, from Williams et al. (2013b)). Cross-section surveys of the Rees River braidplain have been undertaken on five occasions between 1984 and 2006.

1.5. Aims and methods of the present study

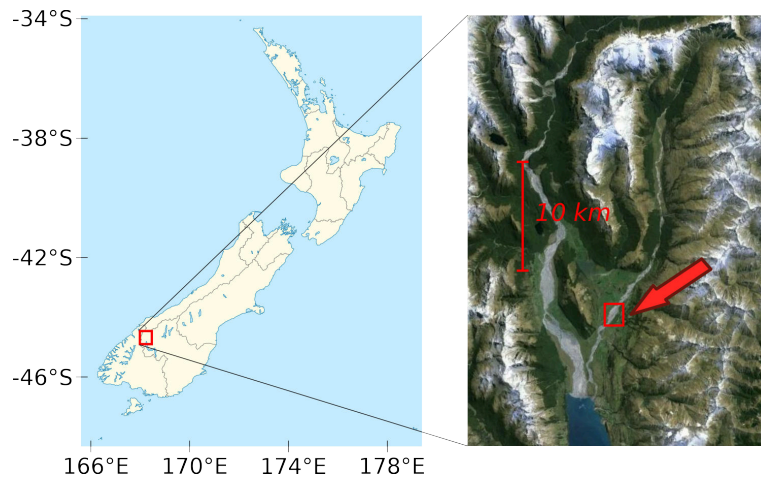


Figure 1.5: Location of the study reach of the Rees River (Otago, New Zealand).



Figure 1.6: Aerial view of the study reach of the River Rees. Flow is from left to right.

The reach slope is around 0.57% and at low flows approximately the 7% of the braidplain is typically inundated (Williams et al., 2013b). The few vegetated patches within the study reach are growing on unstable bars which are susceptible to reworking during flow pulses.

The Tagliamento River, Italy

The Tagliamento River is a large gravel-bed braided river in North-East Italy, relatively pristine and highly dynamic (e.g. Tockner et al., 2003; Bertoldi et al., 2010).

The total length of the river is 178 km, the catchment area is 2870 km² and the width of the active corridor is up to 1.5 km (Van der Nat et al., 2003). The upper part of the catchment experiences precipitations up to 3000 mm (Doering et al., 2013). Absence of large artificial reservoirs ensures nearly-natural flow

1.5. Aims and methods of the present study

Percentile	Mean [mm]	Standard dev. [mm]
d_{16}	10.4	5.0
d_{50}	19.9	10.4
d_{84}	35.2	19.2
d_{90}	40.5	21.9

Table 1.1: Grain size distribution of the reach (Williams et al., 2013b).

(Bertoldi et al., 2009b), characterised by in bimodal (with spring and autumn peaks), flashy, pluvio-nival hydrological regime (Welber et al., 2012).

At the Pioverno gauging station (drainage area 1880 km^2) the maximum discharge over the period 1932 ÷ 1976 was $4050 \text{ m}^2 \text{ s}^{-1}$, with mean and minimum discharge $81 \text{ m}^3 \text{ s}^{-1}$ and $15 \text{ m}^3 \text{ s}^{-1}$ respectively (Surian et al., 2009a).

Our focus is on a 21 km -long reach where airborne *LiDAR* data are available after the survey in May 2005. Bertoldi et al. (2011a) estimated the topography of the submerged areas on the basis of the red-over-green band intensity of colour air photographs; furthermore they evaluated the bed morphology under vegetated area by appropriately filtering the high density *LiDAR* measurements. Median grain size and slope within the reach are substantially constant (Bertoldi et al., 2011a) and equal to $d_{50} = 40 \text{ mm}$ and $S = 0.35 \%$ respectively.

Although the water level measurements is measured at different locations along the river, quantification of the hydrological regime is still uncertain due to the difficulties in constructing a reliable flow-water stage relationship (Welber et al., 2012). A rough estimation is provided by Bertoldi et al. (2010) who reported a 3-years return period discharge of $Q = 1700 \text{ m}^3 \text{ s}^{-1}$.

The Sunwapta River, Alberta, Canada

The Sunwapta is a small pro-glacial river in the Jasper National Park, Alberta, Canada (Ashmore et al., 2011). Due to its accessible location and predictable hydrological regime it has been extensively studied (Ferguson et al., 1992; Goff and Ashmore, 1994)

The study area is located 3.5 km downstream the Athabaska Glacier, where the river is braided, not vegetated and is around $100 \div 150 \text{ m}$ wide (see figure 1.8). The reach slope is approximately 1.5% and the grain size is around $d_{50} = 4 \text{ cm}$ and $d_{90} = 11 \text{ cm}$. The peak daily discharge due to the glacier melting, measured over a period of 17 days in 1999 and 12 days in 2003, ranged from 8 to $18 \text{ m}^3 \text{ s}^{-1}$. The 16 cross-sections measured during August 1999 cover a range of 150 m (approximately one river width).



Figure 1.7: Image of the River Tagliamento from Monte Ragogna in the upstream direction. From www.comitato-arca.it.

1.5.2 The experimental setup

Flume experiments were performed at the hydraulic laboratory of the Trento's University (figure 1.9). The facility is 25 m long, 2.9 m wide and covered by a $\simeq 0.2$ m thick layer of well-sorted sand with median diameter $d_{50} = 1$ mm.

The slope can be changed (within the range $0 \div 1.7$ %) by varying the thickness of the sand mattress along the flume. A schematic of the experimental setup is shown in figure 1.10.

Water supply is recirculated using a pump controlled by an inverter, which enables to adjust the discharge with a resolution of 0.1 $l s^{-1}$. The sediment is supplied by a helical screw conveyor, for which a calibration curve has been constructed.

Input water and sand fluxes can be automatically controlled through a computer software.

An electromagnetic current meter enables to measure the pumped water flux while the output sediment is collected and weighted by a system of load cells (resolution of 0.01 l/s and 0.01 kg respectively). A laser scanner mounted on a carriage, moving on two rails through the flume, enables to measure the bottom topography with a vertical resolution of 0.1 mm; because of the limited penetration of the laser beam into water, the runs must be suspended in order to have a dry channel network. A second carriage is used for the initial levelling of the bed and for manually measuring wetted and active area during the run.

1.6. Outline of the thesis



Figure 1.8: Picture of the River Sunwapta (Alberta, CA). Flow is towards the camera. From Bertoldi (2005).

The flume width can be reduced by placing a plastic sheet at the centre of the flume, which confines the stream between two straight banks.

1.6 Outline of the thesis

The present manuscript is organised in six main chapters, which follow the different methodologies we adopted for approaching the problem, starting from the analysis of complex, natural braided river, increasing the level of abstraction with laboratory and numerical models and ending up with the theoretical study of the fundamental unit processes of channel bifurcations.

This section provides the thread which links the contents of the different parts of this thesis.

Within *Chapter 2* we study the morphological changes during different flow events in a natural gravel-bed braided river (the Rees River, NZ) and we propose a morphological method to estimate the sediment transport rate on the basis of repeated topographic measurements.

Such an analysis is possible *a posteriori*, once the river morphology and its changes through time are known. However, if we are interested in predicting the long-term morphological evolution and its response to varying external controls,



Figure 1.9: Photograph of the Trento's flume; from Welber (2013). Flow is towards the camera.

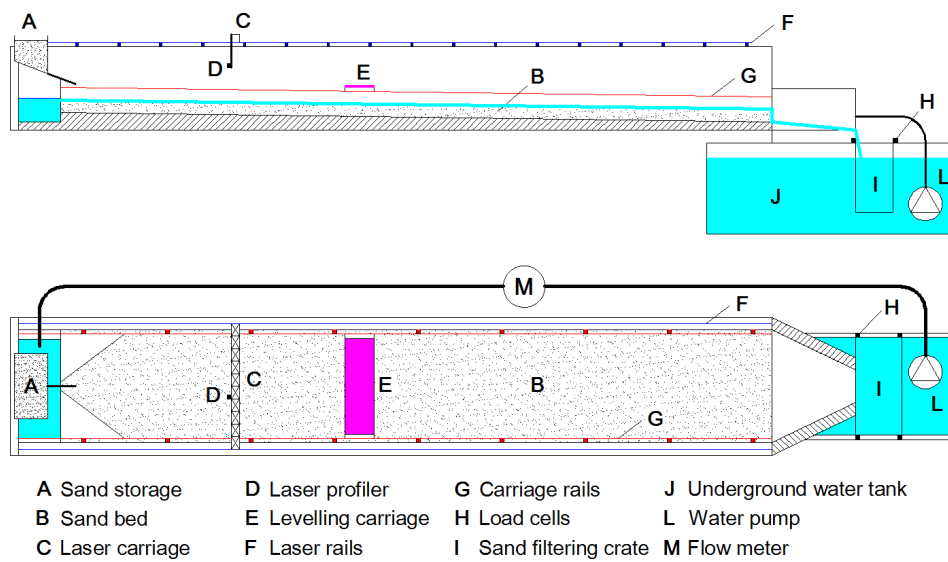


Figure 1.10: Sketch of the Trento's flume. Upper part: longitudinal section; lower part: planimetric view. Based on the Welber (2013).

1.6. Outline of the thesis

we must change our approach and study the regime morphodynamics.

This is possible through laboratory models, which enables to fully control the experimental conditions. For example we can study the regime morphology attained by a braided network subject to constant flow. The following *Chapter 3* is devoted to the analysis of how these regime morphological properties and the sediment transport at the reach-scale depend on discharge, slope and confinement width.

This represents only a first, albeit important, starting point. Nevertheless the constant-discharge experiments are far from the typical hydrological regime of natural braided river, which shows flow pulses and floods rapidly varying through time. Within *Chapter 4* we study the role of the discharge unsteadiness on the sediment transport; this is possible through a series of repeated experiments which enable to build an ensemble statistics of the transport rate during varying flow.

The second controlling factor which may vary in a natural river is the sediment supply, whose the augmentation or reduction can significantly impact the braided morphodynamics. Albeit clearly connected with the variation of water discharge, the effect of the sediment availability is different; indeed the diverse storage capacity leads to completely distinct spatial and temporal scales. This processes is explored in *Chapter 5* where we analyse, again using laboratory experiments, the propagation of the aggradation and degradation waves resulting from change of the sediment feed rate.

Within the third part of the present manuscript, we studied the problem from a different perspective, abandoning the reach-scale description and focusing on the single unit processes. Indeed, braided rivers are formed by a series of fundamental unit process, which act at similar temporal scale and interact each other in a complex, non-linear way. Albeit this complex interaction, it is sometimes useful to study the individual processes separately. Indeed isolating the elementary problems from the remaining complex system enables to deeply study its morphodynamics. This is not different from what we do in the previous chapter, when we isolate the reach scale from the large, complex and unpredictable external world.

Specifically, we focus on one of the fundamental processes of braiding network morphodynamics, namely the channel bifurcations. The goal is to provide analytical support to the experimental findings of Bertoldi and Tubino (2007), who noticed a strong connection between the bifurcation morphodynamics and the theory of the morphodynamic influence derived by Zolezzi and Seminara (2001). We begin our study by considering a simple problem, which clearly shoes the phenomenon of the upstream influence. Indeed within *Chapter 6* we solve the two-dimensional, depth-averaged model for a localised obstacle in a straight gravel-bed channel. Using a perturbation method we derive the analytical solution, which highlights the role of the aspect ratio to define the upstream or downstream direction of the morphodynamic influence.

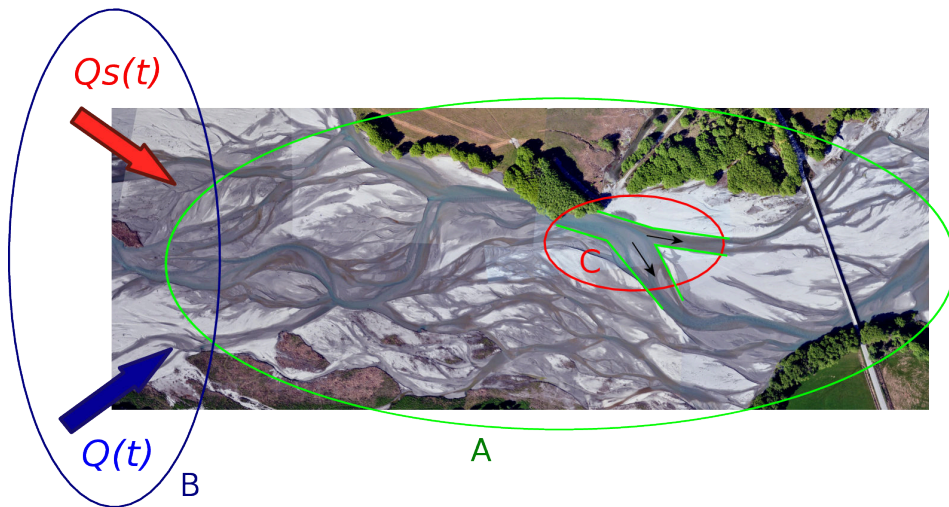


Figure 1.11: Representation of the main perspectives we adopted for the analysis of a braided reach.

This analysis represents a first step to understand the dynamics of channel bifurcations. Indeed in *Chapter 7* we adopt the perturbation approach to solve the $2D$ model to the more complex geometrical configuration which represents a diffluence. This approach enables to explore the close relation between the upstream relation and the bifurcation instability which is responsible of the unbalance configuration often observed in gravel-bed bifurcations.

1.6. Outline of the thesis

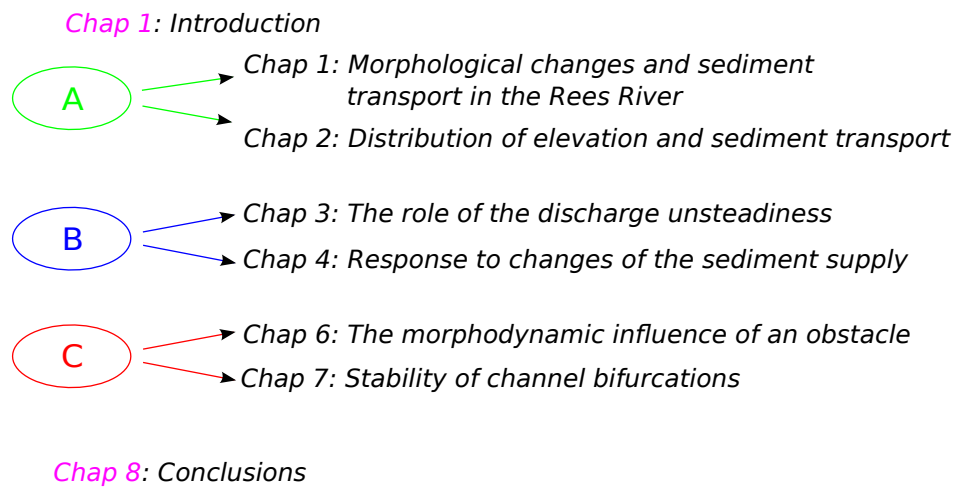


Figure 1.12: Schematic description of the thesis structure. Letters refers to the three main parts: 1) Study of the reach-scale morphodynamics; 2) Effect of the variation through time of water and sediment supply; 3) Analysis of fundamental unit processes.

Chapter 2

Morphological changes and sediment transport: The Rees River (New Zealand)

2.1 Introduction

It is well known that braided rivers are remarkably active even for discharges well below bankfull (e.g. Surian et al., 2009b; Bertoldi et al., 2010). However quantitative analysis, through direct measurements of scour and fill volumes is particularly challenging in braided rivers. Indeed multi-channel networks are typically shallow, highly heterogeneous and change rapidly through time; therefore high temporal resolution and accuracy is needed to capture the topographical variations at the flood event scale Williams et al. (2013b).

In spite of recent developments in new observation technologies such as digital photogrammetry, Structure from Motion and airborne *LiDAR* (Gao, 2009; Marcus and Fonstad, 2010) difficulties persist with the acquisition of morphological data at time and space resolutions suitable to quantify fluvial morphodynamics. In particular, as pointed out by (Ashmore, 2013) there are not yet sufficient data to determine how the frequency distribution and areal extent of elevation changes depend on the flood intensity.

The present work aims to address this weakness, and attempts to quantify the morphological variation and study the linkage between volumes and distributions of morphological changes and flood characteristics. This has been possible thanks to the dataset introduced by Brasington (2010) which quantifies the changing morphology of a 2.5×0.8 km reach of the Rees River in New Zealand, through sequential floods in 2009-2010 (Williams et al., 2013b).

A second relevant problem this chapter seeks to address is application of morphological change data to estimate sediment transport rate indirectly.

Direct measurement of bedload in a braided reach is complicated because of

2.1. Introduction

the high number of samples needed to cover the lateral and temporal variation (Bertoldi et al., 2009a). Many existing indirect methods, such as sediment budgeting are often not applicable because of they need the knowledge of the material inflow which is often difficult to estimate.

An alternative morphological method is based on the travel distance of the particles during the event, (e.g. Einstein, 1937; Ashmore and Church, 1998). The estimation of this distance, called also path length is the main challenge of this approach. As pointed out by Pyrcce and Ashmore (2003a), existing research has often assumed or inferred that the travel distance is correlated with the morphological scale and in particular with the meander wavelength (e.g. Neill, 1971, 1987), the bar-pool distance or multiples of channel width (McLean, 1990; Ham and Church, 2000) or with the distance between sites of erosion and deposition (Goff and Ashmore, 1994; Ashmore and Church, 1998; McLean and Church, 1999; Eaton and Lapointe, 2001). In many of these studies the estimated bedload is in a good agreement with more traditional methods such as trap sampling or bedload functions (Pyrcce and Ashmore, 2003a).

However this is in contrast with direct measurements of the path length using tracers, which reveal a large variety of results (Pyrcce and Ashmore, 2003a) usually poorly related with the bar spacing. As explained by Pyrcce and Ashmore (2003b) this is probably due to the low Shields stresses which cause partial mobility or to discharges which are well below the formative; indeed they observed that in a laboratory meandering and alternate bars channels the formative discharge produces a symmetric distribution of the path length which well represented by the bar pool (or meander wavelength) spacing. These considerations suggests that attention must be paid to generalise results obtained for a particular river pattern (i.e meandering) and for particular flow conditions (i.e. bankfull) to different systems (i.e. braided rivers) characterised with a different morphodynamics.

Even more complex is the application of the method to braided rivers where there is neither regular spacing between bar and pools nor a clear connection between the scour and deposition areas. Ashmore and Church (1998) identified two possible approaches for estimating the path length on the basis of morphological variations. The first procedure, called match-up, requires the identification and paring of erosion and deposition areas. While clear in principle, this approach is often not applicable because of the sediment redistribution across the network (transferring between braids during avulsions for example) makes direct matching patches often impossible. The second possibility is to determine a mean travel distance on the basis of the pool-pool or bar-bar spacing (Hundey and Ashmore, 2009; Ashmore, 2013)

While these approaches offer indirect solutions to path-length estimation, their application is not straightforward and difficult to validate for a number of reasons. First, there current exist datasets that could provide a adequate morphological and transport data (and similarly no laboratory models) to validate

the model and quantify the capability to predict the reach averaged bedload. Secondly, as highlighted by Ashmore and Church (1998), whether topographic surveys before and after a flow event alone, are sufficient to capture the patterns of scour and deposition that may involve multiple cycles of cut and fill within a single flood. Indeed laboratory modelling by Lindsay and Ashmore (2002), revealed that compensatory fill and cut occurs over a wide range of temporal scales and makes practically impossible to capture all the volume variations. Thirdly, there are insufficient studies that quantify the dependence of the path length on the elapsed time. While, this effect has been proven not to be important in meandering laboratory channels, no similar studies are available for braided networks. In particular it is not clear to what extent an estimation based on the characteristic length is representative of the transport with different discharges and in particular during below threshold flow. Finally, there is the more practical issue of manually identifying channels, bifurcations and confluences in order to measure the characteristic length scales - observations which themselves may also be biased by the water stage.

The research presented here outlines a novel procedure, based on the automatic detection and measurement of erosion and deposition patches, to identify the scale of the morphological changes and this is used to examine the sensitivity of transport rates estimated from repeated morphological surveys of a braided reach of the Rees River.

2.2 The study site

2.3 Data collection

Within the Rees-scan project detailed topographic surveys were undertaken before and after 10 sequential storm events covering a wide range of flow magnitudes and durations, over the period October 2009 to May 2010 (Brasington, 2010). At the same time continuous hydrological data were acquired, thereby allowing an estimate of the discharge history.

This section describes this dataset briefly and the procedures followed used to construct the relevant topographic models. For more comprehensive and detailed explanation see Williams et al. (2013b).

2.3.1 Topographic data

The backbone of the surveys involved data acquired using the *ArgoScan* system, which incorporated a Terrestrial Laser Scanner, an *RTK-GPS* and a panoramic camera mounted on an amphibious vehicle (Williams et al., 2013b).

This enabled static laser scans to be obtained at very high resolution, from multiple sites across the study reach at high speed. Most of the surveys incorporated measurements from over 300 locations, separated by a distance of

2.3. Data collection

approximately $70 \div 90$ m. At each location a point cloud of about $10 \div 15 \cdot 10^6$ was acquired with a point spacing of 15 mm at a range of 30 m, and two GPS-located targets were positioned 10 – 15 m from the scanner, to provide georeferencing information to estimate the scanner coordinates. The large dataset was then transformed in a 0.5 m DEM through the post-processing method detailed by Brasington et al. (2012).

The infrared laser scanner used did not penetrate through the water, so the inundated topography (< 10 % at low flow) was estimated using standard optical-bathymetric techniques (e.g. Marcus and Fonstad, 2008; Gao, 2009). For this purpose aerial RGB photographs were acquired from an helicopter at a height of 1200 m above the ground (object space resolution of 0.2 m) and selected to minimise sun glint. These were subsequently geo-referenced and resampled to the same coordinate system as the scan data (Williams et al., 2013b). Acoustic measurements of the water depth taken along two different transect enables a calibration of the observed depth with the blue/red band intensity ratio to obtain maps of the water depth. This map was then combined with an estimation of the water surface level, based on the assumption of linear variation of the free surface across each anabranch, in order to obtain the topography of the submerged areas.

A comparison with independent GPS-RTK measurements reveals a mean standard deviation of the DEM error of 0.044 m for the exposed bars and 0.128 m for the submerged channels.

During the study, a short period of mining activity occurred between surveys 05 and 06 a small ($\simeq 3.39 \cdot 10^3$ m³) volume of material was extracted. In order to exclude this artificial change from the analysis the mining site was manually identified and removed. Finally DEMs were rotated by an angle of -120° (using a bilinear interpolation method) to align the system of reference with the (approximate) mean direction of the flow and thus minimise the effects of numerical resampling across path in subsequent analysis.

2.3.2 Hydrological and sediment transport data

Water level data were sampled every 15 min minutes during the period from September 2009 to March 2011 at a gauging station located 1 km downstream the confluence between the Invincible Creek and the Rees River, where the stream is confined in a relatively stable, single channel that enabled calibration of a flow-stage curve Williams et al. (2013a).

The resulting flow record is reported in figure 2.1 and provides a clear indication of the range of different duration and magnitude events sampled. The mean flow was 18 m³s⁻¹ and the maximum peak 419 m³s⁻¹.

Wild et al. (2008) offer an estimation of the Dart-Rees delta deposition rate during the period 1966–2007, obtained from measurements of delta propagation from aerial photography and echo-sounder profiles. They estimate the combined

2.3. Data collection

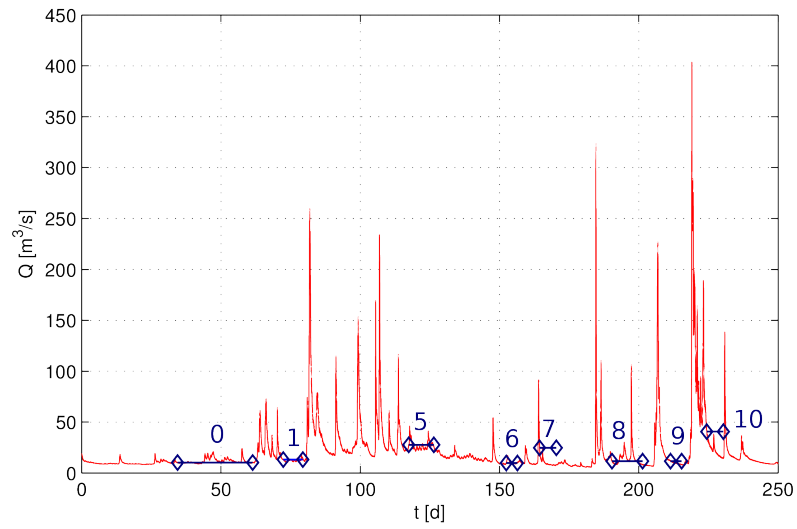


Figure 2.1: Estimated discharge during the study periods. Numbers and relative segments indicates the duration of the morphological surveys.

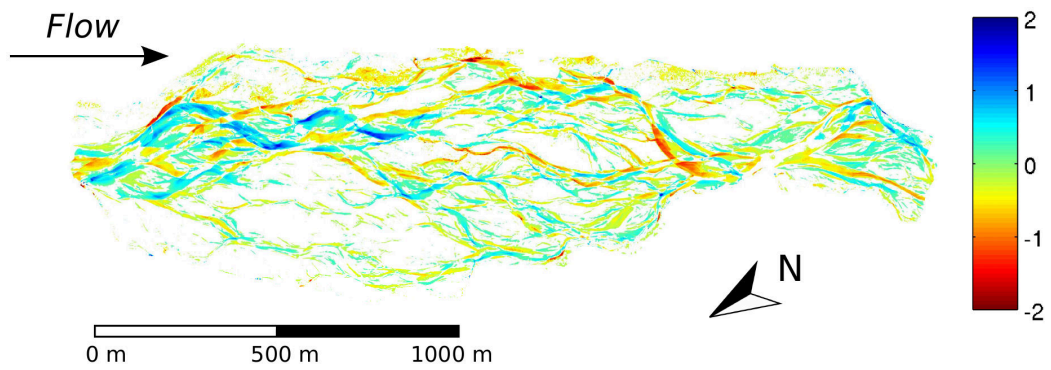


Figure 2.2: DEM of difference during the more intense flood event. Flow from left to right.

2.4. Methods

sedimentation rate to be of the order $270 \pm 30 \cdot 10^3 \text{ m}^3/\text{year}$. The fraction of this amount carried by the Rees River can be roughly estimated comparing the stream power of the two rivers; specifically Wild (2012) assumed a power law with exponent 1.75 which, considering the similar slope and the hydrological regime of the two contributors leads to

$$\frac{Q_{S_{Dart}}}{Q_{S_{Rees}}} \simeq \left(\frac{Q_{Dart}}{Q_{Rees}} \right)^{1.75} \simeq 3.1 \div 7.2 \quad (2.1)$$

which gives a mean annual transport rate of the Rees in the range $V_t = 30 \div 70 \cdot 10^3 \text{ m}^3/\text{year}$.

2.4 Methods

This section described the procedure to obtain *DEM* of Difference (or *DoD*) which quantifies the observed significant morphological changes between two surveys, and also outlines the path length concept and a possible method to apply it, explains the numerical simulations used to provide baseline estimates of bedload transport.

2.4.1 Data manipulation

In order to quantify morphological changes it is fundamental to adopt a procedure to distinguish variability in elevation from spurious differences that may arise from measurement error and interpolation.

Several approaches have been proposed to estimate the *DEM* uncertainties and propagate this errors into the *DoD* (Wheaton et al., 2010).

In this work we follow a probabilistic method (Lane et al., 2003; Brasington et al., 2003; Williams et al., 2011) that starts from a local estimation of the error of the individual *DEMs* and under the hypothesis of random and independent samples give rise to the standard deviation of the *DoD* as

$$\sigma_{1-2}(x, y) = \sqrt{(\sigma_1)^2 + (\sigma_2)^2} \quad (2.2)$$

Assuming a Gaussian probability distribution (e.g. Lane et al., 2003) it is possible to determine, for each point on the map, the error associated with a given confidence interval, namely

$$\Delta z(x, y) = Z \sigma_{1-2}(x, y) \quad Z = \sqrt{2} \operatorname{erf}^{-1}(1 - P) \quad (2.3)$$

where $P = 1 - CI$ represents the probability that the error is larger than Δz and erf^{-1} is the inverse error function.

In this procedure, knowledge of the spatial structure of the uncertainty of the original *DEM* is fundamental (Wheaton et al., 2010). Indeed (Brasington et al.,

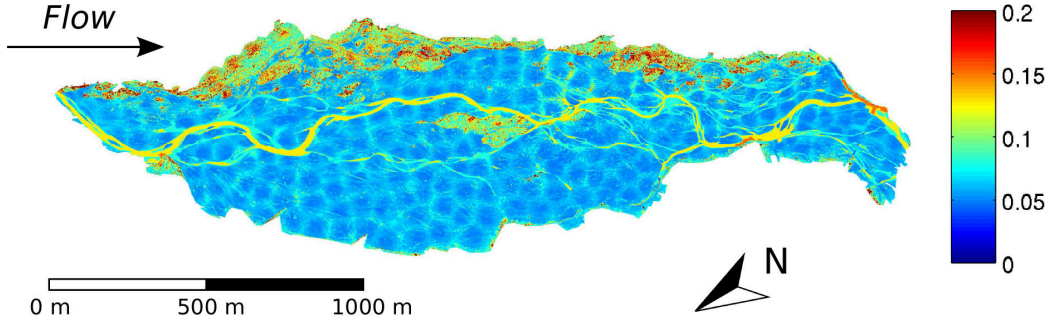


Figure 2.3: Map of the estimated error $\sigma(x, y)$ for the first (00) survey. Values in [m].

2003) found significant spatial differences in *DEM* errors, with low uncertainty in flat and smooth areas with high point densities, and much higher uncertainty in steep zones with large roughness and low measurement density.

In the Rees River dataset, it is clear that different uncertainty is associated to the points of the submerged areas, where the less precise optical-bathymetric technique was adopted. As described by Williams et al. (2013b) independent depth and bed elevation observations acquired with *GPS-RTK* and echo-sounding, enables an estimation *DEM* error in these submerged areas, which was found to have a mean value of

$$\sigma(x, y) = \sigma_{wet} = 0.125 \text{ m} \quad (2.4)$$

While this error is likely to vary across the study reach, there are insufficient data to capture or model the spatial pattern, and in all further analyses, the wet area of the *DEM* were assumed to have constant error. For the exposed bed, more information are available, so that a quantification of the spatial pattern of error is possible. In particular we can distinguish between a global error and a component due to the local variability of the measurements, namely

$$\sigma(x, y) = \sigma_{dry} + \sigma_{loc}(x, y) \quad (2.5)$$

where σ_{dry} is 0.044 m (Williams et al., 2013b) and $\sigma_{loc}(x, y)$, which accounts for the presence of steep regions and high roughness due to cobbles or vegetated patches, varies between $0.01 \div 0.03 \text{ m}$ for the bare ground and $0.3 \div 0.8 \text{ m}$ for vegetated areas.

In the example map shown in figure 2.3 the main channel is denoted to have a constant error of $\sigma = 0.125$ as described above, but the higher uncertainty on the true left reflects greater uncertainty in *TLS* measurements in vegetated area, while the circular spot distribution on exposed gravel reflects increasing uncertainty in laser spot measurement with distance from each scan position.

In order to calculate the distribution of elevations with respect the mean braidplain slope the reach average gradient must be obtained. Since this would

2.4. Methods

be used as a constant reference the slope was computed on the basis of the initial topography represented by the first *DEM*, or *dem 00*. Specifically, the minimum elevation along each cross sections was identified and a longitudinal profile fitted to these measurements using simple linear regression. The resulting surface was then used to compute the difference between each *DEM* and this average trend. As a last step the reference elevation was fixed as the reach-average value of the detrended *dem 00*.

2.4.2 The path length method

As originally derived by Einstein (1937) sediment transport can be computed as the product between the eroded volume V_e (per unit length L_d and time Δt) and the travel distance of the bed material L_t , namely

$$Q_s = (1 - p) \frac{V_e}{L_d \Delta t} L_t \quad (2.6)$$

where p is the porosity of the bed material. This formula is the basis for constructing a family of morphological methods for estimating the sediment transport (e.g. Neill, 1971; Goff and Ashmore, 1994; Haschenburger and Church, 1998; Ashmore and Church, 1998).

The same approach can be applied in terms of volumes of deposition; however in the following, for the sake of notation compactness, we will express all the formula using the erosion volume.

In order to illustrate the fundamentals of this approach let us consider the river reach of length L_d sketched in figure 2.4; let us also suppose the ideal case of an individual volume of sediment $V_{e,i}$ which, during a given period, is eroded and deposited downstream at a longitudinal distance L_i .

The reach-averaged transport is defined as the spatial mean of the volume of sediment passing through each section ($V_t(x)$), namely

$$\bar{V}_t = \frac{1}{L_d} \int_{L_d} V_t(x) dx \quad (2.7)$$

In the example of figure 2.4 the transport is constant for between x_i and $x_i + L_i$ whereas is vanishing outside this region; consequently the averaged transport can be easily computed as

$$\bar{V}_t = \frac{1}{L_d} V_{e,i} L_i \quad (2.8)$$

where L_i is called path length or transport length. More generally if N volumes are eroded and transported downstream we can simply sum the previous expression, obtaining

$$\bar{V}_t = \frac{1}{L_d} \sum_{i=1}^N V_i L_i \quad (2.9)$$

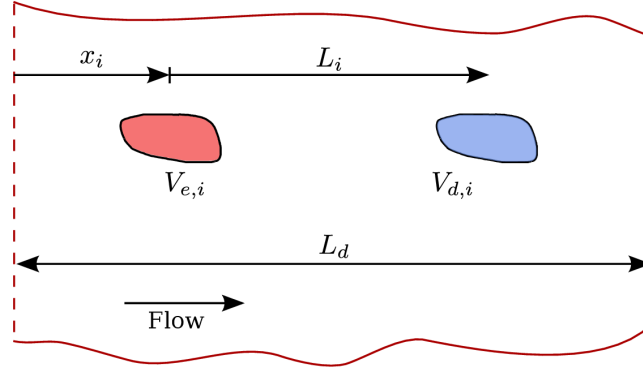


Figure 2.4: Sketch of the movement of volumes for the Ashmore and Church (1998) method. The dashed lines represent the limits of the study reach.

It is clear that the importance of each path length L_i is proportional to the relative volume; therefore a suitable definition of the average transport length should be weighed with the volume, namely

$$L_t = \frac{1}{V_e} \sum_{i=1}^N V_{e,i} L_{t,i} \quad (2.10)$$

which allows to calculate the volume transported during the time interval Δt by combining reach averaged parameters as follows

$$V_t = Qs(1-p)\Delta t = \frac{V_e}{L_d} L_t \quad (2.11)$$

Since each particle follows a different trajectory we should in principle apply Eq. 2.10 by considering volume and path length of each individual grain, so that N should be the number of displaced particles. As this is practically impossible a suitable approximation is to estimate the average path length of the grains within each single erosion and deposition unit, which can be identified as disconnected erosion/deposition patches.

It is also useful to underline that in order to obtain a statistically significant spatial average the reach extension should be large enough to capture the spatial variability of the bedload. Some observations about this problem are reported in appendix 2.9.3.

This simple derivation provides a useful linkage between erosion and deposition volumes and sediment transport. However, it does not solve the problem of the transport estimation, due to the uncertainties in the estimation of L_t . Ultimately, this approach transforms the problem from the estimation of the transport to the evaluation of the path length; the advantage of this change is that the length scale, can however, be inferred from the geometry of the river.

2.4. Methods

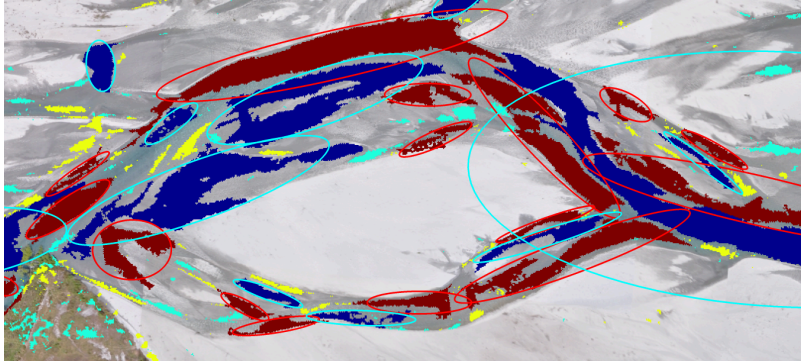


Figure 2.5: Example: deposition and erosion patches (blue and red areas respectively) and relative ellipses. In this example the patches having $A < 100 \text{ m}^2$ are excluded from the analysis (yellow colour for erosion, cyan for deposition).

Analysis of scour and deposition patches

Once the series of *DoDs* have been computed and significant elevation changes filtered, it is possible to identify the patches scour and deposition, count their number and measure their extension. To achieve this semi-automatically individual patches were defined as sets of pixels having at least one corner in common (the so-called 8-connectivity) to measure the area A_p and the volume of the scour or fill within the patch. In addition we defined the length of the patches L_p as the major axes of the ellipse which has the same second order moments, namely

$$\sigma_x = \frac{1}{A} \int_A (x - \bar{x})^2 dA \quad \sigma_y = \frac{1}{A} \int_A (y - \bar{y})^2 dA \quad \sigma_{xy} = \frac{1}{A} \int_A (x - \bar{x})(y - \bar{y}) dA \quad (2.12)$$

where the overbar indicates the mean values (coordinates of the mass centre). An automatic procedure that computes it for each individual patch was implemented. In this way we obtain a fully-automatic procedure which avoid biases due to subjective interpretations.

An example of how the fitted to patches is illustrated in figure 2.5.

Since we are interested in the relation between the morphological changes and the path length we need to introduce a reach scale metric which takes into account also the number of particles moved from/to the patches; in particular the definition of Eq. 2.10 suggest that the single length should be mass by the volume. Following this consideration we defined the weighted patches length as

$$L_{pw} = \frac{1}{V_e} \sum_{i=1}^N V_e L_p \quad (2.13)$$

<i>Parameter</i>	<i>Symbol</i>	<i>Value</i>
Representative sediment size	d_{84}	35.2 mm
Nikuradse roughness length	k_s	0.08 m
Mean grid size		$\simeq 2$ m
Horizontal eddy viscosity	ν_H	$0.1 \text{ m}^2 \text{ s}^{-1}$
Secondary currents coefficient	β_c	0.5
Gravitational acceleration	g	9.81 m s^{-2}
Time step	dt	1.2 s

Table 2.1: Most important parameters of the numerical simulations; the same values of Williams et al. (2013a) have been adopted.

2.4.3 Numerical simulations

Direct measurements of the bedload across the entire reach are not available and practically almost impossible because of the high number of samples needed to cover the lateral and temporal variation (e.g. Bertoldi et al., 2009a).

One possible way to overcome this dearth of data is to estimate transport rates using an independent numerical model. Unfortunately, in spite of the recent development of numerical schemes for predicting the morphological evolution of braided rivers (e.g. Shimizu and Itakura, 1989; Jang and Shimizu, 2005), such computer models are still in early stages and remain to be fully tested.

For this reason we preferred to follow an alternative approach based purely on more established hydrodynamic simulation methods. In this case it is assumed that despite that the morphological evolution through time, such adjustment does not significantly change the distribution of stresses for a given water discharge. In this case we expect that the reach-averaged bedload depends on the driving discharge but not on the current precise, deterministic morphological configuration.

This idea is supported by the observation of some morphological reach-averaged indicator changes between different flood events. For example in figure 2.8 shows hypsometric curves obtained by removing a constant slope and the mean elevation (slightly different for each *DEM*). It is clear that the elevation distribution does not vary significantly between the events, which suggests that dependent reach-scale properties, such as the bed shear stress distribution may also be relatively constant in time and vary only with water stage.

Under this hypothesis we can run a numerical simulation for a frozen morphology, determine the distribution of the shear stresses, use a bedload relation $Q_s(Q)$ to estimate the total transport during the event.

This approach was implemented using depth-averaged *Delft3D* model. For this, the model setup (grid, boundary conditions, formulation and parameters) was based on the similar work by Williams et al. (2013b) for the same reach of the Rees River. A list of the more relevant parameters adopted in this model

2.4. Methods

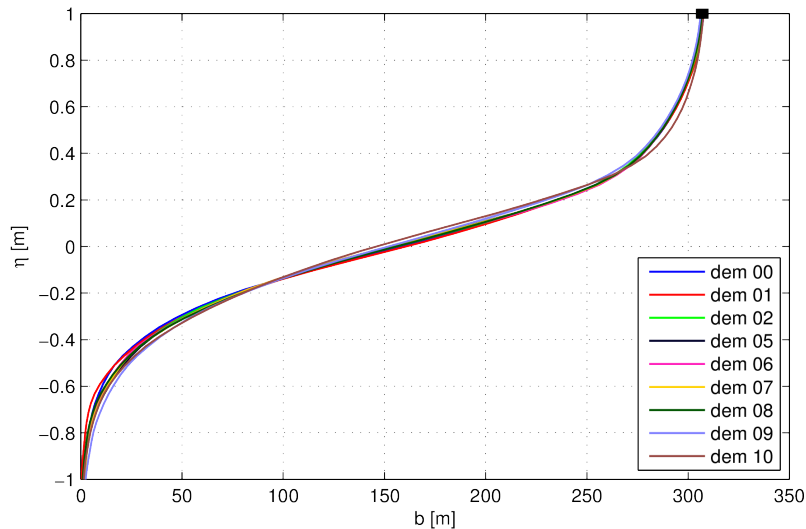


Figure 2.6: Hypsometric curves of the bottom elevation of the different surveys after removing a constant slope $S = 0.574\%$. Only the area common between the different DEMs has been considered.

is reported in figure 2.1.

Specifically, simulations involved a relatively slow ($0.1 \text{ m}^3 \text{ min}^{-1}$) linear growth of the discharge from a basic value $Q = 30 \text{ m}^3 \text{ s}^{-1}$ to the peak $Q = 420 \text{ m}^3 \text{ s}^{-1}$, for a total duration of approximately 68 h. The increase is slow enough in order to ensure a quasi-equilibrium state at each instant, so that the discharge is approximately uniform throughout the reach.

Figure 2.7 illustrated an example of the water depth predicted by the numerical model, and clearly demonstrated the complexity of the channel network and the broad distribution of depths.

Using this simulations, the distribution of stresses was extracted at regular intervals of discharge, the local bedload intensity determined using established transport formulae developed for gravel bed rivers. The most critical step at this point is the choice of a representative particle diameter which can strongly affect the results at least from a quantitative point of view. This problem can be partially circumvented by considering a multi-grain bedload representation, in which the different classes of bed material of diameter d_i and an a relative abundance f_i are selected, grouped here into four representative classes (see table 2.2) and used to parameterise the standard bedload formula.

For example the transport relation of Wong and Parker (2006b), is given as

$$qs_i = 4.93 (\theta_i - \xi_i \theta_{cr})^{1.6} \quad (2.14)$$

where the coefficient ξ_i takes into account the exposure/hiding effect for the individual class i and, according to Ashida and Michiue (1972), depend on the

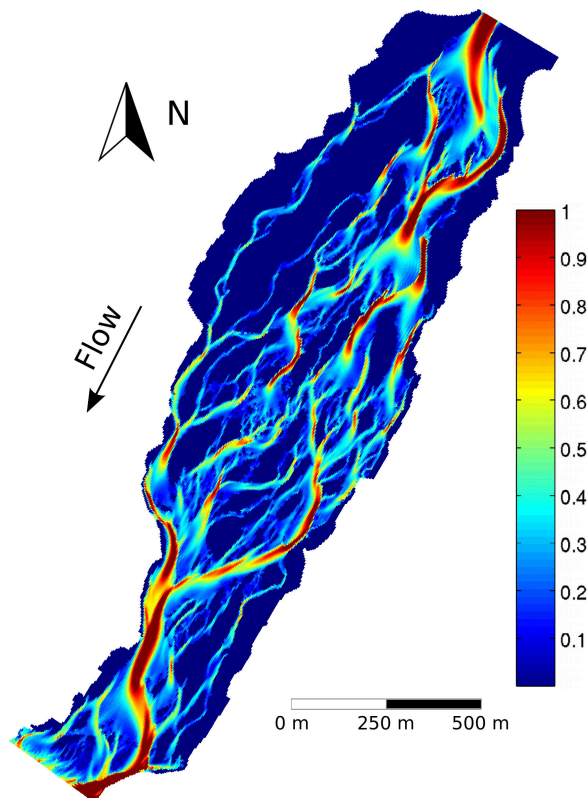


Figure 2.7: Example: water depth (in [m]) predicted by the numerical model for $Q = 120 \text{ m}^3 \text{ s}^{-1}$.

2.4. Methods

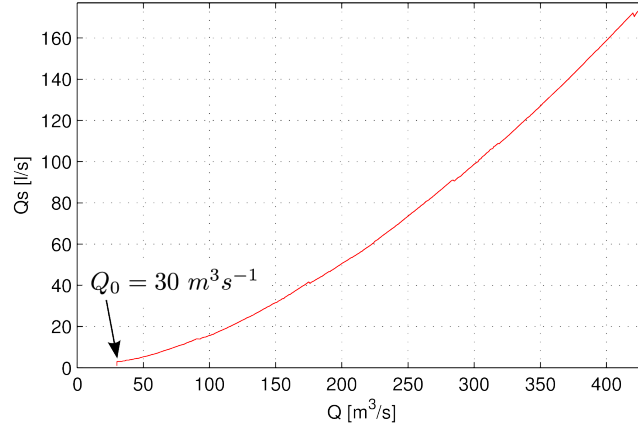


Figure 2.8: Sediment rate curve resulting from the numerical model. The topography of *dem 08* has been considered.

sediment size distribution as follows

$$\begin{cases} \xi_i = 0.843 \bar{d}/d_i & \bar{d}/d < 0.4 \\ \xi_i = \left(\frac{\log_{10}(19)}{\log_{10}(19) + \log_{10}(d_i/\bar{d})} \right)^2 & \text{otherwise} \end{cases} \quad (2.15)$$

where \bar{d} is the mean diameter.

If we consider Eq. 2.14 for each class and multiply the result by the relative abundance f_i

$$qs = \sum_{i=1}^N f_i qs_i \quad (2.16)$$

we obtain an estimation of the local bedload intensity.

Moreover if this calculation is then repeated at regular time intervals during the growing discharge simulation described above, it is possible to obtain a full scale sediment rating curve, as plotted in figure 2.8.

Class	Size d_i [mm]	Abundance f_i [%]
d_{16}	10.4	33
d_{50}	19.9	34
d_{84}	35.2	30
d_{90}	40.5	13

Table 2.2: Grain size classes adopted for the bedload estimation.

2.5 Results

This section presents the result analyses in terms of deposition and scour volumes, distributions of these volumes, characteristic length and connection between morphological changes and sediment transport.

2.5.1 Analysis of deposition and scour volumes

The analysis of the erosion and deposition volumes and of the relative active areas reveals several interesting features which can be summarised as follows:

[1] As one expects, both the erosion and deposition volumes (figure 2.9, upper panel) depend on the magnitude of the storm event; however not only the peak discharge but also the flood duration is important for determining the morphological changes. For example the event 00-01 produces volumes of erosion and deposition which are very similar to the event 07-08 in spite of the much lower peak discharge; similarly the sequence of peaks in the period 01-05 moves much more material than the storms 07-08 and 08-09 even with a similar maximum flow.

For this reason the maximum discharge is poorly correlated with the amount of material excavated or deposited (see figure 2.11, upper panel); but a more consistent relationship exists with the flow volume exceeding the threshold value (lower panel) albeit the pattern is nonlinear and with relatively high V_e occurring for the smallest events.

[2] Morphological activity across the braided network was significant even at modest flows. For example the peak discharge of the event 00-01 ($Q = 73 \text{ m}^3 \text{ s}^{-1}$) was much smaller than the 18-months maximum ($Q = 475 \text{ m}^3 \text{ s}^{-1}$) and corresponds to a return period of less than one month. In spite of this, the event mobilised a volume of $20 \cdot 10^3 \text{ m}^3$ and re-arranged 10 % of the braidplain.

[3] Notwithstanding the role of small events, the biggest flow pulses, and especially event 09-10, result significant net erosion. However from our data it is not possible to assess whether this is the result of fluctuations longer than the study area or the product of an incision trend of the reach (i.e. whether the upstream or autogenic supply dominates).

[4] The mean thickness of the scour/deposition sites (figure 2.9, middle panel) varies on weakly between events (from 0.32 m to 0.42 m for the erosion sites). This means that the higher volumes moved by the bigger events are mainly due to increases in the area of mobile bed, rather than local increases in the intensity of transport that would give rise to deeper scour or fill.

The comparison between the frequency distribution of the changes (figure 2.10) during events with completely different magnitudes confirms the absence of strong differences in the variations of elevation between distinct floods. However, as one expects, due to the higher number of samples available, the distribution of the 09 – 10 event is more regular and it seems to be well approximated

2.5. Results

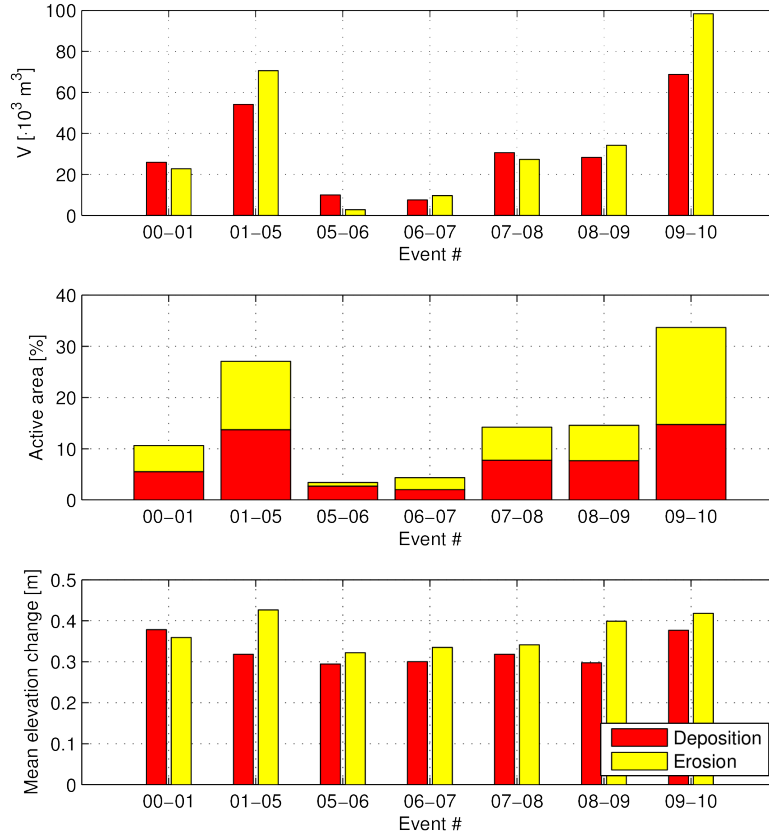


Figure 2.9: Scour and deposition volumes (upper panel), active areas (central panel) and mean variation of elevation in the active areas (lower panel) for the different events.

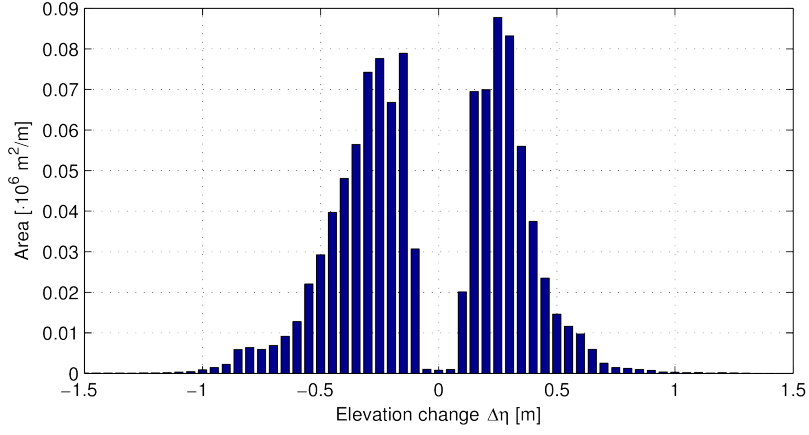
by a Gaussian curve (red line of figure 2.10b).

2.5.2 Characteristic length and sediment transport

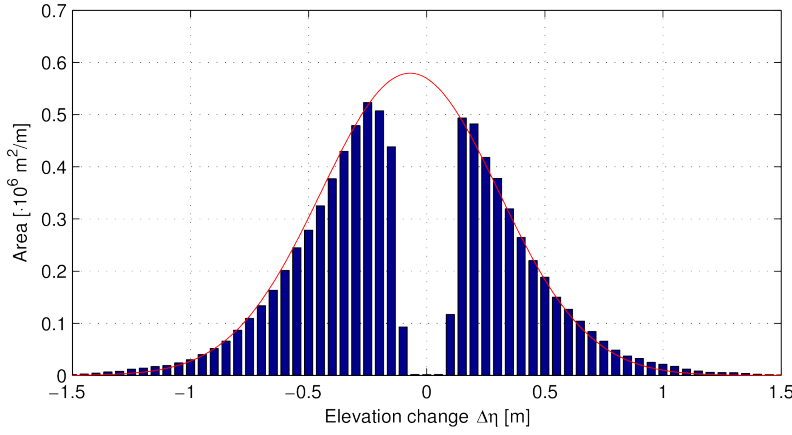
In this section we will analyse the metrics of the scour and deposition patches and their variation between events. This analysis is extended to provide a first-order estimate of the transport rates morphologically, by assuming that the mean patch size is representative of the particle travel distance. The result of this morphological prediction are presented, and correlated with flood magnitude and duration.

Analysis of scour and deposition patches

Initial inspection of *DEM* of difference suggest different bedload responses with flood magnitude, characterised by variations in the mean size of the erosion and deposition patches. Specifically, minor flood pulses are characterised by



(a) Small event (06-07).



(b) Largest event (09-10).

Figure 2.10: Histograms of the bed level changes. Each bar represents the extension of the area that experienced the elevation change $\Delta\eta$. The red line on the lower panel represents the best-fitting Gaussian distribution.

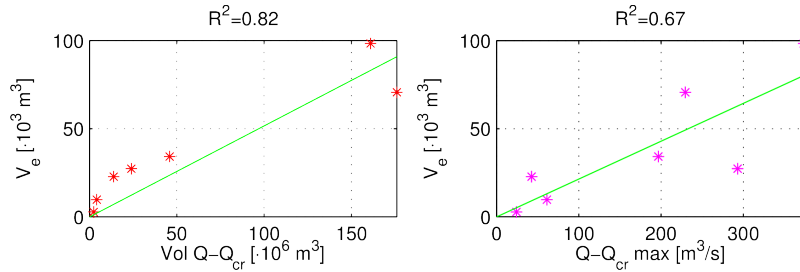


Figure 2.11: Correlation between erosion volumes and the different parameters adopted in order to quantify the intensity of the storm event. Vol represents the volume of water exceeding the threshold $Q_{cr} = 30 \text{ m}^3\text{s}^{-1}$.

2.5. Results

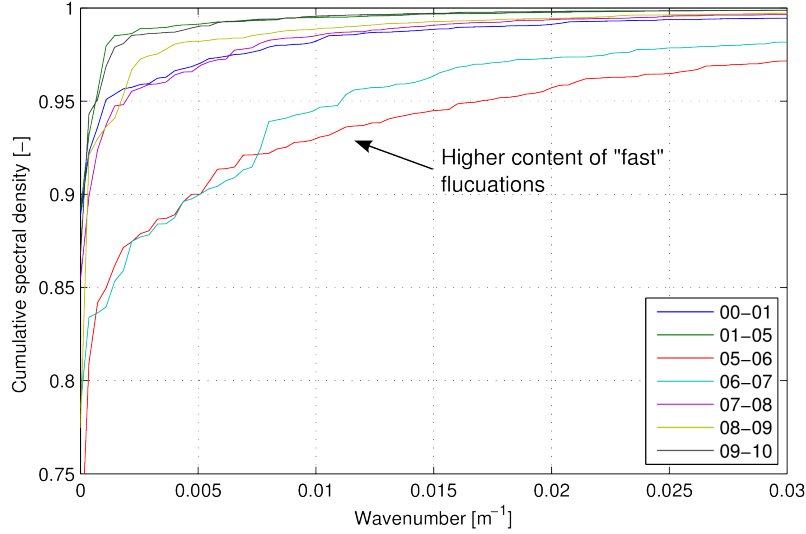


Figure 2.12: Cumulative (and normalised) spectral density of the cross-section averaged profiles for the different events. The total (sum of erosion and deposition across the section) volume has been considered.

small areas of morphological change, which are related principally to in-channel processes.

Some insight to the spatial scale of the morphological variations by spectral analysis of the cross-section averaged longitudinal profiles.

Specifically, the cumulative power spectral density, can be computed as follows

$$CSD(\lambda) = \int_0^\lambda |\hat{\eta}(\lambda)|^2 d\lambda \quad (2.17)$$

where $\hat{\eta}$ indicates the Fourier transform and represents the percentage of signal variance contained in wavenumbers lower than a given value. If we compute this function for the longitudinal profiles of the cross-section averaged volumes and normalise the results we obtain results shown in figure 2.12. This plot illustrate that for the smaller events (05-06 and 06-07), the wavenumbers > 0.005 (i.e. wavelengths ≤ 200 m) comprise the 10 % of the variability, whereas for the larger flood events 01-05 and 09-10 the same region of the spectrum contains less than 1 % the total variance of the signal.

Despite this evidence, a quantitative analysis of the characteristic length from cross-section averaged quantity is complicated, because the computation of the averages regions containing different length-scales, so that the resulting profile contains superimposed information. Furthermore this analysis condenses variability into a single value of length, without any appreciation of the spatial variation in the volume of each erosion and deposition.

In order to overcome these limitations a frequency analysis of the ero-

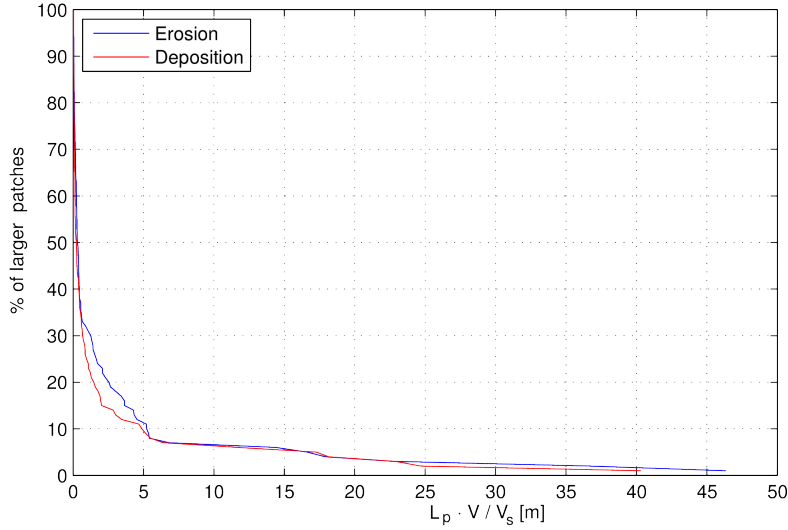


Figure 2.13: Cumulative frequency distribution of the weighted major axis length of erosion and deposition patches.

sion/deposition patches size was undertaken, as described earlier in the methods section.

The result shows a large variability from site to site and gives rise to an heavy tailed distribution (see for example figure 2.13). An important consequence of this result, is the likely sensitivity of estimates of the mean size of patches, to the method of computation.

If we consider the simple mean values (upper and middle panels of figure 2.14) we can see that both A_p and L_p significantly change between the events. In particular it is clear that the bigger floods produce patches which are on average larger; we can also observe that the differences are stronger in terms of area, which indicates, as one may expect, that both the principal dimensions of the patches are increasing with the flow duration and magnitude.

However, as we implied in Eq. 2.13, if we are interested in the mean travel distance of the particles the arithmetic mean must be weighted by the importance of each patch using its associated erosion volume (which is a measure of the number of eroded particles). This weighted metric is much more sensitive to area and, as shown in figure 2.14 (lower panel), produces much higher (longer) values (of the order of few hundreds of meters).

Referring only to the erosion patches (yellow bars) the values range from 50 m for the event 05-06 to 300 m for the sequence of flow peaks in the interval 01-05 and emphasise the dependence to the patches size to the driving discharge. Comparing L_{pw} with the volume of erosion of figure 2.9 (upper panel) it is clear that a good correlation exist; only the relative importance of the event 01-05 and 09-10 is exchanged, with the previous having an higher patches length and

2.5. Results

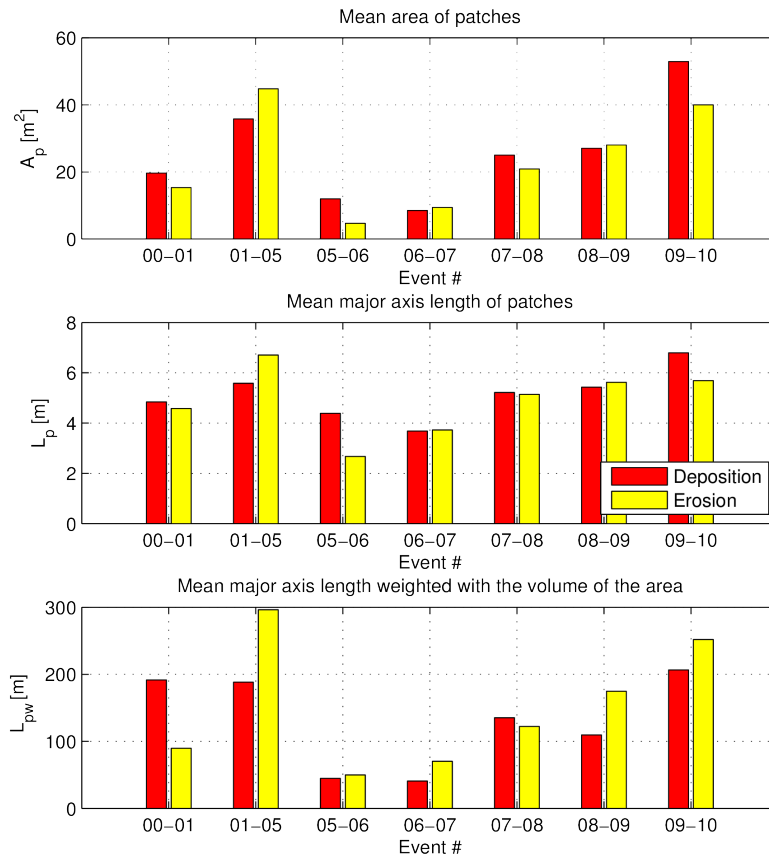


Figure 2.14: Analysis of size of the scour (yellow bar) and deposition (red bar) patches. Upper panel: mean area. Central panel: mean length of the semi-major axes of the ellipse having the same second-order moments. Lower panel: mean length of the semi-major axes.

Event	$V_e [m^3]$	$V_d [m^3]$	$V_{t,e} [m^3]$	$V_{t,d} [m^3]$
00-01	22.8	26.0	1.02	2.49
01-05	70.6	54.2	10.46	5.10
05-06	2.8	9.9	0.069	0.22
06-07	9.7	7.5	0.34	0.15
07-08	27.3	30.6	1.67	2.07
08-09	34.2	28.3	2.99	1.55
09-10	98.4	68.8	12.38	7.10
Cumulative	266	225	28.9	18.7

Table 2.3: Estimated volume of the bedload transport for different storm events. $L = 2 \text{ km}$ and $p = 0.3$ are adopted as parameters.

the latter a larger scour volume.

In terms of deposition, however, the results are significantly different. In particular the L_{pw} of the first two events becomes very similar and comparable with the one of the event 09 – 10. The reason of this relevant difference is not clear; in particular we do not know whether it is related to the limited extension of the reach which makes the statistics not sufficiently robust or to the fact the incision is globally dominant. Some consideration about the effect of compensation as well as the comparison with numerical results suggest that the erosion pattern may provide more consistent results. For this reason in the calculation of the transport we will adopt the L_{pw} of the scour pattern. However further investigation is clearly needed to understand this variation.

Sediment transport

As highlighted previously, an estimation of the path length allows determination of transport on the basis of the volumes of scour and fill.

Taking the mean weighted semi-major axes of the scour patches as a measure of the path length ($L_t = L_{pw}$), as described above, Eq. 2.11 can be applied to estimate the volume transported during the event. The resulting transport rate for each event is presented in table 2.3. Despite the physical basis for this approach further empirical support and robust testing is clearly needed.

The validity of these results can be tested through three approaches. First, we can compare the cumulative volumes of table 2.3 with the estimate of the annual transport for the Rees obtained by (Wild, 2012) ($V_t = 30 \cdot 10^3 \div 70 \cdot 10^3 \text{ m}^3/\text{year}$), based on the estimates of the delta growth. Because no hydrological records are available for the period considered by (Wild, 2012), direct comparison with 2009-2010 is clearly hazardous. However, this comparison places both estimates in the same order of magnitude and that if anything, the morphological approach is possibly an underestimate the actual bedload.

Secondly, the estimated transport volume can be compared to the hydrological forcing. As discussed earlier, rather a simple dependence on the peak

2.5. Results

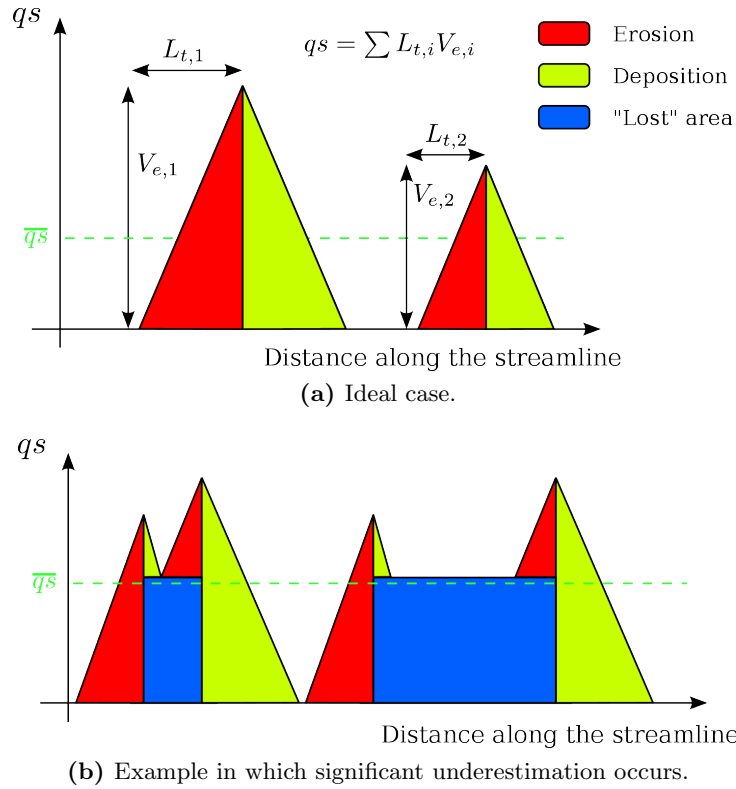


Figure 2.15: Schematic representation of the relation between the average transport and the estimation based on patches length and erosion volume.

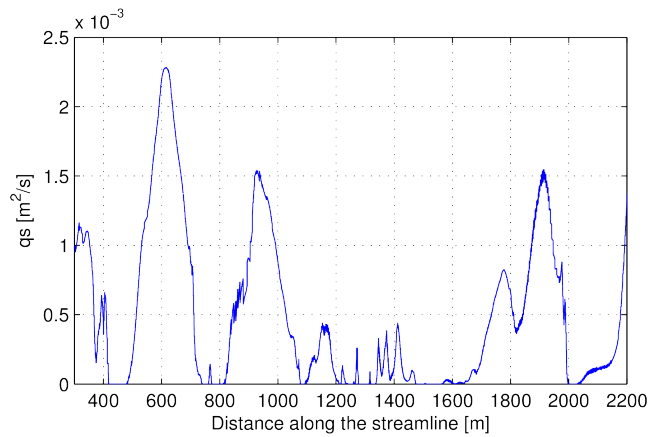


Figure 2.16: Example of variation of the bedload along a streamline. Results from numerical model with $Q = 323 m^3 s^{-1}$.

discharge, a proportional relation with a nonlinear transport law, such as

$$V_t \propto \int Q^\delta dt \quad (2.18)$$

where, according to the laboratory studies of Bertoldi et al. (2009a), the exponent is, for unconfined networks, of the order $\delta = 1.5 \div 1.7$ might be expected. This formula does not enable estimation of the transport but can provide an indication of the relative role of storm magnitude and duration (Bertoldi et al., 2010).

If we compare the transport estimate against predictions based on Eq. 2.18 for different values of the exponent (ranging from 1.5 to 2.0) the result reveal a very strong correlation.

Nevertheless the transport during the smallest event (05-06) is evidently overestimated by Eq. 2.18 which, being a simple power law without any threshold, predicts a significant transport during long periods of very low flow. Field observations suggest us that significant morphological adjustment is uncommon at discharges below $Q_{cr} = 30 \text{ m}^3\text{s}^{-1}$ so this was used to threshold effective discharges, $Q > Q_{cr}$. By thresholding the driving discharge in this way, the correlation between the morphological transport rate and discharge is presented in figure 2.17, for a range of Q exponents. This demonstrated the very high correlation for exponents in the range $1.5 \div 2.0$ which are expected to be representative of the transport for varying discharge.

Finally we can directly compare the V_t from the path length method with the transport estimated through the numerical model. As one might expect the result (reported in figure 2.18) is dependent upon the bedload formula and the representative diameter adopted; for instance from the biggest flood the numerical outcome indicates a conveyed volume varying from 11 to $31 \cdot 10^3 \text{ m}^3$. The choice of transport formula and particle parameters constitute a prime source of uncertainty, that make any comparison complicated. However, here we consider the multi-grain estimation based on the Wong and Parker (2006b) formula as a reasonable approach, and this demonstrate (see 2nd panel of figure 2.18) that the morphological approach slightly ($\approx 30\%$) underestimates the reach-averaged bedload.

Nevertheless the strong correlation between the two estimation methods is clear (figure 2.18). As these two approaches, are completely independent seems reasonable to assert that the path length estimation is, at the very least, broadly representative of the relative magnitude of the sediment transport measured between different flood events.

Inverting Eq. 2.6 enables an alternative perspective on this comparison, namely in terms of transport length. Again the value of L_t strongly depends on the formulation and the parameters adopted; nonetheless the variability of the path length between the events is correctly captured. This is relevant because methods based on the bar or confluence bifurcation spacing as proposed by Ash-

2.5. Results

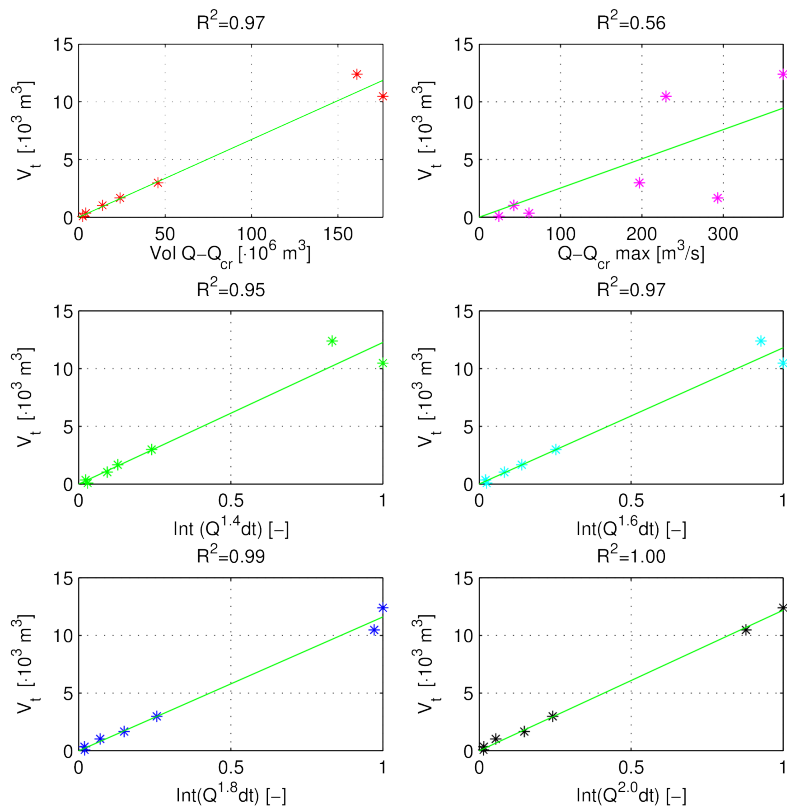


Figure 2.17: Correlation between the estimated volume of bedload transport and the different metrics considered in order to quantify the intensity of the storm events. *Int* indicates the temporal integral normalised with the larger value, *Vol* represents the volume of water exceeding the threshold $Q_{cr} = 30$ m³/s. .

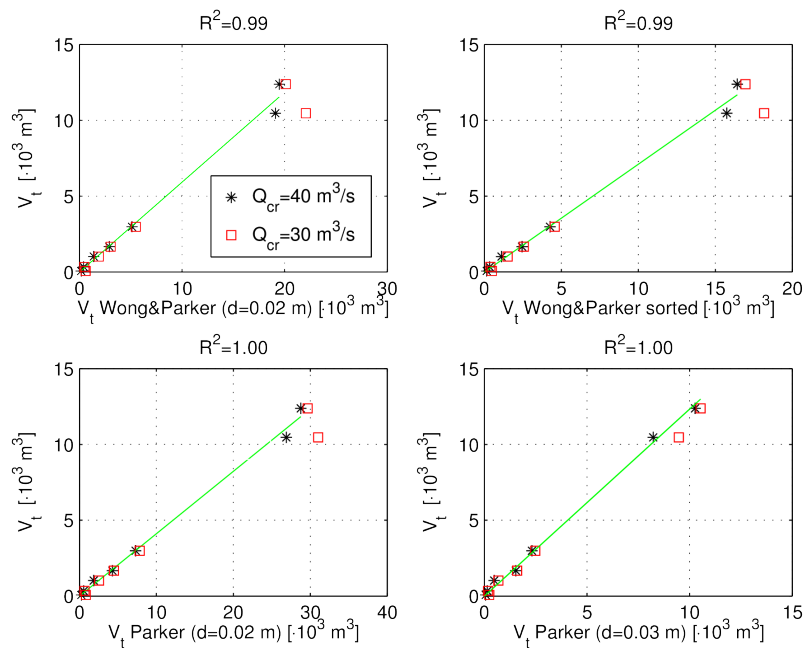


Figure 2.18: Reach-averaged sediment transport, computed from the numerical model and using our approach (considering scour patches). Upper panels: Wong and Parker (2006b) (Eq.2.14). Lower panel: Parker (1990). Two different values of the critical discharge have been considered, the regression refers to $Q_{cr} = 40 \text{ m}^3\text{s}^{-1}$; porosity is fixed to $p = 0.3$.

2.5. Results

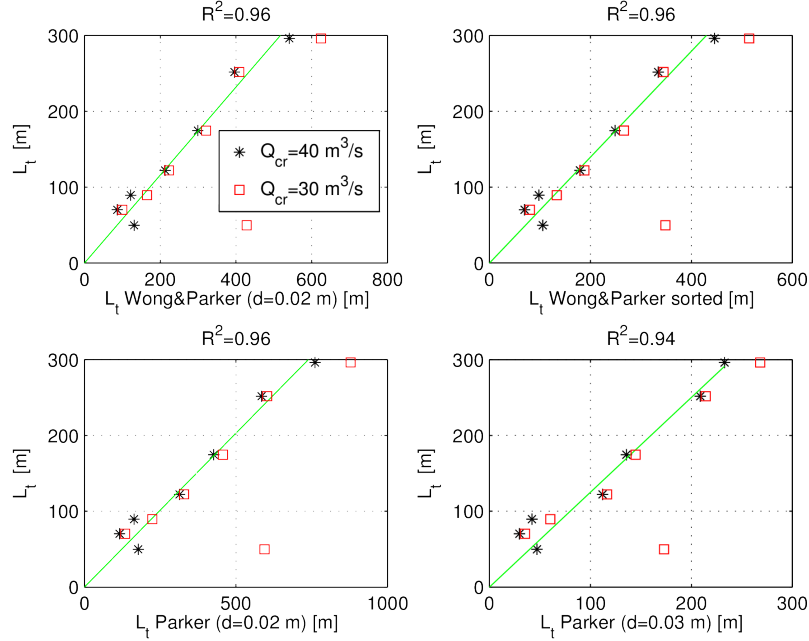


Figure 2.19: Path length computed from the numerical model and using the present approach (considering scour patches). Upper panels: Wong and Parker (2006b) (Eq.2.14). Lower panel: Parker (1990); two different values of the critical discharge have been considered, the regression refers to $Q_{cr} = 40 \text{ m}^3 \text{ s}^{-1}$; porosity is fixed to $p = 0.3$.

more and Church (1998); Ashmore (2013) lead to a number which is invariant to discharge and consequently would produce a much weaker correlation with the numerical results.

It is valuable to underline that the result also depends on the threshold chosen; in particular the L_t of the event 05-06 is rather sensitive to the value of Q_{cr} and would triple changed from 40 to $30 \text{ m}^3 \text{ s}^{-1}$. Nevertheless the other points are substantially stable and the positive correlation between the two estimate is independent to any choice of the parameters.

Summarising the review of the results presented above, highlights the following key points:

- The size of the patch strongly varies between the different event.
- The path length derived from the numerical method is also variable.
- A significant correlation between the path length and the patches size exist.

In the following sections we will discuss how a variation of the path length between the event can be expected on the basis of some considerations about the compensation effect.

2.6 Discussion

The results presented in the previous section are based on measurements that are unavoidably limited by the accuracy, spatial extent and spatio-temporal resolution of the morphological data. While it is impossible to mitigate these effects entirely, a robust analysis of the sensitivity of the results obtained to these effects is needed.

In the following sub-sections an analysis of the methodological sensitivity is undertaken that considers the influence of: a) the temporal resolution of the survey data; b) the spatial extent of the study area; and c) the confidence interval adopted to distinguish between significant and spurious elevation changes identified in the DoD .

2.6.1 Relationship between patches size and path length

In the previous analysis of transport we assumed there was a connection between the size of the erosion patches and the path length.

This principle, while lacking an unambiguous physical basis, was justified through the identification of a clear variation in the characteristic length scale of patches with forcing discharge rather than on a detailed study of the actual mechanics of sediment transport.

Further corroboration for this approach was provided through a comparison of the estimated transport rate with those obtained from an independently-derived numerical model.

The following discussion aims to review the physical principles governing sediment transport, in order to better understand the potential but also the limitations of the patch-based approach to derive the path-length.

Starting with a simple ideal example; it is useful to consider a generic hydraulic streamline at a given instant of time, from which it is possible to compute the bedload intensity along this curve, giving rise to results similar to those shown in figure 2.15a. The average sediment discharge on the streamline is proportional to the total area of the triangles, namely

$$\bar{qs} = \frac{1}{L} \int_{x=0}^L qs(x) dx = \frac{1}{L} \sum_{i=1}^N L_{t,i} V_{e,i} \quad (2.19)$$

where $L_{e,i}$ is the length of the erosion (growing qs) sites.

Since the reach-averaged transport at any instant of time can be computed as the integral along all the possible streamlines it is clear that if the bedload followed a similar “peaked” behaviour throughout the network, the approximation to path length provided by patch size would provide a reliable estimation.

However if we consider the signal on figure, here the streamlines incorporates multiple peaks and the area of the triangles does not account for the total transport. The blue areas, which represent a flux throughout different patches

2.6. Discussion

is not included in the computation of Eq. 2.19. The magnitude of this error depends on the intensity and the distance of this movement across multiple patches.

By extension, the most severe error would occur when a significant fraction of material moves throughout the river without leading to erosion and deposition. In the case of straight channels with migrating alternate bars, analytical theories (e.g. Colombini et al., 1987) reveal that, as long as the bar height is relatively small, only a minor fraction of the bedload is involved in scour and fill processes. Under these conditions there is not direct connection between any morphological signal and bedload transport and thus no opportunity to infer the path length from the bed level changes.

In braided rivers, significant temporal variability in transport rates is well established (Ashmore, 1991; Warburton and Davies, 1994; Bertoldi et al., 2009a) and, not surprisingly associated with large spatial fluctuations, as confirmed by event-scale morphological budgeting Lane et al. (1994); Goff and Ashmore (1994).

In order to investigate effects of spatial variation in the Rees River, a simple particle tracking model, based on the hydraulic simulations of the depth average model was developed. In this, the trajectory of several particles seeded at equally spaced points across the entrance section, was determined by allowing them to follow streamlines neutrally. Computing the stress variation along each streamline, and applying a bedload formula provides estimates of the longitudinal transport, as illustrated in figure 2.16. This reveals that the transport rate vanishes to zero several times along the reach, which is encouraging as it suggests the absence of significant throughput. In addition some peaks are relatively smooth and with a single relevant maximum, albeit not perfectly triangular as sketched in figure 2.15. On the other hand some areas of transport show a multiple maximum which produce a disconnection between the erosion sites and consequent an underestimation of the transport.

The computing the erosion patches size is, however, different from the one-dimensional representation we depicted above. The advantage of the two dimensional patches analysis lies in that a small isolated interruption of the scour does not necessarily cause a disconnection of the patches as in the $1D$ example. The confounding problem of the multiple peaks, represents a flux through patches, suggests, that if anything, the patch based approach might lead to an underestimate of the path length and consequently of the transport. Evidence from the particle tracking model, however, suggests that this effect is likely to be limited for the Rees, and not significantly variable between different events so that we are able to capture the relative bedload intensity between the events.

2.6.2 Volume compensation and temporal resolution

It is well known that subsequent phases of scour and refill (or viceversa) produce a compensation effect which can lead to a significant underestimation of the volumes (Goff and Ashmore, 1994; Lindsay and Ashmore, 2002).

The probability of compensation and the consequent effect of volume estimation increases with elapsed time between topographic surveys. For this reason Ashmore and Church (1998) suggested that it is important to assess what temporal and spatial resolution of morphological data is necessary for a comprehensive estimation of the erosion and deposition volumes.

Ultimately the choice of resolution is likely to be as much based on practical (site access, instrumentation, cost, manpower) issues that limit the survey quality and frequency, as theoretical concerns. However it is not clear whether simple intensification of the sampling interval between events will necessarily (and predictably) result in an improvement in the estimation of cut and fill volumes (Ashmore and Church, 1998; Ashmore, 2013).

For example the laboratory experiments of Lindsay and Ashmore (2002) suggest, in fact, that the compensation is significant even at relatively short timescales, so that is often practically impossible measure the total variation.

This section outlines an evaluation the impact of sampling interval on the volumes of erosion and deposition in the Rees. The following section 2.6.3, extends this analysis to consider, from theoretical and empirical perspectives, the impact of this sampling effect on estimates of transport rate.

Let us consider three *DEMs* measured at the time instants t_0 , t_1 , t_2 , from which we compute the volume of erosion between them. Due possible compensation effects, the following inequality holds

$$V_e^{0-2} \leq V_e^{0-1} + V_e^{1-2} = \tilde{V}_e^{1-2} \quad (2.20)$$

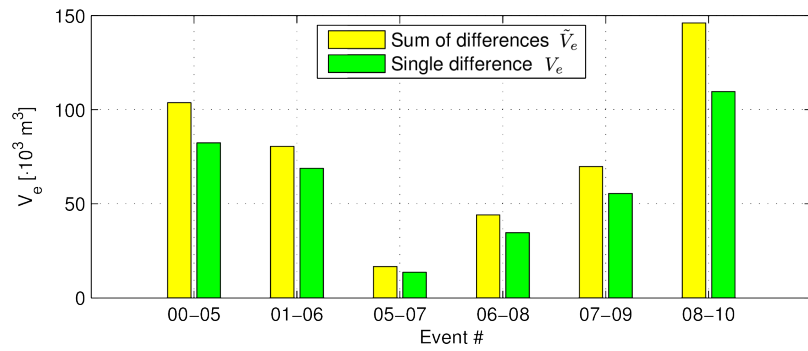
where the superscript indicates the interval of the volume calculation and we defined \tilde{V} as the sum of the intermediate volumes.

If we compute these quantities for each couplet of measurements we obtain the result of figure 2.20, which shows reported V_e and \tilde{V}_e in terms of erosion (upper panel) and deposition (lower panel). From this it is clear that the “missing” volume due to compensation is of the order of 20 ÷ 30 % for all the couplets observed. It is trivial to prove that this underestimation, as evident in figure 2.20, is exactly the same in the erosion and deposition volumes.

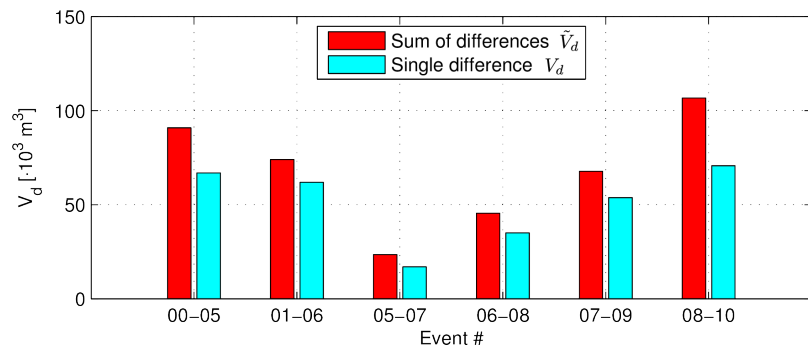
The key question that ensues is, how does the undersampling of volume scale with the elapses time between surveys. This can be addresses by considering the same theoretical experiment reported above, but involving more than two steps in the calculation.

For example, we can estimate the volumes of scour and deposition during the entire entire period $\tilde{V}_e^{00-10}(N)$ by using a different number of differences N between $N+1$ intermediate surveys. For $N = 1$ we have simply V_e^{00-10} , whereas

2.6. Discussion



(a) Erosion.



(b) Deposition.

Figure 2.20: Comparison (in terms of global erosion and deposition volumes) between the the difference between two *DEM*s and the sum of the differences with an intermediate *DEM*.

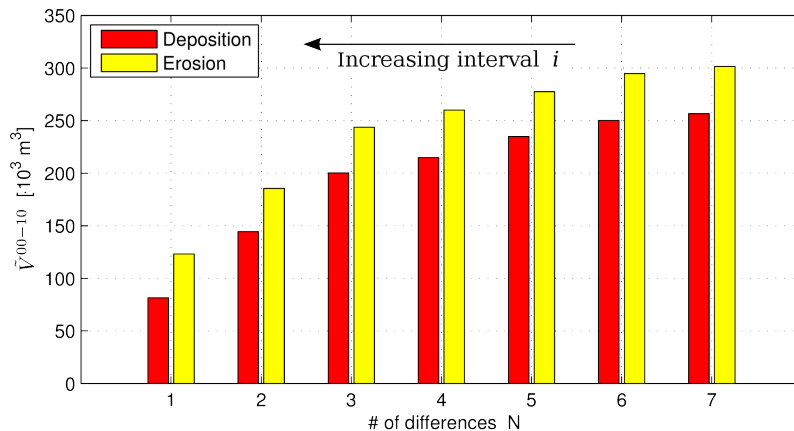


Figure 2.21: Volume of scour/deposition for the entire period 00-10 estimated by using a different number of *DEMs*, from two (first and last only) to eight (sum of seven differences between intermediate *DEMs*).

for $N = 7$ we are summing the differences between all the available surveys (while 10 surveys were undertaken, only 7 *DEMs* have been fully developed), whereas all for others values of N we selected the *DEMs* in order to distribute the volumes in the more uniform way possible

The result of this experiment are shown in figure 2.21. which reveal that the compensation volumes estimated from the first and last topographies ($N = 1$) is significantly lower than the volume obtained by increasing the number of intermediate surveys. However, by using just $N = 3$ (i.e. involving *DEMs* 00, 05, 08, 10) over 80 % of the volume of the whole dataset ($N = 7$) is obtained.

While this sampling experiment provides some useful insights into the scaling of compensation losses, the available data are clearly insufficient to ultimately identify the possible magnitude to all missing volumes of scour and fill.

The laboratory experiments of Lindsay and Ashmore (2002) suggest that such a measurement frequency would be difficult to achieve. They observed that the volume of erosion/deposition during an interval Δt increases with the frequency of measurements as follows

$$\tilde{V}_e = a + \frac{b}{i} \quad V_e = a + \frac{b}{\Delta t} \quad (2.21)$$

where a and b are empirical constants and i is the interval between surveys.

Accordingly, even for small intervals the missing volumes increased dramatically tending towards infinity ($V = \infty$ for $i \rightarrow 0$). Nonetheless, the authors highlighted that, although an infinite volume is physically unreasonable, a large volume would result if we were able to capture the individual grains movements. However practical restrictions of the minimum detectable variations make it im-

2.6. Discussion

possible to reach the temporal and spatial resolution needed for capturing these values (Lindsay and Ashmore, 2002).

2.6.3 Effect of the volume compensation on the transport estimate

The significant compensation effect observed in the laboratory experiments of Lindsay and Ashmore (2002), and to a lesser extent in the Rees River dataset, could be taken to imply that morphological transport estimation based on the path length approach will always be biased.

In meandering channels, such as studied in the experiments of Pyrce and Ashmore (2003b), the compensation effect still occurs at the scale of the grain size. Indeed it is possible to consider the transport and the associated morphological evolution at a larger scale, at which no significant subsequent scour and refill occurs.

Such an approach may, however, not be possible for braided networks which exhibit compensatory elevation changes across a wide range of scales, from individual grain exchanges, to bank erosion and avulsion, and ultimately to a complete reworking of the entire braidplain.

These considerations pose a relevant problem to the usage of the path length method in braided morphologies. Nevertheless the very few applications of the approach used in braided rivers (see Ashmore and Church, 1998) suggest that at the event-scale the method offers tangible results.

In this section we aim evaluate the conditions under which the method could be reliably applied despite the ever present risk of morphological compensation.

The transport during a given period Δt can be computed by applying the path length method (Eq. 2.11) directly for the entire period or using a number of intermediate steps having at regular intervals i , namely

$$V_t = \frac{V_e}{L_d} L_t \quad V_t = \frac{\tilde{V}_e(i)}{L_d} L_t(i) \quad (2.22)$$

Since the result must be the same the following relation holds

$$L_t(i) = L_t \frac{\tilde{V}_e(i)}{V_e} \quad (2.23)$$

and implies a connection between the path length and the compensation. Specifically, if no compensation occurred, the path length would be constant and independent on the interval i . However according to the experiments of Lindsay and Ashmore (2002), this may be not the case and, in particular, their empirical relation (Eq. 2.21) implies

$$L_t(i) = L_t \frac{\tilde{V}_e(i)}{V_e} = L_t(\infty) \frac{i}{b/a + i} \quad (2.24)$$

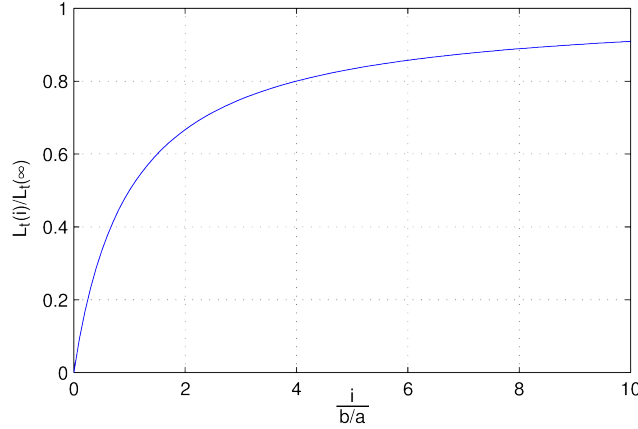


Figure 2.22: Path length as a function of the measurement interval Δt consequent to the formula proposed by Lindsay and Ashmore (2002).

which indicates that the path length can not be constant but must increase with the elapsed time as in figure 2.22.

The variations of L_t are due to the increase in time of the probability of multiple travels of the single particles. From a macroscopic perspective, this is the cause of the compensation, and as such explains why the patch length changes with time on the basis of the compensation effect.

In the case of the Rees River the flow intensity and duration vary considerably and only a limited number of *DEMs* available; thus it is impossible to analyse completely the dependency of transport rates on interval i for a given time period as shown in figure 2.22.

Nevertheless, the results shown in figure 2.21 offers some useful insights. In particular if we compute the transport rate based on the interval 00-10 using only the volume V^{00-10} and then more fully by considering the intermediate differences (volumes $\tilde{V}^{00-10}(N)$), namely

$$V_t^{00-10} = \frac{1}{L_d} V_e^{00-10} L_t^{0-10} = \frac{1}{L_d} \tilde{V}_e^{00-10}(N) \tilde{L}_t^{0-10}(N) \quad (2.25)$$

where $\tilde{L}_t^{0-10}(N)$ is an equivalent travel distance which is the average (weighted with the volume) of each intermediate the path length.

If $\tilde{V}_e^{00-10}(N)$ increases with N the transport length $\tilde{L}_t^{0-10}(N)$ must diminish in order to maintain the same transport.

This results offers an interesting opportunity to examine whether this decrease is also evident in the characteristic size of the scour and deposition patches obtained as the time interval of *DoDs* varies too. Examination of figure 2.23 reveals that the equivalent path length estimated on the basis of the patches sites is actually decreases with N . Consequently the volume lost because of the compensation effect is balanced by an increase of our estimation

2.6. Discussion

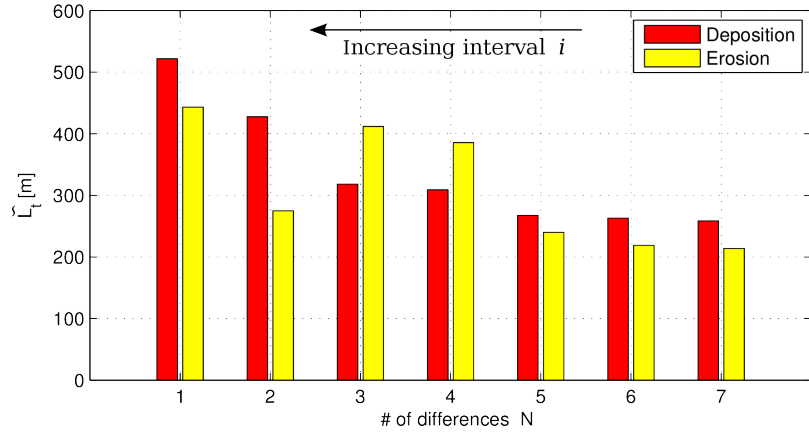


Figure 2.23: Transport length L^{tot} for the entire period 00-10, estimated by using a different number of intermediate *DEMs*.

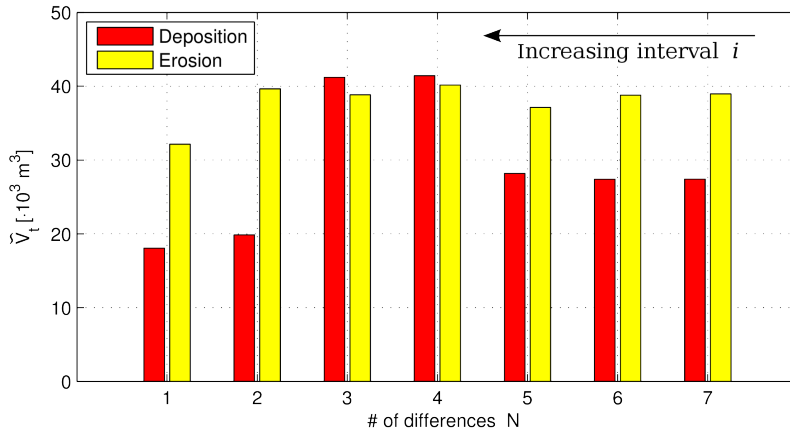


Figure 2.24: Transport volume for the entire period 00-10, estimated through a different number of intermediate *DEMs*.

of the step length and the estimation of the transport (figure 2.24) rather independent on the number of intermediate surveys.

2.6.4 Effect of the confidence interval

As discussed previously, the definition of the *DoD* and consequently of the erosion and deposition pattern, depends on the criteria adopted to distinguish between physical elevation changes and inevitable measurements and interpolation errors. According to the error model described in section 2.4.1, the resulting *DoD* can be classified using a variable confidence interval or *CI* (equal to 80% in the previous sections), which determines the likelihood of distinguishing “real” from “spurious” elevation changes. Importantly this choice will also have

ramifications not only for the total volumes of scour and fill, but also the size of the observed patches and hence estimated path length.

Experimentation varying the CI reveals that increasing the CI (providing a stricter test of significance) results in a reduction in the average patches size because it causes a decrease of the active area but also reduces the connectivity between patches, causing a splitting of some areas.

The results of this sensitivity analysis are summarised in figure 2.25, which reveals that the CI is increased from 70 % to 90 %, the estimated path-length decreases significantly, especially for the larger events, which exhibit a decrease of as much as 40 %. This effect on the path length (or rather patch size) tends towards zero as far as CI increases to 100%. This observation suggests a double dependence of transport rate on the selection of CI , which will affect both the overall volume of erosion measured and the estimation of the path length, and necessitates an examination of the resulting overall bias in transport rates.

Reduction of the CI inevitably introduces greater likelihood of incorporating spurious volumes in the change analysis, which will lead to a consequent overestimate the transport. However if we assume that these errors are spatially uncorrelated, the probability to introduce artificial connectivity between patches should be low, and suggest that a lower value of CI may actually be more appropriate for an estimation of the patch size.

Unfortunately the extent to which the error can be treated as uncorrelated at the pixel scale is unknown so that any concomitant change in L_p cannot be treated as an unambiguous, reliable result. Clearly further examinations of this is necessary in the future.

2.7 Conclusions

From the analysis of the morphological changes of the Rees River, the numerical simulation and some theoretical considerations about the methods it has been possible to clarify the research questions we formulated at the beginning of this chapter.

The reach-scale erosion and deposition volumes depend on both magnitude and duration of the flood. The variation in scour and fill volumes displaced during different floods appear to be related principally to increases in the active area rather than the average depth of the scour or deposition. Also the frequency distribution of the elevation changes appears to be largely independent of the flow magnitude.

Quantitative analysis of the size of the deposition and scour patches based on an automated algorithm reveals a strong dependence of the reach-averaged length to the intensity of the driving event. In particular it is noticeable that the small flow pulses produce much smaller areas of scour and fill than those associated with much large floods.

2.7. Conclusions

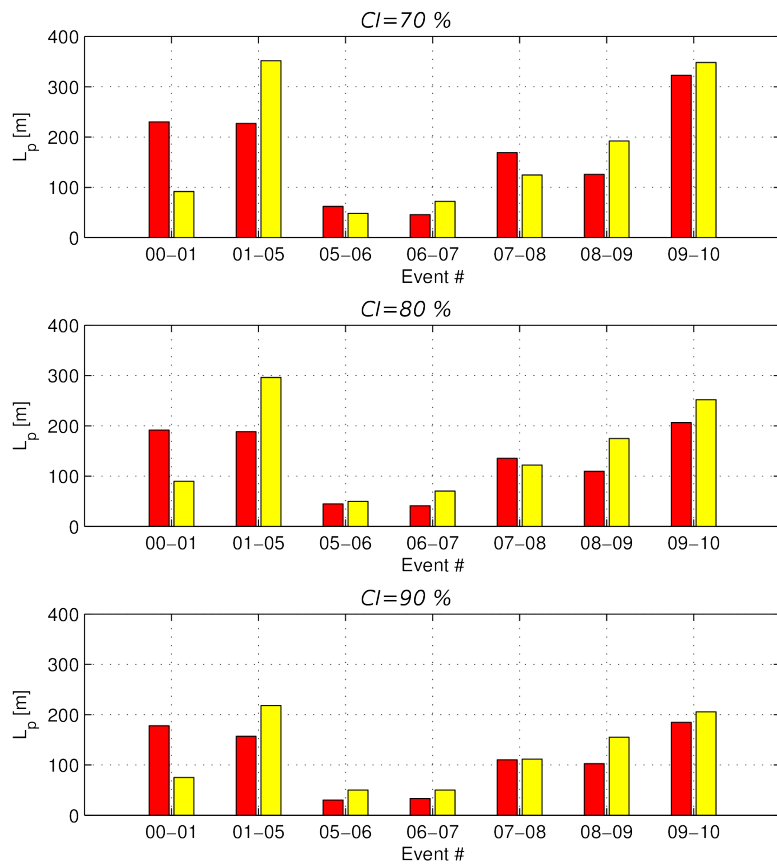


Figure 2.25: Comparison between weighted length of scour and deposition patches computed with different confidence intervals. The central panel represents the result of figure 2.14.

Some observation suggests that the average size of these patches may be representative of the path length. Moreover the comparison with the numerical results confirms that such a relationship probably exists and can be used to estimate the reach-averaged bedload during the different flood events.

Theoretical concerns about the compensation effect suggest that the path length should not be a fixed number, but increases with the elapsed time and with the flow intensity, which is consistent with our observation about the patches size.

The method is relatively robust with respect to the compensation effect despite significant underestimation of the scour/deposition volumes.

The choice of the error model adopted to detect morphological variations affects both the path length as well as detectable morphological change. In particular the confidence interval of the probabilistic error model, despite not being crucial to determine the relative transport between events, significantly influences the absolute values of the resulting bedload.

Due to the high degree of uncertainty, attention must be exercise when employing these results. Indeed due to the lack of direct measurements or reliable estimates of the reach averaged transport it is not possible to assert in which extent the method is suitable for quantitative predictions. Nevertheless the connection between patches size and path length offers useful approach and at the very least, offers insight into the *relative* rate of bedload transport between the events studied, and hence a quantitative scaling between sediment transport and driving hydraulics.

2.8. List of symbols and acronyms

2.8 List of symbols and acronyms

Acronyms

<i>ADCP</i>	Acoustic doppler current profiler;
<i>DEM</i>	Digital elevation model;
<i>DoD</i>	Digital model of the elevation differences;
<i>CSD</i>	Cumulative spectral density;
<i>TLS</i>	Terrestrial laser scanner;
<i>RTK – GPS</i>	Real time kinematic global positioning system;

Symbols

A_p	[l]	Mean area of the patches;
CI	[–]	Confidence interval in the error model;
d_{50}	[l]	Median grain size;
\bar{d}	[l]	Mean grain size;
d_x	[l]	x -percentile of the grain size distribution;
f_i	[–]	Fraction of the grain size i ;
i	[t]	Survey interval;
L_d	[l]	Length of the domain;
L_p	[l]	Mean semi-major axis of the patches;
L_{pw}	[l]	Mean semi-major axis of the patches weighted with the volume;
L_t	[l]	Path length of the particles;
\tilde{L}_t	[l]	Equivalent path length computed using intermediate surveys;
p	[–]	Porosity of the bed material;
t	[t]	Time;
P	[–]	Probability of higher errors ($1 - CI$);
Q	[l^3t^{-1}]	Water discharge;
R^2	[–]	Coefficient of determination;
qs_i	[l^2t^{-1}]	Bedload intensity of the grain size i ;
Q_s	[l^3t^{-1}]	Solid discharge;
V_e	[l^3t^{-1}]	Volume of erosion;
V_d	[l^3t^{-1}]	Volume of deposition;
$\tilde{V}_{e/d}$	[l^3t^{-1}]	Erosion/deposition volume estimated using intermediate surveys;
V_t	[l^3t^{-1}]	Solid volume transported by the river;
\tilde{V}_y	[l^3t^{-1}]	Volume of transport estimated using intermediate surveys;
x	[l]	Longitudinal coordinate;
L_t	[l]	Travel distance of the particles;
y	[l]	Transverse coordinate;
Δt	[t]	Time interval;
λ	[l]	Wavenumber;
ξ	[–]	Exposure/hiding factor of the grain class i ;
θ_i	[–]	Shields parameter of the grain class i ;
θ_{cr}	[–]	Critical Shields parameter;

2.9 Appendixes

2.9.1 Distributions of the morphological variations

In the discussion above we have seen how reach scale volumes of erosion and deposition strongly depend on both duration and intensity of flow pulses. This section addresses the additional question of *where* those fill and cut volumes are located?

First of all we look at how morphological changes are distributed in elevation. For each event we computed for any location the scour/deposition depth and the elevation before the event; we then divided the elevation in 300 classes between -1.5 m and $+1.5\text{ m}$ and we summed the volumes for each class. The resulting distributions, represented in figure 2.26, shows several interesting features. Firstly, the scour distributions (panel 2.26a) reveals that erosion mainly occurs at elevations around zero (average reach elevation); however the position of the peaks seems to depend on the maximum discharge, which is relatively high for events 07-08 and 09-10. Secondly, the second panel 2.26b shows, as one might expect, the deposition occurs in lower areas of the braidplain, and in particular shows a maximum around -0.5 m which is slightly higher, albeit comparable, than the bed relief index (which ranges from 0.32 m to 0.36 m among different DEMs).

As a second step we studied the transverse distribution of the volumes. Figure 2.27 shows significant differences between events having similar erosion volumes; it is evident that event 09–10 involves a wider region of the braidplain than the event 01–05, which is longer in time but less intense.

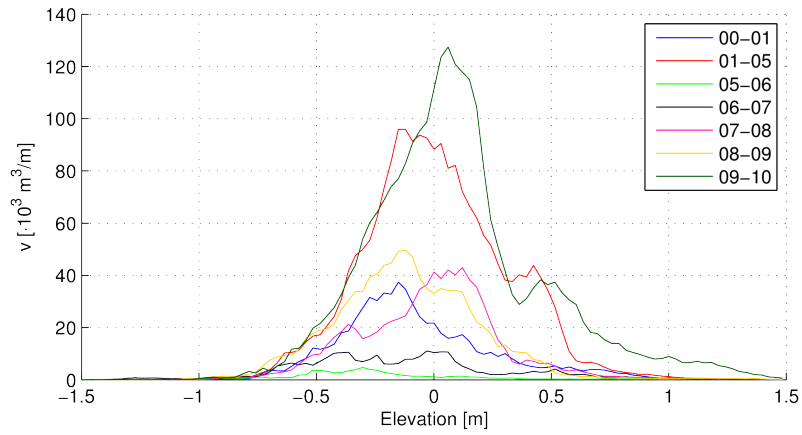
Finally, it is also interesting to analyse how the net erosion which occurred during the bigger events is distributed along the longitudinal direction. Figure 2.28 reveals that during the bigger event (09–10) an evident incision occurs in the narrowing region while during event 01–05 the incision is located more upstream. In addition we can see that the smaller events show a variability only on shorter spatial scales, which is consistent with the idea that the length scale of the morphological variations depend on flood intensity and magnitude.

2.9.2 Comparison between different methods

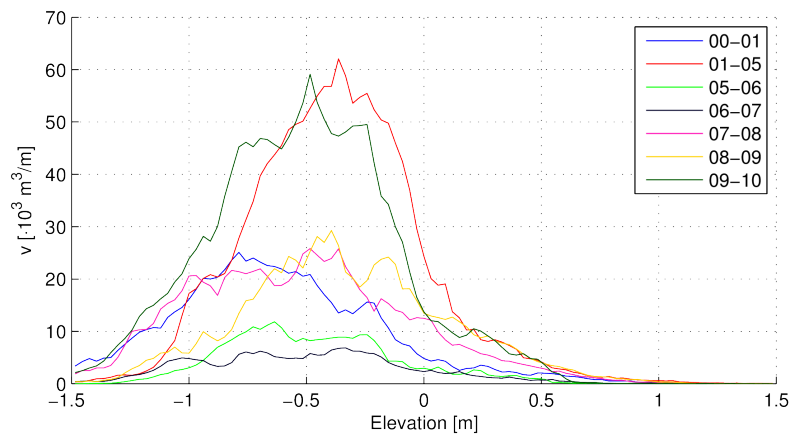
An algorithm to filter the small patches

Many patches of erosion and deposition show a very small area (only one or few pixels). Clearly, size and connectivity between these areas is highly affected by the error model and the confidence interval adopted to filter out the measurement uncertainties; consequently we expect that such small areas are not representative of particles path length and should be excluded from the analysis.

2.9. Appendixes



(a) Erosion



(b) Deposition

Figure 2.26: Distribution elevation of the scour (upper panel) and erosion (lower panel) volumes. The elevation refers to the antecedent topography.

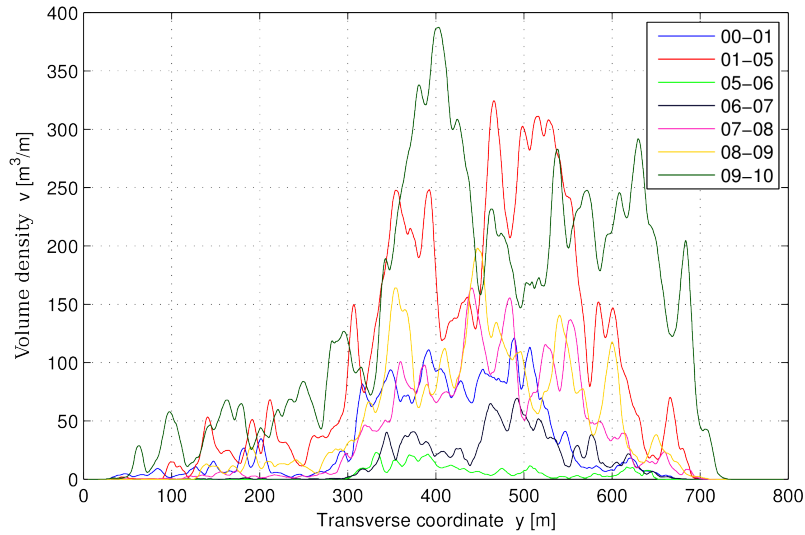


Figure 2.27: Longitudinal integral of the scour volumes as a function of the transverse coordinate y for the different storm events. A 10 m window average has been adopted to filter the signals.

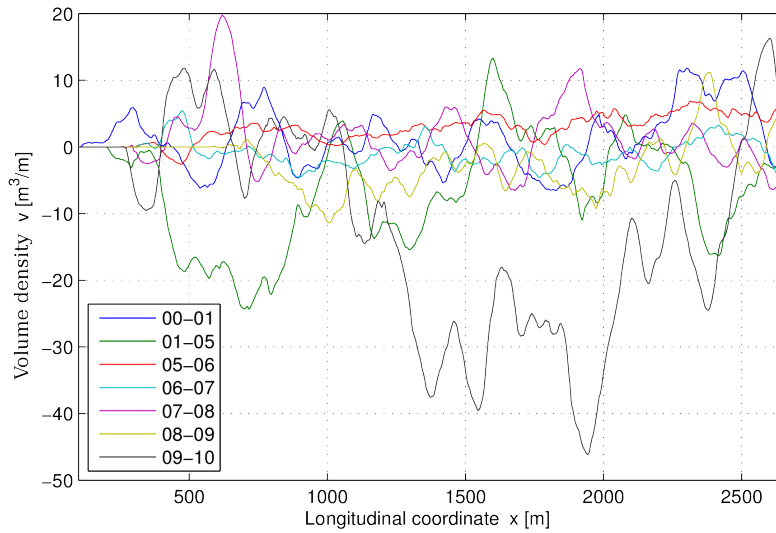


Figure 2.28: Longitudinal profile of the laterally integrated net volume for different storm events. A 100 m window average has been adopted to filter the signals.

2.9. Appendixes

Among the several procedures suitable to eliminate these small patches, the more easy is a simple removal of area smaller than a defined threshold; as one may imagine the disadvantage of this simple approach is the difficulty to define a physically based criterion to determine the threshold.

A more reasonable, although still simplified method is based on the concept that two close area of erosion without any deposition patch in the middle can not be representative of the transport length; indeed the hypothesis that there is no sediment flux across different erosion sites is in this case clearly not satisfied. Many similar situations occurs simply because of the limited accuracy of the *DEMs*, which leads to an apparent separation of patches with are in fact connected. In order to reduce the impact of this side-effect we implemented an algorithm which removes scour zones which are closer to other (bigger) cut areas than to the nearest deposition patch.

Effect on the patches metrics

As one might expect, the effect of filtering out the smaller areas significantly affects any estimation of the average length and area of patches. In particular in table 2.5 we report the result of the two algorithms, namely

1. Simple elimination of patches smaller than 10 m^2 (labelled *Thresh*).
2. Removal of patches close to larger areas of the same type (called *Filt*).

It is evident that the area extension as well as the major axes length is highly dependent on the method adopted to identify the erosion/deposition patches; however it is also clear that in, terms of variation between events both quantities show similar trend. Figures 2.29 and 2.31 compare (in terms of mean area and patches length respectively) results of the two methods for both erosion and deposition. In general there is a good correlation between the different metrics; for example the simple thresholding, albeit reducing about 5 times the length and 8 times the area of patches, gives a coefficient of determination $R^2 \geq 0.93$ with the original, non-thresholded, metrics. This means that, despite the very different magnitude, relative variation of patches size between events is rather independent of the choice of the method.

From table 2.5 we can also see that in terms of weighted patches length L_{pw} (defined in Eq. 2.13) not substantial differences occurs between the methods. This result, which is clear also in figure 2.32, reveals that since the weighted averaged assign more importance to bigger patches, it is robust with respect to the algorithm adopted to eliminate the small, insignificant areas.

2.9.3 Some considerations about the reach extent

When we perform any reach-scale analysis we must always deal with the question of which is the extension needed to obtain a representative sampling and consequently to construct a robust statistics.

<i>Parameter</i>	<i>Type</i>	<i>No-filters</i>		<i>Thresh $A > 10 m^2$</i>		<i>Filt. algorithm</i>	
		Scour	Dep	Scour	Dep	Scour	Dep
Mean area $A_p [m^2]$	00-01	15.3	19.7	115.2	140.1	40.3	50.0
	01-05	44.8	35.8	305.0	258.2	106.0	94.0
	05-06	4.7	12.0	56.4	85.4	7.4	31.0
	06-07	9.4	8.5	86.9	68.3	20.6	18.7
	07-08	20.9	25.0	162.4	177.7	49.4	63.3
	08-09	28.0	27.1	214.6	177.3	66.0	66.8
	09-10	40.0	52.9	325.0	332.0	137.6	111.0
	Mean length $L_p [m]$	00-01	4.58	4.84	24.48	24.44	9.39
	01-05	6.70	5.58	36.09	30.14	13.29	11.74
	05-06	2.67	4.39	17.58	22.38	3.55	8.91
	06-07	3.73	3.68	22.16	19.37	6.46	6.38
	07-08	5.14	5.22	29.03	27.28	10.00	10.54
	08-09	5.62	5.43	32.57	26.79	11.02	10.72
	09-10	5.69	6.79	34.72	33.68	14.94	12.33
Weighted length $L_{pw} [m]$	00-01	89.5	191.4	93.7	199.0	95.2	201.1
	01-05	296.2	188.3	300.2	192.6	301.2	194.3
	05-06	49.8	44.7	59.8	48.1	53.2	49.6
	06-07	70.2	40.8	76.7	45.6	75.9	44.4
	07-08	122.1	135.2	126.9	139.3	125.9	141.3
	08-09	174.6	109.5	178.8	112.6	178.4	115.1
	09-10	251.8	206.4	255.7	208.9	259.4	208.7

Table 2.5: Mean patches area, length and weighted length from the original method and after removing the smaller areas with the two mechanisms we propose. Both the results from the erosion and deposition map are reported.

2.9. Appendixes

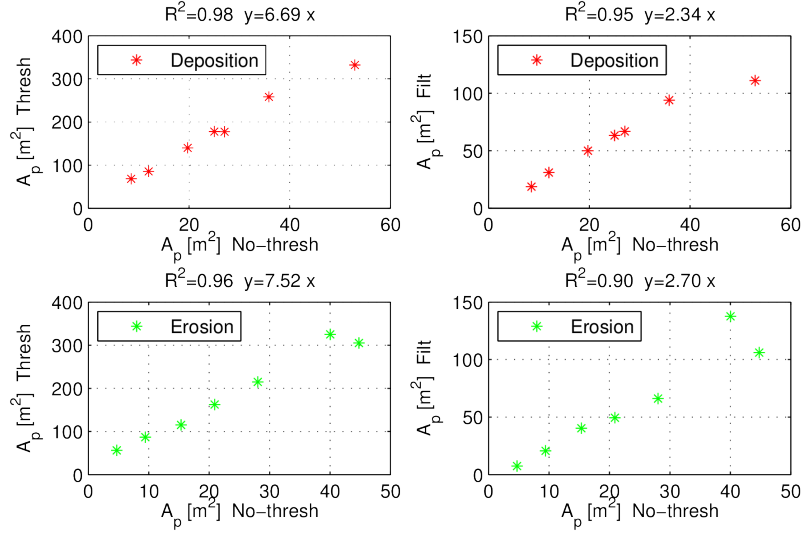


Figure 2.29: Comparison between the mean area computed without any threshold and the mean area obtained *a)* after excluding patches with $A < 10 \text{ m}^2$ (left panels); *b)* after applying the filtering algorithm (right panels). Upper panels: deposition patches, lower panels: scour patches.

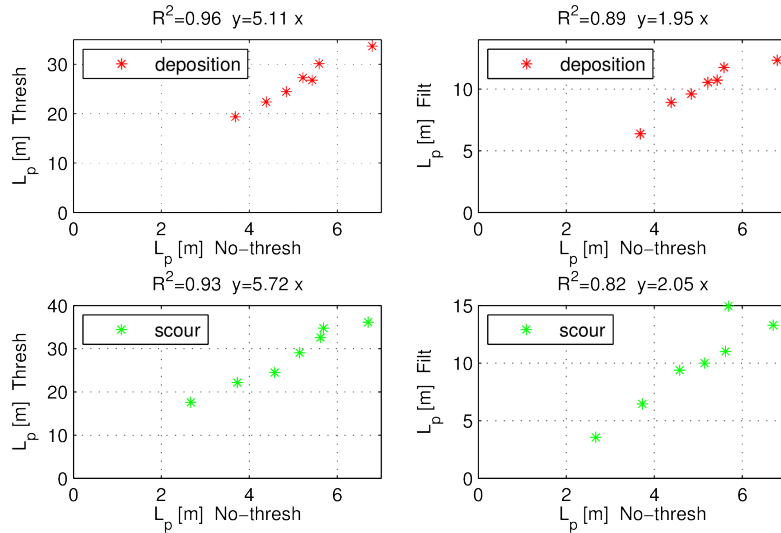


Figure 2.30: Comparison between the mean semi-major length computed without threshold and the one obtained *a)* after excluding patches with $A < 10 \text{ m}^2$ (left panels); *b)* after applying the filtering algorithm (right panels). Upper panels: deposition patches, lower panels: scour patches.

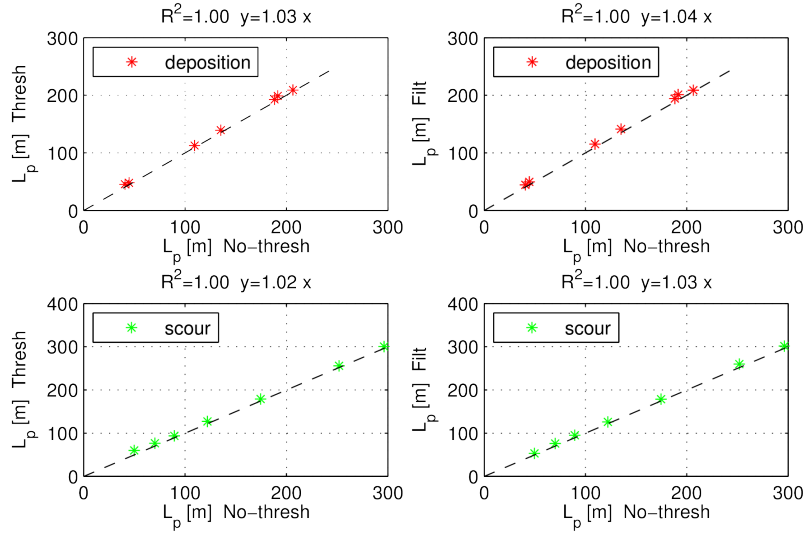


Figure 2.31: Comparison between the weighted mean of the semi-major axes computed with the three methods. Upper panels: deposition patches, lower panel: scour patches. Dashed line represent the 1 : 1 relation.

On the basis of laboratory observations Egozi and Ashmore (2008) suggested that estimation of braiding indexed requires a minimum length of 10 times the average wetted width (measured in formative conditions). However in terms of morphological changes, such as patches size or the erosion and deposition volume the necessary domain length may be different and variable with event magnitude and duration.

We can study this problem for the Rees dataset by computing erosion and deposition volumes (per unit length) with different length of the domain. The result, in terms of erosion volume, is reported in figure 2.32. It is clear that smaller volumes attain a stable value after a distance much shorter than the higher volumes moved by large floods. This is consistent with the observations above about the characteristic scale of erosion and deposition patches.

The need of a larger reach for bigger events is expected to be valid even for the estimate of the path length; indeed it is clear that the number of relatively large areas, which are more relevant for estimating the weighed patches length L_{pw} , tends to reduce for bigger events.

2.9.4 Analysis of channels movements

As we have discussed above, morphological changes, expressed in terms of volume or active area, depend upon both magnitude and duration of storm events.

In spite of the strong reduction of the costs thanks to new technologies, detailed topographic surveys are still expensive and not easy to undertake.

A much simple property to observe is the planar geometry of the channel

2.9. Appendixes

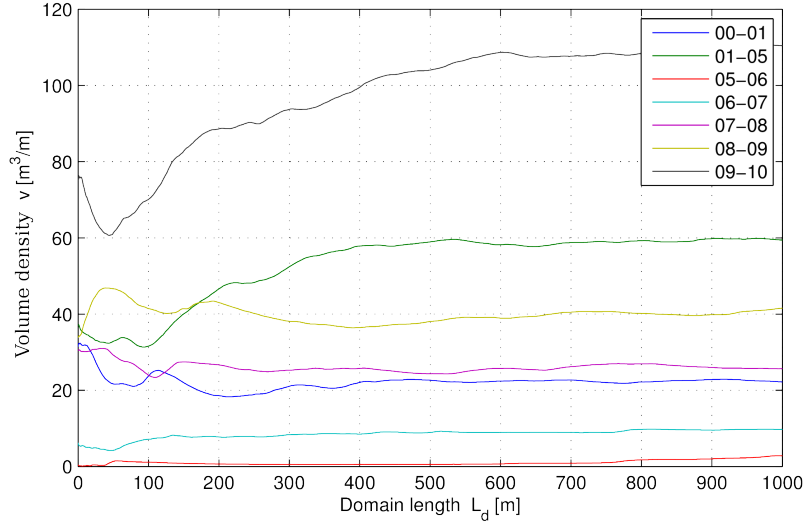


Figure 2.32: Erosion volume per unit length computed on windows of different lengths.

network, which can be identified from aerial or ground-based images collected during periods of relatively low flow. For this reason the analysis of wetted area is probably the more straightforward way to obtain information about the variations in network configuration, due to channel shifting and avulsion, which occurs during floods and flow pulses.

This section investigates the connection between changes in the inundated area and the flood intensity.

As we can see from photograph of figure 1.6 there is not an obvious distinction between dry and wet regions; moreover there are several isolated ponds which should not be identified as channels. For these reason an automated recognition of the channels is not straightforward and we preferred to consider the manual detection of the inundated area performed by Williams et al. (2013a).

If we overlap the maps of different survey (figure 2.33) we can compute the common area (green patches) obtaining the result of figure 2.35 (upper panel) which can be adopted as another indicator of the morphological changes. Unfortunately a direct comparison between the different images is difficult also due to the different discharge at the time of the flight, which varies between 9.0 and 22.6 l/s .

This flow variation is responsible of part of the changes of the inundated area in the range $0.83 \div 1.87 \cdot 10^5 m^2$. In order to reduce this we computed the ratio between the common area and the total wetted area of the two surveys (sum of the red, green and blue pixels of figure 2.33), obtaining the result of figure 2.35 (lower panel). It is clear that a significant inverse correlation between this ratio and the event duration and magnitude exists, which suggests that such

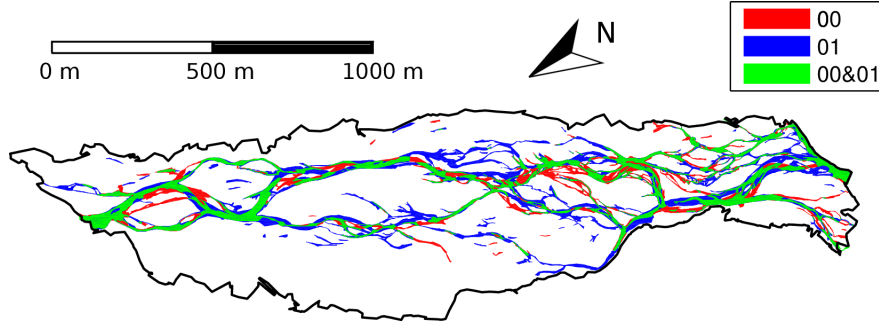


Figure 2.33: Map of the wet area during survey 00 (red area) and 01 (blue area). The common area is depicted in green, the black line represent the extension of the survey.

a simple index may be adopted in order to quantify morphological changes on the basis of aerial images.

2.9.5 Path-length approach in the case of significant compensation

This section provides some consideration about the applicability of the path-length method when significant compensation changes occurs, which as we have seen above is always the case for braided rivers.

Specifically, it is relevant to notice that, from a theoretical point of view, Eq. 2.11 is still valid even after multiple travels of the volumes if, and only if, it is written in the following form

$$V_t = \frac{V_e^T}{L_d} L_t \quad (2.26)$$

where V_e^T is the volume of sediment moved at least once during the period, which is nothing than the volume of the active layer, namely

$$V_e^T = \int_A (\eta_{init} - \eta_{min}) dA \quad (2.27)$$

where η_{init} and η_{min} indicate the initial and minimum bottom elevation during the event and A indicates the entire reach surface.

For example if a volume V_e is eroded, deposited and removed again we can still apply Eq. 2.28 if we consider the total path length composed by two distinct movements.

The volume V_e^T can be significantly different from the volume obtained by capturing all the scour $\tilde{V}_e(0)$. This is evident in the example of figure 2.36, which represents a random variation of the elevation at a given location, where the final volume V_e is less than the minimum one V^T , albeit both are much smaller than the total erosion volume $\tilde{V}_e(0)$.

2.9. Appendixes

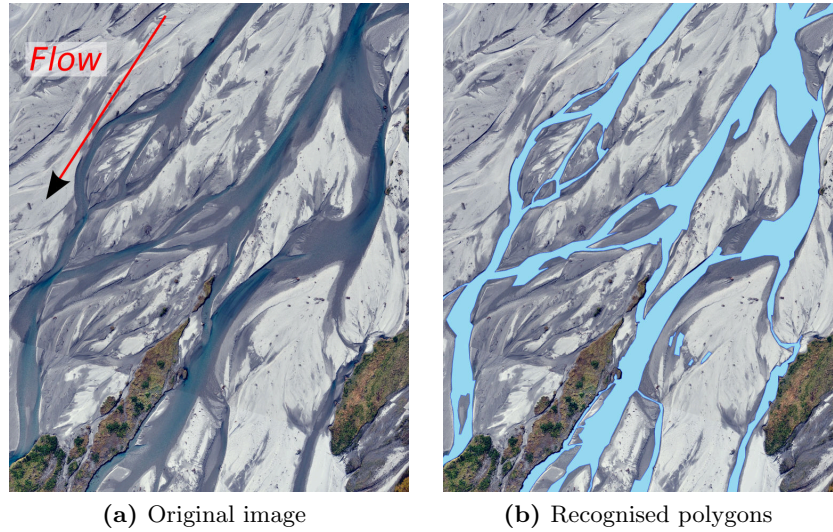


Figure 2.34: Example of manual channel recognition for a portion of the braidplain (survey 09, Williams et al., 2013b).

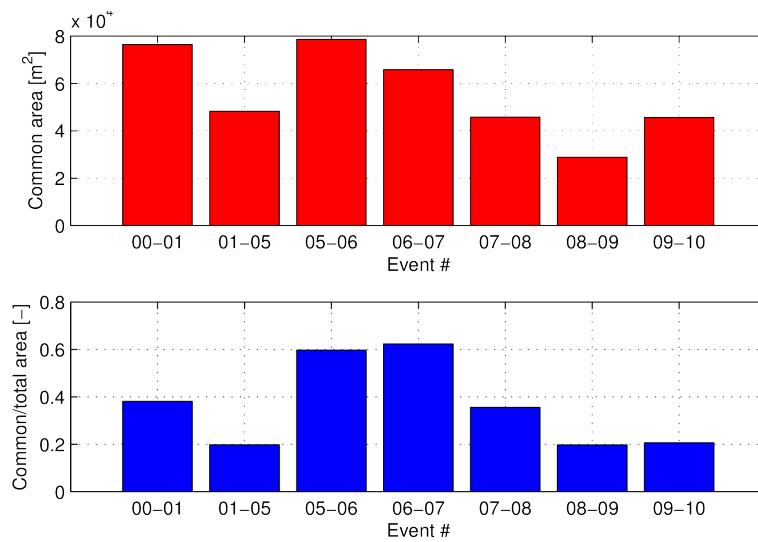


Figure 2.35: Changes of wetted area between different events. Upper panel: wetted area in common. Lower panel: common area divided by the total wetted area of the two surveys.

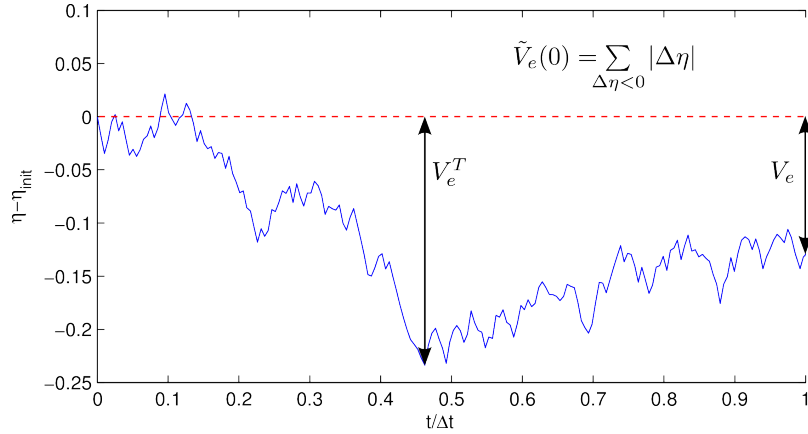


Figure 2.36: Example of the three different definitions of the erosion volumes at a given location. The time evolution is the result of a simple random process.

From this point of view it is not important to capture all the variations (which would be probably impossible) but only V_e^T , so that the important compensation we have to consider is the one between V_e and V_e^T rather than between V_e and V_e^T as investigated by Lindsay and Ashmore (2002).

Unfortunately no laboratory investigations directly studied V_e^T . However if we imagine the scour and deposition at any location as a random process we obtain a relation between the maximum value and the mean absolute value which depends on the process itself.

If a net trend of erosion (as during the events 01-05 and 09-10) occurs it is clear that the V_e and V_e^T would be much more similar than the corresponding deposition volumes because the final scour would tend to be similar than the maximum one. This may provide some support to the choice of using erosion maps for the computation of the transport rate.

In figure 2.37 we report the volume V_e^T for the interval 00-10 estimated using an increasing number of intermediate surveys. We can see that in general this is different from V_e but not as much as the total variation \tilde{V}_e . In addition, with $N = 3$ the major part of V_e^T is already accounted; this may suggest that no more temporal resolution is needed to capture the entire mobilised volume.

In order to make Eq. 2.11 generally valid it is possible to define the path length as follows

$$L_t^{new} = \frac{V_e}{V_e^T} L_t \quad (2.28)$$

which can be different from the physical path length if $V_e \neq V_e^T$. This definition allows to forget for the moment about the difference between Eq. 2.11 and Eq.2.28 and analyse the effect of compensation affects the path length.

2.9. Appendixes

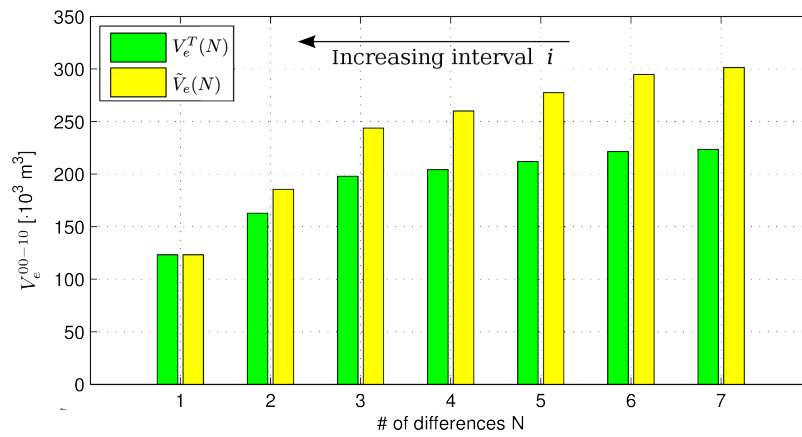


Figure 2.37: Volumes of erosion V_e^T and \tilde{V}_e^T for the entire period 00-10.

Chapter 3

Distribution of elevation and sediment transport

3.1 Introduction

The detailed morphological configuration of a braided river is probably unpredictable over relatively long spatial and temporal scales (Paola, 1996; Paola and Foufoula-Georgiou, 2001). However it is plenty of evidences (e.g Mosley, 1983; Egozi and Ashmore, 2008; Bertoldi et al., 2009d) that statistical properties, such as the reach-scale braiding indexes or the time-averaged bedload transport are not randomly variable but dependent on the controlling parameters.

This statistical description requires the definition of suitable morphological indicators. For this purpose several braiding indexes have been developed in the last decades; for example Egozi and Ashmore (2008) identified different classes (bar index, channel count index, channel length index) and compared the response to forcing conditions during flume experiments. The measurement of these quantities is not trivial and, more importantly, is dependent on the water stage (e.g. Surian, 1999; Van der Nat et al., 2002; Egozi and Ashmore, 2008); for instance the total number of anabranches initially increases with the discharge, then reaches a maximum value and becomes equal one for large flows (Bertoldi et al., 2009d).

An alternative description on the reach-scale morphology, based on merely topographic data, comes from the hypsometric curves, which are widely used in geomorphology as an indicator of catchments and landforms shape (e.g. Willgoose and Hancock, 1988). Indeed the recent development of remote sensing techniques, such as digital photogrammetry, structure from motion, airborne *LiDAR*, terrestrial laser scanning (e.g. Gao, 2009; Marcus and Fonstad, 2010; Brasington et al., 2012) have increased the monitoring possibilities and have made it easier to obtain a detailed elevation model of relatively large portions of the braidplain and consequently to compute the hypsometric curves.

3.1. Introduction

In particular for the analysis of river morphology it is convenient to consider the distribution of elevation with respect to a planar surface inclined with the slope rather than an horizontal reference. This morphological indicator can be adopted for analysing the response to different controls (Bertoldi et al., 2011a); nonetheless this response has not been extensively investigated and the effect of grain size, discharge, slope and degree of confinement on the elevation distribution is still unclear.

One of the most important reach-scale properties of the braided network is the sediment transport rate. Many laboratory studies (e.g. Thompson, 1985; Davies, 1987; Young and Davies, 1990, 1991; Shvidchenko and Kopalani, 1998) have been performed in order to determine the time averaged bedload in regime condition on the basis of the controlling parameters, namely discharge, slope and sediment size. After the first attempts to predict this flux through standard transport formula (Carson and Griffith, 1987; Ashmore, 1988; Griffith, 1989) it became evident (Paola, 1996; Nicholas, 2000; Ferguson, 2003) the great importance of spatial variability of hydraulic parameters, bottom morphology and grain size. Indeed the local bedload transport rate varies nonlinearly with the shear stress and the total bedload flux does not depend only on the average quantities but also on their spatial distribution across the section. This effect is particularly significant in a braided network, where the bed load flux can be several times bigger than in the equivalent uniform, rectangular cross-section (Bertoldi et al., 2009a).

For this reason approaches based on the probability density function of the shear stress, and in particular on the Euler gamma function, have been introduced (Paola, 1996). In particular (Nicholas, 2000) proposed to adopt the distribution of the water depth as a surrogate of the bottom stress; in this way the Euler probability density function can be inferred from the cross-sectional elevation profile. The main disadvantage of this method is the dependence on the water discharge of the distribution parameter (Nicholas, 2000). In spite of this the hypothesis of an analogy between the elevation and the stress distribution seems to be acceptable at least as a first approximation. For this reason the simple $1D$ model proposed by Bertoldi et al. (2009a), which is based on similar assumptions but without the need of fitting a probability function has been proven to correctly capture the averaged bedload measured in a set of laboratory experiments.

These considerations about the transport suggest that a linkage between the reach-scale distribution and the sediment transport probably exists. However such a relation has not been directly explored from previous studies which have mainly focused on the elevation distribution across each single section.

The need to study how the reach-scale morphology depends on the controlling condition and to explore the connections with the sediment transport motivates this work.

A disadvantage of the distribution of the elevation, computed with respect

to a planar surface, lies in the definition of the slope, which is not trivial and may depend on the extension of the studying reach. Moreover the distribution is affected by the areas with higher elevation, so that for instance two different results may arise simply because of a different lateral extension of the computation area.

These considerations suggest to define a different indicator of the braided topography which is more suitable for assessing the morphological response to varying conditions. For this reason we introduced a different definition of the elevation distribution, which does not require the removal of the slope, is insensible to the inclusion of high-elevation areas such as banks of portions of the braidplain, is simple to analyse and apparently strongly connected with the sediment transport.

A series of laboratory experiments and field observation allow us to study how such indicator responds to different conditions in terms of discharge, slope, degree of confinement width and grain size. The flume experiments, together with a depth-averaged numerical model of a natural river, supports the idea that the reach scale elevation distribution is representative to the shear stress heterogeneity and can consequently be adopted for estimating the bedload in a complex topography.

Furthermore if we interpolate the curve with a power-law we can determine analytically the inundation and bedload curves, which allows us to investigate the relation between morphological complexity and response to the hydrological forcing.

3.2 The method

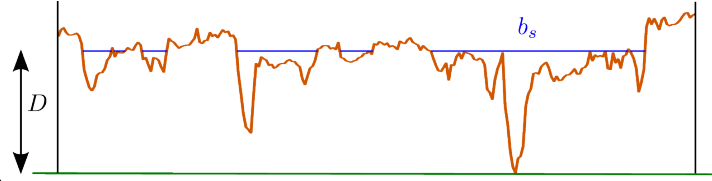
3.2.1 Definition and scaling

The reach-scale indicator we propose here is based on the bottom elevation with respect to the lowest point across the braided section; therefore it requires the definition of cross-sections which are orthogonal to the principal direction of the river. While in a laboratory experiment we can adopt the flume direction, the definition of a river direction in a natural case is less straightforward.

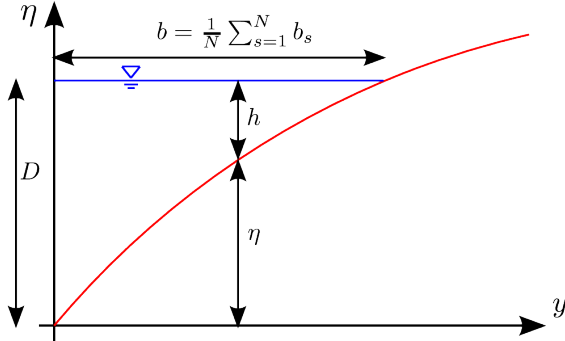
Since we are interested in the average flow direction at the reach scale we must define a river direction which varies on the same longitudinal scale. For this purpose for the River Tagliamento, whose direction is significantly varying within the study areas, we considered a series of 1 *km* spaced points located at the centre of the braidplain and we defined the river axis as the cubic spline passing through these points to define the river axis.

Once the river axis is identified we can define D as the elevation with respect to the lowest point and b_s of each cross-section “ s ” as the width of the portion of the bottom which lies below this height (cumulative length of the blue segments of figure 3.1a). Imaging a horizontal free surface (as in Nicholas, 2000; Bertoldi

3.2. The method



(a) Example of section.



(b) Average section and notation.

Figure 3.1: Definition of the $b(D)$ curve for each cross-section. b_s is the cumulative length of the blue segments. By repeating the procedure for each section of a braided river reach we obtain the averaged $b(D)$ curve.

et al., 2009a) the $b_s(D)$ curve represents how the wetted width depends on the maximum water depth across the section.

If we repeat the procedure for all the N sections covering a braided river reach and we compute the mean value of b_s

$$b = \frac{1}{N} \sum_{s=1}^N b_s \quad (3.1)$$

we obtain an averaged curve $b(D)$ which represents the cumulative distribution of elevation relative to the deepest point of the section.

In principle there is not a well-defined upper limit of the curves; however since we are interested in the morphologically active area rather than the flood-plain we need to fix a certain elevation D ; for this purpose we can limit b to the mean wetted width in formative conditions b_0 , which can be estimated from the formative discharge according to the method we will present later.

The curve we obtain can be conveniently approximated as a power-law, namely

$$b = kD^\alpha \quad (3.2)$$

where k fixes the scale and α is an indicator of the curve shape.

For a single-thread channel with compact section the $b(D)$ curves simply indicate the section shape. For example, in the contest of estuarine morphology

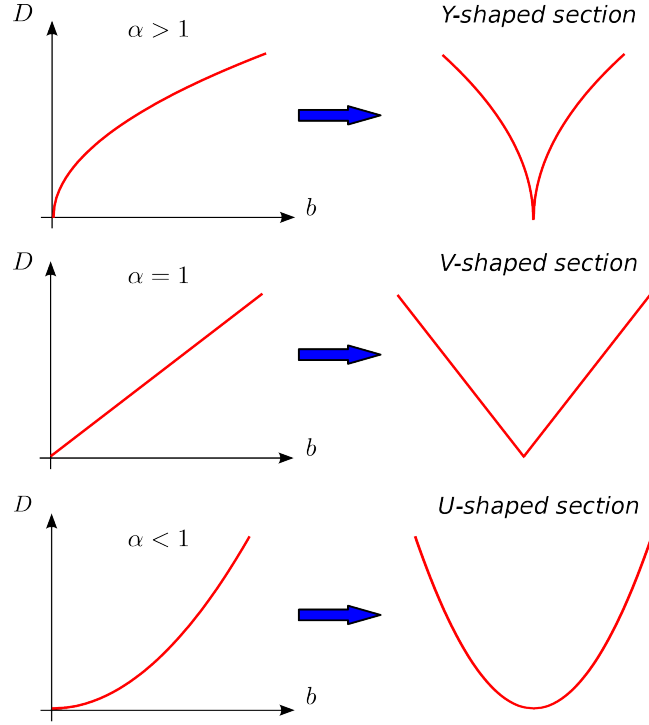


Figure 3.2: Definition of the Average section (right side) on the basis of the $b(D)$ curves and distinction in different shapes on the basis of the coefficient α , following Toffolon and Crosato (2007).

Toffolon and Crosato (2007) adopted the power-law approximation of that curve to identify three different section types on the basis of the curve concavity as represented in figure 3.2.

In the case of a braided morphology the actual section geometry is complex and variable along the reach; nevertheless we can still define an equivalent compact section having the same $b(D)$ distribution we call “Average section“. In particular we consider a section developing on only one side (with a vertical bank, like in figure 3.1b), which can be specified as

$$\eta(y) = D(b) \quad \forall \eta = D \quad (3.3)$$

where η is the bottom elevation along the section as sketched in figure 3.1b.

Before investigating how this average property of the braided network depends on the river features it is convenient to work with dimensionless parameters; in particular if we consider the gravitational acceleration g and the mean sediment size d_s as scaling parameters we can write the solid and liquid discharges as

$$Q_s^* = \frac{Q_s}{\sqrt{g\Delta} d_s^{5/2}} \quad Q^* = \frac{Q}{\sqrt{g} d_s^{5/2}} \quad (3.4)$$

3.2. The method

where Δ is the relative submerged weight of the sediment. Similarly we can define

$$b^* = \frac{b}{d_s} \quad D^* = \frac{D}{d_s} \quad W^* = \frac{W}{d_s} \quad (3.5)$$

where b and D are the parameters of our curve and W is the confinement width, defined as the distance between fixed or relatively stable banks, which ranges from relatively small values in the case of a strongly confined flow to the large values characteristics of relatively free, unconfined networks.

As commonly assumed in the analysis of braided networks (e.g. Egozi and Ashmore, 2008) we can consider that the reach-scale statistical properties depend on the external controls only; in particular in an equilibrium condition with constant discharge and uniform slope and confinement width we expect the $b(D)$ curve and the average transport Qs to depend on the following parameters

$$\{b(D), Qs\} = fct(Q, S, W, \rho, \rho_s, g, d_s, \sigma) \quad (3.6)$$

where ρ and ρ_s are water and sediment density respectively, d_s is a representative grain size (for instance the median value) and $\sigma(d/d_s)$ is the sediment size (d) distribution.

Using the π -theorem we can reduce the number of parameters by writing the functional dependence in dimensionless form, namely

$$\{b^*(D^*), Qs^*\} = fct(Q^*, S, \Delta, \sigma, W^*) \quad (3.7)$$

This relation, which is independent of the problem scale, holds as far as the braided network is big enough to avoid the so-called ‘‘scale effects’’ induced by the water viscosity and the surface tension (e.g. Young and Warburton, 1996) like development of ripples or cohesion of bed material.

If we neglect the role of Δ , which is usually not much variable within the most common river minerals, and we restrict our attention on well-sorted grain size distribution we end up with

$$\{b^*(D^*), Qs^*\} = fct(Q^*, S, W^*) \quad (3.8)$$

which is the relation between morphodynamical response and controlling parameter we are going to investigate within the present work.

3.2.2 Flume experiments data

Three different sets of laboratory experiments, performed at the University of Trento, were considered for the present analysis (Garcia Lugo et al., 2013; Bertoldi et al., 2009a; Welber et al., 2012). Specifically, 58 experiment were accomplished in different conditions of slope, water discharge, banks spacing and sediment size.

Parameter	Symbol	TN1	TN2	TN3
# of runs	N	26	5	27
Grain size	d_{50}	0.63 mm	1.0 mm	1.0 mm
Slope	S	0.3 ÷ 1.5%	1.0%	1.0%
Confinement width	W	2.90 m	2.90 m	0.15 ÷ 1.5 m
Water discharge	Q	0.3 ÷ 4.0 ls^{-1}	1.8 ls^{-1}	1.5 ÷ 2.5 ls^{-1}
Mean sediment flux	Q_s	0.68 ÷ 5.28 gs^{-1}	$\simeq 2.4$ gs^{-1}	1.04 ÷ 7.73 gs^{-1}
Scanning resolution	$dx \times dy$	10 × 1 cm	2.5 × 0.5 cm	5 × 0.5 cm

Table 3.1: Summary of the main features of the laboratory experiments.

The supply of well-sorted sand was adjusted in order to maintain a long-term mass balance of the network while the duration of each single run has been chosen in the range 1.5 h to 110 h in order to allow the system to attain a statistical equilibrium state.

The first (TN1) series of runs (Bertoldi et al., 2009a) encompass 5 different slopes, various water supply and well-sorted sand with grain size 0.63 mm. In the second (TN2) experimental set (Welber, 2012, unpublished) fixed discharge and slope have been considered, for all the 5 runs. The role of the network confinement was investigated in the TN3 experiment (Garcia Lugo, 2014) where three different values of discharge were considered for each of seven channel widths. A summary of the main features of the laboratory experiments is reported in table 3.1.

3.3 Results

On the basis of the three sets laboratory experiments and the field data we can investigate how the $b(D)$ curves depend upon the controlling conditions.

The Average section of relatively unconfined networks

The TN1 and TN2 series of experiments reproduced the morphodynamics of relatively unconfined braided networks; consequently we do not expect any significant influence of the flume width W^* , so that the morphological response should depend, according to Eq. 3.8 on Q^* and S only. In the present laboratory dataset the slope changes in the interval 0.3 ÷ 1.7 % while the dimensionless discharge Q^* ranges from $0.9 \cdot 10^4$ to $13 \cdot 10^4$.

Considering the bed elevation scan at the end of each run and excluding the first 2 m in order to remove local effects at the flume inlet we can compute the curves reported in figure 3.3.

The first feature we can notice is that the curves have the typical *Y-shape* represented figure 3.2), which show an opposite concavity with respect to the typical sections of single-thread rivers. Writing the results in dimensionless

3.3. Results

form allows for a direct comparison of the TN2 and TN3 in spite of the different sediment size (0.63 mm and 1 mm respectively).

The second important characteristics we can recognise in figure 3.3) is a clear dependence of the curves on the mean channel slope S , which suggests that steeper braided networks may be more shallow.

The effect the two controls S and Q^* on the bed relief can be analysed by computing the reach-average of the elevation difference within each section (figure 3.4a) or the reach-averaged Bed Relief Index (figure 3.4) as defined by Hoey and Sutherland (1991) and scaled using the sediment size. While apparently there is not a significant influence of the discharge, the slope is clearly inversely correlated with the bed relief. A possible interpretation of this behaviour follows the tendency of the gravel-bed channels to maintain a Shields stress not far from the critical value for sediment motion; indeed in we consider that the average stress is proportional to the mean water depth multiplied by the slope it is not surprising that the channel depth respond inversely to gradient variations.

After this considerations the relevant question which arises is: "What about the shape? How does it depend on the experimental conditions? ". In figure 3.3 we can notice that for example the blue lines are less curved than the orange plots; a quantitative analysis of the growth of b with D can be performed by computing the exponent of the best-fitting power-law α ; if we plot this coefficient against the discharge we obtain the result of figure 3.5a) where apparently an inverse correlation exists. However it is again not easy to decouple the roles of slope and discharge.

One may argue that the stream power, rather than the discharge is the most suitable parameter to describe the variation in the exponent; however the plot of figure 3.5b) shows an higher scatter of the points, a tendency of the higher slopes to give larger α and suggests that the stream power may be not the correct parameter to define the shape of the distributions. Interestingly this observation is consistent with the results of Bertoldi et al. (2009d), which reveals that the parameters which describe the global complexity of the network depend on the discharge while indexes related to the instantaneous morphological activity are more related to the stream power.

It is worth to say that for the experiment with relatively large Q^* we can not exclude a significant impact of the flume banks, which bounds the maximum width of the network; for this reason we could interpret the lower of α in figure 3.5a) as a consequence of the confinement effect rather than a variation of discharge or gradient. This is not the case for runs with $S \geq 0.7\%$, for which the belt width, defined as the area subjected to morphological processes was significantly smaller than the flume width (for instance $< 2 m$ in run 10, Bertoldi et al. (2009d)); Thanks to the third series of experiments (TN3) we will address this problem in the following section.

In terms of slope, dimensionless width and discharge the conditions of the

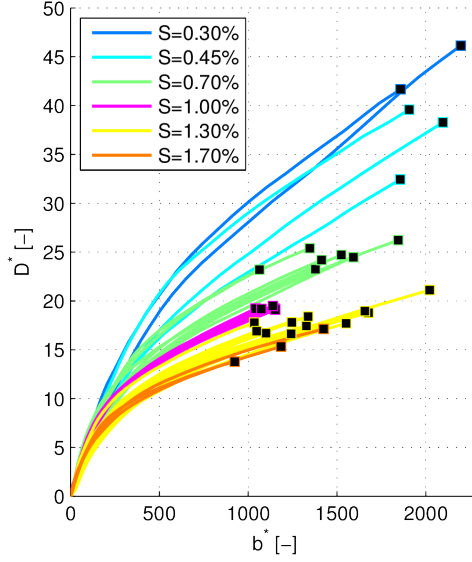


Figure 3.3: $b(D)$ curves of the TN1 and TN2 experiments. The square marker at the end of each curve indicates the formative condition as defined by the simple uniform flow model of section 3.4. Different colours represent different slopes.

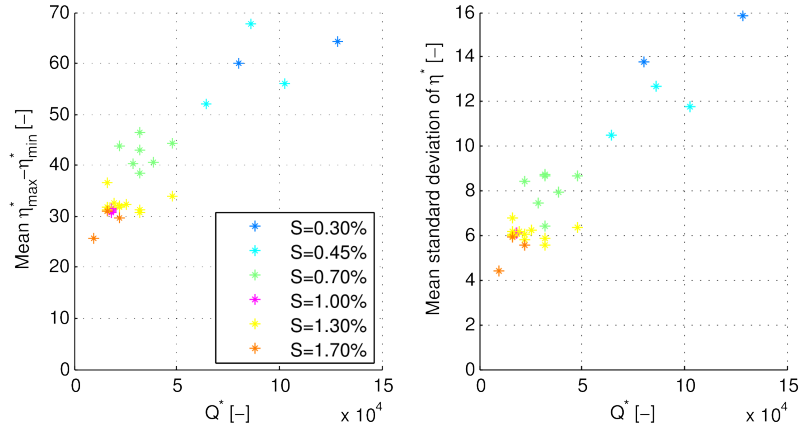
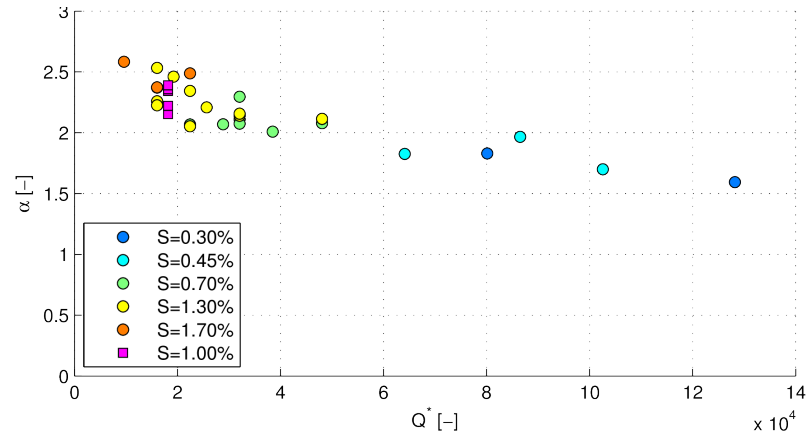
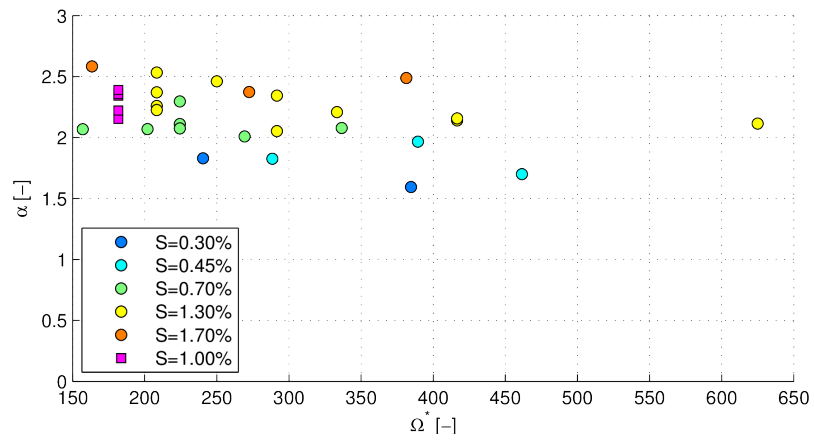


Figure 3.4: Mean variation of elevation across the section, as a function of the discharge, for TN1 and TN2 experiments. Left panel: difference between the highest and lowest point of the section; right panel: standard deviation of $\eta(y)$.

3.3. Results



(a) α as a function of the total dimensionless discharge Q^* .



(b) α as a function of the total dimensionless stream power $\Omega^* = Q^* S$.

Figure 3.5: Coefficient of the power law which best fitting the TN1 (circular markers) and TN2 (squared markers). Different colours represent different slopes.

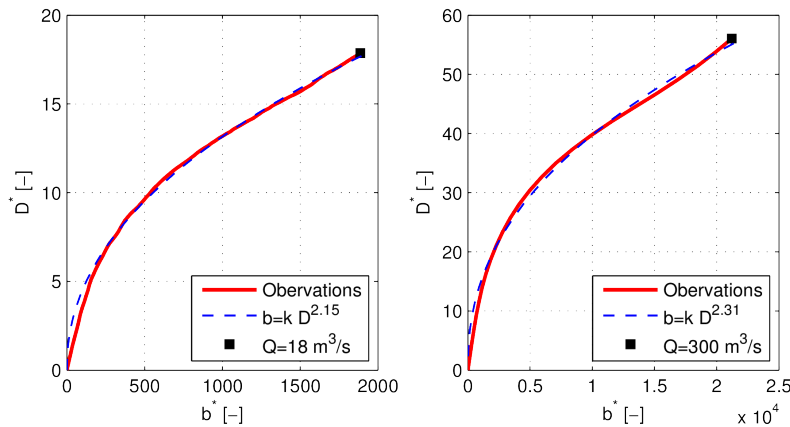


Figure 3.6: $b(D)$ curves of river Sunwapta (left panel) and Rees (right panel). The dashed line represents the best fitting of the power law $b = kD^\alpha$.

River Sunwapta are similar to the TN1 and TN2 laboratory experiments. Indeed, considering a representative discharge $Q = 18 \text{ m}^3\text{s}^{-1}$ we have $Q^* = 1.8 \cdot 10^4$, which is approximately the value adopted during five of the TN1 runs with $S = 1.3 \%$; in addition also the width of the braidplain $W \simeq 150 \text{ m}$ is similar (in dimensionless form) to the one of the TN1 experiments ($W^* \simeq 3.8 \cdot 10^3$ in the river and $W^* \simeq 4.6 \cdot 10^3$ in the flume).

The comparison between figure 3.6 and figure 3.3 confirms the analogy in terms of $b^*(D^*)$ distributions between braided networks having different scales but similar S , Q^* and W^* .

The conditions of the Rees River are rather different, especially for what concern the hydrological forcing. Indeed, due to the large variability of discharge compared with the pro-glacial Sunwapta River, as well as the limited duration of the water stage record it becomes difficult to identify a representative formative discharge. It is clear that the discharge is much higher in the Rees River: if we roughly consider $Q = 300 \text{ m}^3$ (value exceeded for 10 h in the 18-months period covered by hydrological data) we obtain a dimensionless value $Q^* = 1.7 \cdot 10^6$, two orders of magnitude larger than the flume experiments.

The effect of this large flow is appreciable in the right panel of figure 3.6; if we compare the curves with flume results relative to similar slopes ($S = 0.57 \%$) we notice an important increase of the wetted width in formative condition b_0^* and only a minor effect on the correspondent D_0^* .

At this point it is important to spend some words about the coefficient k : this parameter depends on both the horizontal and vertical scale of the curves and can be written as

$$k^* = \frac{b_0^*}{D_0^{*\alpha}} \quad (3.9)$$

with b_0^* indicating the wetted width in formative conditions and D_0^* the corre-

3.3. Results

sponding point on the curve. We have seen that D_0^* is mainly dependent on the slope, the b_0^* can strongly increase with the discharge whereas α may depend on both S and Q^* . This complicate behaviour does not enable, due to the limited dataset available, to express a general formulation for the coefficient k^* . For this reason we focus our analysis on the response of the curve shape, expressed through the coefficient α rather than on a complete description of the regime morphology.

Similar conditions occur also in the River Tagliamento; however in this case the morphology is more heterogeneous due to the presence of geological confinement and the significant impact of the vegetation (Bertoldi et al., 2011a).

The intensity of the flood events (in terms of dimensionless discharge) is again much larger than in the laboratory; for instance if we assume $Q = 1000 \text{ m}^3 \text{ s}^{-1}$, which correspond to a wetted area of 90% at the *Cornino* reach, (Welber et al., 2012) we have $Q^* = 1 \cdot 10^6$, the same order of magnitude larger of the one measured in the Rees Reach.

A detailed analysis of the morphological variations within the river can be performed by dividing the 21 *km*-long reach in the 12 areas of figure 3.7b, which display different characteristics in terms of slope, vegetation height and density, and geological constrains.

At the *Area 5* an important bedrock outcrop is located at the middle of the river corridor and at the *Area 9* a geological confinement causes a reduction of width up to 130 *m* (Bertoldi et al., 2011a). In addition, as reported by the same authors, differences in the vegetation dynamics produces significant impact on the morphological development of the different sub-reaches.

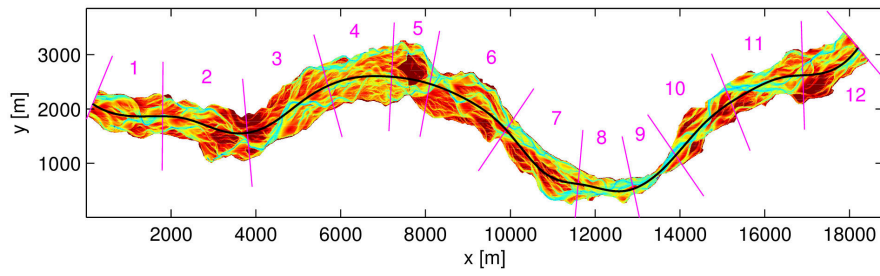
From the analysis of the $b(D)$ curves 3.7b we can immediately see the effect of the gorge at *Area 9*, where a *U-shaped* section can be observed; the narrowing can be also clearly felt on the adjacent *Area 8*.

Interestingly the stable rocky island of *Area 5* does not affect significantly the curve shape; this observation could be explained by considering that the river has enough lateral space to attain a fully-developed braided state even in the presence of a central stable island.

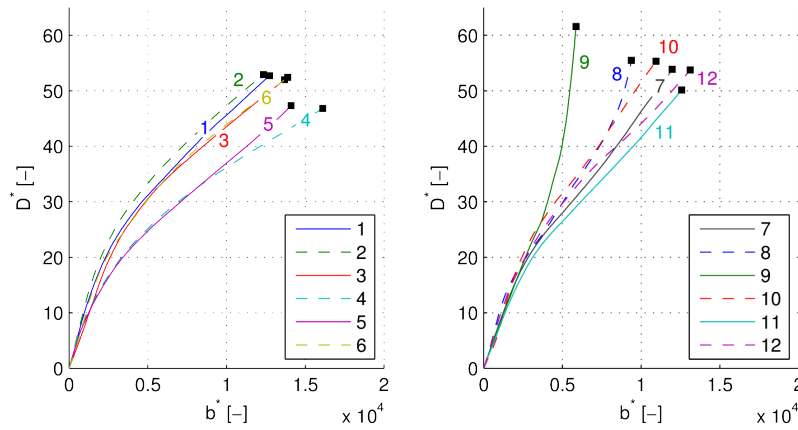
On the other hand the curves for the wider sub-reaches (e.g. Areas 4,5,11,12) are similar to the Rees River results of figure 3.6.

It is clear that some of the curves of figure 3.7, for example the number 8, does not exactly follow a power law; for this reason the result we obtain by fitting 3.2 has to be interpreted as an indication of the curve concavity rather than an accurate approximation of the $b(D)$ relation.

The analysis of the exponent (figure 3.8) reveals that there is a significant inverse correlation between the α and the wetted width b .



(a) Map of the selected areas. Flow is from left to right.



(b) $b(D)$ curves.

Figure 3.7: $b(D)$ curves for different areas of the study reach. The black squares represent the estimated width with $Q = 1000 \text{ m}^3 \text{ s}^{-1}$.

3.3. Results

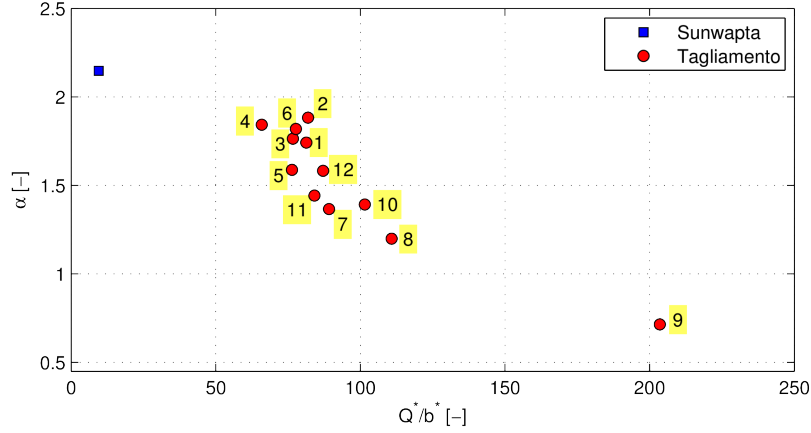


Figure 3.8: Exponent of the $b(D)$ curves as a function of the specific discharge for the Sunwapta River and for the different sub-reaches of the Tagliamento River. A representative discharge $Q = 1000 \text{ m}^3\text{s}^{-1}$ was adopted. The labels refers to the sub-areas of figure 3.7a.

The effect of the network confinement

In the River Tagliamento the presence of vegetation, the highly variable discharge, the spatial heterogeneity of the geological conditions and the vegetation characteristics, make it difficult to understand the role the parameters which control the morphological response. For this reason it is convenient to first analyse the effect of the confinement in a laboratory braided network, where we can keep constant and uniform controlling conditions within each experimental run.

Results of the TN3 experiments, reported in figure 3.9 reveals several significant features. For the wider runs the curves resemble the *Y-shape* of the previous experiments, while increasing the confinement rate the $b(D)$ relation becomes less curved (decreasing α). Ultimately, for $W \simeq 60 \text{ cm}$ ($Q = 1.5 \text{ ls}^{-1}$ and $Q = 2.0 \text{ ls}^{-1}$) or for $W \simeq 80 \text{ cm}$ ($Q = 2.5 \text{ ls}^{-1}$) an almost linear trend ($\alpha \simeq 1$) can be observed and, following Toffolon and Crosato (2007), we can call the resulting curve *V-shaped*. ù

By comparing the curves relative to different experiments we can notice that the transition between different shapes does not depend only on the flume width W^* but also on the discharge; in particular, as one may expect, the specific discharge Q^*/W^* is apparently a more proper parameter to determine the morphological effect due to network confinement. Indeed if we plot the exponent α of the best power-law fitting as a function of the specific discharge (figure 3.10) we can observe a descending trend which is similar for the three data series. This monotonic trend is interrupted by some high values around $Q^*/W^* = 40$; these points correspond to morphological transition between alternate bars pattern and braided network and are represented by curves which are not well interpolated with the simple power law (for example the black,

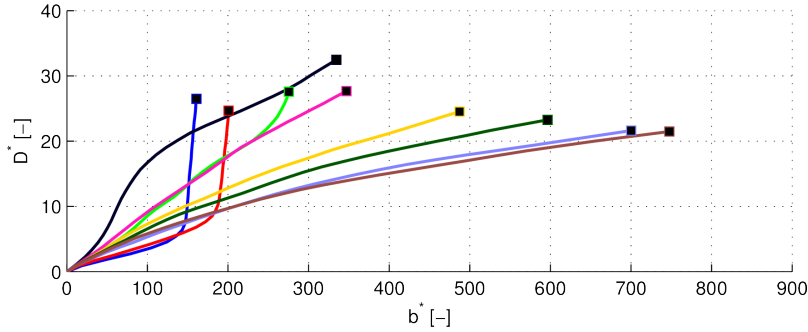


Figure 3.9: $b(D)$ curves of the TN3 experiments with $Q = 2.0 \text{ l s}^{-1}$. Different colours indicates a different confinement width W ; The square marker at the end of each curve indicates the formative conditions as defined by the simple uniform flow model defined in section 3.4.

$W = 40 \text{ cm}$ curve of figure 3.9)

If we consider the entire set of flume experiments and we analyse the response of the exponent α to varying specific discharge we obtain the plot of figure 3.11a, where we can see that the coefficient is well correlated with Q^*/W^* and decreases monotonically from values $\alpha > 2.5$ to values $\alpha < 0.5$; on the contrary in terms of total dimensionless discharge (figure 3.12) there is not an unique trend and highly different exponents can be found for similar values of Q^* .

In the analysis of figure 3.11a we should distinguish between two type of regimes. The first one occurs for $Q^*/W^* < \sim 100$ and correspond to fully developed and relatively unconfined braided networks (which show a coefficient $\alpha \geq 2$); the second appear for higher specific discharges and is dependent on the reduction of available width which leads to a simpler morphology.

The plot of figure 3.11a can be useful to determine the point at which the confinement effect becomes relevant. However it is worth to underline that for unconfined networks, which by definition do not depend on W , the specific discharge Q^*/W^* might not be the parameter which controls α ; indeed the alignment of the points we observe in the left region of figure 3.11a might occur simply because no runs with different W are available for TN1 and TN2 experiments.

A similar plot (figure 3.11b) can be obtained by considering the discharge per unit of wetted width, defined on the basis of the simple (and approximate) $1D$ model we will detail in the following sections. For the TN1 and TN2 experiments this parameter is significantly correlated with α , whereas for confined configurations is still representative of the morphological variation due to the limited space available relatively to the water discharge. Because the parameter Q^*/b^* does no implicitly contain the confinement width W^* it might be parameter which describes α variation in both confined and unconfined networks.

3.4. Elevation distribution and sediment transport

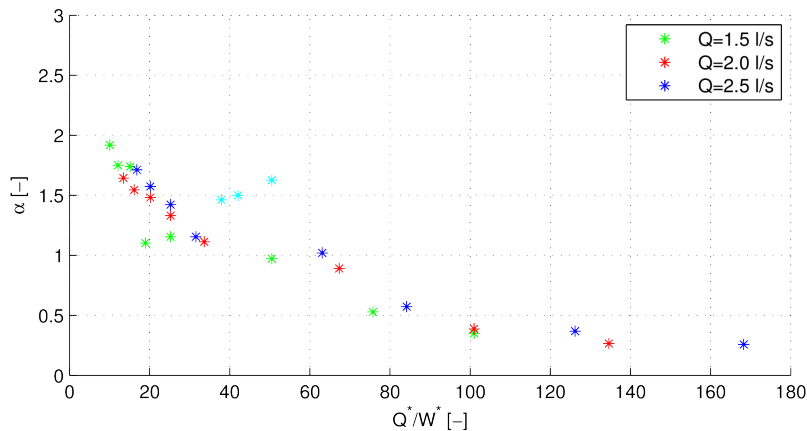


Figure 3.10: Exponent of the power law which is best fitting the $b(D)$ curves of TN3 experiments, as a function of the dimensionless specific water discharge. Colours indicate different Q , the cyan points refer to transition networks, for which a power-law interpolation may be inappropriate.

3.4 Elevation distribution and sediment transport

3.4.1 Introduction

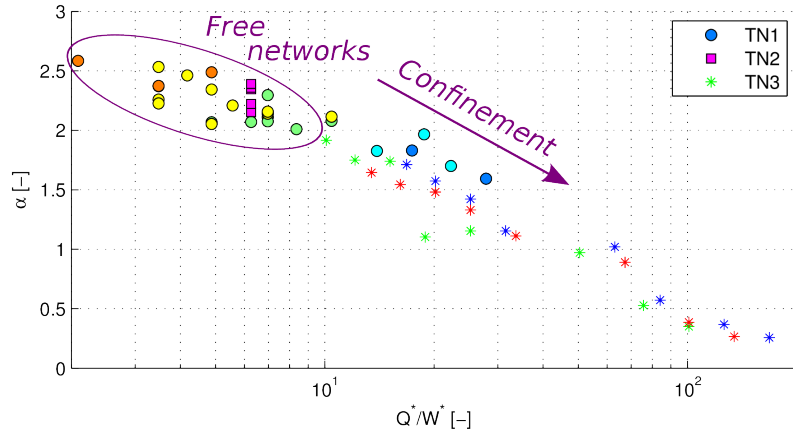
The $b(D)$ curve we defined above contains information about depth, width and heterogeneity of the channels network, which are the ingredients crucial for determining the bedload transport rate (e.g Paola, 1996; Nicholas, 2000; Ferguson, 2003). Therefore the question which arises is whether we can use this synthetic information to estimate the solid discharge.

A similar idea, but based on the cross sectional morphology rather than a reach-scale indicator, has been proposed by Nicholas (2000) whose method assumes that the cross-sectional geometry can be adopted to estimate the stress distribution, to fit the Euler probability function and to estimate the local bedload. This fitting can be highly dependent on the discharge; in order to overcome this issue Bertoldi et al. (2009a) proposed a simple $1D$ model which assumes horizontal free surface and local uniform flow at each cross-section, bypassing the usage of a probability density function.

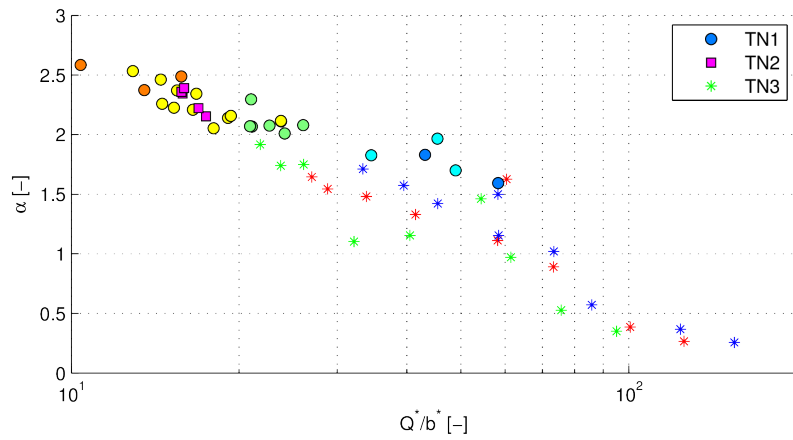
The hypothesis behind this method are often not satisfied locally; however if the procedure is repeated for a number of sections covering the reach scale the resulting average bedload is consistent with flume measurements. Indeed the Bertoldi et al. (2009a) model is capable to take into account the spatial variability of the hydraulics and consequently to correct the strong under-estimation which arises by assuming a constant stress across the section.

In the present work we make a step further by considering not the distinct cross section but the elevation distribution at the reach scale. Albeit being a natural extension of the existing approaches, estimation of the bedload on

3.4. Elevation distribution and sediment transport



(a) α as a function of the specific discharge per unit flume width W .



(b) α as a function of the specific discharge per unit wetted width b .

Figure 3.11: Exponent of the power law which is best fitting the $b(D)$ curves of TN1, TN2, TN3 experiments as a function of the dimensionless specific water discharge.

3.4. Elevation distribution and sediment transport

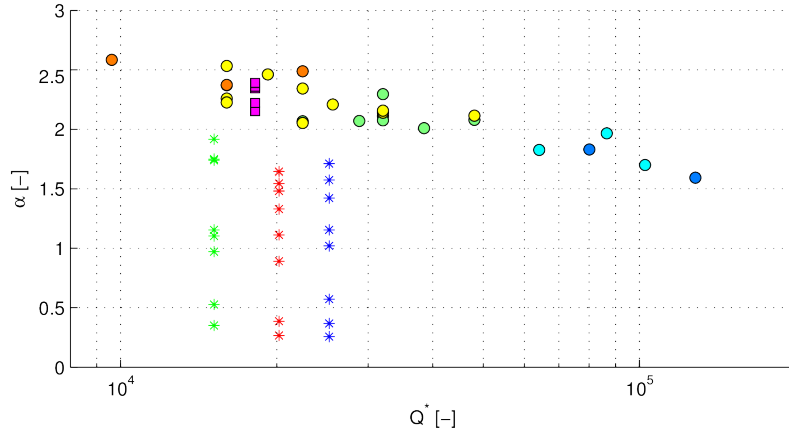


Figure 3.12: Exponent of the power law which is best fitting the $b(D)$ curves of TN1, TN2, TN3 experiments as a function of the total dimensionless discharge.

the basis of a reach-scale average geometry such as the *Average section* is not straightforward but requires discussion and validation on the basis of experimental data.

3.4.2 A reach-scale bedload estimator

If we assume uniform flow conditions in the equivalent *Average section* we can calculate the distribution of the hydraulic quantities; consequently we can estimate bedload flux (as well as wetted and active width) accounting for spatial variability of the flow over the complex morphology.

Firstly, we apply locally an uniform flow formula and integrate along the section in order to find a stage-discharge relationship; in particular considering dimensionless variables we write

$$Q^* = \int_0^{b^*} C\sqrt{S} h^{*3/2} dy^* \quad (3.10)$$

where the local depth h^* depends on the maximum depth D^* as follows (see figure 3.1b)

$$h^*(y^*) = D^* - \eta^*(y^*) \quad (3.11)$$

The dimensionless Chèzy coefficient can be estimated as (Engelund and Fredsoe, 1982)

$$C = 6 + 2.5 \log \left(\frac{h^*}{2.5} \right) \quad (3.12)$$

or alternatively, by adopting the Gauckler-Strickler formula, which can be expressed as (Strickler, 1923)

$$C = C_0 h^{*1/6} \quad C_0 = \frac{k_s}{\sqrt{g} d_s^{1/6}} = 6.74 \quad (3.13)$$

3.4. Elevation distribution and sediment transport

where k_s is Gauckler-Strickler coefficient.

If we numerically integrate Eq. 3.10 we obtain the $D(Q)$ curve and consequently the $b(Q)$ relationship.

Similarly we can estimate the solid discharge by assuming that a standard bedload formula is locally valid and integrating along the section as follows

$$Qs^* = \int_0^{b^*} \Phi(\theta) dy^* \quad (3.14)$$

where the dimensionless bedload per unit width Φ is usually (e.g. Meyer-Peter and Müller, 1948) expressed as a function of the local Shields stress, which depends on the flow depth through the uniform flow formula

$$\theta = \frac{Sh^*}{\Delta} \quad (3.15)$$

that enables to close the problem of computing the $Qs(D)$ and $Qs(Q)$ relationships.

Numerical modelling

In order to explore the connection between the reach-scale morphology described through the $b(D)$ curve and the Shield stress distribution, we performed a fixed-bed numerical simulations; in particular we used the depth-averaged hydrodynamic model *Delft3D* to simulate the hydrodynamic response of a natural braided morphology. The setup, calibration of validation of that model for the Rees River was performed by (Williams et al., 2013a); on the basis of this work we can estimate of the distribution of the hydraulic parameters within the reach for different flow conditions.

We started the simulations by supplying a small discharge and we increased it until we reached the target Q , defined as the discharge measured at the peak of the last flood events $Q = 323 \text{ m}^3 \text{ s}^{-1}$; this peak discharge was maintained until a steady state hydraulic configuration occurred. As a second test case we repeated the simulation with a lower ($Q = 200 \text{ m}^3 \text{ s}^{-1}$) discharge.

The most important parameters of the hydraulic simulations are reported in table 3.2.

In order to investigate the at-a-station response to varying discharge we also simulated the effects of a flow hydrograph ranging from a basic value ($Q = 30 \text{ m}^3 \text{ s}^{-1}$) to a peak flow $Q = 430 \text{ m}^3 \text{ s}^{-1}$. In order to avoid effects related to the local inertia of the hydrodynamics as well as delays due to the propagation of the flow pulse throughout the network we consider a very slow ($6 \text{ m}^3/h$) linear growth of the discharge; in this way we obtain a response which depends only on the instantaneous discharge and not on the actual shape of the hydrograph.

3.4. Elevation distribution and sediment transport

Parameter	Symbol	Value
Representative sediment size	d_{84}	35.2 mm
Nikuradse roughness length	k_s	0.05 m
Mean grid size		$\simeq 2$ m
Horizontal eddy viscosity	ν_H	$0.1 \text{ m}^2 \text{ s}^{-1}$
Secondary currents coefficient	β_c	0.5
Gravitational acceleration	g	9.81 m s^{-2}

Table 3.2: Most important parameters of the numerical simulations.

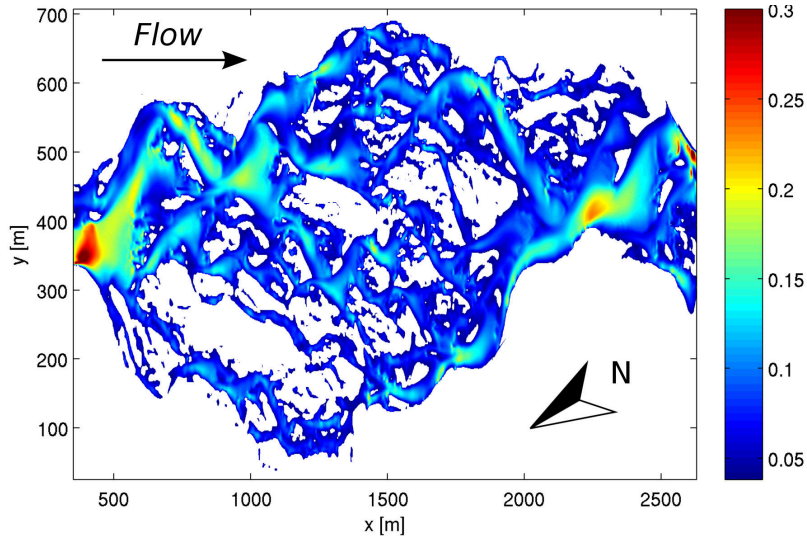


Figure 3.13: Map of the Shields stress of the Rees River from the hydrodynamic model with $Q = 323 \text{ m}^3 \text{ s}^{-1}$. Only areas with $\theta > 0.038$ are represented. Flow is from left to right; axes are not to scale.

3.4.3 Results

The results of the two-dimensional modelling can be adopted for testing our hypothesis that the a simple uniform-flow method applied on a representative *Average section* can approximately reproduce the variability of the bottom stress in braided networks.

The map of the Shields stress for the Rees River (figure 3.13) shows that, during the peak discharge, a relatively large area is active and a very heterogeneous distribution of the stress occurs, ranging from $\theta > 0.2$ in few small regions to $\theta < 0.1$ within approximately the 75 % of the active area.

The comparison with the stress distribution predicted by the *Average section* method, for both the peak ($Q = 323 \text{ m}^3 \text{ s}^{-1}$) and a smaller ($Q = 200 \text{ m}^3 \text{ s}^{-1}$) discharge, is represented in figure 3.14, which show that the simple model is able to capture the overall stress distribution. However these curves reveals that

3.4. Elevation distribution and sediment transport

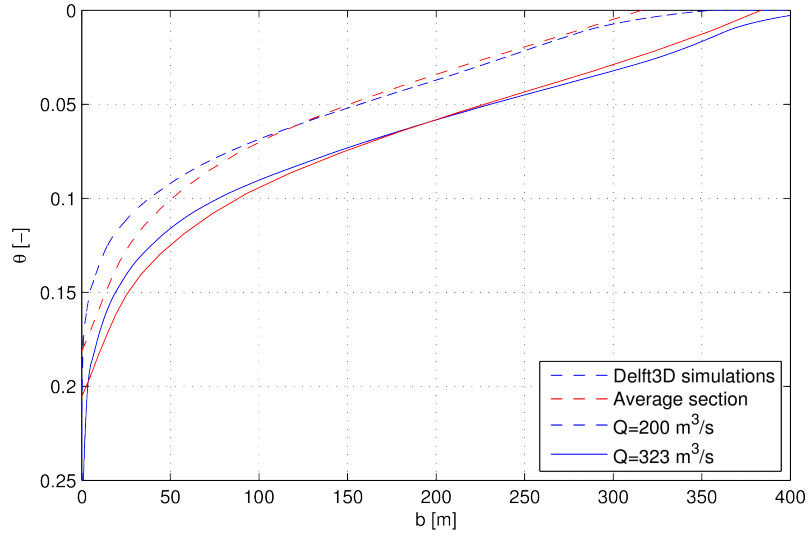


Figure 3.14: Cumulative Shields stress distributions of the Rees River reach from the shallow water model (blue lines) and from the *Average section* method (red lines), with discharge $Q = 323 \text{ m}^3 \text{ s}^{-1}$ (continuous lines) and $Q = 200 \text{ m}^3 \text{ s}^{-1}$ (dashed plots). b indicates the area divided by the reach length; the θ axis has been reversed in order to easily recognise the *Average section* profile.

the *Average section* method tends to slightly over-predict the higher stresses, especially for the smaller discharge, which leads to an overestimate of the reach-averaged solid discharge (table 3.3). Nevertheless, considering the simplicity of the approach and the large uncertainties of the bedload estimate in a braided river, we can accept this error.

Models based on the stress distribution Paola (1996); Nicholas (2000); Ferguson (2003) implicitly assume that the bedload is mainly longitudinal; indeed in order to compute the flux across the sections only the normal component qs_x should be accounted rather than the absolute value $|qs|$ which can be estimated on the basis of the Shields stress.

Results of numerical model offers the possibility to test this hypothesis and reveals that the assumption $qs_x \simeq qs$ leads to a relatively small (approximately $6 \div 8 \%$) overestimation of the reach-averaged bedload.

Observation of numerical results suggests that our simple method is able to capture the spatial variability of the shear stress and consequently the average transport. However the depth-averaged model is still an highly simplified representation of a braided network, especially for what concern the transport mechanisms; this consideration claims for an analysis of the simple method on the basis of flume experiments.

In this section we compare the average bedload transport measured during TN1 and TN3 experiments with both (Bertoldi et al., 2009a) and the *Average*

3.4. Elevation distribution and sediment transport

Q [$m^3 s^{-1}$]	Transport formula	Q_s [$m^3 s^{-1}$]	Q_s <i>D3D</i> [$m^3 s^{-1}$]	Difference
323	Parker (1990)	0.223	0.199	-11 %
323	Meyer-Peter and Müller (1948)	0.284	0.258	-9 %
323	Wong and Parker (2006a)	0.136	0.123	-10 %
200	Parker (1990))	0.119	0.085	-29 %
200	Meyer-Peter and Müller (1948)	0.158	0.123	-22 %
200	Wong and Parker (2006a)	0.075	0.057	-24 %

Table 3.3: Reach-averaged bedload from the *Average section* method and from *Delft3D* hydrodynamic simulations; two values of discharges and three different transport formulas have been tested.

Section method.

The results reported in figure 3.15 reveals that our method is capable to reproduce approximately the trend observed in the laboratory, with an error comparable with the method proposed by Bertoldi et al. (2009a); as pointed out by the same authors this result is relevant when compared with the strong underestimation obtained by simply considering the cross-sectional averaged hydraulic parameters.

Similarly we can estimate the average solid discharge for the confined gravel-bed river reproduced in the TN3 experiments; in addition in this case we can also compare the active and wetted width predicted by the model with the spatially averaged values manually measured in the laboratory.

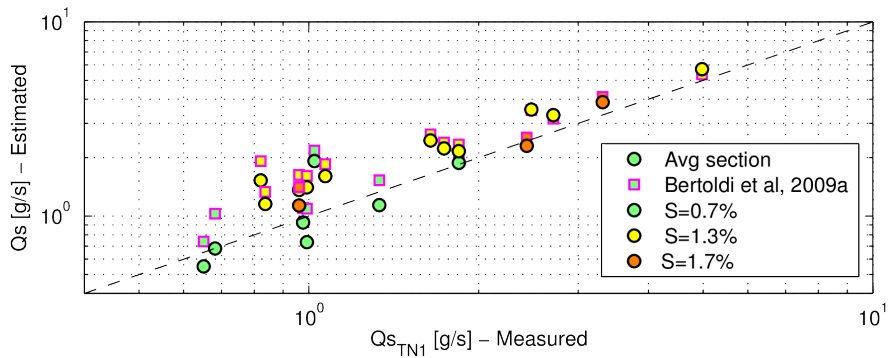
The results of figure 3.16 shows that in this case our method (as well as the Bertoldi et al. (2009a) approach) tends to overestimate the average solid discharge, especially adopting the Parker (1990) bedload formula; it is also clear that this error is relatively more important for smaller values of solid discharges (wider channels and lower discharges).

Nevertheless both the methods are able to capture the variation of the solid discharge in a wide set of morphological condition, from an almost flat bed to an alternate bars pattern to a highly complex braided morphology with significant fraction of dry area. If we compare the experiments with the prediction obtained by simply applying the same transport formula in a simply a rectangular cross-section of width W (or in other words, considering the mean hydraulic parameters without including the lateral distribution) we obtain the result of figure 3.16. Evidently such a prediction is not acceptable because leading to an underestimation of more than, in the most complex morphology, can exceed two orders of magnitudes.

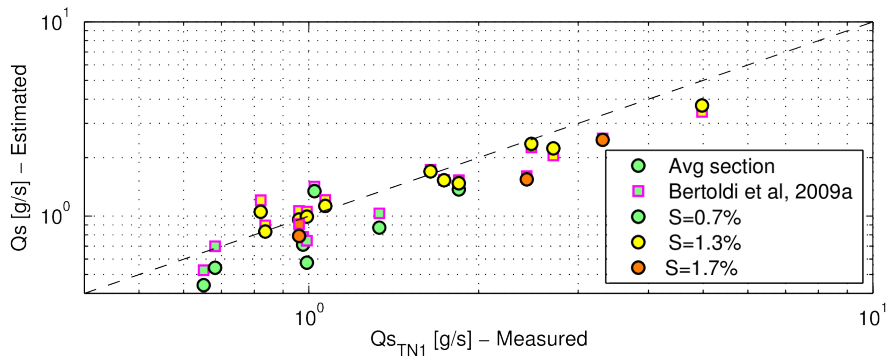
At-a station variability

Bertoldi et al. (2009a) adopted their simple $1D$ model to explore the at-a-station variability, namely the response to flow variations which are fast enough not to produce significant morphological changes. However the validity of this model

3.4. Elevation distribution and sediment transport



(a) Parker (1990) bedload formula.



(b) Wong and Parker (2006a) bedload formula.

Figure 3.15: Comparison between TN1 laboratory observations, the (Bertoldi et al., 2009a) (black circles) method and the *Average section* method (magenta squares) in terms of average solid discharge. The logarithmic formula (Eq.3.12) has been adopted for the hydraulic resistance. Different filling colours represent different flume slopes.

3.4. Elevation distribution and sediment transport

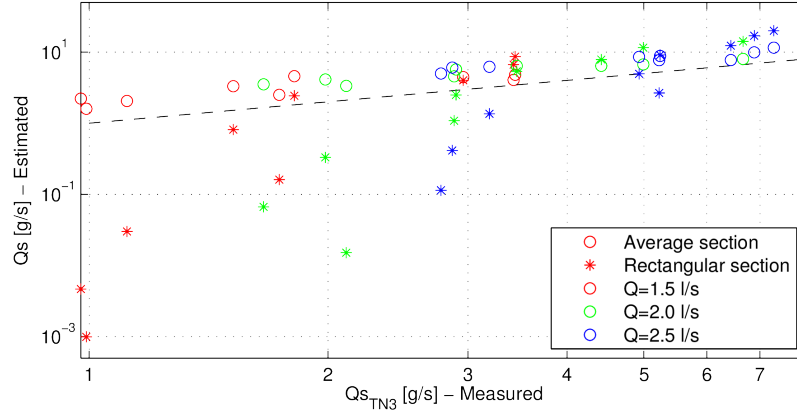


Figure 3.16: Comparison between TN3 laboratory observations, the *Average section* method and the estimation based on cross-section averaged parameters. The Parker (1990) formula has been adopted for bedload transport, the Engelund formula (Eq.3.12) for the hydraulic resistance. Different colours indicates different discharges.

has not been directly tested because of the lack of data.

Similarly we can adopt the *Average section* method to analyse this response and compare the results with the at-a-station variation predicted by the numerical model for the Rees River as well as the inundation curves observed in the river Tagliamento.

Figure ?? illustrates the results from the fixed-bed numerical model under slowly increasing discharge, which allows to consider a sequence of quasi-steady states. The response of wetted width to varying flow is predicted rather accurately, whereas the bedload tends to be overestimated for lower flow. It is worth to underline that the purpose of this analysis is to understand the influence of the reach-scale average geometry to the at-a-station response rather than a quantitative prediction of the response to varying discharge.

If we estimate the inundation curve of a braided river during a flood event in the hypothesis of negligible variation of the average properties of the network during the event. Let us consider for examples the areas of *Flagogna* and *Cornino* of the river Tagliamento; The two study reaches are characterised by largely different vegetation abundance (4% and 21% of the total area respectively), whereas discharge, longitudinal slope and grain size keep similar (Welber et al., 2012). If we approximate the $b(D)$ curve with an power law we obtain an estimation of the wetted area at distinct locations, which comparison with the inundation curve of the river Tagliamento is reported in figure 3.18.

3.4.4 Discussion

We have seen how the simple reach-scale curve we propose contains the most important information needed for an approximate estimation of the wetted

3.4. Elevation distribution and sediment transport

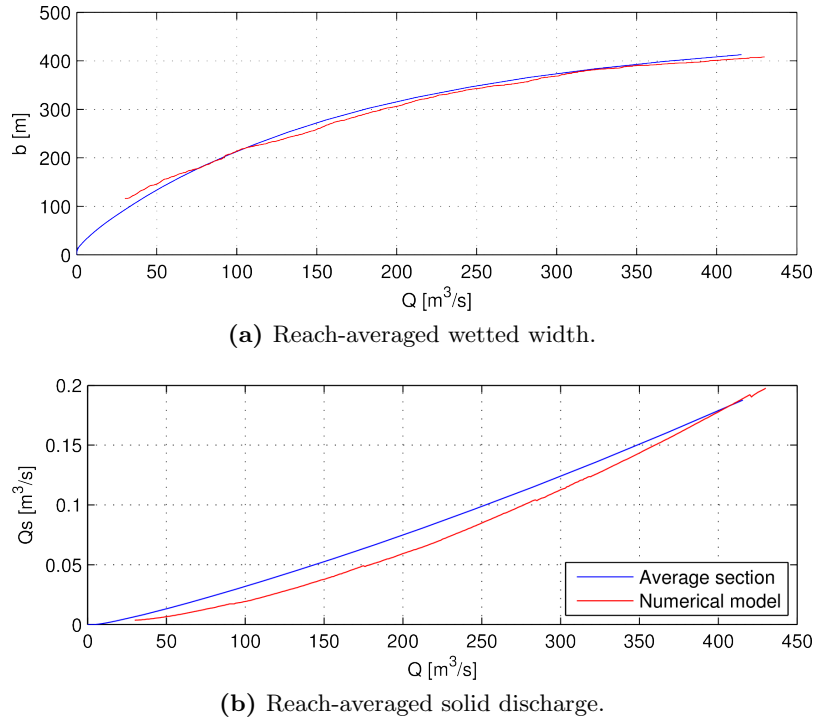


Figure 3.17: Comparison between at-a-station response of the numerical model and of the *Average section* method.

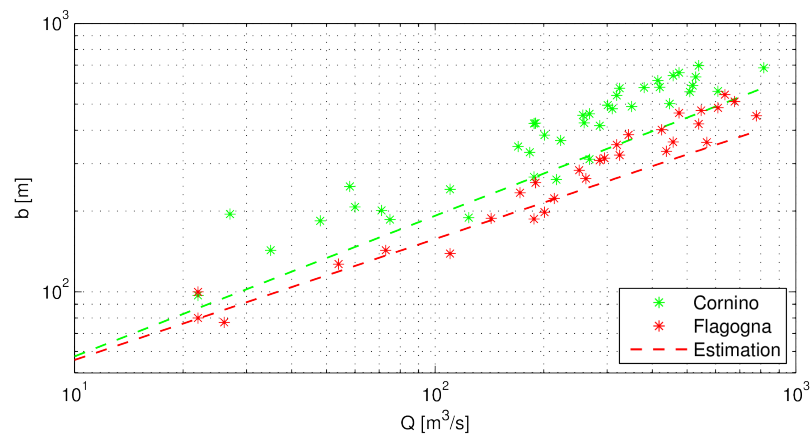


Figure 3.18: Measurements of inundated areas at *Cornino* and *Flalogna* sub-reaches (green and red points respectively), from Welber et al. (2012), and estimations using the analytic solution. $S = 0.35\%$, $d_s = 4$ cm are adopted as parameters.

3.4. Elevation distribution and sediment transport

width and the sediment transport in both formative and at-a-station conditions.

Bertoldi et al. (2009a) suggested, on the basis of a simple 1D modelling of the TN1 experiments, that the at-a-station variability is similar to the response in formative conditions. An explanation of this behaviour comes from the observation of the *Average section* of figure 3.3 which does not change dramatically for different discharges; for this reason moving between a single curve gives a similar response, in terms of width and bedload, than moving between different curves.

This is not the case of the confined network for which a variation of the discharges produces a significant modification of the *Average section*; consequently we expect the at-a-station and formative response to be more different than in the unconfined case.

Our simple approach also allows for a simple understanding of the at-a-station response of a complex river to varying hydraulic conditions. Indeed if we consider the power-law approximation of the $b(D)$ curve (Eq 3.16) we can write, according to Eq. 3.3

$$y^* = k^* \eta^{*\alpha} \quad \eta^* = \left(\frac{y^*}{k^*} \right)^{1/\alpha} \quad (3.16)$$

where k^* is the coefficient of the power law expressed in dimensionless form. This simple expression of the bottom elevation allows for an analytical computation of the cross-sectional integrated variables.

The Gauckler-Strickler resistance formula (Eq. 3.13) allows for writing the cross-section integral of Eq. 3.10 as

$$Q^* = C_0 \sqrt{S} \int_0^{b^*} h^{*5/3} dy^* \quad (3.17)$$

If we substitute the local depth h^* obtained from Eq. 3.16 we have

$$Q^* = C_0 \sqrt{S} \int_0^{b^*} \left[D^* - \left(\frac{y^*}{k^*} \right)^{1/\alpha} \right]^{5/3} dy^* \quad (3.18)$$

The solution of this integral can be expressed through the definition of the following function

$$\mathcal{F}(\alpha, \delta) = \int_0^1 \left(1 - z^{*1/\alpha} \right)^\delta dz = \frac{\Gamma(1 + \alpha) \Gamma(1 + \delta)}{\Gamma(1 + \alpha + \delta)} \quad (3.19)$$

where $\Gamma(x)$ is the Gamma function. The resulting discharge-stage relation reads

$$Q^* = \mathcal{F}(\alpha, 5/3) C_0 k^* \sqrt{S} D^{*\frac{5}{3} + \alpha} \quad (3.20)$$

which reveals, in the case of relatively high values of the exponent α , a remarkably strong dependence of the discharge on the water depth.

3.4. Elevation distribution and sediment transport

This reflect the well-known (e.g. Mosley, 1982; Ashmore, 2013) feature of braided rivers, whose water depth increases much slowly with the discharge than in a single-thread channel. This different behaviour is apparent in Eq.3.20 where the exponent of D in a *Y-shaped* section is significantly bigger than the typical $5/3$ value we can find for a *U-shaped* channel. For instance for $\alpha \simeq 2$, as typical of relatively unconfined braided topographies, we obtain a big exponent of D , namely

$$Q^* = \frac{9}{44} k^* C_0 \sqrt{S} D^{*11/3} \quad (3.21)$$

Even more interesting, because easier to define on the basis of planimetric measurements, is the at-a-station response of the wetted areas. If we invert Eq. 3.20 and remember Eq 3.2 we obtain a power-law relationship between the water discharge and the wetted width, namely

$$b^* = k^* \left(\frac{Q^*}{\mathcal{F}(\alpha) k^* C_0 \sqrt{S}} \right)^\varphi \quad \varphi = \frac{3\alpha}{5 + 3\alpha} \quad (3.22)$$

which gives an estimation of how the inundation area increased with the discharge in a complex morphology.

A wide range of values for the exponent φ have been estimated for braided rivers. For example Mosley (1983) and Smith et al. (1996) reported low values ($\varphi < 0.5$), whereas Ashmore and Sauks (1996) measured a nearly linear $\varphi \simeq 1$ relation.

According to Ashmore and Sauks (1996) it is unlikely that there is a universal width-discharge relationship applicable generally to braided rivers. Smith et al. (1996) showed that the three rivers sampled in their study had substantially different width-discharge relations that could be ascribed mainly to differences in channel pattern (braiding intensity).

From our model the $b(Q)$ curve is strongly dependent the section shape; indeed the coefficient φ tends to be higher in complex (larger α) sections ranging, according to Eq. 3.22) from $\varphi \simeq 0$ (*U-shaped* section) to $\varphi = 1$ ($\alpha \rightarrow \infty$).

In order to visualise how the at-a-station response of the reach-averaged wetted width may change in different morphological conditions let us consider an *Average section* having an arbitrary value of the constant $k = k_0$ and call Q_0 the correspondent formative discharge; in addition let us consider two similar section having a different k (blue and red curves of figure 3.19). For a given α we can thus calculate on the basis of Eq. 3.22 the inundation curves of figure 3.20. As one may expect the wetted width depends on the curve coefficient k ; in particular for a given depth (for example at the bankfull conditions indicated by the black marker) both the discharge and the width are proportional to k which is simply scaling the curves on both axes. For higher values of α , as clear from Eq. 3.20, the inundation curves becomes more linear and less affected by variations of k .

3.4. Elevation distribution and sediment transport

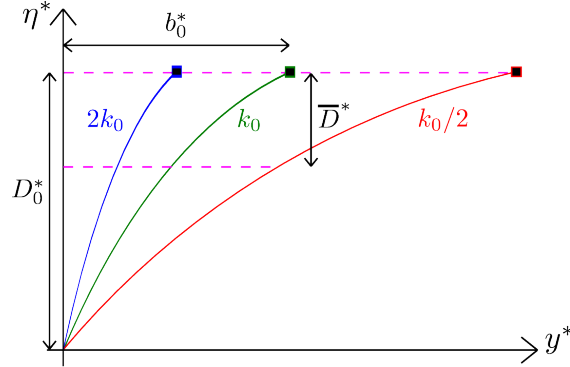


Figure 3.19: Test sections adopted for the analysis of the model response. For a given α the green curve represents the reference section, whose bankfull conditions (square marker) correspond to a discharge Q_0 and a maximum depth D_0 . The red and blue curves indicate wider and narrow sections characterised by the same bankfull depth.

Few information are available about the at-a-stage response of the bedload in a braided network. Indeed the laboratory investigation usually refers to formative condition and the only analysis available is the one proposed by Bertoldi et al. (2009a) on the basis of the simple $1D$ modelling.

If we integrate Eq. 3.14 and we assume a simple bedload formula for the local transport, we can obtain an analytical expression for the average solid discharge.

The Shield stress computed by Eq 3.15 is proportional to the local depth, which can be computed through Eq 3.2, and can be written as

$$\theta = \frac{Sh^*}{\Delta} = \frac{SD^*}{\Delta} (1 - z^{1/\alpha}) \quad z = \frac{y^*}{k D^{*\alpha}} \quad (3.23)$$

and consequently and the integral of Eq. 3.14 becomes

$$Q_s^* = k^* D^{*\alpha} \int_0^1 \Phi(\theta_D, z, \alpha) dz \quad (3.24)$$

In particular if we assume a bedload formula of the type

$$\Phi = c(\theta - \theta_{cr})^\delta \quad (3.25)$$

(e.g. Meyer-Peter and Müller, 1948; Wong and Parker, 2006a) we can express Eq. 3.24 as

$$Q_s^* = k^* c (D^* - D_{cr}^*)^{\alpha+\delta} \left(\frac{S}{\Delta}\right)^\delta \mathcal{F}(\alpha, \delta) \quad (3.26)$$

which, if combined with Eq. 3.20 provides a discharge-bedload relationship for the complex morphology.

3.4. Elevation distribution and sediment transport

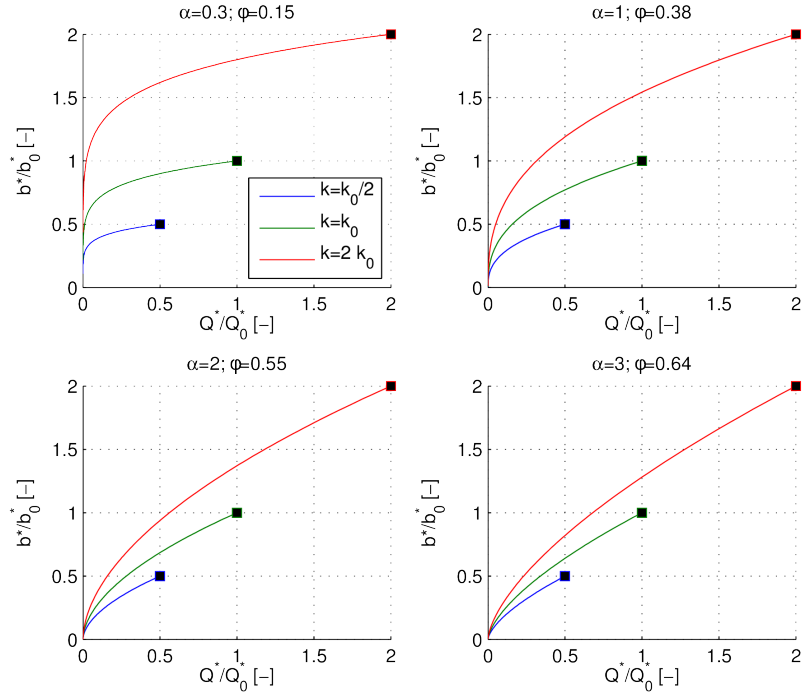


Figure 3.20: Wetted width as function of the water discharge, for distinct values of the exponent α and the coefficient k of the *Average section*. The black markers correspond to average Shields stress $\bar{\theta} = 0.06$; slope is $S = 0.5\%$.

In order to graphically explore this relation we considered a slope $S = 0.5\%$ and we fixed the limit of the curves in order to have a mean Shields stress $\bar{\theta} = 0.06$, namely

$$D_0^* = \bar{D}^*(\alpha + 1) = \frac{\bar{\theta}}{\Delta S}(\alpha + 1) \quad (3.27)$$

In this way we can investigate how the bedload discharge depends on discharge and the shape of the *Average section*; in particular in figure 3.21 we can notice that the curves for higher α are only weakly nonlinear and does not show a relevant threshold for sediment motion. This is much much different from the behaviour of *U-shape* sections which shows a strongly nonlinear behaviour in the region close to the critical threshold for sediment motion.

As one may imagine the Q_s for a given discharge decreases with the width of the section k ; however it is interesting to notice how this effect which can be dramatic in the case of small α is less important for complex morphologies. This means that for a braided morphology the dependence of the transport to variations of the *Average section* width may be weaker than in a single thread for which a relatively small widening can lead to Shield stresses below the critical value.

3.4. Elevation distribution and sediment transport

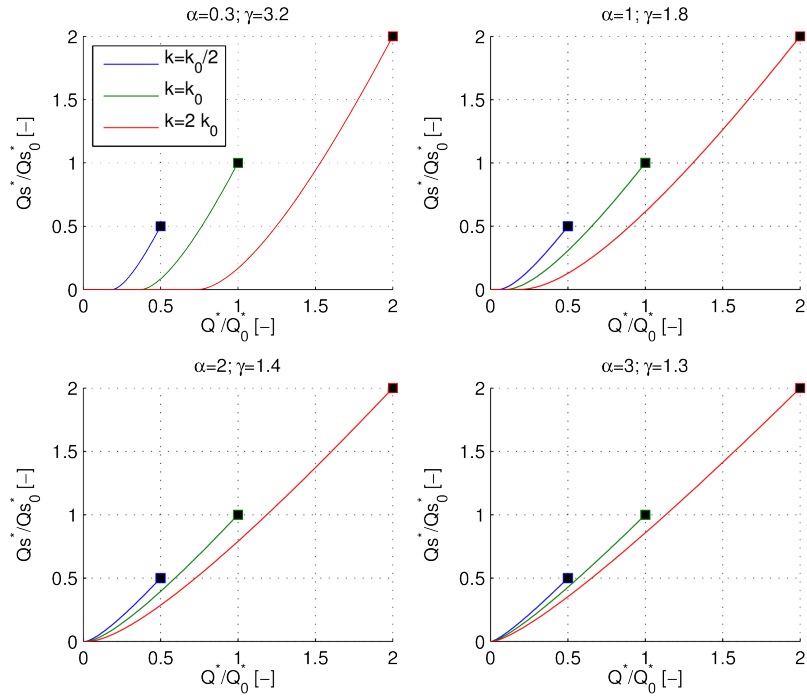


Figure 3.21: Sediment flux curves for distinct values of the exponent α and the coefficient k of the *Average section*. The black markers correspond to a value of the average Shields stress $\bar{\theta} = 0.06$. The Meyer-Peter and Müller (1948) transport formula and a slope $S = 0.5\%$ is adopted; δ indicates the exponent of the power-law which fits the curves.

3.5 Conclusions

In this work we presented an indicator of the reach-averaged braided morphology which represents the portion of braidplain lying below a given elevation, where the elevation is calculated with respect to the deepest point of each individual cross-section. This indicator is expressed as a curve which can be taken as representative of the reach-averaged geometry; we called therefore *Average section* an equivalent compact section having exactly the same width-depth curve.

The reach-scale geometry of a braided network is expected to respond to the controlling conditions we identified through dimensional analysis. Specifically, if the bed material is well-sorted and the effect of vegetation is negligible, the morphology is expected to depend only on slope, discharge and confinement width. The role of these parameters was assessed through flume experiment, which enable to study the simplest case of constant (through time) and homogeneous (along the flume) conditions. Specifically, we analysed an existing dataset of 58 experiments carried out at the hydraulic laboratory of the Trento's University and we supported the results with morphological data of three natural braided rivers.

Correlation between the channels depth and the flume slope occurs in the laboratory experiments, whereas the shape of the *Average section*, represented by the exponent α of the fitting power-law is significantly impacted by the degree of confinement and ranges from $\alpha > 2$ (indicating the *Y-shape* typical of braided morphology) to $\alpha < 0.5$ (representative of the *U-shape* characteristics of single-thread channels).

The reach-scale indicator can be adopted in order to account for the spatial distribution of the Shields stress, which is recognised to be a crucial ingredient for the estimation of the solid discharge in a braided network. Numerical hydrodynamic simulations suggest that the proposed procedure is able to capture the shear stress variability; furthermore a comparison based on the set of laboratory experiments with different discharges, sediment size, slope and confinement width confirms the capability of the simple method to approximately predict the average sediment transport rate within a wide range of morphological conditions, from the nearly single-thread alternate bars pattern to fully-developed braided networks.

This method allows for a very simple investigation of the at-a-station response of the braided network to changing discharge. Indeed, assuming a power-law interpolation of the curves we can compute analytically the bedload and active width and analyse the connection between average geometry and at-a-station response.

3.6. List of symbols and acronyms

3.6 List of symbols and acronyms

<i>DEM</i>		Digital elevation model;
*		Dimensionless quantity;
a_d, b_d	[<i>l</i>]	Coefficients of river stage duration curve;
b	[<i>l</i>]	Wetted width;
b_a	[<i>l</i>]	Active width;
b_a	[<i>l</i>]	Wetted width in formative conditions;
C	[–]	Dimensionless Chèzy coefficient;
C_0	[–]	Coefficient in the power-law formula for C ;
D	[<i>l</i>]	Maximum water depth along the section;
D_0	[<i>l</i>]	Depth of the <i>Average section</i> corresponding to b_0 ;
D_{cr}	[<i>l</i>]	Critical depth for sediment motion;
d_s	[<i>l</i>]	Sediment size;
\mathcal{F}	[–]	Transverse integral for the computation of Q ;
\mathcal{G}	[–]	Transverse integral of the bedload formula;
h	[<i>l</i>]	Local flow depth;
k	[<i>k</i>]	Coefficient of the $b(D)$ curve;
g	[lt^{-2}]	Gravity acceleration;
t	[<i>t</i>]	Time;
Q	[l^3t^{-1}]	Liquid discharge;
Q_s	[l^3t^{-1}]	Solid discharge;
S	[–]	Slope;
V_s	[l^3t^{-1}]	Solid volume transported by the river;
W	[<i>l</i>]	Confinement width;
x	[<i>l</i>]	Longitudinal coordinate;
y	[<i>l</i>]	Transverse coordinate;
α	[–]	Exponent of the $b(D)$ curve;
β	[–]	Half width to depth ratio;
γ	[–]	Exponent of the $Q_s(Q)$ power-law formula;
γ_w	[$Ml^{-2}t^{-2}$]	Specific weight of water;
Δ	[–]	Relative submerged density of sediment;
δ	[–]	Exponent of the power-law bedload formula;
η	[<i>l</i>]	Bottom elevation;
ρ	[Ml^{-3}]	Water density;
φ	[–]	Exponent of the inundation ($b(Q)$) curve;
Φ	[–]	Dimensionless bedload flux intensity;
σ	[–]	Grain size distribution;
θ	[–]	Shields parameter;
θ_{cr}	[–]	Critical Shields parameter;
θ_D	[–]	θ at the deepest point of the cross-section;
Ω	[Mlt^{-3}]	Total stream power;

3.7 Appendix

3.7.1 Averaging length and spatial scales of braiding

The indicator we proposed above is defined at the reach-scale, where the length of the reach should be sufficiently large to obtain a statistically significant estimation of the $b(D)$ curve. At this point some natural question arises: “which is this length?”, “How does it scale?” As one may image, behind these technical questions of practical relevance there is the more theoretical concept the longitudinal scale of the braiding network.

We can have an idea of the problem by looking at how the curves change while reducing the length of the analysis windows. If we consider a region of length L which starts from the flume outlet we obtain, for different runs of the *TN3* experiments, the curves of figure 3.22. Apparently a 2 m -wide window is sufficient to obtain a significant estimation of the curve; however this result may be misleading because dependent on the portion of the flume where the average is computed; for example if we repeat the curves of figure 3.22d by moving upstream the $L = 1 \div 5$ windows we obtain the result of figure 3.23; in this case the estimation obtained with a $L = 5 m$ moving average is rather different and reveals that this length is not sufficient for a reliable computation.

A more general picture of this problem can be obtained by considering the variability of these curves along the flume. We can consider for example the width of the section which correspond to $D^* = 15$, reported in figure 3.24; this signal contains important fluctuations which reflects to the spatial variability of the braided morphology. For this reason computing the “average section” on the basis of a single curve would lead to almost random results; a more stable (but sill variable) b estimation is obtained by performing a moving average on a window $L = 5 m$ whereas a more robust result occurs if $L = 10 m$.

At this point a more fundamental question arises: “which is the characteristic spatial scale of this braiding networks?”.

We considered the wetted width $b(x)$ computed through the Bertoldi et al. (2009a) method; the signal, reported in figures shows again an important variability whose frequency content can be studied in the Fourier domain.

Before performing this analysis it is worth to recall some useful definitions namely the discrete Fourier transform, which reads

$$\hat{\eta}_m = \sum_{i=0}^{N-1} \eta(idx) e^{2\pi im/N} \quad (3.28)$$

and the power spectral density, which can be estimated through the so-called periodogram

$$PSD\left(\lambda = \frac{i}{L}\right) = \frac{2}{N} |\hat{\eta}|^2 \quad (3.29)$$

3.7. Appendix

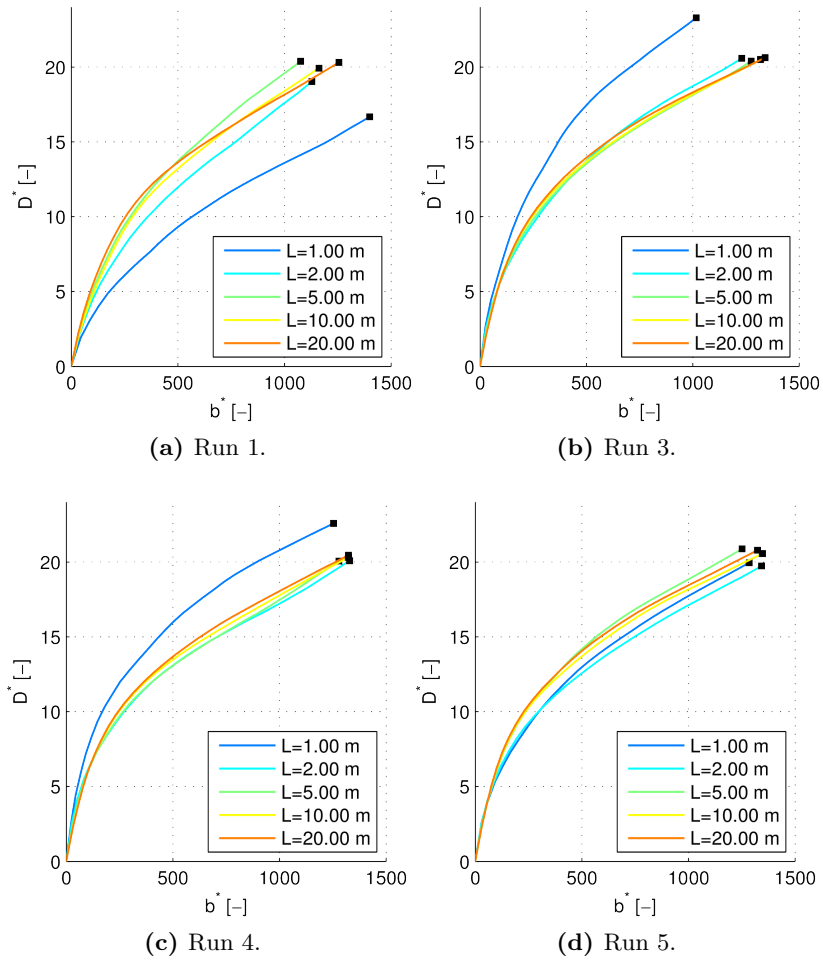


Figure 3.22: Average section of the TN3 experiments, computed on different windows of length L placed at the downstream portion of the flume. Different panel refers to different runs.

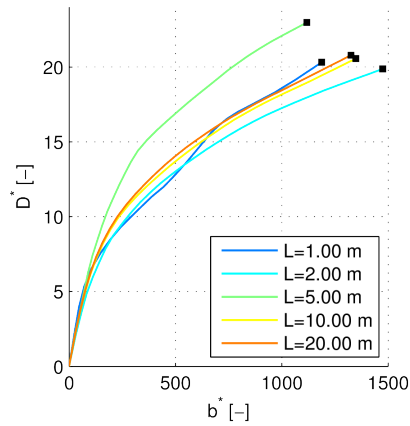


Figure 3.23: Average section of the run 5 of the TN3 experiments, computed by positioning the windows in order to avoid overlapping (except for the bigger window $L = 20\text{ m}$ which overlaps all the others).

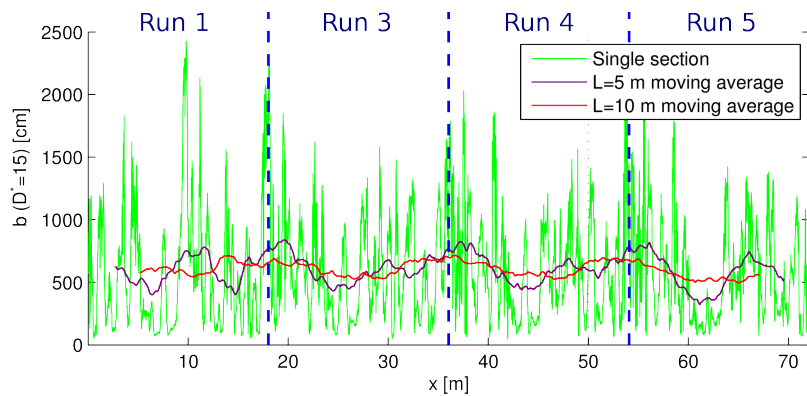


Figure 3.24: Longitudinal profiles of $b(D^* = 15)$ of the TN2 experiments. The vertical dashed lines separate different runs.

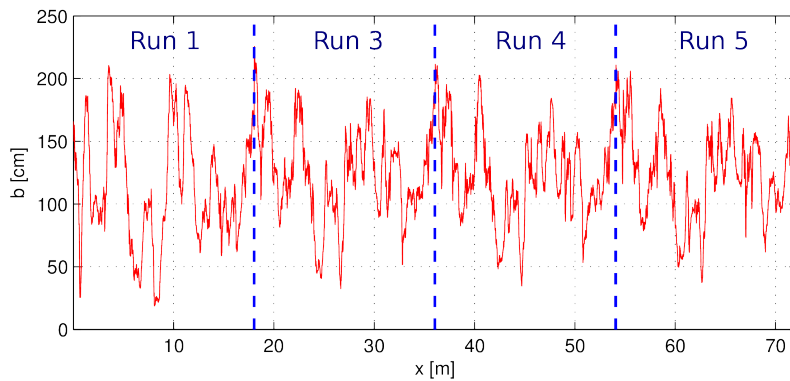


Figure 3.25: Longitudinal profiles of wetted width of the TN2 experiments according to the Bertoldi et al. (2009a) method. The vertical dashed lines separate different runs.

3.7. Appendix

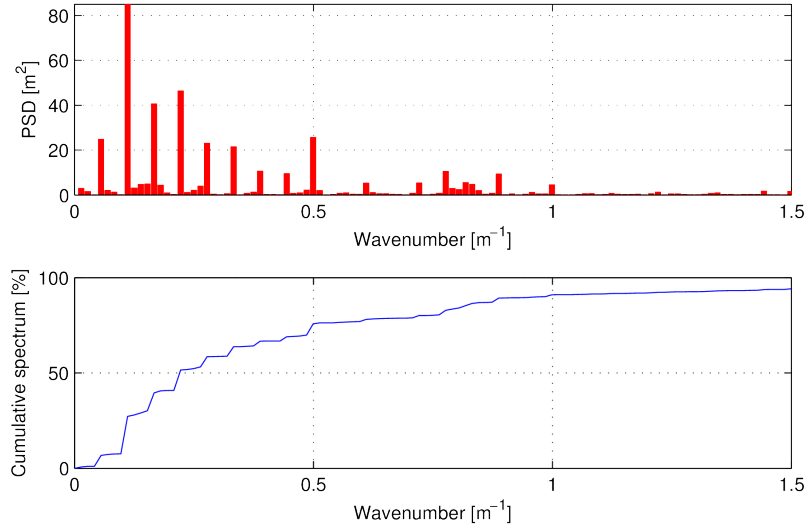


Figure 3.26: Fourier spectrum of the $b(x)$ signal. Upper panel: single components, lower panel: cumulative energy content.

where λ is the wavenumber (the number of oscillations per unit length) and PSD represents how the variance of the signal is distributed in frequency, with the mean of all the components representing the variance (also called the power) of the signal.

The computation of these quantities leads the results of figure 3.26, where we can see that the more powerful harmonics correspond to a wavelength of $\simeq 9 \text{ m}$,

The initial three wavelength contain only a small variability which indicated a negligible variation between the four different experiments; for the same reason the higher component are associated with wavenumbers with are multiple of $1/18 \text{ m}^{-1}$, which corresponds to the channel length.

On the right part of the spectrum the small amplitude of the high modes suggests that no rapid variation occurs or, from another point of view, that a correlation between close sections exists. For this reason the longitudinal resolution of the measurement is not affecting that much the statistics, indeed what happens at relatively close sections (the dx of the TN3 is only 2.5 cm) is highly correlated and not additional information is added if the number of sections is increased.

This analysis allows for an global overview of the $b(x)$ spectrum in the series of four experiments but does not tell us anything about how the frequency content varies between different runs and in space within each single run; this variation can be appreciated by a combined space-frequency analysis obtained with a wavelet transform.

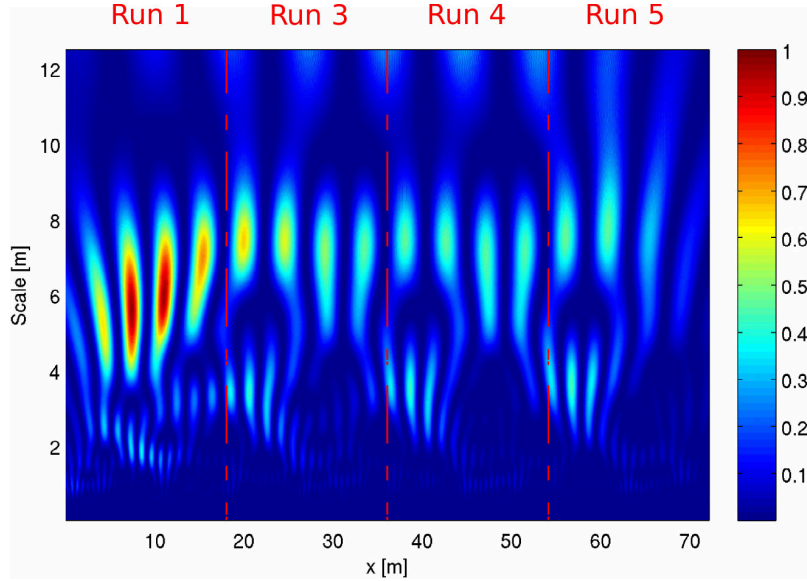


Figure 3.27: Map of the (normalised) continuous wavelet transform of the $b(x)$ signals of the TN3 experiments. The Morlet scaling function has been adopted; the vertical dashed lines separate different runs.

In particular we consider the so-called Morlet wavelet which is defined as

$$\psi(x) = e^{-x^2/2} \cos(5x) \quad (3.30)$$

which represents a damped cosine of periodicity $2\pi/5 \simeq 1.25$.

In figure 3.27 we can see that most of the power of the signal is contained in a region between 4 and 8 m; notice that this length represents the scale of the wavelets and not directly the wavelength. The first *Run 1* contains clearly more variability which peaks at a slightly smaller scale, while the other runs are more homogeneous both in terms of total energy and distribution in wavelength. Within each experiment there are not big changes but an higher content of smaller scales ($\simeq 3 \div 4$ m) seems to be more important in the upper portion of the flume.

Having an idea of which are the most relevant scales of this problem we can face the question of how these scales change in different conditions, and in particular with the flume width.

In a channel with alternate bars the wavelength of the bed level fluctuations is proportional to the width; for this reason we expect in the narrower experiments of the TN3 series a length scale which increases with the channel size W . Following this idea we want to investigate whether such a scaling is valid also in a wider, braided network.

Some hints about this intriguing question can be obtained by analysing the profile of the minimum elevation across the sections. In particular we can

3.7. Appendix

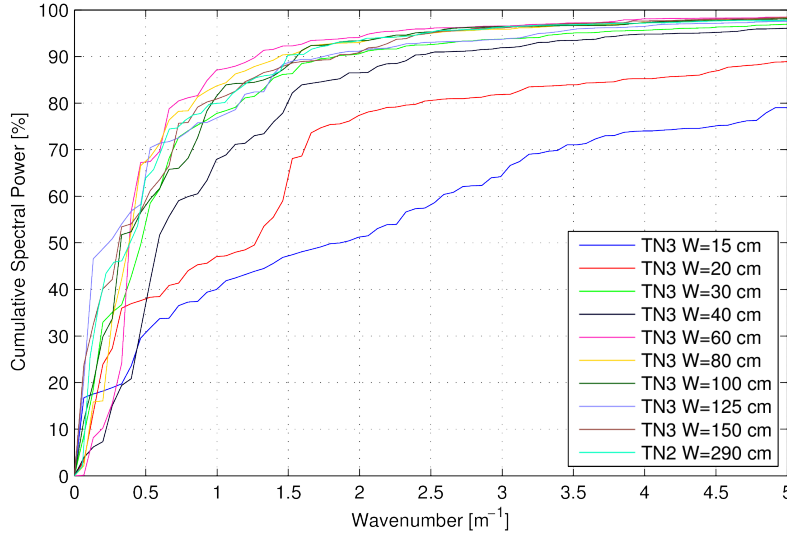


Figure 3.28: Cumulative spectrum of TN1 and TN3 experiments.

compute the (cumulative) Fourier spectrum for each of the 27 runs and we take the average of the three runs with the same width W ; In this way we obtain nine curves which, together with the results of the TN2 experiments, are reported as a cumulative distribution in figure 3.28. By comparing these plots we can notice that for relatively narrow $W \leq 30 \text{ cm}$ runs a significant fraction of the signal variance is contained in the upper region of the spectrum (i.e. fast spatial variability) whereas for all the other curves the smaller wavenumbers dominates.

The spectra for $W \geq 40 \text{ cm}$ are rather similar, which suggests that in these wide configurations the characteristic length may not scale W . This is not surprising because in the limit of very wide flumes we do not expect the banks to play any role and consequently no correlation between W and the spatial scale.

Similar observations come from the estimation of the path length determined on the basis of the Ashmore and Church (1998) method, which enables to determine the volume V_t transported during a time interval Δt on the basis of the volume of erosion V_e through the following formula

$$V_t = Qs(1 - p) \Delta t = \frac{V_e}{L} L_t \quad (3.31)$$

where L is the length of the surveyed area and L_t is the mean travel distance of the sediment grains.

Repeated measurement of the braided topography at the end of part of the TN3 experiments enables to compute the volume of erosion as a difference of *DEMs*, while the transported volume is known from weight measurements.

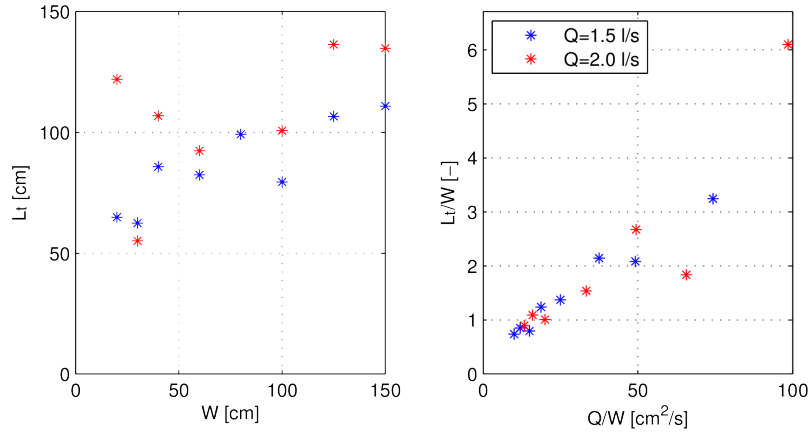


Figure 3.29: Path length of the TN3 experiments, computed through the inverse application of the Ashmore and Church (1998) method.

In particular the measured variations are in the range $\Delta z = 0.22 \div 0.46$ in a time interval between 5 and 300 *min* chosen in proportion to the Exner timescale in order to: a) ensure measurable changes b) limit as much as possible the compensation of scour and deposition volumes, which causes underestimation of V_e (i.e. Lindsay and Ashmore, 2002).

Considering a fixed sediment porosity p we can invert Eq. 3.31 in order to find an estimation of L_T . The results on figure 3.29 (left panel) suggest that there is not a clear relation between L and W .

3.7.2 Sensitivity of the coefficient α to the curve extension

As we mentioned before, the upper limit of the curves has been chosen on the basis of the wetted width computed with a simplified method which requires to identify a representative discharge, whose choice is arbitrary.

This degree of uncertainty affect the curves extensions and consequently the estimation of the best-fitting power law. In this section we will briefly analyse the impact of this choice on the exponent α .

In figure 3.30 we can see how the exponent change with the maximum depth, expressed as a ratio with the original one (D_{form}), in TN1 and TN2 experiments. Notice that the variation of the depth of +33 % correspond to a much higher ($\simeq +100$ %) increase of the liquid discharge.

If we repeat the analysis of figure 3.11 by varying the formative discharge of $\pm 50\%$ with respect we do not notice significant variations in the trend between the exponent α and the specific discharge. Similar consideration arises from the analysis of the river Taglimento sub-reaches with an increased water flow ($Q = 1500 \text{ m}^3\text{s}^{-1}$).

3.7. Appendix

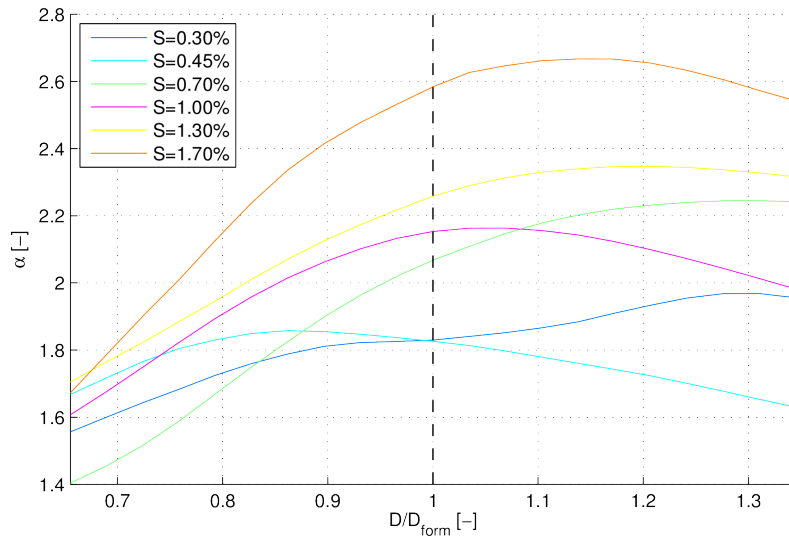


Figure 3.30: Variability of the coefficient α with the maximum D adopted as a limit of the curves. Only a single run for each slope (the one with lower Q) of the TN1 and TN2 experiments is considered. The dashed line correspond to D_{form} , which is the value adopted in the previous analyses.

Chapter 4

Sediment transport and discharge unsteadiness: a laboratory study

4.1 Introduction

Prediction of sediment transport in braided rivers is a challenging task because of its high spatial and temporal variability and due of difficulties to model the morphodynamical evolution on relatively long periods of time.

Many laboratory experiments were performed in the last two decades in order to analyse the morphological response of the braided network to different controlling parameters (e.g. Ashmore, 1982, 1991; Egozi and Ashmore, 2008; Bertoldi et al., 2009d). Most investigations focused on the regime conditions attained, after an initial transitory, by flume networks subject to constant water and sediment supply. Due to the complexity of the system, detailed morphological evolution is not predictable in the long term (e.g. Paola, 1996); however it is possible to predict the averaged properties at the reach scale, which are expected to respond to experimental conditions (e.g. Egozi and Ashmore, 2008), namely slope, grain size distribution and water discharge.

Similarly it is possible to study how the time-averaged sediment transport, in the case of constant discharge and sediment supply, depends on controlling factors (e.g. Ashmore, 1982; Warburton and Davies, 1994; Bertoldi et al., 2009a,d) Such outcomes provide an useful indication of bedload intensity, when the morphology is in equilibrium with the flow conditions.

However braided rivers are subject to flow pulses and floods which are often rapidly varying through time (e.g. Brasington et al., 2000; Van der Nat et al., 2003), so that the equilibrium rarely occurs. It is therefore important to investigate the response of the system to varying discharge. Egozi and Ashmore (2009) studied such a problem in terms of reach-averaged braiding indexes,

4.2. Background

analysing the transitory phase during which the total and active number of channels adapts to new, different flow conditions. At present there are not similar investigations about the response of the sediment transport rate; indeed the laboratory studies which considered a variable discharge (Young and Davies, 1990; Shvidchenko and Kopaliani, 1998; Marti and Bezzola, 2006) focused on the total transport during a single or multiple flow events rather than on the “instantaneous” (i.e. shorter than the flow variations) response of sediment transport rate during the flow hydrograph. Consequently it is not clear to what extent predictions derived by assuming bedload in equilibrium with the instantaneous discharge are valid during natural flood events which show a flashy nature.

Aim of the present research is to investigate the impact of unsteadiness (i.e. time variation) of the flow on sediment transport rate in braided networks. This apparently simple task is actually challenging because: a) even in laboratory flumes direct surveys of the local bedload throughout the flume are difficult; b) indirect measurements such as morphological methods (i.e. Ashmore and Church, 1998) are not sufficiently accurate for a detailed estimation of the instantaneous sand flux at the different sections.

For this reason most of the laboratory investigations are based on transport measurements at the flume outlet which, being not spatially averaged, shows strong, low frequency, variability though time (Ashmore, 1988; Warburton and Davies, 1994). If we are interested in the cumulative transport during one or multiple flow events this is not a big issue; indeed we can simply compute the average transport over a sufficiently long time period (i.e. longer than the time scale of the fluctuations).

Conversely, if we want to study the detailed time evolution of bedload during a flow hydrograph, we can filter the signal only through a moving average having a window shorter than the flow variations. This time average does not enable to eliminate the internally-generated bedload fluctuations, because they are typically much longer than the flow changes.

In this work we intend to overcome this problem by introducing a statistical approach. In particular the present strategy, which is not new but never applied for investigating transport in braided streams, is to repeat several times the flow hydrograph in order to construct an ensemble statistics which enables to appreciate variations of the mean transport due to changes of discharge.

4.2 Background

Before starting the description of the experiments it is worth to clarify two fundamental concepts, namely the unsteadiness of the transport in a complex morphology and the stochastic nature of braided networks.

4.2.1 Example: the role of the unsteadiness in alternate migrating bars morphology

Several transport models for gravel-bed channels assumed the bedload to be in equilibrium with the instantaneous discharge, so that a unique sediment rate curve can be defined. However when the discharge is varying through time significant deviations with respect to the equilibrium may cause hysteresis effect often observed in natural gravel-bed rivers (Lee et al., 2004; Kuhnle, 1992; Humphries et al., 2012; Mao et al., 2014). Specifically, as summarised by Humphries et al. (2012), the bedload may show a delay with respect to flow because of a lag in the development of the bedforms, the time needed to remove the armour layer, inertial properties of the bed and differences in mobility between consolidated and loose bed (Neill, 1957; Griffith and Sutherland, 1977; Bell and Sutherland, 1983; Reid et al., 1985; Jain, 1992; Plate, 1994).

In addition to these in-channel processes the river morphology often shows macroscopic bedforms due to presence of the alternate, central bars or braiding channels. In this case a possible approach is to forget about the local bedload (at a given cross section) and to focus on the spatially averaged transport, which shows relevant hysteresis effects due to the “inertia” of the morphological adaptation to the current flow conditions.

The channel morphology in regime conditions is expected to depend on the discharge and consequently can be treated as a dependent variable; it is therefore possible to define an equilibrium transport rate as a function of the discharge which does not need knowledge of the actual morphological configuration.

A similar approach is valid under equilibrium conditions, which occurs when the discharge is constant or slowly varying. However when the flow conditions is relatively rapidly varying through time the morphology, and consequently the transport, may significantly differ from the equilibrium with the instantaneous flow.

The complexity of braided networks makes it difficult to predict the response of the bedload rate during varying discharge. For this reason we prefer to start our discussion with a simple example, namely a channel with alternate bars, for which some theoretical considerations are possible on the basis of analytical solutions of the two-dimensional morphodynamical models.

Several theoretical studies (see Seminara and Tubino, 1989; Seminara, 1995, for a comprehensive review) revealed that migrating alternate bars are the product of an instability mechanism which arises if the aspect ratio of the channel exceeds a critical value β_{cr} . This threshold can be determined through a linear stability analysis, whereas the equilibrium state attained by the bars under super-critical conditions can be described only by a nonlinear model.

The weakly nonlinear theory of Colombini et al. (1987), based on the analytical solution of the two-dimensional model, enables to predict equilibrium

4.2. Background

amplitude, as well as temporal evolution, of the migrating alternate bars; according to this approach the equilibrium amplitude increases with the following parameter

$$\epsilon = \frac{\beta - \beta_{cr}}{\beta_{cr}} \quad (4.1)$$

where β is the aspect ratio and β_{cr} depends on the flow discharge because it is a function of the Shields stress and the relative submergence.

As the discharge increases both the Shield stress and the relative submergence increases, while the aspect ratio decreases. It is easy to prove that ϵ , and consequently the equilibrium amplitude of the bars, diminishes with the discharge until the aspect ratio is large enough to prevent the formation of alternate migrating bars.

The adaptation to the new flow conditions is not instantaneous but needs time to develop; according to Tubino (1991) we can determine the evolution of the bar height A under varying discharge from a weakly nonlinear approach, which leads to the following equation

$$\frac{dA}{d\tau} = (1 + \alpha_1 \Delta Q) A + \alpha_2 A^3 \quad (4.2)$$

where τ is a dimensionless time, scaled with reference to the linear growth rate of bars and ΔQ is the variation of discharge with respect to a basic state (in this example the lower discharge).

From Eq. 4.2 we can determine the equilibrium amplitude for a given discharge perturbation, namely

$$A_e = \sqrt{\frac{1 + \alpha_1 \Delta Q}{\alpha_2}} \quad (4.3)$$

If we indicate with the underscript 0 the reference state we can write the correspondent equilibrium amplitude as

$$A_0 = \sqrt{\frac{1}{\alpha_2}} \quad (4.4)$$

In order to analyse the response of this model we consider a very simple flow sequence illustrated in figure 4.2, namely a periodical variation of the discharge between two constant values Q_0 and $2Q_0$. As one may expect the response depends on the duration of the flow pulses with respect to the timescale of the bar growth.

Specifically, if the period is sufficiently long, alternate bars have time to fully develop before any significant change of discharge. For example in figure 4.2a we report the solution of Eq. 4.2 for a relatively long hydrograph; we can see that the amplitude of the bars significantly varies, with an higher growth/damp rate after the Q increase/decrease and reduces when the amplitude approaches the equilibrium value.

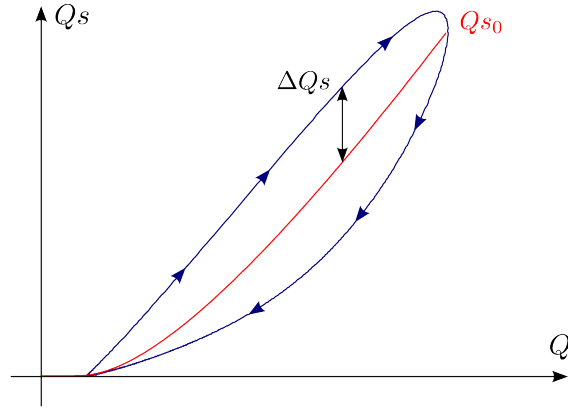


Figure 4.1: Example of hysteresis of the transport rate curve due to flow unsteadiness. The red curve shows the response in equilibrium (i.e. constant discharge through time) conditions. Clockwise hysteresis indicates an advance (i.e. negative lag) of the sediment transport with respect to the water discharge.

On the opposite case if the variation are very fast there is no time for any significant morphological change and the bars maintain (after the transitory phase at the beginning of each cycle) a constant height which correspond to the equilibrium amplitude for an intermediate, equivalent discharge (sometimes called “formative”). Figure 4.2b illustrates the solution for a rather short period; we can see that, after a transitory which depend on the initial conditions, the oscillations in amplitude are small and approximately linear.

Once the morphological response has been found we can investigate the impact on the unsteadiness on the bedload transport Q_s .

In order to separate the effect of the discharge per-se in time and the effect of the temporal variation of the flow, we can introduce the following decomposition

$$Q_s = \underbrace{Q_{s0}(Q)}_{\text{Equilibrium bedload}} + \underbrace{\Delta Q_s(Q, A)}_{\text{Effect of unsteadiness}} \quad (4.5)$$

where $Q_{s0}(Q)$ is the transport in equilibrium with the discharge Q (i.e. long-term response with a constant Q) and the residual component ΔQ_s depends on the instantaneous morphology (represented by the bar height A) and the current discharge Q .

During the rising and falling limb of the hydrograph we may have (depending on the sign of ΔQ_s) a positive or negative lag of the response of the transport rate to varying discharge, which leads to a counterclockwise or clockwise hysteresis as exemplified in figure 4.1.

Equation 4.5 also highlights the two ingredients that can in general affect the reach-averaged transport in a braided morphology, namely

1. the instantaneous discharge;

4.2. Background

2. the morphological condition.

An estimation of the effect of the unsteadiness (second term on the right hand side of Eq. 4.5) is possible on the basis of the results by Francalanci et al. (2012), who studied what they called “morphologically averaged” sediment transport and resistance. They found that the spatial heterogeneity of the Shields stress induced by the alternate bars pattern causes, because of the non-linear response of the bedload to stress variations, an increase of transport rate.

Consequently, for a given discharge the average bedload increases with the bars amplitude.

For the qualitative description of the phenomenon we do not need to determine the exact expression for $\Delta Q_s(Q, A)$ but we can simply model this effect as a linear response, namely

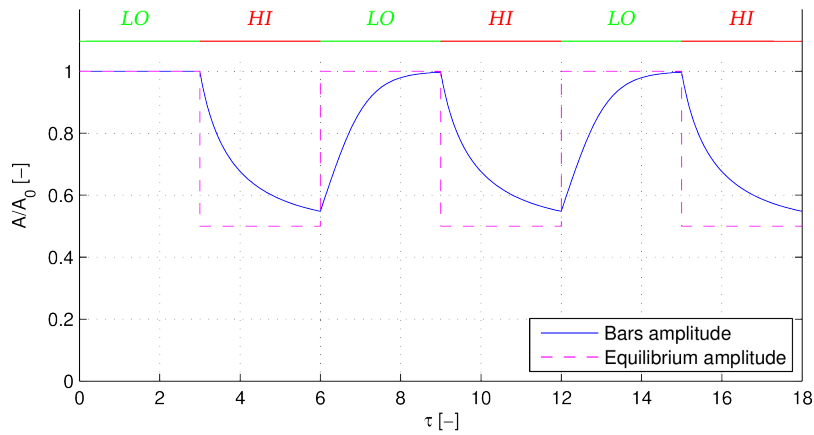
$$\Delta Q_s = k (A - A_e(Q)) \quad (4.6)$$

where k is a positive constant.

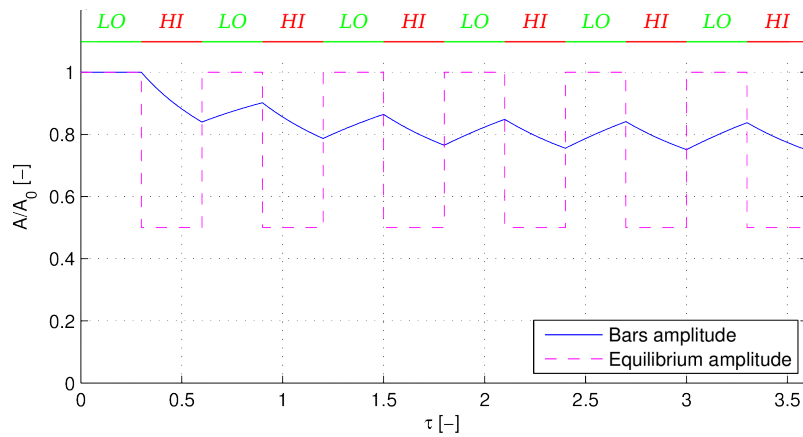
According to Eq. 4.6 the disequilibrium of the transport depends on the difference between bars amplitude and the equilibrium value; consequently if the discharge variations are sufficiently slow we do not expect significant deviation with respect to Q_{s0} whereas for rapid changes the contribution of ΔQ_s may be important. Figure 4.3 illustrates the response of the bedload to the flow and bar height variation of figure 4.2. In the case of relatively long period (figure 4.2a) the instantaneous disequilibrium is important after the discharge variations but tend to vanish as the discharge is kept constant. If the period of oscillations is short, such as in figure , the bar amplitude and consequently the transport are never in equilibrium because the duration of the constant discharge phase is not sufficient to allow a full adaptation to the current flow.

This interesting theoretical outcome is valid for alternating bars channels. and provides an example of adaptation process of river morphology to varying discharge.

From this starting point we can move towards our main question about the response of wider gravel-bed rivers having braided morphology. In this case the analytic bar theory does not enable to fully explore the complex morphology and sediment transport, which can be described only through fully nonlinear mathematical models or laboratory experiments. However we expect some similarities with the migrating bars response; indeed if the duration of the flow variations (relative to the timescale of the braiding morphology) is small, the morphology, and consequently the stress distribution, might be not in equilibrium. Since the reach-averaged sediment transport depends on the morphology trough the stress distribution (Paola, 1996; Nicholas, 2000; Ferguson, 2003; Bertoldi et al., 2009a), the morphological disequilibrium is expected to produce, analogously to the alternate bars case, an hysteresis of the transport rate.



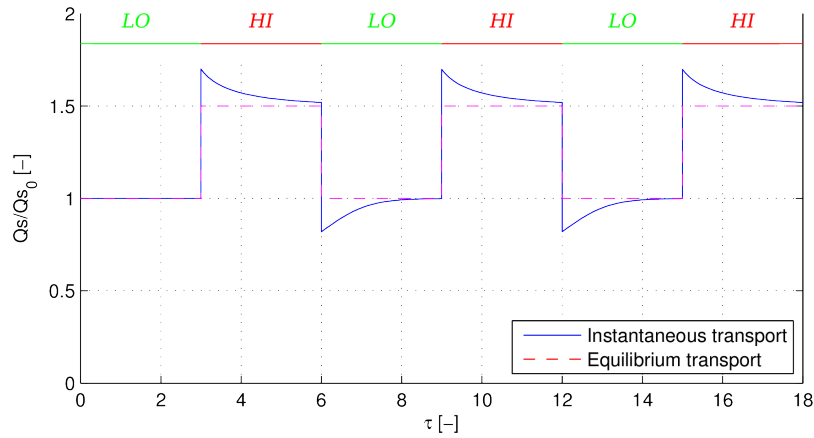
(a) "Long" hydrograph.



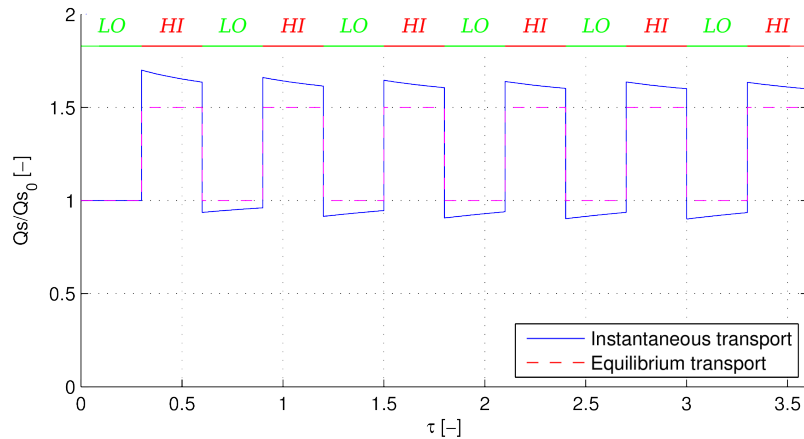
(b) "Short" hydrograph.

Figure 4.2: Height of the alternate bars predicted by the Tubino (1991) theory for a channel subject to periodic variations of the water discharge between two constant values. HI and LO indicate the high and low flow phases respectively; the dashed line represent the equilibrium amplitude of the alternate bars; time is relative to the timescale of the bar growth.

4.2. Background



(a) “Long” hydrograph.



(b) “Short” hydrograph.

Figure 4.3: Bedload transport of a channel subject to periodic variations of the water discharge between two constant values, according to the result of figure 4.2 and to the transport estimation of Eq. 4.6. HI and LO indicate the high and low flow phases respectively; the dashed line represent the equilibrium transport rate; Time is relative to the timescale of the bar growth.

4.2.2 Variability of sediment transport rate: a fundamental problem

It is well established that the bedload transport follows a stochastic behaviour (Einstein, 1937). In a simple channel under uniform flow conditions the transport fluctuations are induced by randomness of flow turbulence and consequently are characterised by relatively small timescales. For this reason these bedload pulsations can be easily filtered out using a time average, so that for most practical applications we can forget about the random nature and model the bedload transport as a deterministic function of the Shields stress.

As far as the morphological complexity increases the bedload pulsations can act on longer timescales. Specifically, it is well established (Ashmore, 1988; Warburton and Davies, 1994; Bertoldi et al., 2009a) that the transport rate in braided networks shows important, low-frequency fluctuations which reflects the complex, unpredictable morphological evolution. For example in figure 4.4 we report the solid discharge measured at the flume outlet during a laboratory run with constant discharge; from the red and blue lines, obtained by removing the frequency components faster than $1 h$ and $5 h$ respectively, we can see important bedload fluctuations even on relatively long timescales.

The instantaneous bedload is not uniquely dependent on the controlling factors such as discharge, slope, type of sediment (which in this case are kept constant). Indeed it is expected to be different between repeated experiments and it can be modelled, similarly to the turbulent motion within the channels, as a random process (Paola, 1996). This random field has a complicate, and to a large extent unknown, spatial and temporal structure which is resulting from the dynamics of “coherent” structures which are not ejections, sweeps, or vortical structures such as in turbulence, but bars, confluences, bifurcations, avulsions,...

The statistical (for example the mean and the standard deviation) are expected to depend deterministically on the external controls. Moreover if the channel is homogeneous and the conditions stationary, both the spatial and the temporal averages can be adopted as a surrogate of the statistical mean, so that they depend on the experimental conditions rather than being a random value. This properties allows to study how the reach-averaged morphological indexes (e.g. Egozi and Ashmore, 2008) or the time-average sediment transport rate (e.g. Bertoldi et al., 2009a) depend on slope, discharge, grain size. The spatial/temporal average is statistically robust if computed over a sufficiently large interval, specifically much larger than the integral scale of the process we are going to study.

Things are different under unsteady conditions. Indeed if the variation of the discharge is faster than the minimum averaging time needed to filter out the internal variability it is not possible to obtain a robust statistics using the temporal average. This is often the case in braided rivers, as we can see

4.3. Method

from some simple rough calculations. Figure 4.4 shows that a 5 h average is not sufficient to obtain a reliable transport estimate. The Trento's flume can be considered as a 1 : 50 model of a prototype river having $d_{50} = 50$ mm, width 150 m and slope 1.0% (i.e. not much dissimilar to the river Sunwapta, see section 1.5.1); since the Froude scaling implies that the temporal scale is the square root of the length one (e.g. Young and Warburton, 1996) the evolution through time of the prototype is $\sqrt{50} \simeq 7$ times slower than in the model. Therefore we can say that an average on a window of $5 h \times 7 = 35 h$ would not be sufficient to estimate the transport rate. The discharge during typical flood event can significantly vary within few hours, much faster than the minimum averaging time (which is significantly longer than 35 h); consequently it is clearly impossible to remove the internal fluctuations and at the same time maintain the temporal resolution needed to capture the effect of the flow variations.

This poses a fundamental problem in the analysis of braided network under unsteady conditions; indeed if we want to study the effect of relatively fast temporal variation of the controlling conditions (such as water or sediment supply) we cannot distinguish between that effect and the internal pulsation which are invariably occurring in a braided system.

Due to the strong fluctuations generated by the system the result of a single hydrograph is almost meaningless, in the sense that can be completely different in repeated experiments. For Egozi and Ashmore (2009) this problem was not fundamental because their analysis was focused on the morphological response in terms of channel pattern and braiding indexes for which a spatial, reach scale average can be computed; indeed as clear from Egozi and Ashmore (2008) the spatial average allows for filtering out the major part of the fluctuations, obtaining a statistics which depend on the controlling factor rather than being unpredictable such the local values.

This is not possible for the sediment transport because at present there are not reliable methods for the estimation of the spatial pattern of the instantaneous bedload throughout the channel. Consequently we can only study the transport rate at the outlet; this signal contains significant, long-period fluctuations which cannot be simply filtered out. This poses a fundamental limit to the interpretation of the result of a single experiment.

4.3 Method

In order to overcome the fundamental limitation described above we follow a novel methodology in the analysis of laboratory braided networks, namely a statistical approach based on repeated experiments under identical conditions.

Constructing an ensemble statistics over a sufficiently large number of experiments enables to distinguish between variations of bedload due to changing discharge and internally-generated random fluctuations.

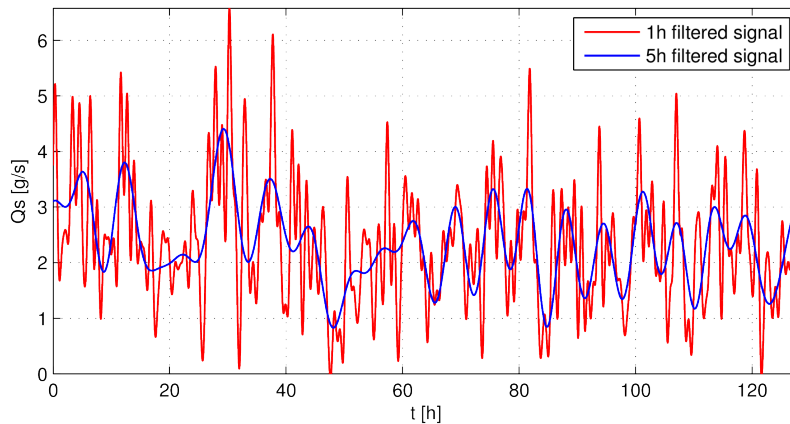


Figure 4.4: Time averaged sediment output measured during the constant-discharge run W3 EQ2.5 RW. Two different cut-off periods (1 *h* and 5 *h*) have been adopted to filter out high-frequency oscillations.

The number of repetitions needed to build a significant statistics is not easy to assess and is as usually the result of a balance between the need of accurate estimates and the limited resources (time, manpower) available. We will further discuss this point in the following.

Another important step is the choice of the discharge curve. For this purpose two different approaches are possible: the more direct is to reproduce the typical shape of a natural flood (Young and Davies, 1990; Shvidchenko and Kopalani, 1998; Marti and Bezzola, 2006); a second option is to adopt a simple hydrograph, more suitable to highlight the unsteady effects in the response of the system. In the present work we are interested in understanding changes of sediment transport due to morphological adaptation to new flow conditions; therefore the natural choice is a stepwise varying discharge as adopted by Egozi and Ashmore (2009). This approach enables to clearly distinguish between bed-load variations due to the increase of the discharge per se and those due to the morphological adjustment to new flow conditions. In the following we consider a hydrograph varying very quickly between two constant values (high flow and low flow phases) such as in figure 4.6.

4.3.1 Experimental set-up

We performed two sets of experiments at the hydraulics laboratory of the University of Trento (see section 1.5.2).

The choice of the discharge values was based on a balance between different needs: a) the high discharge should not be too high, in order to maintain a relatively unconfined network when the total width of the flume is used; b) the low discharge should be significantly different from the high flow but, at the same time, large enough to ensure a sufficient morphological activity. Consid-

4.3. Method

ering that previous experiments on the same flume investigated the equilibrium state with $Q = 1.5 \text{ l/s}$ and 2.5 l/s (Garcia Lugo, 2014) we selected these values as the low and high discharges of the adopted stepwise hydrograph.

Similarly the slope $S = 1\%$ was adopted in order to be consistent with previous data of the same flume; this gradient ensures a relatively high stream power without increasing too much the discharge which, according to Bertoldi et al. (2009d), would need a much wider flume to maintain unconfined conditions.

In order to ensure a global mass balance of the flume and prevent the development of aggradation and degradation waves due to an excess or deficit of the sediment supply, we varied the sand feed rate with the discharge according to the sediment rate curve derived on the basis of existing equilibrium experiments in the same flume (Garcia Lugo (2014), see appendix 4.8.1).

Previous experiments (see *Chapter 3*) shows that a different morphological response to varying discharge occurs in the degree of confinement of the braided network. Within the present work we intend to investigate the transport rate in both the relatively unconfined and confined configurations, obtained by adopting the total width the Trento's flume ($W = 2.9 \text{ m}$) and a reduced ($W = 1 \text{ m}$) width respectively; the latter was obtained in a practical and relatively quick way by placing in the larger flume a plastic sheet, adjusted in order to form an U-shape section whose bottom was covered by a sufficiently thick sand layer (see figure 4.5).

Experiment W1

During the first experiment we reduced the width to $W = 1 \text{ m}$. In this case morphology and sediment transport can be significantly impacted by the presence of channel banks; this is true, in particular, at the high flow $Q = 2.5 \text{ l/s}$, whereas at low discharge $Q = 1.5 \text{ l/s}$ the network morphodynamics and bedload transport are more similar to those observed in the wider, unconfined case.

Five constant-discharge runs were performed (see table 4.1a). Specifically, in addition to the existing TN3 runs, we performed, for the two reference discharges (1.5 l/s and 2.5 l/s) two longer runs (101 h and 39 h respectively); this enables a more robust estimate of the equilibrium transport rate. These runs started with a sloping planar surface or with the braided morphology resulting from previous experiments; during the first, transitory phase the braided network developed, until a statistically stationary state was attained.

In order to explore the connection between the morphological changes and the sediment transport we used the final morphology of the three TN3 experiments, which was scanned with a resolution of $5 \times 0.5 \text{ cm}$ in the longitudinal and transverse direction respectively.

Afterwards we proceeded with the stepwise-variable discharge, by repeating 26 times the hydrograph of figure 4.6

The duration of the high flow phase (2 h) was selected in order to allow the



Figure 4.5: Picture of the flume during experiment W1 ($W = 1\text{ m}$). Flow is from the camera, discharge is $Q = 2.0\text{ l/s}$.

Run	Discharge	Duration	Run	Discharge	Duration
W1 Q1.5 TN3	1.5 l s^{-1}	52 h	W3 Q2.5 RW	2.5 l s^{-1}	72 h
W1 Q1.5 RW	1.5 l s^{-1}	101 h	W3 Q1.5 RW	1.5 l s^{-1}	100 h
W1 Q2.0 TN3	2.0 l s^{-1}	38 h	W3 Q1.8 TN2	1.8 l s^{-1}	-
W1 Q2.5 TN3	2.5 l s^{-1}	24 h			
W1 Q2.5 RW	2.5 l s^{-1}	39 h			

(a) Experiment W1 ($W = 1\text{ m}$).

(b) Experiment W3 ($W = 2.9\text{ m}$).

Table 4.1: Summary of the long-lasting, constant discharge runs of the W1 and W3 experiments.

4.3. Method

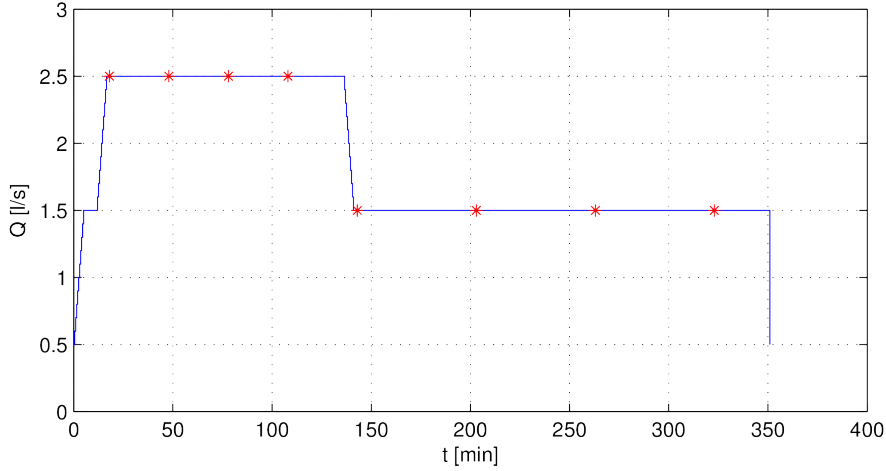


Figure 4.6: Hydrograph adopted during experiment *W1*. The red points represent the instants of the manual surveys of wetted and active widths.

development of significant morphological changes; The discharge within each cycle, represented in figure 4.6, was initially increased from 0.5 l/s (the minimum possible value of our pumping system) to 1.5 l/s and then, after a period of 7 min, increased again to 2.5 l/s for 120 min and finally reduced to 1.5 l/s until the end of the 350 min cycle. Each flow variation followed steps of 0.1 l/s at intervals of 30 s. Only the last decrease was instantaneous in order to avoid as much as possible morphological variations due to the low flows. Between the cycles a morphologically inactive, very small flow prevented sand drying. The first five cycles were performed only to ensure that the morphological state is not influenced by the initial conditions but the result of the periodic flow variations; for this reason only the last 21 hydrographs were adopted for the statistical analysis.

We manually surveyed the dry and active area at 20 sections equally spaced between $x = 3 m$ to $x = 22 m$, where $x = 0$ indicates the flume entrance; we performed eight measurement during six different cycles (cycles 1, 5, 9, 13, 17, 21) at regular intervals of 30 min and 60 min for the low flow and high flow phases respectively (see figure 4.6). For more details see section 4.8.2.

Experiment W3

In this set of experiments the width of the flume was set to $W = 2.9 m$, which allows to minimise the confinement effect due to the presence of the lateral walls.

In order to characterise the equilibrium morphology and transport rate we firstly performed two long, constant-discharge runs (see table 4.1b). We started from a flat, sloping bed with a small channel drawn in the middle in order to



Figure 4.7: Picture of the flume during W3 C5 ($W = 2.9\text{ m}$). Flow is from the camera, discharge is $Q = 1.5\text{ l/s}$.

4.3. Method

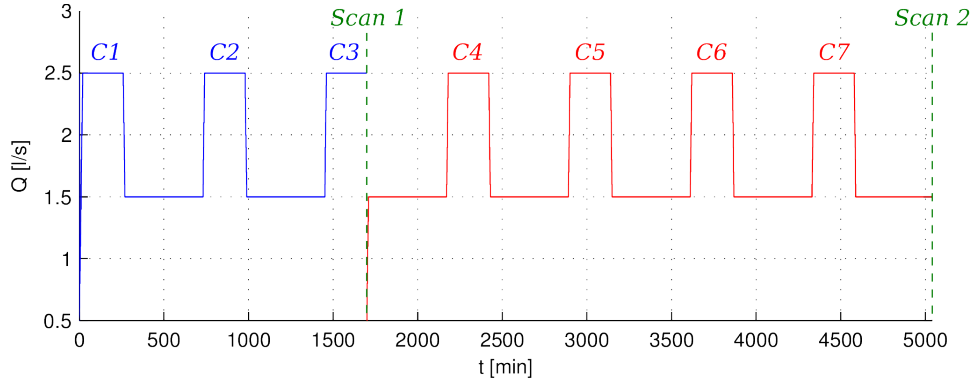


Figure 4.8: Liquid discharge during experiment W3. The vertical dashed lines indicate interruptions of the flow needed for the laser scanning. The whole sequence was repeated three times (plus three additional cycles), for a total of 24 cycles and 6 scans.

speed up the initial phase of braided development; a $Q = 2.5 \text{ l/s}$ was maintained for approximately 72 hours (with few pauses needed for emptying the sediment trap at the outlet) and followed with a 100 h period with low flow $Q = 1.5 \text{ l/s}$.

For the non-equilibrium runs we repeated the flow cycle 24 times; we adopted a hydrograph similar to the experiment W1 but with total duration of the cycle of 12 h, with 8 h of high flow ($Q = 2.5 \text{ l/s}$) and 4 h of low flow ($Q = 1.5 \text{ l/s}$). We chose a longer duration with respect of the W1 experiments because of reduced sediment transport observed (for a given discharge) for the wider flumes (see appendix 4.8.1), which implies lower bedload intensity and probably slower morphological evolution. The phases of flow growth and decline were formed by 1 min-long steps of 0.1 l/s.

Differently from the W1 experiment measured the bottom topography during the cycles. Since the laser scanner needs a dry network we periodically stopped the flow at the end of both high and low flow phases. Specifically, practical considerations about laboratory timetables and the periodic need to supply new dry sand to the feeder suggested to adopt the two flow sequences reported in figure 4.8, which was repeated three times and followed by three additional cycles.

The dashed lines of figure 4.8 represents the instant of the topographic survey, having a resolution of $5 \times 0.5 \text{ mm}$ in the longitudinal and transverse direction respectively; the laser scanning covered a maximum width of 2.5 m, so that it did not enable to survey the morphology of the external part of the flume (20 cm for each side).

An example of the channel morphology is reported in figure 4.9.

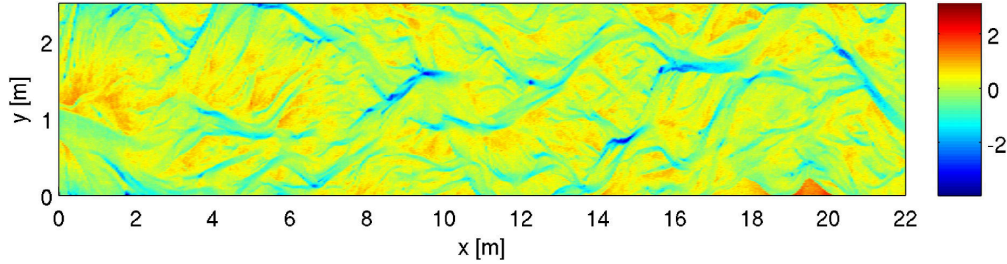


Figure 4.9: Morphology at the end of the end of the W3 1.5 RW. Axes are not to scale (2 : 1 aspect ratio). Elevations in [cm] with respect to the initial slope.

Q [$l s^{-1}$]	W [m]	Q_s [$g s^{-1}$]	T_{skip} [h]
1.5	1.0	1.42	6.5
2.5	1.0	3.64	3
1.5	2.9	0.68	12
2.5	2.9	2.36	4

Table 4.2: Sediment transport rate from the equilibrium experiments of table 4.1. T_{skip} indicates the initial time needed for the development of the braided network, not considered in the computation of the averaged transport rate.

4.4 Results

In order to analyse the effect of the flow variations through time, it is important to obtain a reliable estimate of the equilibrium transport rate; this is possible from the long-lasting, constant-discharge runs listed in table 4.1. By eliminating the initial transitory phase (needed for the full development of the braided network) from each run, and computing the average transport rate, we obtained results of table 4.2; they show a strong dependence of the sediment transport on the water discharge, as well as a lower bedload rate in the wider, unconfined flume. A more comprehensive analysis of the role of discharge and confinement rate on the sediment transport under equilibrium is reported in appendix 4.8.1.

Before starting the analysis of the flow cycles, it is worth to consider that the variability of measured bedload is not only due to transport rate fluctuations but is also caused by additional sources of noise produced by the gauging system (see the description of section 1.5.2). Indeed, the weight we acquire is influenced by oscillations of the water level in the tank, as well as by electronic noise and round-off errors introduced by the the digital signal processing. This additional variability is mainly affecting the short timescales, so that it can be strongly reduced by applying a time filtering. For this reason we pre-processed the signals using a moving average with a time window of 20 *min*. The choice of this time constant derives from a balance between two opposite needs: a) eliminating as much as possible the variability due to the gauging system and to small-scale bedload fluctuations; b) maintaining a sufficient time resolution

4.4. Results

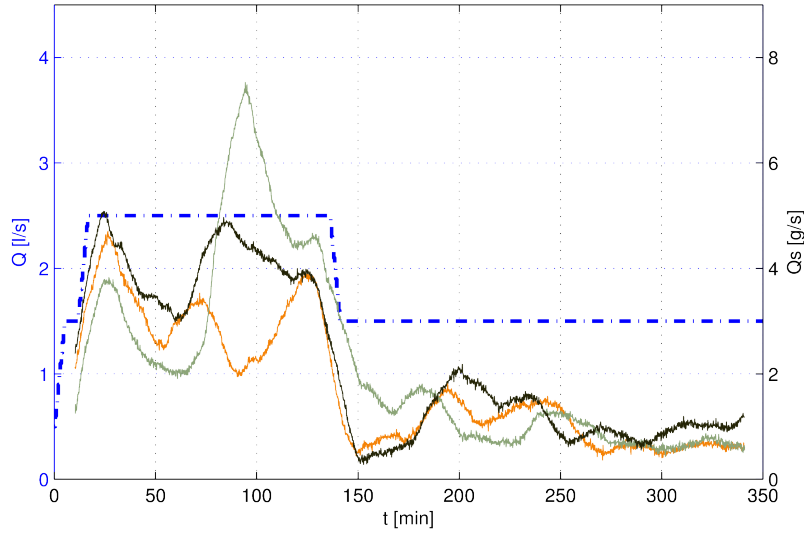


Figure 4.10: Example: variability of the bedload during the first three cycles of experiment W1. The dashed line shows the liquid discharge.

to appreciate the temporal variations of the response.

Figure 4.10 illustrates the filtered transport rate measured during the first three flow cycles of the W1 experiment. Different signals show some common features, such as the peak after around $t = 20 \text{ min}$ followed by a minimum, as well as a clear positive correlation with the water discharge. Nevertheless the resulting signals are remarkably different, and consequently no statistically significant information, about the bedload rate, can be retrieved from a single flow cycle.

By considering the entire set of flow cycles we can build a statistics of the measured transport rate. In figure 4.11, where we report the percentiles of the 21 recorded signals, we can see that median bedload rate increases approximately five times with the discharge; however the variance of the ensemble is rather large, so that the minimum value during the high flow phase and the maximum at low flow are comparable. If we repeat a similar analysis for the experiment W3 (figure 4.12) we obtain an even larger variability of the sediment transport rate, so that it is not rare to observe a lower transport (20 *min*-averaged) at high discharge than at low flow. Another clear difference with the experiment W1 is the lower median value of the transport rate, consistent with the result of the equilibrium experiments of table 4.2.

After this first analysis of the statistical response, we can analyse the most interesting quantity for our investigation, namely the ensemble mean of the transport rate. In figure 4.13, relative to the W1 experiment, we can see that mean bedload rate is much less oscillating than the single realisation of figure 4.11.

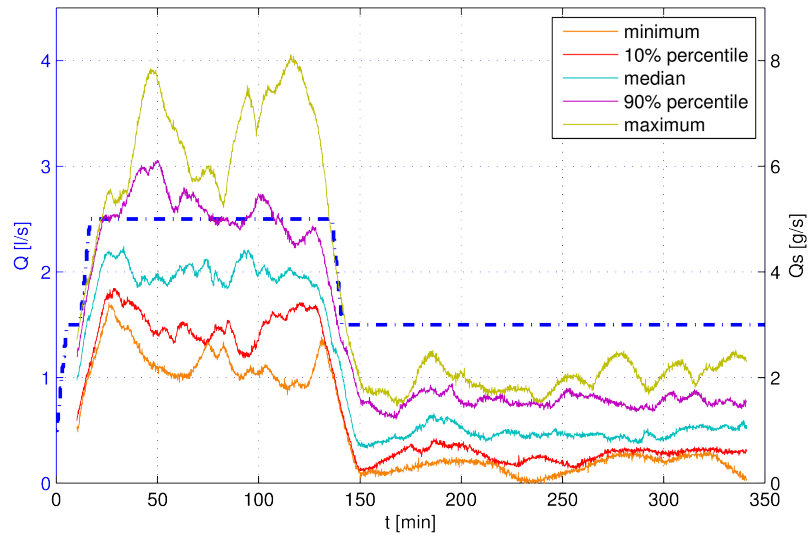


Figure 4.11: Statistics of the bedload during experiment W1. A 20 min moving average filter has been applied. The dashed line shows the liquid discharge.

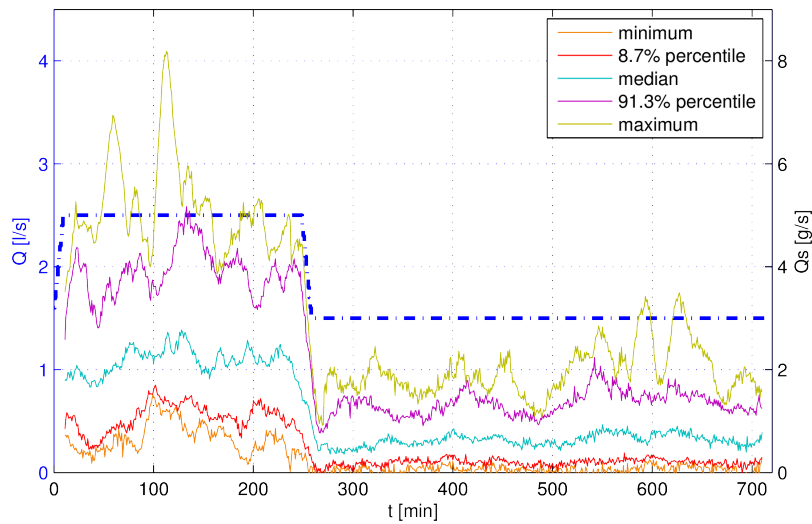


Figure 4.12: Solid discharge during the 24 cycles of the run W3, after a 20 min moving window averaging. The dashed line shows the liquid discharge.

4.4. Results

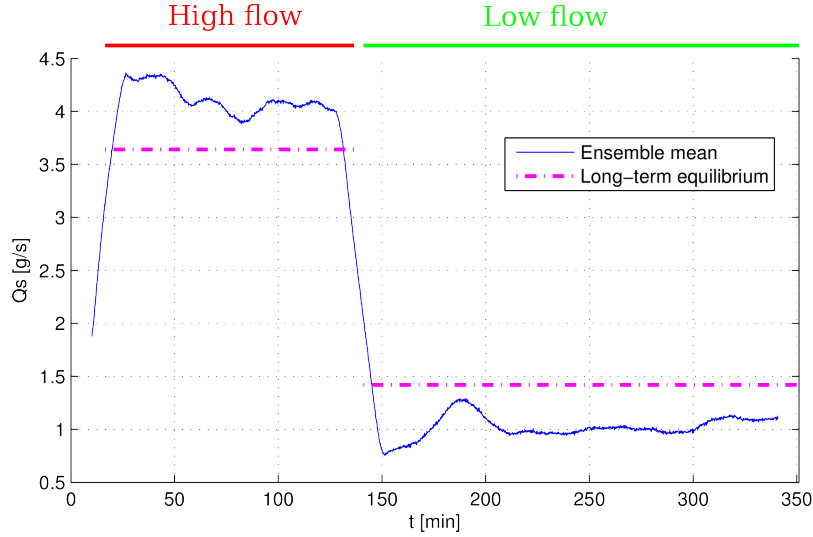


Figure 4.13: Mean solid discharge of the 21 cycles of the experiment W1. A 20 *min* moving average filter has been applied. The blue dashed line shows the liquid discharge; the red and magenta lines indicates the equilibrium values measured during equilibrium runs.

The signal tends to decrease during the high flow period and to increase during the low flow phase; however these variations within the constant discharge phases are rather small relatively to the uncertainties embedded in the estimation.

Assessing whether the observed changes are statistically significant or simply a random outcome is not banal; indeed sediment transport can not be modelled as a simple sequence of independent random samples, but it is the result of a complex system, whose statistical properties are, to a large extent, unknown. For example we do not know whether the samples are normally distributed and which is the correlation between observations at different time instants and at different locations in space.

Nonetheless we can derive some simple, albeit not strictly precise, considerations by dividing the flow cycle in different windows and comparing the average bedload rate between them. Specifically, we selected for each phase four equal window having length 29 and 52 *min* (high and low flow respectively).

The ensemble average and the correspondent standard deviation for the eight windows is reported in figure 4.14; it is clear that the variability within the single window is much larger than the differences between the bars. In order to test whether some changes are statistically significant we need to apply a suitable test; however, since the samples are not uncorrelated we can not use classic tests such as t-test or analysis of variance. A more reasonable hypothesis might be that the *differences* between each signal are uncorrelated and normally

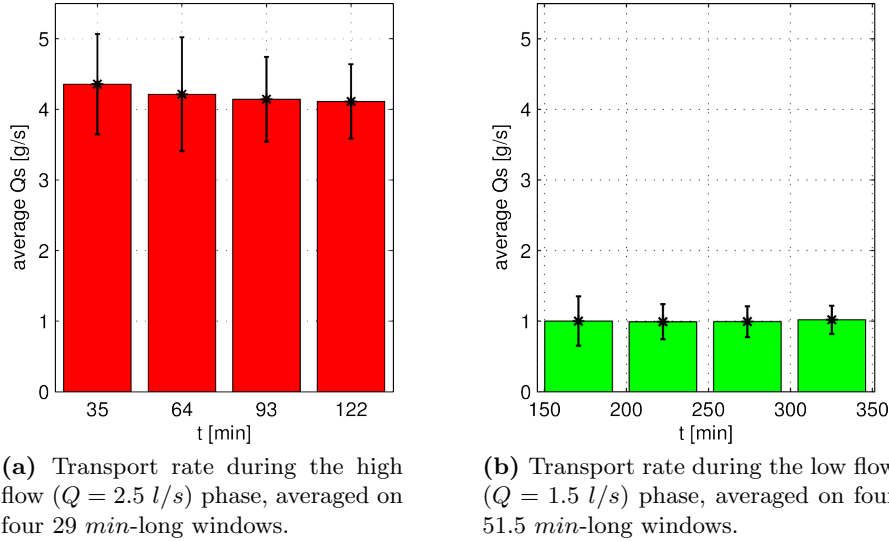


Figure 4.14: Analysis of transport during experiment W1. The error bars indicate the standard deviation between the 21 cycles.

distributed, which enables to compare each couple of windows using a simple t-test.

Results of table 4.3a reveal that the difference between the first (1) and the last (4) window is significantly negative, which indicates a decrease of the transport during that interval. However, since the hypothesis which are behind this simple approach are not fully tested, we should consider this result as a qualitative indication rather than a strict probabilistic outcome.

More evident, and more robust from a statistical point of view, is the comparison of this within-cycle transport rate with the equilibrium values measured during equilibrium runs (dashed lines of figure 4.13). Indeed, this comparison reveals clear differences; specifically, if we treat the equilibrium transport as an “error-free” value and we compare each single window with a t-test we obtain that the null hypothesis that the equilibrium and non-equilibrium values are the same is very low, which indicates an significant increase of the bedload with respect to the equilibrium conditions.

The transport rate recorded at low flow (table 4.3a) shows only a slight increase during the phase with constant discharge; therefore it is not possible to asses any statistically relevant variation. Again the difference is much more clear with respect to the equilibrium transport measured in the long-term runs with constant discharge $Q = 1.5$ l/s. Indeed also in this case the t-test shows, with high confidence interval, that the non-equilibrium transport rate is significantly lower.

Nevertheless it is important to remember that the equilibrium values are

4.4. Results

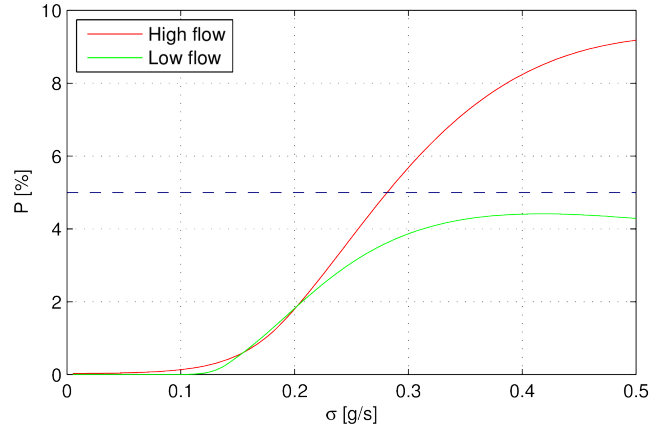


Figure 4.15: Probability that the difference between equilibrium and within-cycle transport rate is zero, as a function of the uncertainty in the knowledge of equilibrium bedload. The dashed line represent a 5% threshold; when the curves are below this line we can assume a statistically significant difference.

	$\Delta\bar{Q}_s$ [gs^{-1}]	SD [gs^{-1}]	$P(x > \bar{x})$		$\Delta\bar{Q}_s$ [gs^{-1}]	SD [gs^{-1}]	$P(x < \bar{x})$
1-2	-0.143	0.390	5.4%	1-2	-0.009	0.263	41.2%
2-3	-0.072	0.446	23.6%	2-3	0.000	0.136	55.9%
3-4	-0.031	0.285	31.3%	3-4	0.026	0.102	49.8%
1-4	-0.245	0.589	3.5%	1-4	0.018	0.362	12.4%

(a) high flow period. (b) low flow period.

Table 4.3: Mean, standard deviation and probability associated to each difference. In red we marked the cases for which the probability of the zero-mean hypothesis is $< 5\%$.

resulting from a temporal average of a relatively long-lasting, but still limited run; therefore the assumption of “error-free” equilibrium transport rate is not exact, so that it is worth to account also for the uncertainty of that estimation. A detailed evaluation of this uncertainties is very difficult on the basis of the present dataset; however we can make some considerations by assuming a Gaussian distributed error with variance σ^2 . As expected, such uncertainty reduces the confidence that the equilibrium and within-cycle transport rates are different; nonetheless, as reported in figure 4.15, the result remains significant as far as the standard deviation is less than $0.3 g/s$.

The mean transport rate during the cycle is remarkably different within the relatively unconfined experiment W3. Figure 4.16) shows the mean of the 24 repeated cycles, which contains some variations (for example the peak after two hours of high flow) which seems to be irregular and therefore might be more related to a residual random component than to significant oscillations of the bedload response through time.

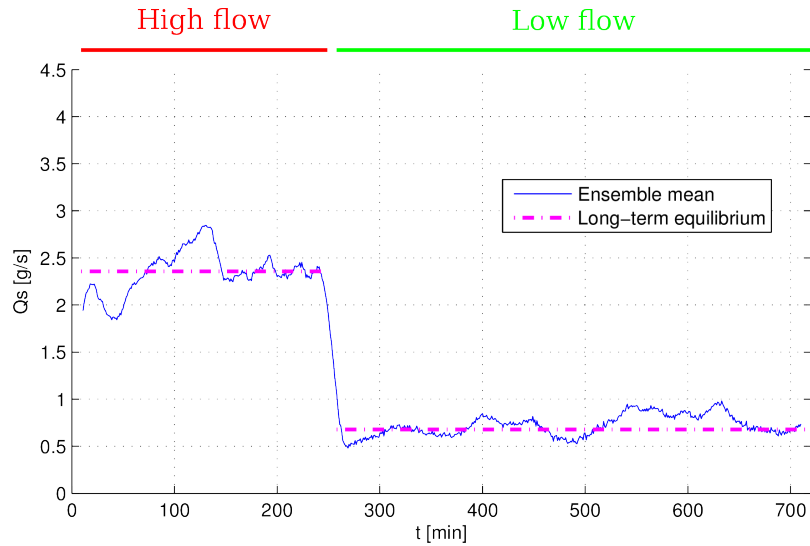


Figure 4.16: Mean solid discharge of the 24 cycles of experiment W3. A 20 min moving average filter has been applied. The blue dashed line shows the liquid discharge; the red and magenta lines indicates the equilibrium values measured during equilibrium runs.

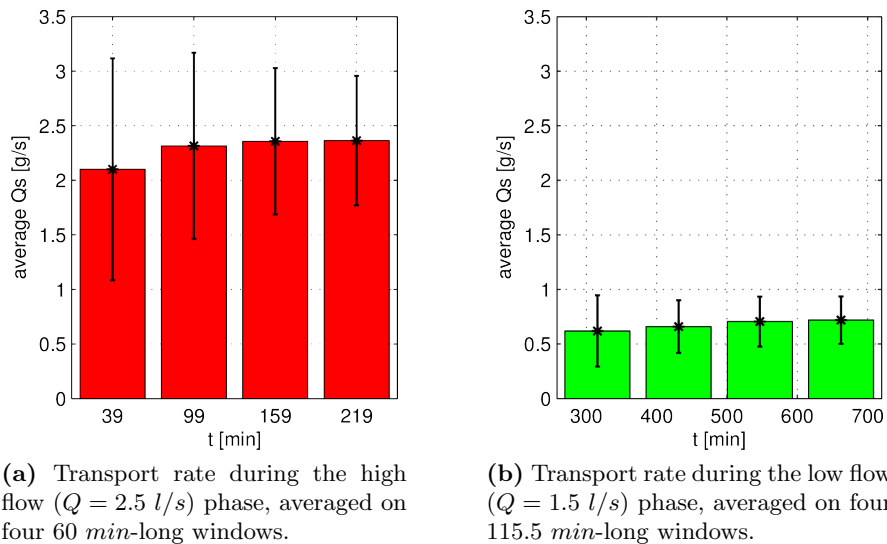


Figure 4.17: Analysis of transport during experiment W3. The error bars indicate the standard deviation of the average.

4.5. Discussion

	ΔQ_s [gs^{-1}]	SD [gs^{-1}]	$P(x > \bar{x})$		ΔQ_s [gs^{-1}]	SD [gs^{-1}]	$P(x > \bar{x})$
1-2	0.007	0.235	0.95%	1-2	0.041	0.198	33.5%
2-3	0.264	0.804	62.9%	2-3	0.046	0.155	17.2%
3-4	0.216	0.373	89.3%	3-4	0.013	0.092	49.9%
1-4	0.042	0.407	12.2%	1-4	0.010	0.312	14.%

(a) High flow. (b) Low flow.

Table 4.4: Mean, standard deviation and probability associated to each difference. In red we marked the cases for which the probability of the zero-mean hypothesis is $< 5\%$.

We can still proceed as before by testing the differences between four windows. As reported in table 4.4, the only significant variation we can observe is the increment at the beginning of the high flow stage and in particular between first and second hour.

More interestingly, if we compare the equilibrium transport rate (dashed line of figure 4.16) with the mean value during the cycle we do not appreciate, differently from figure 4.13, any clear deviation induced by the flow unsteadiness. The t-test confirms, as expected, that the within-cycle and the equilibrium transport rates comes, with an high level of significance, from the same statistical population.

Within this section we have shown only results relative to sediment transport rate. For some considerations about the observed of the response in terms of wetted and active areas see appendix 4.8.2.

4.5 Discussion

We have seen that, in the confined case, the transport rate is significantly different during varying discharge than in equilibrium conditions. This effect can be related to the morphological changes occurring during the varying flow; specifically we can study these variation using the reach-scale morphological indicator we developed in *Chapter 3* and we called *Average section*, which is nothing than a (cumulative) distribution of elevation with respect to the lowest point of each section.

Unfortunately due to malfunctioning of the scanning device no topographic survey were possible during W1 experiment. Nevertheless we can compute those curves for the bed topography measured at the end of different equilibrium experiments, obtaining the result of figure 4.19. We can clearly see that in the narrow ($W = 1 m$) channel a different distribution develops depending on the water discharge. This is not surprising because consistent with the result of *Chapter 3*, which indicates, in the case of relatively confined channels, a strong dependence of the morphology with the specific discharge Q/W . Moreover it

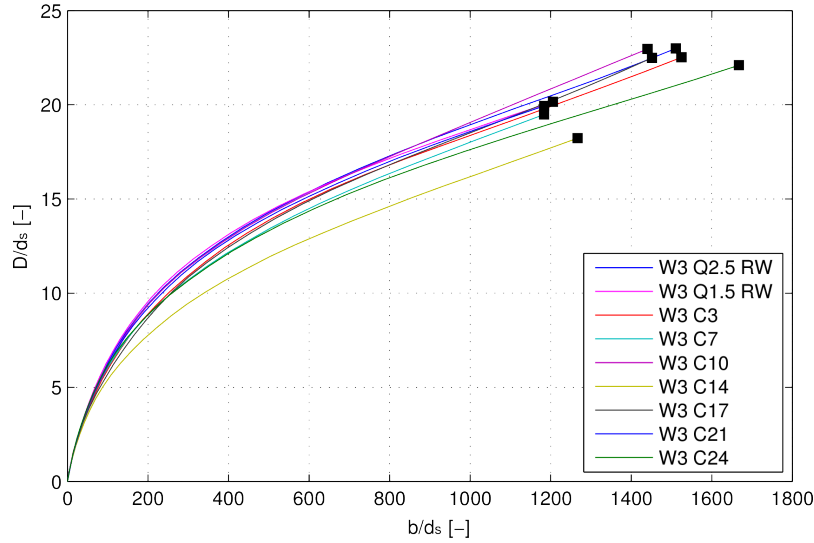


Figure 4.18: Average section during W3 experiment. Cx indicates the topography measured during the x -th cycle.

is something we may expect if we imagine to increase the discharge until the aspect ratio becomes favourable for the development of alternate bars, which would lead to completely different morphological distributions with respect to the complex braided network which develops for relatively low flows.

Variations of the morphological configuration may explain the reason of the overshooting we observe. Indeed after the increase of the discharge the morphology needs time to adapt to the new flow condition and, during the transitory period, the braided network and its transport rate are not in equilibrium. This is totally analogous to the process we described, for the case of migrating alternate bars, in section 4.2.1; indeed in that case the disequilibrium of the morphology due to relatively fast variations of the water discharge was causing an excess or deficit of the bedload rate.

More challenging is to understand the reason why the non-equilibrium response is overshooting and undershooting during positive and negative variation of the discharge respectively (clockwise hysteresis of the transport rate such as in figure 4.1). A possible interpretation comes from the analysis the hypsometric curves of the three equilibrium W1 runs (figure 4.20), which represent the portion of the bed which lies below a given elevation η with respect to the initial slope. It is clear that passing from lower to higher discharges induces scour of the deepest areas and deposition over the more elevated zones; since the global mass balance is in equilibrium the two effects compensates in order to give a zero net variation; however this transfer of mass might enhance the transport and cause the observed overshooting. Conversely the opposite transition from $Q = 2.5 \text{ l/s}$ to $Q = 1.5 \text{ l/s}$ produces a flattening of the morphology (filling of

4.5. Discussion

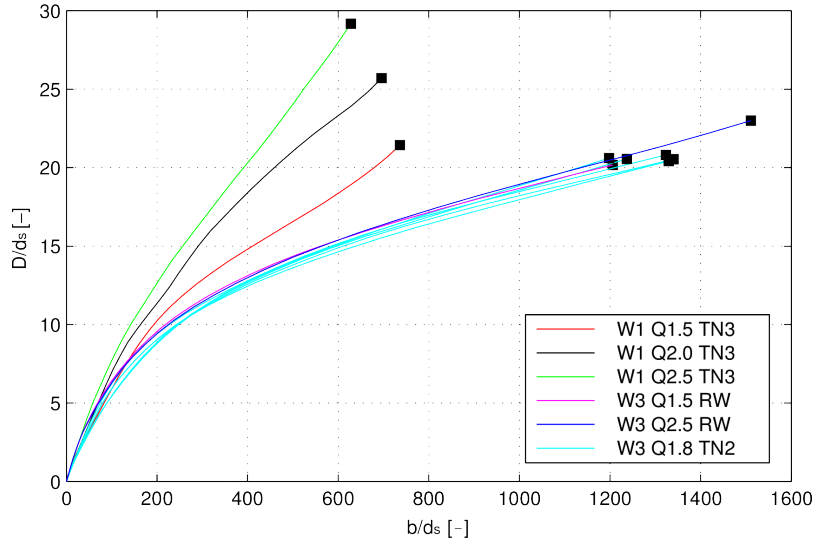


Figure 4.19: Average section during different constant discharge runs, both in the confined (W1 series) and unconfined (W3 experiment) case.

the deepest areas and erosion of the more elevated regions) which might involve only a local transfer of mass, thus producing a lower transport. Unfortunately the absence of detailed information about morphological changes through time does not enable to investigate more deeply the mechanism responsible of the transport hysteresis.

Nonetheless, the connection between the reach-scale morphological variations and the unsteadiness of the transport rate is supported also by the analysis of the relatively unconfined W3 experiments. Our observations of *Chapter 3* suggest that the morphology of a free, unconfined network is less affected by the formative discharge than in the confined case. This is confirmed by the analysis of the morphological variation throughout the W3 experiments: indeed the curves of figure 4.19 are largely independent of the discharge for the unconfined case W3; this means that, in spite of significant re-arrangement of the channel network, the reach scale statistical properties are not significantly flow-dependent. Consequently it is expected that the sediment transport rate quickly adapt to flow variation because it does not need significant morphological adjustment which would require a long time to develop. This is also consistent with the results of Bertoldi et al. (2009a), which suggested that the at-a-station response of the transport is similar to the response in formative conditions. Those arguments explains the mean bedload rate of the 24 repeated cycle, which shows a rapid adaptation to quasi-equilibrium conditions.

A possible interpretation of this phenomenon is that an unconfined braided network can react to flow variations by adjusting not only the specific values of discharge, stress and transport (such as a confined network or a single-thread

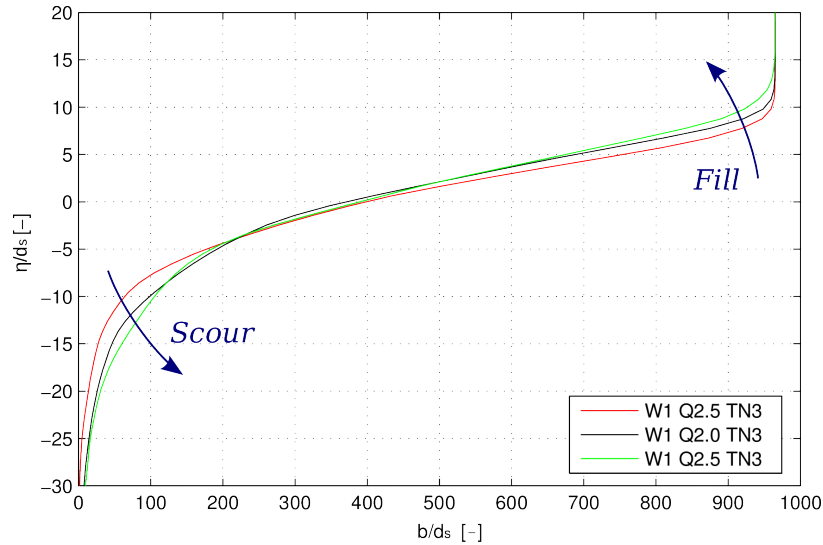


Figure 4.20: Distribution of elevation during different equilibrium runs of the W1 (confined) experiment. Arrows indicate the changes of the equilibrium distribution with increasing discharge.

channel) but also by increasing the width; this is probably causing a more gentle response of the transport and, more generally, a higher resilience to varying conditions.

Natural flood events do never follow a stepwise variation such as the hydrograph we analysed. However on the basis of the present results we can infer that the expected transport during a “real” flood event is larger during the rising limb and lower (for the same discharge) during the flow decay. The effect, which is rather limited within our experiments might be more important in natural braided rivers; indeed they often show not only fast variations of the flow but also a very wide range of morphologically active discharges, much wider than the 2.5/1.5 ratio we explored within this work. For example the Rees River (see *Chapter 2*) shows significant reworking with remarkably small flow pulses (return period of less than 1 month), approximately one order of magnitude lower than the annual peak. These great discharge variations are expected to cause a larger morphological disequilibrium and consequently a more important hysteresis of the transport rate with respect to our laboratory observations.

This set of experiments also does not enable to fully investigate the effect of different confinement rates. However we know, from the results of *Chapter 3*, that the degree of confinement probably depends the unit discharge Q/W , so that the important parameter is probably the width relative to the discharge; for example the experiment W3, which is relatively unconfined for $Q = 2.5 \text{ l/s}$ is expected to be affected by the confinement for higher discharges (larger Q/W), which would therefore lead to significant hysteresis.

4.5. Discussion

It is worth to underline that the present analysis is limited to well-sorted bed material. Indeed in a natural gravel-bed river the heterogeneity of the grain size can induce phenomena of selective transport, changes of the bed texture and armouring effects which may significantly affect the response of the braided network to the flow variations (e.g. Hassan et al., 2006).

Within the present analysis we assume that the propagation of the discharge variations along the flume is almost instantaneous. Indeed in the Trento's flume experiments the time required for a flow pulse to reach the flume outlet was of the order of $2 \div 3 \text{ min}$, so that sufficiently small to neglect the delay and the variations of the hydrograph shape between the different sections. However, for longer channels and for shorter duration of the hydrograph, a significant delay and change of the flow curve may occur (in particular a decrease of the peak discharge due to the lamination effect); in this case attention should be paid to treat the problem as spatially homogeneous and to assume that the measurements at the outlet is representative of the transport rate throughout the braided network.

Finally it is worth to clarify the role of the sediment supply in the braided network morphodynamics and consequently on the sediment flux at the flume outlet. Indeed, since we are not recirculating the sediment but independently fixing a feed rate, it is not possible to ensure an exact mass balance for two reasons:

- It is not possible to predict the fluctuation of the bedload.
- Even the response in terms of mean bedload was unknown before the analysis of the experiment.

Therefore we adjusted the sand supply on the basis of the mean values measured during the constant-discharge experiment, and afterwards we checked that a long-term mass balance is maintained.

You may argue that in this way we may introduce periods of aggradation or degradation which may affect the resulting transport rate. However, as we will see in *Chapter 6* (Redolfi and Tubino, 2014), any downstream propagation of such a perturbation would require a very long time; we expect consequently that any effect due to fluctuation of the sand supply will produce only a local effect, similarly to the “boundary layer” observed by Wong and Parker (2006b) during cycles of varying discharge and constant sediment feed rate. Moreover visual inspection and analysis of the topographic data reveals that no significant aggradation nor degradation occurs even in the upper portion of the flume.

Another potential problem we can not a priori exclude, is that the first cycles might be affected by the initial conditions, so that the cycles might be not statistically identical because of the presence of a long-term transitory. Nevertheless, the morphological response represented in figure 4.18 does not show any relevant long-term trend; this is confirmed in terms of transport by

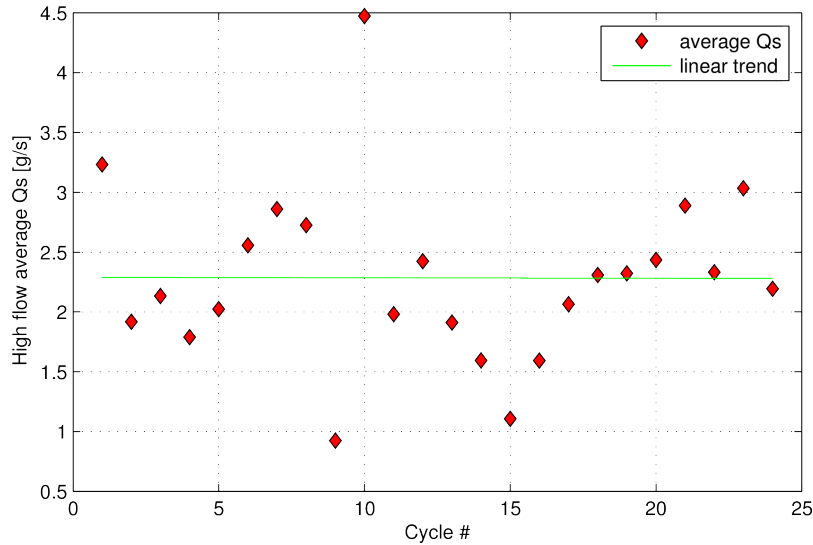


Figure 4.21: Average during the high flow phase of the different cycles. The green line indicates the linear trend.

the result of figure 4.21, where we report the mean transport between different cycles and its linear interpolation.

4.6 Conclusions

Within this work we tackled for the first time the question of the effect of the discharge unsteadiness on the sediment transport rate in a braided network. We studied the problem using a laboratory-scale physical model, which enables to control the water discharge and to measure the sediment transport at the flume outlet.

It is well established that in a braided network the transport rate at a given section (as the flume outlet) shows great variability even in an experiment with constant controlling conditions; this represents a fundamental limitation when studying the effect of changing discharge because these fluctuations do not enable to distinguish between the response of the mean bedload and the stochastic component. Indeed the timescale of the externally driven flow variations is short if compared with the timescale of the internally generated fluctuations, so that a simple filter like time averaging does not allow to remove this “noise” without hiding the effect of unsteady flow. In order to overcome this issue we adopted a novel methodology in the analysis of laboratory braided networks based on a statistical approach; in particular we repeated several time identical simple hydrographs, in order to determine a mean, statistical response of the system. The ensemble mean contains much less variability and, if the number of repetitions is sufficiently large, is expected to depend on the external controls, namely

4.7. List of symbols

shape, magnitude and duration of the flow hydrograph.

The flume observations reveal a different response depending on the degree of confinement of the braided network. When the river is significantly confined we notice a response of the transport rate to increasing discharge, which exceeds the equilibrium value (overshooting) whereas a decrease of the discharge produce with a strong decrease of the transport rate, which falls below the long-term equilibrium (undershooting). This short-term response is followed by a phase of gradual adaptation towards the long-term equilibrium conditions. As a consequence of this non-equilibrium response we expect a clockwise hysteresis whose importance depends on the rapidity of the flow variations.

The response to changing flow is significantly different for the experiments with wider, relatively unconfined braided networks, when the transport rate due to the flow unsteadiness seems to rapidly adapt to the new equilibrium conditions.

A possible interpretation of this behaviour comes from the analysis of the morphological network response to the varying flow, measured through distributions of elevation at the reach scale. For relatively confined braided networks, such a distributions changes significantly with the discharge. Since these changes are not instantaneous but needs time to fully develop, there is a transitory phase when transport rate is different from the long-term equilibrium value.

This is not the case for relatively free braided networks, which does not show any significant variation of bed elevation distributions throughout the run; this suggest the absence of relevant morphological adjustment to the new flow conditions. Consequently the effect of unsteadiness on the transport is weak and not detectable in our observations, and therefore do not undergo any significant morphological adjustment to the new conditions.

Within the present work the limited number of experiments does not enable to quantify how the magnitude of the overshooting effect and the temporal scale of the adaptation to equilibrium conditions depend on the discharge and on the confinement rate. In addition our analysis is limited to well-sorted sediment and to very simplified, artificial hydrographs. For these reasons further investigations are needed to fully explore the problem and to give more insight to the morphodynamical processes which leads to the observed hysteresis.

4.7 List of symbols

Symbols

*		Dimensionless quantity;
A	[L]	Amplitude of the alternate bars;

4.7. List of symbols

b	$[l]$	Wetted width;
b_a	$[l]$	Active width;
g	$[lt^{-2}]$	Gravitational acceleration;
D	$[l]$	Water depth across the section;
d_{50}	$[l]$	Median grain size;
dx	$[l]$	Longitudinal resolution of the laser scan;
dy	$[l]$	Transverse resolution of the laser scan;
g	$[lt^{-2}]$	Gravitational acceleration;
t	$[t]$	Time;
τ	$[-]$	Time scaled with the linear growth rate of alternate bars;
Q	$[l^3t^{-1}]$	Water discharge;
Q_s	$[l^3t^{-1}]$	Solid discharge;
W	$[l]$	Flume width;
x	$[l]$	Longitudinal coordinate;
y	$[l]$	Transverse coordinate;
Δ	$[-]$	Relative submerged density of sediment;
β	$[-]$	Aspect ratio of the channel;
β_{cr}	$[-]$	Critical aspect ratio for the formation of alternate bars;
ΔQ_s	$[l^3t^{-1}]$	Component of transport due to flow unsteadiness;

4.8 Appendices

4.8.1 Equilibrium response of braided network with different confinement width

In this section we analyse the response of the braided network to varying flow and confinement width in equilibrium conditions, which is needed as a starting point to understand the braided morphodynamics during unsteady flow.

Most of the measurements reported here comes from the experimental work of Garcia Lugo (2014), which provide useful information about equilibrium transport, active and wetted area for different discharges and confinement width. Therefore this part does not represent a result of the present study but a collocation of the new equilibrium experiment in a pre-existing dataset.

The experiments of Garcia Lugo (2014) have been carried out using the same experimental setup we adopted, in particular same flume facility with equal slope and sediment size. A total of 27 runs were performed with three different discharges ($Q = 1.5, 2.0, 2.5 \text{ l/s}$) and nine different confinement width in the range $W = 0.15 \div 1.5 \text{ m}$.

In general we can assume that the averaged bedload transport Qs and the active and wetted width (b_a and b respectively) depend on the external controls; in particular for the case of an homogeneous channel with well-sorted sediment the statistical properties are expected to be function of the sediment calibre and density, the water density, the gravity acceleration, the channel width and slope; consequently if we consider the π -theorem we can write in dimensionless form

$$\{Qs^*, b^*, b_a^*\} = fct(Q^*, S^*, W^*, \Delta) \quad (4.7)$$

where Δ is the relative submerged weight of the sediment, fct indicates a generic function and we defined the following dimensionless widths

$$b^* = \frac{b}{d_s} \quad b_a^* = \frac{b_a}{d_s} \quad W^* = \frac{W}{d_s} \quad (4.8)$$

whereas, similarly to Bertoldi et al. (2009a), we made the discharge dimensionless as follows

$$Q^* = \frac{Q}{\sqrt{gd_s^3}} \quad Qs^* = \frac{Qs}{\sqrt{g\Delta d_s^5}} \quad (4.9)$$

where g is the gravitational acceleration and d_s the (nearly uniform) grain size.

For a given slope and sediment density we can recombine the parameters of Eq. 4.7 in order to write

$$\left\{ \frac{Qs^*}{W^*}, \frac{b^*}{W^*}, \frac{b_a^*}{W^*} \right\} = fct\left(\frac{Q^*}{W^*}, Q^*\right) \quad (4.10)$$

following the idea that a linkage exists between the unit (per unit width) discharges (Bertoldi et al., 2009a) we can imagine that the role of Q^* it is weaker

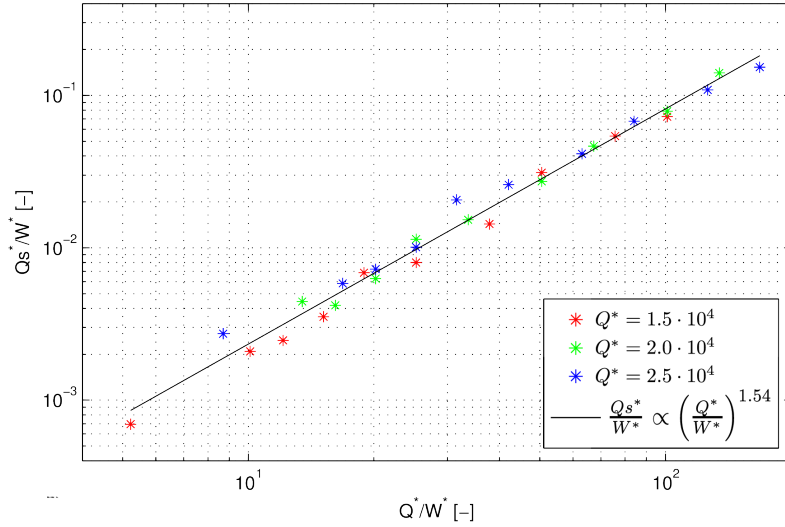


Figure 4.22: Solid discharge during equilibrium runs in different conditions of discharge and flume width (TN3 (Garcia Lugo, 2014) and present experiments). Different colours correspond to different discharges. the black line represents the log-linear fitting.

than the impact of Q^*/W^* . Indeed from the experimental observations we report in figure 4.22 it seems that a functional relation between the unit discharge and transport approximately holds; this dependence can be expressed through a power law of exponent 1.54 (black line of figure 4.22).

The scatter of the data is probably dependent on both a residual content of randomness (due to the limited duration of the equilibrium run) and the role of the factors we ignored, and in particular total discharge Q^* . Indeed the experiment with the highest Q^* show a transport rate which is on average 11 % larger than the prediction of power-law approximation, whereas points with the lowest Q^* are 11 % smaller than the fitting curve; this indicates that the parameter Q^*/W^* does not explain the whole variability of the specific transport but a small dependence on the total discharge Q^* still remains.

The behaviour of the wetted and active width is reported in figure 4.22. We can see that both the series depend on the specific discharge and reach a saturation (i.e 100 % of the available area) for sufficiently high values of Q^*/W^* .

4.8.2 Analysis of active and dry area during the experiment W1

In this section we analyse the measurements of wetted and active area we performed during six different cycles of the experiment W1. The objective is to determine whether there are significant variations within phases of constant discharge, which may help the interpretation of the observed mean response of

4.8. Appendices

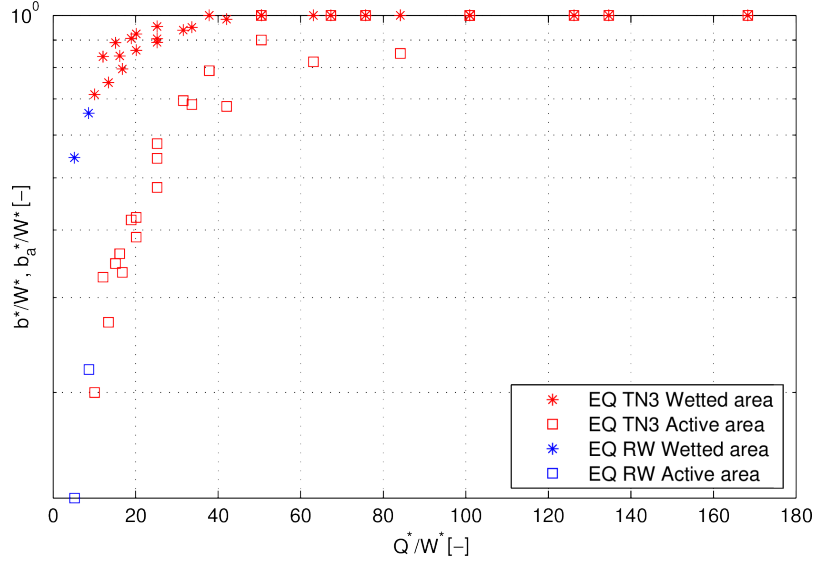


Figure 4.23: Mean active (asterisk marker) and wetted (square markers) width during equilibrium run in different conditions of discharge and flume width. Red points: TN3 experiments (Garcia Lugo, 2014), blue points: present (RW) experiments.

the bedload. As a secondary aim we intend to check whether repeated measurements throughout the flume enable to retrieve some information about the spatial and variability of the active and wetted width.

As we mentioned before for cycles 1, 5, 9, 13, 17, 21 we surveyed eight times (see figure 4.6) at regular intervals of 30 *min* and 60 *min* (high and low phases respectively) the entire length of the flume, manually measuring the channels at 20 sections having a regular 1 *m* spacing.

The active width was defined as the portion of the section in which some gravel movements can be noticed within an interval of few seconds. Probably more difficult to define, and consequently more inclined to personal interpretation, is the measurement of the wetted area; indeed a significant fraction of the bed is covered by a thin layer of water which can not be straightforwardly classified. In order to reduce as much as possible the degree of subjectivity we decided to account as dry only the bars where most of the grains were emerging whereas we classified as wet the areas covered by a thin water film; in spite of that some measures may be affected by errors and dependent upon the operator and environmental factors such as the conditions of illumination. In order to speed up this operation each of the two people surveyed half of the flume, exchanging their role for each time in order to avoid biases due to the personal interpretation of the above definition.

According to Egozi and Ashmore (2008) an estimation of the braiding index with a standard deviation of $\pm 20\%$ can be obtained by considering a reach which is approximately ten times longer than the average wetted width. In the

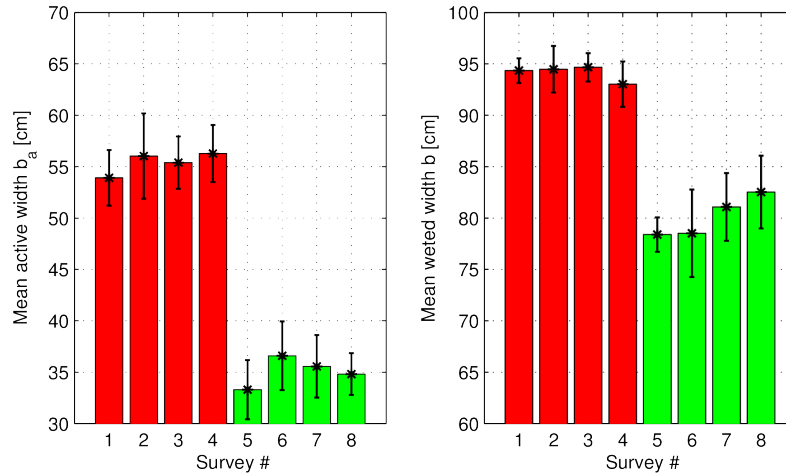


Figure 4.24: Spatial and ensemble average of the active and wetted width during the cycle. Red and green colours indicated high and low discharge respectively.

present case the standard deviation of the error is lower (of the order of $2 \div 4\%$) probably because the channel is significantly longer (approximately $25 \div 30\%$) but also because the width is an indicator less variable than the channel count index.

The changes during the cycle of the ensemble average (figure 4.24) shows as expected a strong variation with the discharge; in particular the active width changes approximately from 55% to 35%.

The variations within a phase of constant discharge are more difficult to detect and to interpret; the t-testing of the differences between the surveys 1-4 and 5-8 of figure 4.24 reveals the following statistically significant changes

- An increase of the active width ($p = 4.5\%$) between the 1st and 4th survey during the high flow period (see table 4.6a)
- A decrease of the wetted width ($p = 1.9\%$) between the 3rd and 4th survey during the high flow period (table 4.7a)
- An increase the wetted width ($p = 3.2\%$) between the 1rd and 4th survey during the low flow period (table 4.7b)

From this first results it seems that the wetted area follows the trend of the sediment transport, whereas the active width, at least during the high flow, tends to vary in the opposite way. However the small number (six) of available samples and the uncertainties related to the assumption of independent and normally distributed samples which is behind the t-test makes these findings relatively weak.

It is also interesting to have a look to the spatial variations of active and wetted width reported in figures 4.25 and 4.26; we immediately notice that

4.8. Appendices

	Δb_a [cm]	SD [cm]	$P(x > \bar{x})$		Δb_a [cm]	SD [cm]	$P(x > \bar{x})$
1-2	2.1	3.3	17.6	1-2	3.3	3.5	6.7%
2-3	-0.6	4.3	73.2%	2-3	-1.0	2.4	34.0%
3-4	0.9	2.0	33.8%	3-4	-0.8	4.9	72.5%
1-4	2.4	2.2	4.5%	1-4	1.5	2.7	23.0%

(a) High flow. (b) Low flow.

Table 4.6: Mean, standard deviation and probability associated to each difference. In red we marked the cases for which the probability of the zero-mean hypothesis is $< 5\%$.

	Δb [cm]	SD [cm]	$P(x > \bar{x})$		Δb [cm]	SD [cm]	$P(x > \bar{x})$
1-2	0.1	1.3	81.8	1-2	0.1	4.1	94.3%
2-3	0.2	1.7	79.6%	2-3	2.6	2.6	6.2%
3-4	-1.6	1.2	1.9%	3-4	1.5	2.5	21.8%
1-4	-1.3	1.4	7.5%	1-4	4.1	3.3	3.2%

(a) High flow. (b) Low flow.

Table 4.7: Mean, standard deviation and probability associated to each difference. In red we marked the cases for which the probability of the zero-mean hypothesis is $< 5\%$.

some sections show a remarkably different (in this case higher) both active and wetted width with respect to the neighbour cross-section. For example in figure 4.27 we can notice that, throughout the whole series of surveys the section 11 tends to have (during the high flow period) a lower wetted and active width with respect to section 10; a similar result, albeit less strong, can be obtained by comparing sections 3 and 4. This observation suggest that a persistence of the network in space may exist in terms of width; however the limited dataset available does not allow to deeply explore this interesting behaviour.

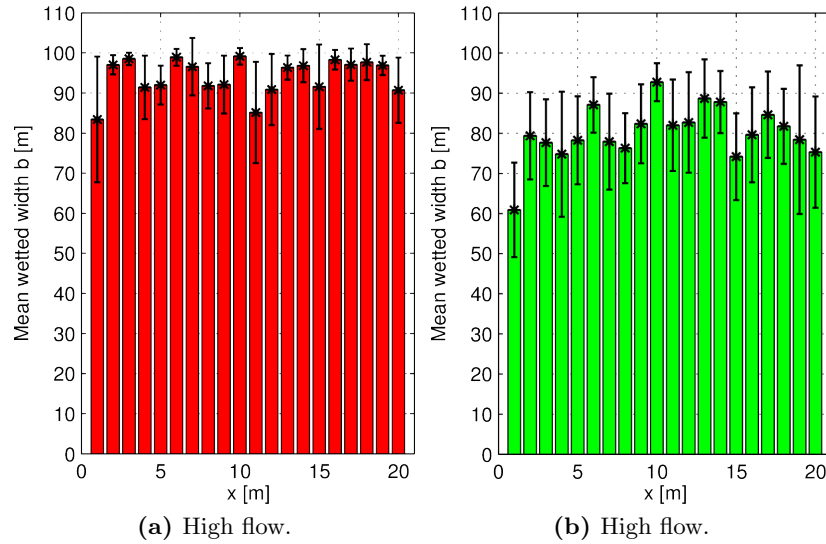


Figure 4.25: Ensemble mean of the wetted width at different locations. Error bars indicate the standard deviation of the single ($6 \times 4 = 24$) measurements.

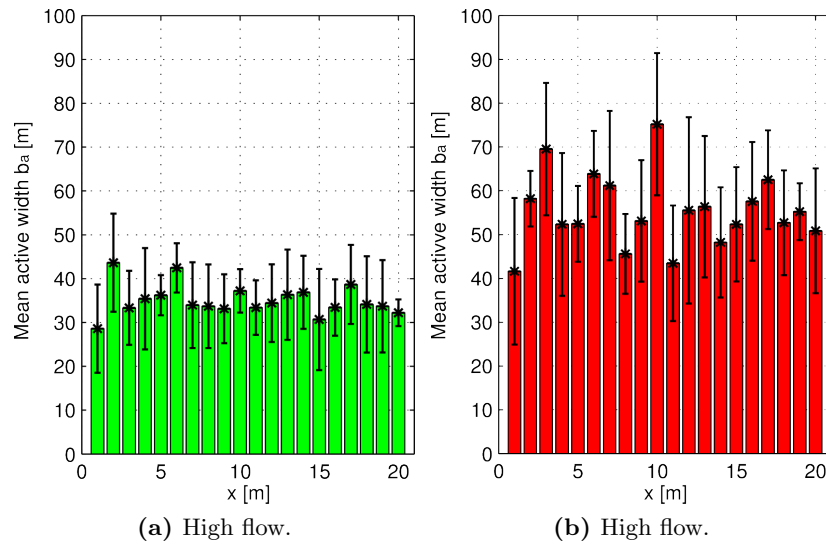


Figure 4.26: Ensemble mean of the active width at different locations. Error bars indicate the standard deviation of the single ($6 \times 4 = 24$) measurements.

4.8. Appendices

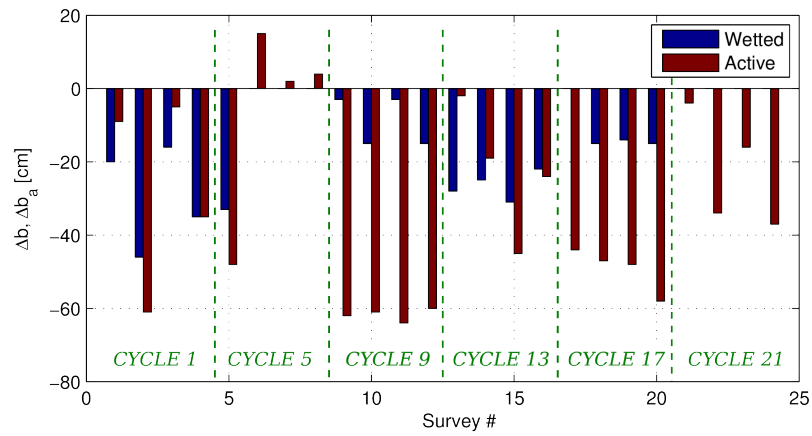


Figure 4.27: Difference of wetted and active width between sections 10 and 11, repeatedly measured during the high flow phase of different cycles.

Chapter 5

A diffusive 1D model for the morphological response to varying sediment supply

5.1 Introduction

Braided rivers are often heavily impacted by human activities such as gravel mining, embankments, hydropower schemes, which can compromise the morphological and an ecological functionality (Rinaldi et al., 2005, e.g.). In particular many braided rivers experienced degradation often associated with decreasing of the braiding index and narrowing of the active corridor; in some cases a dramatic change of river morphology from multi-thread to single channel was observed (Gurnell et al., 2009; Liebault et al., 2012).

Similar processes can be seen also at laboratory scale where reduced sediment availability produces morphological changes and often a complete modification of the river pattern (Germanoski and Schumm, 1993; Marti and Bezzola, 2006).

In the case of single-thread river the 1D model can be approximated, under the hypothesis of locally uniform flow, with a simple diffusive scheme which in some cases can be solved even analytically, providing useful insight on the behaviour of the system (e.g Vreugdenhil and de Vries, 1973; Jaramillo and Jain, 1984; Wong and Parker, 2006b).

The above assumption is acceptable only if the longitudinal variations are relatively smooth, as pointed out by Ribberink and Van der Sande (1984) on the basis of the solution of the more complete linear hyperbolic model. Their criterion can reformulated as follows

$$\left| \frac{D}{SL} (1 - Fr^2) \right| \ll 1 \quad (5.1)$$

where D is the water depth, S the slope, Fr the Froude number and L the

5.1. Introduction

length scale of the longitudinal variations. It is clear that in the case low-depth and high slope channels the length scale of the adjustment to the uniform flow L is relatively short, especially if the Froude number is close to the critical value; these conditions are more common in gravel bed rivers, for which the simple diffusive model can be adopted in order to predict the morphological evolution due to variations of sediment supply, discharge or perturbation of the bed level (e.g. Lisle et al. (1997); Wong and Parker (2006b)).

If the previous condition (Eq. 5.1) is not satisfied the solution of the complete hyperbolic model is required; the linear version, which can be solved analytically (Gill, 1988), has been adopted (Zhang and Kahawita, 1990) to reproduce the experimental results in aggrading laboratory channels (Soni et al., 1980).

In single-tread channels the long term adaptation of the bed profile to a variable sediment input mainly results in a slope adjustment able to accommodate the required transport capacity. However, in the case of a poorly sorted gravel bed, the development of an armouring layer during degradation can induce a reduction of sediment transport even without significant variations of slope (Lisle and Church, 2002; Madey et al., 2009; Pryor et al., 2011).

In addition a braided river has a supplementary way to adjust the sediment transport through the variation of the network morphology. Indeed the bedload of a braided river is, for given hydraulic conditions, highly dependent on the complexity of the network (Paola, 1996; Ferguson, 2003; Bertoldi et al., 2009a); for this reason different transport rates are possible with the same gradient and bedload formulas derived for equilibrium braided networks may be not applicable. Our hypothesis, based on experimental observations, is that this effect is only temporary and the river eventually reaches the equilibrium conditions. In this case, we can derive a simple diffusive model for predicting the long term evolution of the bed level profile.

Both the diffusive and the hyperbolic model can be solved, in the case of relatively small variation, assuming a linear approximation; however in some cases this assumption may be rather inaccurate (Jaramillo and Jain, 1984; Zhang and Kahawita, 1987). This is because if the flow in a single-thread channel is close to the critical Shields stress condition the bedload depends relatively strongly on slope variation. In the case of a braided river the wide distribution of the Shields stress, as well as the variations of the active width cause a more smooth dependence of the sediment transport with the stream power, which leads to a significant transport even at low-flow conditions (see Bertoldi et al., 2009a). For this reason the model can be linearized and analytically solved and, if the magnitude of the variations is relatively small, the result furnishes a rather accurate approximation.

5.1.1 The diffusive model

Many laboratory investigations have focused on the analysis of the sediment transport in braided rivers. The sediment is either recirculated or adjusted in order to ensure a global sediment balance; as a consequence, after a transitory phase during which the braided network develops, the system attains a condition of dynamical equilibrium, in which the statistical properties keep constant.

In this situation the mean solid discharge can be estimated as a temporal average calculated on a sufficiently long period of time and the slope can be measured as a spatial average along the entire flume.

For a given uniform bed material we can assume the general expression

$$qs = \sqrt{g\Delta d_s^3} \mathcal{F}(Q, S, W) \quad (5.2)$$

where qs , Δ and d_s are the specific solid discharge, the relative submerged weight and the grain size respectively and \mathcal{F} is a function of the flume width W , the reach-averaged slope S and the water discharge Q .

The main assumption of the diffusive model is that, considering S as the local slope and qs as the local sediment transport, the same formula is valid also during aggradation or incision phases. This hypothesis is not straightforward but requires some discussion.

First of all the definition of the local quantities in a braided river is not immediate because of the relevant fluctuations which appear on relatively long spatial and temporal scales.

Secondly the assumption of a sediment transport which is locally in equilibrium is not fulfilled in general. Indeed the transport in a braided river does not depend only on the gradient but also on the spatial distribution of the stress, which in turn depends on the river morphology. Since after rapid variations of the bed elevation the morphology is clearly not in equilibrium with the local slope we expect the same non-equilibrium also for the sediment transport.

Nevertheless, as we will see in the following, this effect seems to be transitional and in the long term the morphology adapts to the new transport.

The one-dimensional (cross-section averaged) Exner equation reads

$$\frac{\partial \eta}{\partial t} - \frac{\partial qs}{\partial x} = 0 \quad (5.3)$$

where η is the mean bottom elevation and x the longitudinal coordinate. If we substitute Eq. 5.2 into the Exner Eq. 5.3 we obtain the following parabolic model

$$\frac{\partial \eta}{\partial t} - k \frac{\partial^2 \eta}{\partial x^2} = 0 \quad (5.4)$$

whose diffusion coefficient can be expressed as

$$k = \frac{\mathcal{F}_0 \mathcal{F}_S}{S_0} \frac{\sqrt{g\Delta d_s^3}}{(1-p)} \quad \mathcal{F}_S := \frac{S_0}{\mathcal{F}_0} \frac{\partial \mathcal{F}}{\partial S} \quad (5.5)$$

5.1. Introduction

where S_0 is the reference slope, p the sediment porosity and $\mathcal{F}_0 = \mathcal{F}(S_0)$ represents the reference bedload. Notice that, being $\mathcal{F}(S)$ a nonlinear function, \mathcal{F}_S and k are not constants but depend on the local slope S .

If we define T , L and $H = S_0L$ as the time, longitudinal (x) and vertical (η) scales respectively we can express the diffusion Eq. 5.4 in dimensionless form as

$$\frac{\partial \eta^*}{\partial t^*} - k^* \frac{\partial^2 \eta^*}{\partial x^{*2}} = 0 \quad k^* = k \frac{T}{L^2} \quad (5.6)$$

From the previous equation the following ratio between the horizontal and temporal timescales arises

$$T = L^2 \frac{S_0}{\mathcal{F}_0 \mathcal{F}_S(S_0)} \frac{1-p}{\sqrt{g \Delta d_s^3}} \quad (5.7)$$

which leads to $k^*(S_0) = 1$.

The spatial scale L depends on the process we want to study. If we are interested in the evolution of the entire channel we can choose $L = L_c$, where L_c is the channel length.

Analysis of the model

Let us consider a channel of length L_c with fixed elevation downstream and constant water and sediment supply. In the long-term we expect a braided network in a dynamical equilibrium, having all the statistical properties constant in space and time. In this condition the slope is constant, so that the bed elevation profile can be expressed as

$$\eta_0^* = -(x^* - L_c^*) \quad (5.8)$$

where the subscript 0 indicates the initial reference state.

If we suddenly decrease the sediment supply the evolution of the system can be predicted by the diffusive model after the definition of a suitable formulation for the transport function. Different authors (Ashmore, 1988; Young and Davies, 1990; Bertoldi et al., 2009a) proposed empirical formulas based on the stream power. Regression on the data from a series of 27 equilibrium experiment with $Q = 1.5 \div 2.5$ l/s and $W = 0.15 \div 1.5$ m performed in the Trento's flume (Garcia Lugo et al., 2013) suggests the following relation between specific liquid and solid discharge

$$q_s \propto (q S)^\gamma \quad \gamma = 1.6 \quad (5.9)$$

where $q = Q/W$ is the specific discharge.

Since the experiments do not explore the different slopes we have to rely on the assumption that the stream power is the important quantity which affects

the transport. However due to the lack of direct investigations we must consider the exponent γ only as approximated value.

We can compare the linear and nonlinear model by solving numerically the diffusive equation through a finite differences scheme. The result, expressed in terms of variation of elevation with respect to the initial state (denoted with the subscript $_1$) is reported in figure 5.1. This analysis reveals that, if the variations of the sediment supply are of the order of $\pm 30\%$, differences between the linear and the complete model are small and practically negligible.

This is often the case because according to 5.9 a decrease of the sediment supply of -50% will eventually lead to a slope with is 35% lower than the initial gradient which is rather high if compared with the variations we are usually interested in.

A comparison with the case of a single-thread gravel-bed channel reveals that, for the same variation of the long-terms equilibrium slope the nonlinear effects can be significantly more important (see figure 5.2). This is not surprising, because of the strong non-linearity of the bedload transport formula, especially when the Shields stress is close to the critical threshold.

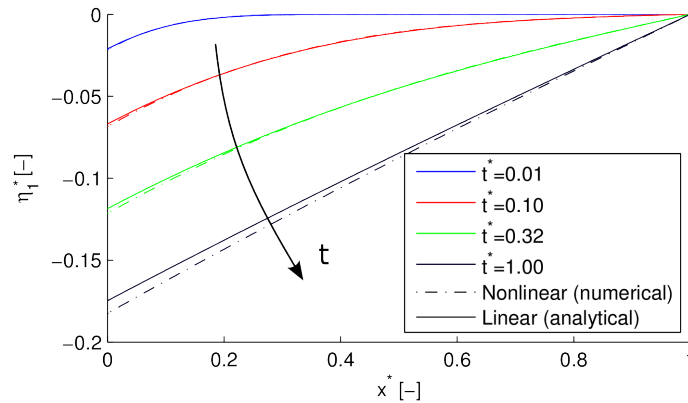


Figure 5.1: Comparison between the linear and the nonlinear solution (continuous and dashed lines respectively) after a 30 % reduction of the sediment supply from an initial condition $S_0 = 1\%$. An exponent $\gamma = 1.6$ has been adopted.

If we consider the linearized ($k^* = const = 1$) version of the model we can write the diffusion equation 5.6 directly in terms of the variations with respect to the initial state

$$\frac{\partial \eta_1^*}{\partial t^*} - \frac{\partial^2 \eta_1^*}{\partial x^{*2}} = 0 \quad (5.10)$$

which can be solved analytically for different boundary conditions, included stepwise modification of the sediment supply (sediment decrease or augmentation) and/or of the downstream bottom elevation (base-level rising or lowering).

It is important to notice that according to Eq. 5.7 the temporal scale of the variations is proportional to the square of its length; this means that the time

5.1. Introduction

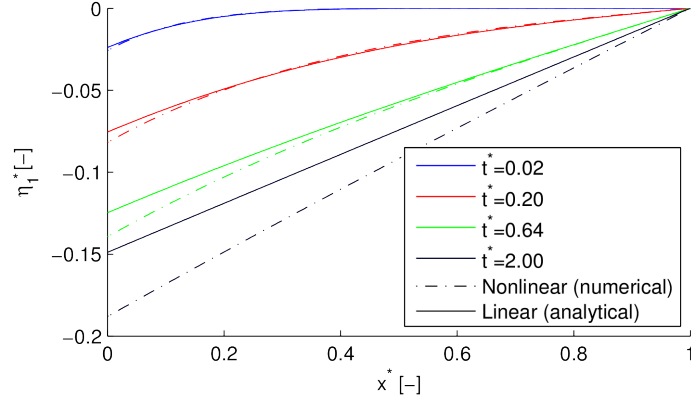


Figure 5.2: Comparison between the linear and the nonlinear solution (continuous and dashed lines respectively) after a reduction of the sediment supply which will produce the same long-term profile of figure 5.1 for the case of a single-thread channel. The Parker (1990) transport formula with an initial Shields stress $\theta_0 = 0.06$ has been adopted.

needed for any change increases quadratically with the distance.

The sediment transport at the downstream boundary of the flume depends on the time with respect to the timescale T , which is proportional to the square of the domain length L_c .

5.1.2 The hyperbolic model

The validity of a flux-gradient relation in a gravel-bed river is limited by other effects which can significantly affect the transport capacity, including variations of channel morphology, roughness and bed surface texture. Among these the adjustment of the braided morphology is, in the case of a poorly-sorted bed material, the most important factor, which affects the transport during aggradation and degradation; this effect is expected to be increasingly relevant when the variations of the bed elevation are relatively fast if compared with the time needed by the braided network to approach an equilibrium morphology.

From these considerations two important questions arises:

- Which are the spatial and temporal scales at which the non-equilibrium of the morphology plays an important role?
- What is the response of the bed elevation profile if the variations are relatively fast?

In order to address these questions we have built a simple linear model in which we consider an additional contribution to the solid discharge due the non-equilibrium of the braided morphology, which is assumed to be proportional to the aggradation/erosion speed

$$\Delta q_s = -\sqrt{g\Delta d_s^3} \tilde{a} \frac{\partial \eta^*}{\partial t} \quad (5.11)$$

where \tilde{t} represents the time divided by the Exner timescale, which reads

$$T_E = \frac{HW(1-p)}{\mathcal{F}_0 \sqrt{g\Delta d_s^3}} \quad (5.12)$$

This choice comes from the assumption that the time required for the formation of an equilibrium morphology is given by the ratio between the volume which has to be moved and the sediment transport, where the previous can be estimated at the product of a vertical scale H and an horizontal scale which is assumed to be proportional to the width W . Further investigation would be necessary to asses whether or not such scaling is valid; however what is really important in our discussion is that for a given configuration the increment of Δqs , depends only on the incision rate.

Remembering Eq. 5.7 we can calculate the following relation between the different dimensionless times

$$\tilde{t} = \frac{t}{T_E} = t^* \frac{T}{T_E} = t^* \frac{L^2}{HW} \frac{S_0}{\mathcal{F}_S} = t^* \frac{L}{W} \frac{1}{\mathcal{F}_S} \quad (5.13)$$

If we sum Eq. 5.2 and Eq. 5.11 we obtain the following expression for the bedload

$$qs^* = \mathcal{F}(q^*, S) - \tilde{a} \mathcal{F}_S \frac{W}{L} \frac{\partial \eta^*}{\partial t^*} \quad (5.14)$$

and consequently the linearized form of Eq.5.4 becomes

$$\frac{\partial \eta^*}{\partial t^*} - k^* \frac{\partial^2 \eta^*}{\partial x^{*2}} - a^* \frac{\partial^2 \eta^*}{\partial x^* \partial t^*} = 0 \quad (5.15)$$

where the new parameter a^* is defined as

$$a^* = \tilde{a} \frac{k^* W}{\mathcal{F}_0 L} \quad (5.16)$$

Eq. 5.15 is a linear scalar *PDE* of hyperbolic type which describes the evolution of the bed elevation.

A more general closure should take into account the history of the morphological evolution and not only the instantaneous variation. Indeed we can imagine that the actual transport depend on the incision speed in the last period and not only on the current scour rate. For this reason we have introduced the following formulation

$$\Delta qs^* = -a^* \int_0^\infty G(\tau^*) \frac{\partial \eta^*}{\partial t^*}(t^* - \tau^*) d\tau^* \quad (5.17)$$

where G is a “memory” function. In particular if we assume that G is a decaying exponential which follows the Exner timescale we can write

$$G(\bar{\tau}) = \frac{1}{\bar{T}_M} e^{-\bar{\tau}/\bar{T}_M} \quad G(\tau^*) = \frac{1}{T_M^*} e^{-\tau^*/T_M^*} \quad (5.18)$$

5.1. Introduction

where \bar{T}_M is a constant parameter and T_M^* depends on the scale of the variations we are studying

$$T_m^* = \bar{T}_m \mathcal{F}_S \frac{W}{L} \quad (5.19)$$

In this way we find a model in which a^* gives the magnitude of the non-local effect and T_M^* indicates its (relative) timescale.

After substituting the closure relation of Eq. 5.17 into the Exner equation we obtain

$$\frac{\partial \eta^*}{\partial t^*} - \frac{\partial^2 \eta^*}{\partial x^{*2}} - a^* \int_0^\infty G(\tau^*) \frac{\partial^2 \eta^*}{\partial x^* \partial t^*} (t^* - \tau^*) d\tau^* = 0 \quad (5.20)$$

This formulation is very general and can be used even to model processes which never lose memory of the initial state; in particular if we define $b^* = a^*/T_M^*$ and we let $T_M^* \rightarrow \infty$, we can write Eq. 5.17 as

$$\Delta q s^* = b^* \eta^* \quad (5.21)$$

which represent the storage volume transport relation proposed by Lisle and Church (2002) to account for the armouring effect in degrading channels.

In practice the behaviour of the system is much more complex than what can be seen with this simple model; however this approach allows simple description of the main processes involved in the river dynamics under unsteady conditions, which can be useful for predicting, at least in a qualitative way, the bed level evolution.

Analysis of the model

Our analysis reveals the presence of two different temporal scales T and T_E , the previous representing the time of the evolution of the bed level profile and the latter indicating the time needed for the development of a braided morphology at the reach scale. This important consideration allows to neglect the contribution of the hyperbolic component if the variation of the bed level elevation is relatively slow ($T \gg T_E$) or, equivalently, when the longitudinal scale of the slope variation is sufficiently long; indeed if L increases the contribution of the non-diffusive term (Eq. 5.13) becomes smaller and eventually (for large L) negligible.

The general solution of the hyperbolic model can be determined by solving in the Laplace space the integro-differential Eq. 5.47. The result for the case of an abrupt decrease in the upstream flux is reported in figure 5.3; we can see that the relative importance of the hyperbolic component is more important in the early stages of the process, when the elevation change is more rapid.

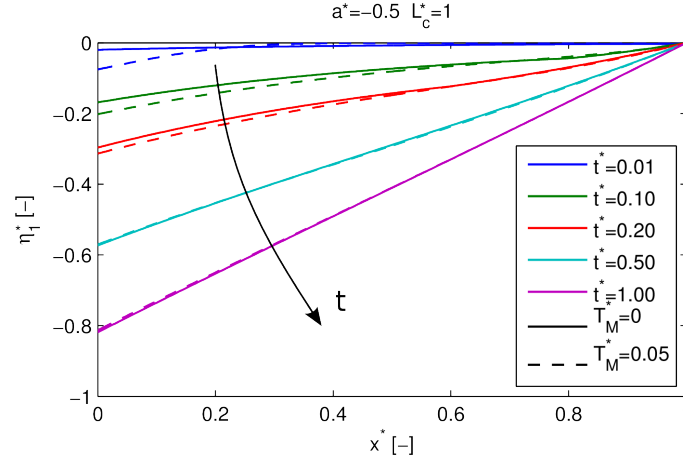


Figure 5.3: Evolution of the bottom level profile according to the hyperbolic model. Continuous line: $T_M^* = 0$, dashed line: $T_M^* = 0.05$.

5.1.3 Laboratory experiments

Experimental setup

We performed the experiments at the hydraulic laboratory of the Trento University .

In particular we carried out two experiments, one with a reduction of the sediment supply (erosion) and one with an increase of the sand input (aggradation). The main features of this experiments are summarised in tables 5.1 and 5.2.

Exp 1

In this experiment we firstly performed a 35 *h*-long equilibrium run, in which we maintained the sand supply in balance with the averaged output. In particular starting from a flat bed with $S = 1 \%$ and a small channel traced in the middle we fed the flume with a constant discharge and with a sand flux $Q_{s_{in}} = 2.5 \text{ g/s}$, which is approximately equal to the temporal average measured during this phase. After this period we sharply reduced the sand supply to 1.0 *g/s* for a period of 130 *h*. The bed topography was surveyed at the end of the equilibrium phase and twice during the subsequent degradation.

Exp 2

We started from a flat bed with a small channel cut in the middle and we fed a constant sediment flux $Q_{s_{in}} = 1.6 \text{ g/s}$ which, being very close to the temporal average of the output bedload, allowed to maintain a global equilibrium of the flume, with a constant slope $S = 0.85 \%$. After a long (354 *h*) period the

5.1. Introduction

Run Type	Feature	Value
Equilibrium	Duration	35 <i>h</i>
	Mean active width	39 <i>cm</i>
	Mean wetted width	92 <i>cm</i>
	Sand supply $Q_{s_{in}}$	2.5 <i>g/s</i>
	Sediment output Q_s	2.53 <i>g/s</i>
	Slope S	1.0 %
	Number of scan	2
Degradation	Duration	130 <i>h</i>
	Sand supply $Q_{s_{in}}$	1.0 <i>g/s</i>
	Number of scan	2

Table 5.1: Main features of *Exp 1*

Run Type	Feature	Value
Equilibrium	Duration	354 <i>h</i>
	Mean active width	41 <i>cm</i>
	Mean wetted width	92 <i>cm</i>
	Sand supply $Q_{s_{in}}$	1.6 <i>g/s</i>
	Sediment output Q_s	1.61 <i>g/s</i>
	Slope S	0.85 %
	Number of scan	9
Aggradation	Duration	64 <i>h</i>
	Sand supply $Q_{s_{in}}$	2.5 <i>g/s</i>
	Number of scan	4

Table 5.2: Main features of *Exp 2*

sand supply was incremented to $Q_{s_{in}} = 2.5 \text{ g/s}$, which is approximately the equilibrium value we measured with $S = 1 \%$.

5.1.4 Experimental results

In this section we present the experimental outcomes in terms of mean bed level profile, elevation distribution and output solid discharge.

Exp 1

During the initial equilibrium phase a braided network develops. Neglecting the initial transitory the average solid discharge is $Q_s = 2.53 \text{ g/s}$ and the bed level profile maintains a slope close to $S = 1 \%$ (red and blue lines of figure 5.5).

After the reduction of the sand supply the upstream region of the flume immediately starts to degrade, decreasing the slope as we can see in the last two profiles of figure 5.5.

The degradation process begin with the incision of an approximately 30 *cm* wide channel near the left bank; this single channel deepens and propagates

downstream, leaving the other channels completely dry and, after 25 h , it reaches a distance of approximately 6 m .

After this initial phase a significant bank erosion causes a widening of the channel, the development of new bifurcations and ultimately a fully braided morphology even in the region close to the flume inlet (see maps of figure 5.7).

The evolution of the incision process can be seen also from the the variation of the bed level at some sections located in the upstream region of the flume (figure 5.4); in particular from the upper panels ($x = 1 m$ and $x = 2 m$) we can notice that after 50 h the erosion involves only the left part of the flume, while at the end the entire section is significantly deeper. At $x = 4 m$ the single channel that have formed at the early stages of the degradation run widens and, after 50 h the scour is already spread across the section. The velocity of the incision is significantly smaller at $x = 8 m$, where a braided morphology persists throughout the duration of the experiment.

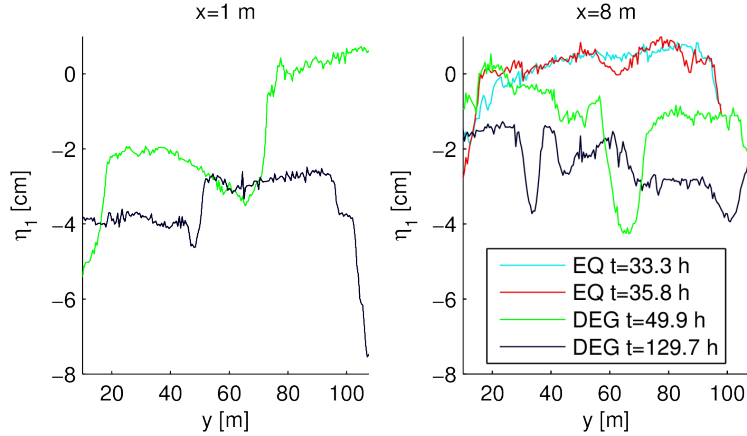


Figure 5.4: Variation in time of the bottom elevation during *Run 1* for several sections located at distance x from the inlet of the flume.

These observations suggest that the long-term evolution of that system could be modelled through a diffusive model.

If we consider $\mathcal{F}_S = \gamma = 1.6$ we can compute the diffusion coefficient following Eq. 5.5, which reads

$$k = \frac{Qs_0}{S_0} \frac{\mathcal{F}_S}{(1-p)} = 0.988 \left[\frac{m^2}{h} \right] \quad (5.22)$$

if we consider $L = L_c = 23 m$ we can easily calculate the temporal scale (Eq. 5.7) obtaining

$$T = L^2/k = 535 [h] \quad (5.23)$$

Since in a finite domain we can consider the diffusion process completed when $t^* \simeq 1$ the latter computation provides an estimation of the time needed to reach the new equilibrium state.

5.1. Introduction

The prediction of the diffusive model are compared with the actual evolution of the profiles in figure 5.5)

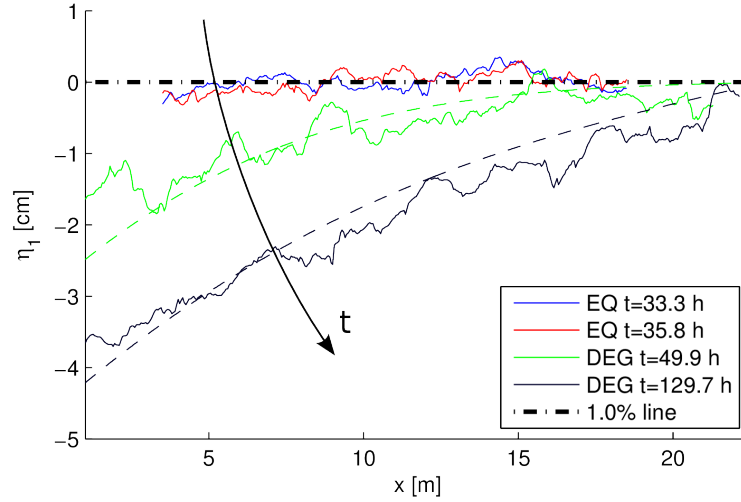


Figure 5.5: Bed level profiles during *Run 1* and analytical solution of the linear model (dashed lines).

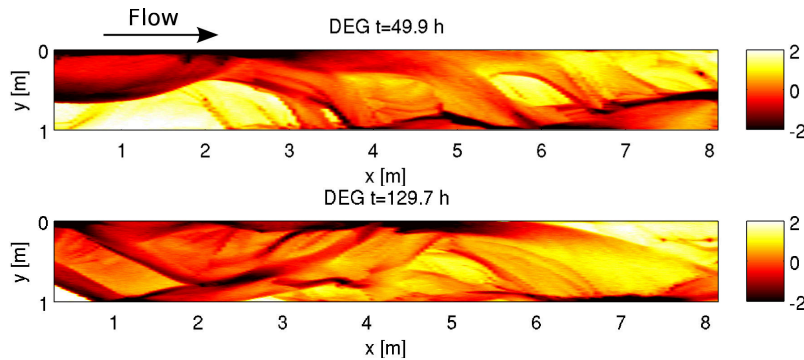


Figure 5.6: Map of the initial part of the flume after 50 *h* and 115 *h* of the degradation phase. Elevation (in *cm*) is relative to the local linear trend.

Exp 2

The rapid augmentation of the sand supply which follows the long equilibrium run induces a deposition starting from the upstream part of the flume which propagates downstream.

The topography of this region during the experiment is reported in figure 5.7, where we can notice that after the increase of the sand supply the deposition produces the formation of a central bar with a relatively flat surface.

Although this observation suggests that a morphological non-equilibrium occurs throughout the whole aggradation phase, the relatively short extension of the area interested by this phenomenon does not allow to appreciate any statistically significant non-equilibrium of the local morphology.

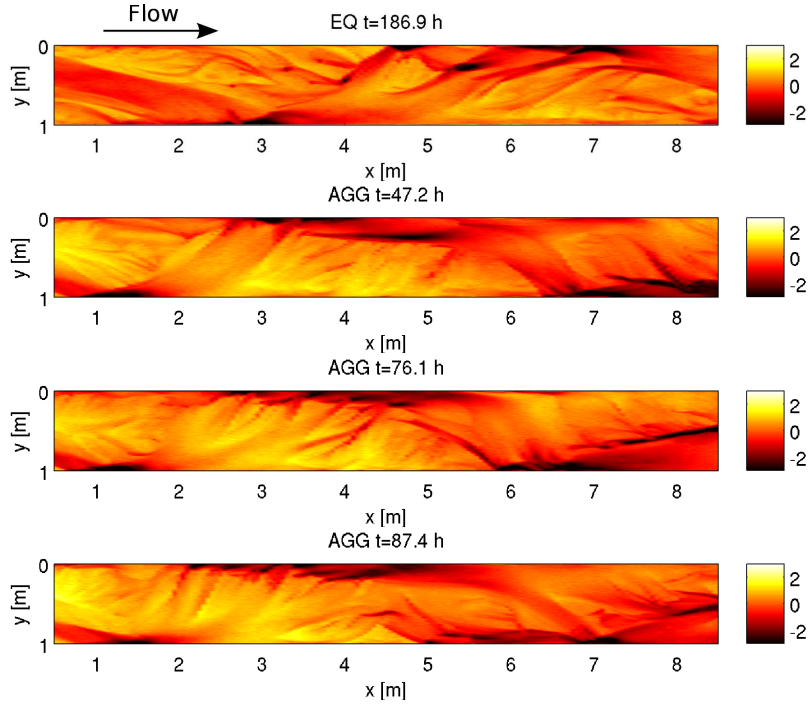


Figure 5.7: Map of the initial part of the flume during the equilibrium (upper panel) and aggradation (lower 3 panels) phases. Elevation (in [cm]) is relative to the local linear trend.

In figure 5.8 we can see how the cross-sectional averaged, bed level profile evolves in time.

The computation of the diffusion coefficient (Eq. 5.22) gives in this configuration $k = 0.744 \text{ m}^2\text{h}^{-1}$, which correspond to a temporal timescale (Eq. 5.23) $T = 711 \text{ h}$. This calculation permits to evaluate, at least in an approximate way, the evolution of the bed level profile illustrated in figure 5.8.

5.2 Discussion

The experimental observations suggest that in the case of a non-cohesive and well-sorted sediment the evolution of the bed level profile of a confined braided network after a variation of the sediment supply can be modelled, excluding the initial stage, as a diffusive process.

The present model also permits the estimation of the temporal variation of

5.2. Discussion

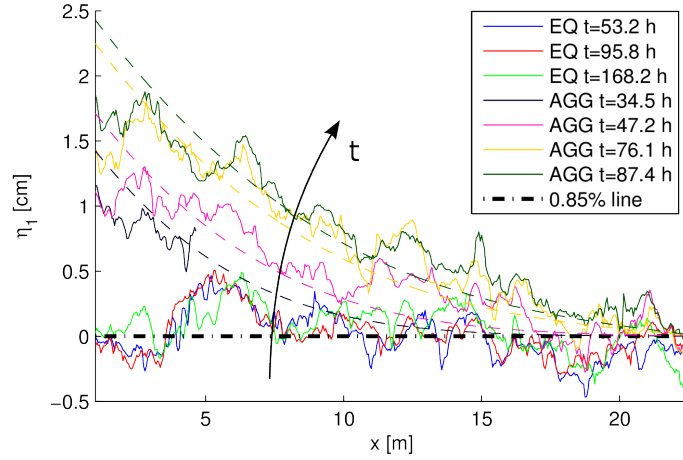


Figure 5.8: Bed level profiles during *Run 2* and analytical solution of the linear model.

the sediment transport measured at the flume outlet. For instance the time needed for a change equal to 10 % the long-term variation is $t^* \simeq 0.18$; in dimensional terms (Eq. 5.23) this correspond, for the *Exp 1*, to $t \simeq 100 h$. Unfortunately the intrinsic variability of the solid discharge which is typical of a braided system (Ashmore, 1988; Warburton and Davies, 1994) makes it difficult to appreciate a variation of the mean bedload transport. Similarly, because of the fluctuations of the local bed slope which can be observed even in an equilibrium experiment, it is problematic to study the initial phase of the profile evolution. Only in the case of relatively smooth variations we can rely on a single experimental outcome, simply performing a spatial average of the quantities. This is the most important reason for which it is difficult to calibrate the constant a of the hyperbolic model.

In our view this is not merely an annoying complication but a fundamental aspect of the analysis of the complex morphology rivers in unsteady condition; in order to face this problem we should adopt a statistical approach, performing a series of identically repeated experiment which would allow to build an ensemble statistics.

Despite this limits, the evolution of the profiles suggests on one hand that a correction of the diffusive model is necessary if we are interested in the initial development and, on the other hand, that the effect is relatively small in the long-term dynamics of the bed level profile. A value $a^* \simeq 0.2$ seems to produce the best matching between model predictions and observations, while we can exclude $a^* > 0.3 \div 0.5$ which would lead to a significantly different evolution. This rough estimation of the morphological disequilibrium furnishes an idea of which conditions allows to study the process through the simple diffusive scheme.

It is worth to underline that the results can significantly vary if further

ingredients are added to the system; for example it is clear that the presence of vegetation, poorly sorted and cohesive the bed material, can strongly affect the river morphodynamics and significantly weaken the incision process.

Further study is also needed to investigate the role of the discharge variability; we expect that the diffusive model can still be adopted if $T \gg T_E$ and $T \gg T_{flood}$ (the latter indicating the timescale of the discharge variations) while a more complex interaction between the different processes is expected if the three temporal scales are similar.

5.3 Conclusions

The diffusive model has been applied for a braided network formed by well sorted cohesiveless bed material and confined between uniformly distant banks.

This choice is motivated by the fact that simple formulation, which was extensively adopted, with variable success, for single-thread rivers, is more appropriate for steep and shallow channels typical of gravel-bed braided networks.

We have seen that in the case of a braided river, due to the relatively smooth dependence of bedload to the stream power, a linear model seems to be appropriate for many applications.

The introduction of a more complete formulation enables to investigate the potential effect of the local non-equilibrium of the braided morphology on the evolution of the bed profiles; our analysis shows that the diffusive model is valid in the limit of slow variation of the bed level elevation.

The simple model seems to capture the evolution of the bed level profile for the two laboratory experiments we performed. However, in order to asses in more details which are the limitation of the diffusive scheme further experiments would be needed.

A direct outcome of the diffusive model we propose is that the temporal scale of the evolution of bed level profiles, T , is proportional to the square of the length scale L and therefore differs from the temporal scale of the local morphological evolution T_E , which is independent of the length L .

5.4. List of symbols and acronyms

5.4 List of symbols and acronyms

Acronyms

BC	Boundary condition;
IC	Initial condition;
\mathcal{L}	Laplace transform;
PDE	Partial differential equation;

Symbols

*		Dimensionless quantity;
$\hat{}$		Laplace transform;
0		Reference state;
1		Variation with respect to the reference state;
Δ	[–]	Variation;
\bar{a}, a^*	[–]	Coefficient of non-equilibrium bedload;
b^*	[–]	Coefficient of the elevation-bedload relation;
c	[–]	Chézy coefficient;
c_D	[–]	Variation of the Chézy coefficient with the water depth;
D	[l]	Water depth;
\mathcal{F}	[–]	Transport function for a braided network;
\mathcal{F}_S	[–]	Variation of sediment transport with the slope;
Fr	[–]	Froude number;
d_s	[l]	Sediment size;
g	[lt^{-2}]	Gravity acceleration;
G	[–]	Memory function;
H	[l]	Vertical length scale;
k	[l^2s^{-1}]	Diffusion coefficient;
L	[lt^{-2}]	Horizontal length scale;
L_c	[l]	Channel length;
p	[–]	Porosity of the bed material;
t	[t]	Time;
T	[t]	Scaling time;
T_M	[t]	Time scale of the memory function;
q	[l^2t^{-1}]	Liquid discharge per unit width;
Q	[l^3t^{-1}]	Liquid discharge;
qs	[l^2t^{-1}]	Solid discharge per unit width;
Q_s	[l^3t^{-1}]	Solid discharge;
s^*	[–]	Laplace variable;
S	[–]	Slope;
U	[l]	Depth averaged velocity;
W	[l]	Channel width;
x	[l]	Longitudinal coordinate;
y	[l]	Transverse coordinate;
γ	[–]	Exponent of the bedload power-law formula;
Δ	[–]	Relative submerged density of sediment;
η	[l]	Transverse mean of the bottom elevation;

5.4. *List of symbols and acronyms*

Φ	[–]	Dimensionless solid discharge;
Φ_T	[–]	Variation of the solid discharge with the Shields stress;
θ	[–]	Shields parameter;

5.5 Appendix

5.5.1 1D models for single-thread rivers

In this section we will derive the diffusive (parabolic) and the hyperbolic 1d models for single-thread channels. The resulting *PDE* have the same structure of the differential equation we derived for a braided network (Eq. 5.10, 5.47, 5.47) and can be solved in a general way through the analytical treatment we propose in the following sections 5.5.2 and 5.5.2.

The diffusive model

Let us consider a cylindrical rectangular bed channel with uniform sediment subject to constant discharge Q .

For a given initial bed profile $\eta_0(x)$ and sediment supply $Qs(t)$ we can predict the evolution by solving numerically the one-dimensional shallow water and Exner model with a closure for the solid discharge which in the case of dominant bedload transport is typically expressed as

$$qs = \sqrt{g\Delta d_s^3} \Phi(\theta) \quad (5.24)$$

If the curvature of the bed profile is relatively small, as specified by Eq.5.1, we can assume that the local hydraulic conditions depend only on the local slope and discharge and can be computed through an uniform flow formula. Following this approach Vreugdenhil and de Vries (1973) proposed a diffusive model for predicting the bed evolution; indeed the Shields stress in uniform flow conditions can be expressed as

$$\theta = \frac{SD}{\Delta d_s} = \frac{S}{\Delta d_s} \left(\frac{q}{k_s \sqrt{S}} \right)^{3/5} \quad (5.25)$$

substituting Eq. 5.25 into the Exner equation gives

$$\frac{(1-p)}{\sqrt{g\Delta d_s^3}} \frac{\partial \eta}{\partial t} + \frac{\partial \Phi}{\partial x} = \frac{(1-p)}{\sqrt{g\Delta d_s^3}} \frac{\partial \eta}{\partial t} + \frac{\partial \Phi}{\partial \theta} \frac{\partial \theta}{\partial x} = 0 \quad (5.26)$$

considering the uniform flow relationship of Eq. 5.24 we have

$$\frac{(1-p)}{\sqrt{g\Delta d_s^3}} \frac{\partial \eta}{\partial t} + \frac{\partial \Phi}{\partial \theta} \frac{7}{10} \frac{\theta}{S} \frac{\partial S}{\partial x} = 0 \quad (5.27)$$

Remembering the definition of slope we obtain

$$\frac{\partial \eta}{\partial t} + k \frac{\partial^2 \eta}{\partial x^2} = 0 \quad (5.28)$$

which represent a diffusion equation whose coefficient is

$$k = \frac{7}{10} \frac{\partial \Phi}{\partial \theta} \frac{\theta}{S} \frac{\sqrt{g \Delta d_s^3}}{(1-p)} \quad (5.29)$$

Since the coefficient k depends on S and consequently on the solution and Eq. 5.28 is nonlinear.

The linear hyperbolic model

In this section we derived an hyperbolic model for the evolution of the bottom profile in a rectangular channel according to the 1D shallow water model. This approach (Zhang and Kahawita, 1990) allows to determine which is the relative importance of the different terms and in particular the conditions in which the simple diffusive model is valid.

Let us consider a small perturbation of the flow with respect to a steady-state condition (uniform flow).

If we neglect the local acceleration term in the momentum equation we can write the linearized for of the shallow water equations as

$$\begin{cases} \frac{\partial U_1^*}{\partial x^*} + \frac{1}{Fr^2} \frac{\partial(D_1^* + \eta_1^*)}{\partial x^*} + \frac{2}{c_0^2} \frac{L}{D} [U_1^* - D_1^* (1 + c_D)] = 0 \\ \frac{\partial D_1^*}{\partial x^*} + \frac{\partial U_1^*}{\partial x^*} = 0 \\ \frac{\partial \eta_1^*}{\partial t^*} + 2\Phi_T \frac{\partial U_1^*}{\partial x^*} - 2\Phi_T c_D \frac{\partial D_1^*}{\partial x^*} = 0 \end{cases} \quad (5.30)$$

where the quantities are made dimensionless by considering a longitudinal scale L , a vertical scale D and the Exner time scale. Φ_T represents the variation of the bedload with the Shields stress whereas c_D the variations of the Chèzy coefficients with the relative roughness

Substituting the water continuity into the momentum and Exner equations gives

$$\begin{cases} \left(1 - \frac{1}{Fr^2}\right) \frac{\partial U_1^*}{\partial x^*} + \frac{1}{Fr^2} \frac{\partial \eta_1^*}{\partial x^*} \\ + \frac{2}{c_0^2} \frac{L}{D} [U_1^* - D_1^* (1 + c_D)] = 0 \\ \frac{\partial \eta_1^*}{\partial t^*} + a_1 \frac{\partial U_1^*}{\partial x^*} = 0 \end{cases} \quad (5.31)$$

where for notation compactness we defined

$$a_1 := 2\Phi_T (1 + c_D) \quad (5.32)$$

Moreover, if we insert the Exner into the momentum equation and compute the x derivative we get

$$-\frac{1}{a_1} \left(1 - \frac{1}{Fr^2}\right) \frac{\partial^2 \eta_1^*}{\partial x^* \partial t^*} + \frac{1}{Fr^2} \frac{\partial^2 \eta_1^*}{\partial x^{2*}} + \frac{2}{c_0^2} \frac{L}{D} (2 + c_D) \frac{\partial U_1^*}{\partial x^*} = 0 \quad (5.33)$$

5.5. Appendix

which, if substituted into the Exner formula gives

$$\frac{\partial \eta_1^*}{\partial t^*} + \frac{1}{b_1} \left(1 - \frac{1}{Fr^2}\right) \frac{\partial^2 \eta_1^*}{\partial x^* \partial t^*} - \frac{a_1}{b_1} \frac{1}{Fr^2} \frac{\partial^2 \eta_1^*}{\partial x^{*2}} = 0 \quad (5.34)$$

where

$$b_1 := \frac{2}{c_0^2} \frac{L}{D} (2 + c_D) \quad (5.35)$$

The resulting Eq. 5.34 represent an hyperbolic *PDE* having the same structure of Eq. 5.34.

If we consider the following uniform flow relation

$$Fr^2 = c_0^2 S_0 \quad (5.36)$$

we can write the coefficient of the mixed derivative as

$$a^* = -\frac{1}{b_1} \left(1 - \frac{1}{Fr^2}\right) = -\frac{1}{2(2 + c_D)} \frac{D}{S_0 L} (Fr^2 - 1) \quad (5.37)$$

For a given length of the process L this coefficient becomes small for steep and shallow channels, and if the condition Eq. 5.1 is fulfilled we obtain the linear diffusive model.

5.5.2 Solution of the diffusive model

In this section we derive, following a well-known approach, a solution in Fourier series of the linear diffusion equation with appropriate initial and boundary conditions.

In particular let us consider the following *PDE* of Eq. 5.10

$$\frac{\partial \eta_1^*}{\partial t^*} - \frac{\partial^2 \eta_1^*}{\partial x^{*2}} = 0 \quad (5.38)$$

with the initial and boundary conditions

$$\begin{cases} \eta_1^*(x, 0) = 0 & IC \\ \frac{\partial \eta_1^*(0, t)}{\partial x^*} = -\frac{\Delta q s^*}{\mathcal{F}_0 \mathcal{F}_S} = -\frac{\Delta S}{S_0} & BC1 \\ \eta^*(L_c^*, t^*) = 0 & BC2 \end{cases} \quad (5.39)$$

It is easy to prove that the solution of this problem can be expressed as

$$\eta_1^*(x^*, t^*) = \frac{\Delta S}{S_0} \left(1 - \frac{x^*}{L_c^*} - z(x^*, t^*)\right) \quad (5.40)$$

where $z(x, t)$ is the solution of the same differential Eq. 5.10 but with homogeneous (i.e. zero) *BC* and the following *IC*

$$z(x^*, 0) = 1 - \frac{x^*}{L_c^*} \quad (5.41)$$

The function $z(x^*, t^*)$ can be found by considering that the triangular *IC* of Eq. 5.41 can be decomposed in Fourier cosine series as follows

$$z(x^*, 0) = \sum_{j=0}^{\infty} \frac{8}{m^2 \pi^2} \cos\left(\frac{m\pi x^*}{2L_c^*}\right) \quad m := 2j + 1 \quad (5.42)$$

It is not difficult to verify the problem with homogeneous *BC* and cosinusoidal *IC* is

$$z_m(x^*, t^*) = \cos\left(\frac{m\pi x^*}{2L_c^*}\right) \exp\left(-\frac{m^2 \pi^2}{4L_c^{*2}} k^* t^*\right) \quad (5.43)$$

Due to the linearity of Eq. 5.10 it is possible to combine Eq 5.43 and Eq. 5.42 obtaining the following solution for the triangular *IC*

$$z(x^*, t^*) = \sum_{j=0}^{\infty} \frac{8}{m^2 \pi^2} \cos\left(\frac{m\pi x^*}{2L_c^*}\right) \exp\left(-\frac{m^2 \pi^2}{4L_c^{*2}} k^* t^*\right) \quad (5.44)$$

$$m := 2j + 1$$

In the case $L_c \rightarrow \infty$ (semi-infinite domain) the solution of the linear diffusion equation becomes

$$\eta_1(x^*, t^*) = 2 \frac{\Delta S}{S_0} \left[\sqrt{\frac{k^* t^*}{\pi}} e^{-\frac{x^{*2}}{4k^* t^*}} - \frac{x^*}{2} \operatorname{erfc}\left(\frac{x^*}{\sqrt{4k^* t^*}}\right) \right] \quad (5.45)$$

if we compute the spatial derivative

$$\frac{\partial \eta_1^*}{\partial x^*}(x^*, t^*) = -\frac{\Delta S}{S_0} \operatorname{erfc}\left(\frac{x^*}{\sqrt{4k^* t^*}}\right) \quad (5.46)$$

we obtain the evolution of the slope and consequently of the bedload.

5.5.3 Solution of the linear hyperbolic model

In this section we derive a solution of the non-diffusive model by adopting the method of the Laplace transform. In particular we will find the analytic solution in the Laplace space, which can be inverted (in general through numerical integration) in order to find the evolution in time.

In particular we consider the following *PDE*

$$\frac{\partial \eta^*}{\partial t^*} - k^* \frac{\partial^2 \eta^*}{\partial x^{*2}} - a^* \int_0^{\infty} G(\tau^*) \frac{\partial^2 \eta^*}{\partial x^* \partial t^*}(t^* - \tau^*) d\tau^* = 0 \quad (5.47)$$

which represents a generalisation of Eq. 5.47, 5.15 and 5.34.

In addition we specify the initial and boundary conditions

$$\begin{cases} \eta_1^*(x^*, 0) = 0 & IC \\ \frac{\partial \eta_1^*}{\partial x^*}(0, t^*) + \frac{a^*}{k^*} \int_0^{\infty} G(\tau^*) \frac{\partial \eta^*}{\partial t^*}(t^* - \tau^*) d\tau^* = -\frac{\Delta q s^*(t)}{\mathcal{F}_0 \mathcal{F}_S} & BC1 \\ \eta_1^*(L_c^*, t^*) = \Delta \eta^*(t) & BC2 \end{cases} \quad (5.48)$$

5.5. Appendix

which represent an initially unperturbed profile subject to a (time dependent) variation of both the sediment supply (Δqs^*) and the downstream bottom elevation ($\Delta\eta^*$).

The Laplace transform (in time) of the independent variable η_1^* is defined as

$$\hat{\eta}_1^*(x^*, s^*) = \mathcal{L}[\eta_1^*(x^*, t^*)] = \int_0^\infty \eta(x^*, t^*) e^{s^* t^*} dt^* \quad (5.49)$$

Since in the linear model $k^* = cost$ and $a^* = const$ we can solve Eq. 5.47 by considering its Laplace transform

$$-k^* \frac{\partial^2 \hat{\eta}_1^*}{\partial x^{*2}} - a^* \mathcal{L}(G) s^* \frac{\partial \hat{\eta}_1^*}{\partial x^*} + s^* \hat{\eta}_1^* = 0 \quad (5.50)$$

where the Laplace transform of the function $G(\tau^*)$ (Eq. 5.18) reads

$$\mathcal{L}(G) = \frac{1}{1 + s^* T_M^*} \quad (5.51)$$

It is worth to notice that, in the limit case $T_M = 0$ the latter equation gives $\mathcal{L}(G) = 1$; in this case $G(\tau^*)$ is a Dirac distribution and Eq. 5.50 represent the Laplace transform of the memoryless hyperbolic model of both Eq. 5.15 and Eq. 5.34.

The general solution of the ordinary differential equation 5.50 can be expressed as

$$\hat{\eta}_1^*(x^*, s^*) = c_1 e^{\lambda_1(s^*)x^*} + c_2 e^{\lambda_2(s^*)x^*} \quad (5.52)$$

where the coefficients $\lambda_{1/2}$ can be computed as the root of the characteristic polynomial

$$\lambda_{1/2} = \frac{1}{2k^*} \left[a^* s^* \mathcal{L}(G) \pm \sqrt{a^{*2} s^{*2} \mathcal{L}^2(G) - 4k^* s^*} \right] \quad (5.53)$$

Although a more general function can be easily implemented let us consider, for the sake of notation simplicity, a stepwise variation of both Δqs^* and $\Delta\eta^*$ at $t^* = 0$; under this assumption the boundary conditions of Eq. 5.48 can be written in term of Laplace transform as

$$\begin{aligned} \frac{\partial \hat{\eta}_1^*}{\partial x^*}(0, s^*) + \frac{a^*}{k^*} \mathcal{L}(G) s^* \hat{\eta}_1^*(0, s^*) &= -\frac{1}{s^*} \frac{\Delta qs^*}{\mathcal{F}_0 \mathcal{F}_S} \\ \hat{\eta}_1^*(L_c^*, s^*) &= \frac{\Delta\eta^*}{s^*} \end{aligned} \quad (5.54)$$

if we substitute Eq. 5.52 we can fix the constants (in x) c_1 and c_2 .

$$\begin{aligned} c_2 &= -c_1 e^{(\lambda_1 - \lambda_2)L_c^*} - \frac{\Delta\eta}{s} e^{-\lambda_2 L_c^*} \\ c_1 &= \frac{-\frac{1}{s^*} \frac{\Delta qs^*}{\mathcal{F}_0 \mathcal{F}_S} + \frac{\Delta\eta}{s^*} e^{-\lambda_2 L_c^*} \left(\lambda_2 + \frac{a^*}{k^*} \mathcal{L}(G) s \right)}{\left(\lambda_1 - \lambda_2 e^{(\lambda_1 - \lambda_2)L_c^*} \right) + \frac{a^*}{k^*} \mathcal{L}(G) s^* \left(1 - e^{(\lambda_1 - \lambda_2)L_c^*} \right)} \end{aligned} \quad (5.55)$$

obtaining the particular solution in the Laplace space $\hat{\eta}_1^*(x^*, s^*)$. The solution in the time domain $\eta_1(x, t)$, can be found by computing for each point x , the numerical inverse of the Laplace transform.

In the case of a semi-infinite domain and a memoryless process ($\mathcal{L}(G) = 1$) an analytical solution can be found, in terms of Bessel functions, following the approach of Gill (1988).

If we define $b^* = a^*/T_M^*$ and we consider $T_M^* \rightarrow \infty$ (linear transport-storage model) Eq.5.51 becomes

$$a^* \mathcal{L}(G) = b^* \tag{5.56}$$

and we can use the solution in the Laplace transform to predict the degradation of a poorly-sorted gravel-bed river according to the model of Lisle and Church (2002).

5.5.4 Analysis of the hyperbolic model

In this section we study, through several examples, the behaviour of the linear hyperbolic model represented by the solution of Eq. 5.52.

If a^* tends to zero Eq. 5.47 represents the diffusive model whose solution is reported in the case of a finite ($L_c^* = 1$) and infinite domains in figure 5.9).

Eq. 5.52 allows also for studying the diffusive process in the case of a sudden downstream bed level lowering, as reported in figure 5.10 for the case of a constant sediment supply.

The model response is much different if $a \neq 0$ (figure 5.11). In particular if $a^* < 0$ (super-critical conditions in of Eq. 5.34) the non-local effects cause a smoother solution. This behaviour is related to the well-known properties of super-critical currents to propagate downstream the information, so that the sediment transport depends on the upstream slope. Conversely if $a^* > 0$ (sub-critical flow in Eq. 5.34) the information travels upstream and a discontinuity occurs (see Gill (1988) for a fully-analytical treatment of this case).

As one may expect the memory of the recent history ($T_m > 0$) causes a smoothing effect which is more evident in the discontinuous case $a^* > 0$ (dashed lines of figure 5.11).

In the case of Eq. the mathematical nature of the model changes completely; indeed we have in this case an advection-diffusion model with unitary diffusion coefficient and advection speed $-b^*$. As clear in both the panels of figure 5.12 the diffusion progress with time, producing a smoother and smoother front which widens with $\sqrt{t^*}$. However, since the advection speed is $(-b^*t^*)$ the diffusion length becomes smaller if compared with the front travel; for this reason, the front appears to be steeper on the left panel even though the elapsed time is significantly higher than in the left plots.

5.5. Appendix

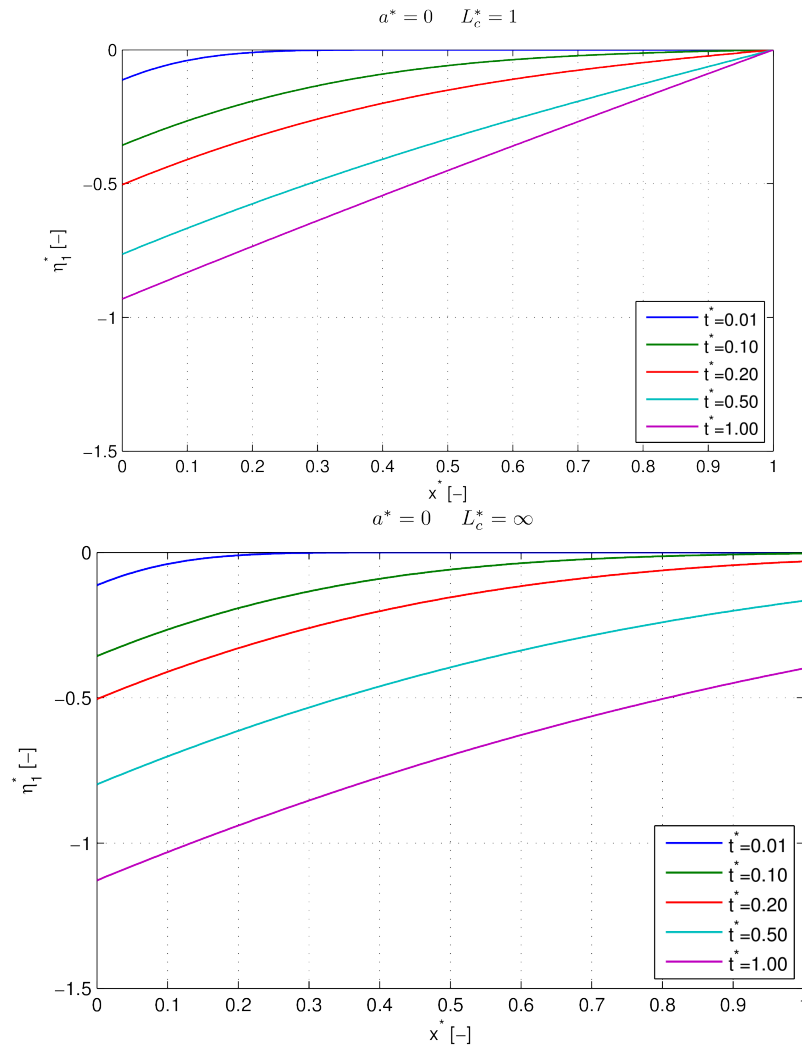


Figure 5.9: Evolution of the bottom level profile according to the diffusive model. Upper panel: finite domain; lower panel: infinite domain

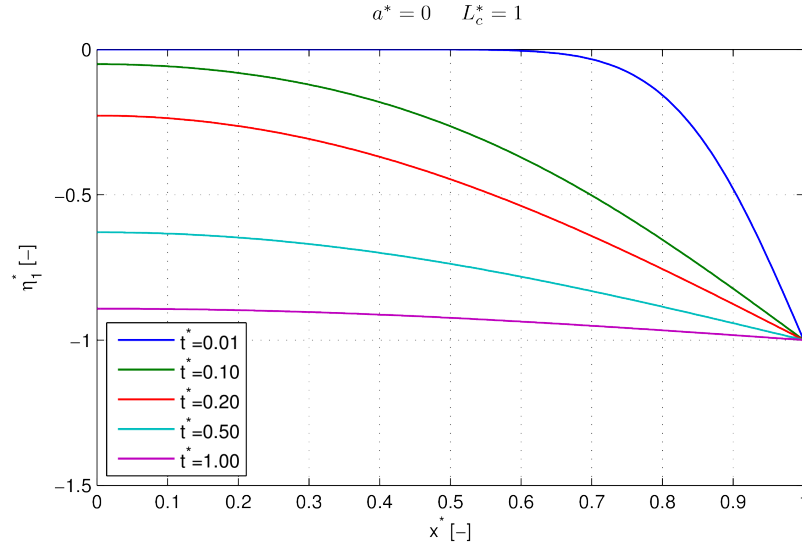


Figure 5.10: Evolution of the bottom level profile according to the diffusive model in the case of a sudden bed level lowering at the downstream boundary.

5.5.5 A statistical approach

In the previous analysis we treated all the quantities in a deterministic way; however it is clear that the local evolution is actually unpredictable and can be interpreted as a random process. Although in practice we can forget the random fluctuation by considering spatial/temporal averages this is not always possible. For this reason it is important, at least from a conceptual point of view, to consider the problem in a statistical way as briefly discussed in the present section.

Due to the complex nature of the braiding dynamics the local evolution is unpredictable and local observations in (almost) identical experiments can be completely different. In the case of a statistically stationary (or slowly variable) configuration this fundamental problem can be partially avoided by studying the reach-averaged or the time-average properties which. Indeed if the spatial/temporal domain is sufficiently long we expect that the averages are not a mere random result but deterministic values which are approximately equal in repeated experiments.

As we mentioned in the discussion section this is not possible if we want to study processes which changes relatively fast in time and space. In order to understand the reason let us consider the example of the solid discharge and denote with $\langle \cdot \rangle$ the ensemble mean operator so that $\langle Qs(x, t) \rangle$ is the solid discharge we would ideally obtain as an average over a large number of experiments repeated under identical conditions.

If a braided network is in dynamical equilibrium we can assume a stationary

5.5. Appendix

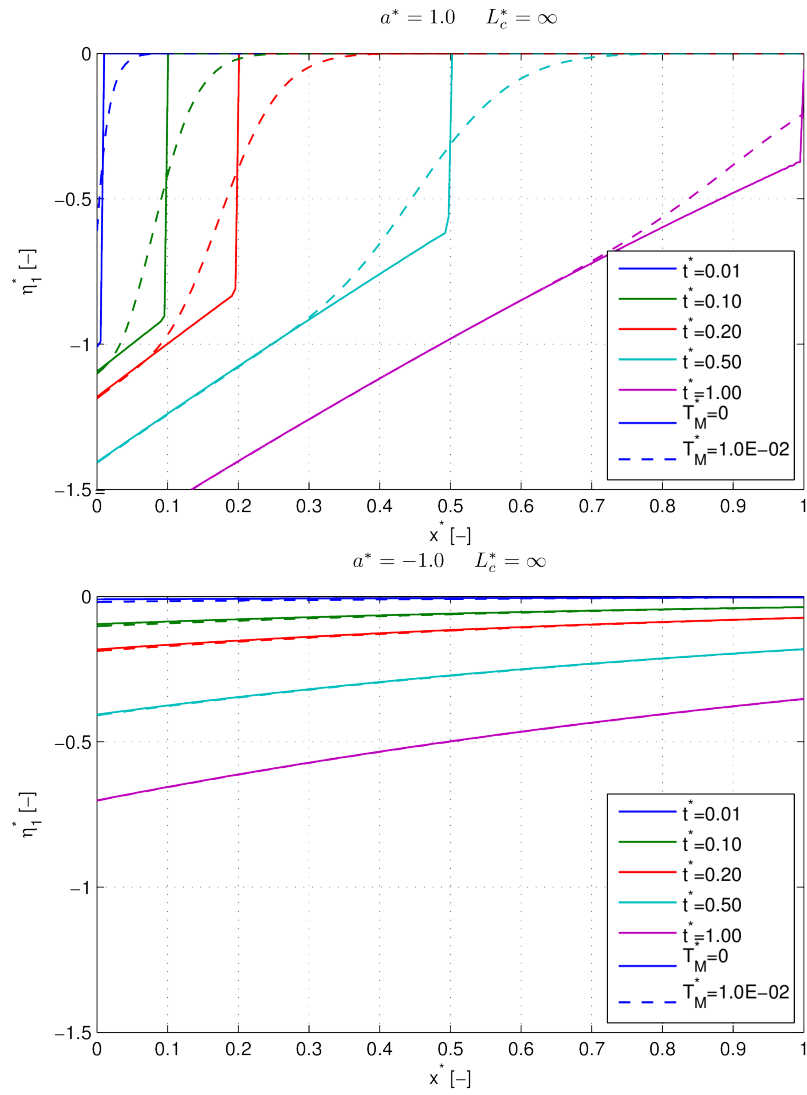


Figure 5.11: Evolution of the bottom level profile according to the hyperbolic model in the case of semi-infinite domain. Upper panel: positive unsteady effect. Lower panel: negative unsteady effect. Continuous line: $T_M^* = 0$; dashed line: $T_M^* = 1 \cdot 10^{-2} a^*$.

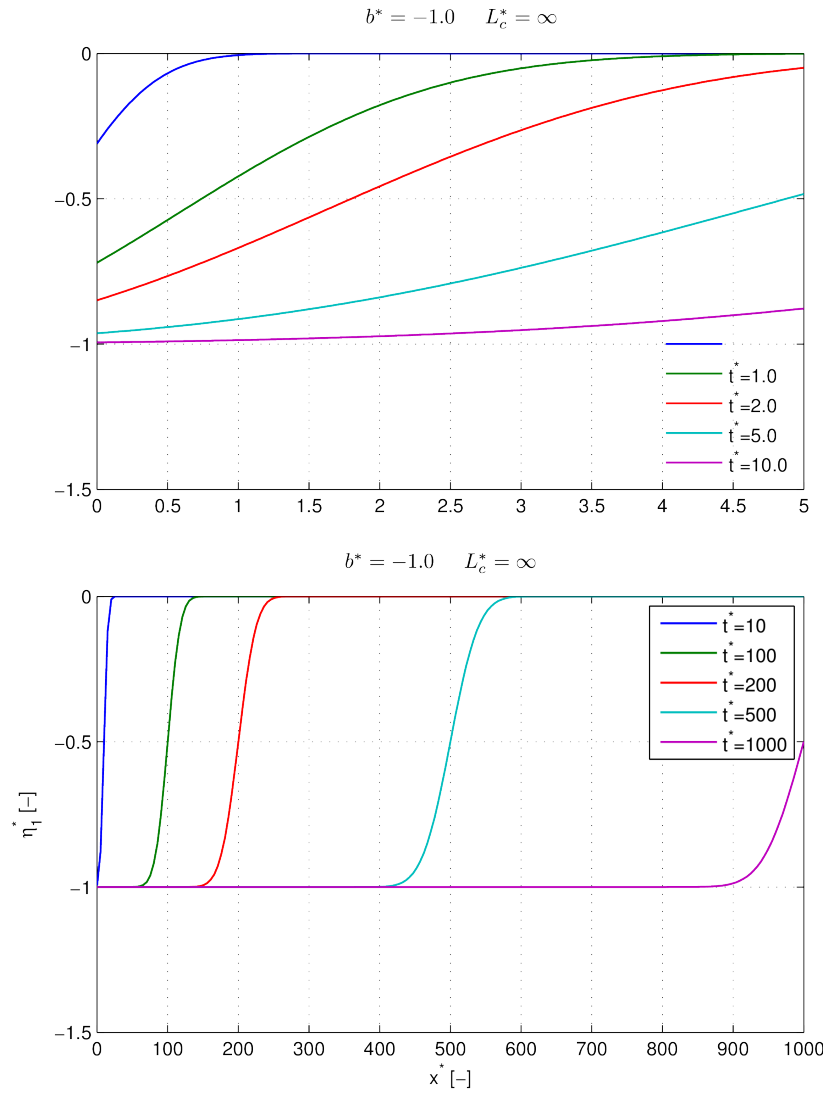


Figure 5.12: Evolution of the bottom level profile according to the volume-storage model in the case of semi-infinite domain. A unitary negative variation of $\Delta qs^*/|b^*|$ is considered. Upper panel: evolution at the unitary scale, at which the diffusion and the storage processes have the same magnitude. Lower panel: solution on a larger scale, for which the importance of the diffusion is smaller.

5.5. Appendix

process; in this case $\langle Qs(x, t) \rangle$ is constant and can be estimated as a temporal average computed over a sufficiently long period of time.

If, on the other hand, the process is not stationary ($\langle Qs \rangle$ varying in time) we can not estimate it as a temporal average; indeed if we chose a relatively long averaging period we lose the $\langle Qs(x, t) \rangle$ variability whereas if the averaging time is smaller it is not possible to filter out the random fluctuations. In this we must consider the variables η , Qs , S as ensemble averages, which are in general different from the averages of the single experiment.

Example: A real-scale application

The present work suggests that the propagation of an erosion or deposition wave in a confined braided network is proportional to the square of the distance; so that it can be relatively slow. Let us try to quantify the associated time scale in the case of a 50 m wide river with fixed banks and uniform grain size $ds = 50 \text{ mm}$ (50 times bigger than our flume) and $S = 1\%$.

If we call L_R and T_R the ratio between the geometric and temporal scale between the prototype (the study river) and our laboratory model we can assume a Froude similarity between systems having different scales; in particular, since the gravity acceleration g is constant the Froude scaling fixes the following relation

$$T_R = \sqrt{L_R} \quad (5.57)$$

Consequently mere dimensional considerations allows to calculate diffusion coefficient of the prototype as

$$k_{prot} = k \frac{L_R^2}{T_R} = k L_R^{3/2} = 300 \left[\frac{m^2}{h} \right] \quad (5.58)$$

and the water discharge as

$$Q_{prot} = Q \frac{L_R^3}{T_R} = Q L_R^{5/2} = 35 \left[\frac{m^3}{s} \right] \quad (5.59)$$

so that our laboratory experiments are representative of the river with a discharge $Q = 35 \text{ m}^3\text{s}^{-1}$.

From figure 5.13 (green line) we can see that a variation of the bedload transport equal to the 50 % of the long-term value requires $t^* \simeq 1$; this means that the time needed to have such a variation at a distance of $L = 1 \text{ km}$ is

$$t_{prot} = t^* \frac{L^2}{k} = 1 \cdot \frac{(10^3 [m])^2}{300 \left[\frac{m^2}{h} \right]} = 3.3 \cdot 10^3 [h] = 140 [d] \quad (5.60)$$

this time is significantly higher than what we expect for narrower single-thread rivers; for instance the equilibrium specific solid discharge we measured in the

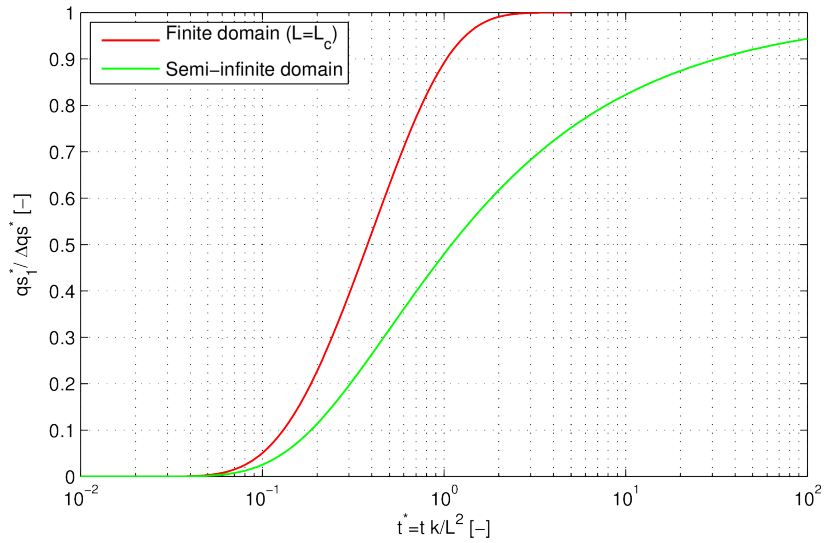


Figure 5.13: Variation through time of the solid discharge at $x = L$ in a semi-infinite channel for an instantaneous unitary variation of the input solid discharge Δq_s^* .

same flume with a distance between banks $W = 0.15 \text{ m}$ (corresponding to $W = 7.5 \text{ m}$ in the prototype) is approximately 22.5 bigger, which leads to an evolution 22.5 times faster.

Although these calculation are strictly valid only in the hypothetical values they are useful to have an idea of which are the time scales and how they change in different conditions.

5.5. *Appendix*

Chapter 6

Analytical solution for a small obstacle in a gravel-bed channel

6.1 Introduction

According to the theory of morphodynamic influence (Zolezzi and Seminara, 2001) the dominant direction of propagation of steady two-dimensional perturbations depends upon the local channel conditions; in particular Blondeaux and Seminara (1985) defined the so-called resonant aspect ratio, which can be calculated as a function of the Shields stress and relative submergence. If the aspect ratio of the channel is higher than the resonant value (super-resonant conditions) an upstream influence occurs, while in the narrower (sub-resonant) case the two-dimensional morphological effects propagate only in the downstream direction. This morphodynamic influence appears as a sequence of nonmigrating alternate bars, whose wavelength and damping rate do not depend on the specific nature of the forcing effect but on the channel conditions in terms of flow and aspect ratio. An experimental support to these theoretical findings has been provided by Zolezzi et al. (2005), who have shown the upstream influence produced, in super-resonant conditions, by a 180° curve connecting two straight channels.

Formation of nonmigrating bars downstream an obstacle which locally restricts the section has been noticed by different studies (e.g. Struiksma and Crosato, 1989; Crosato et al., 2011) whereas, consistently with the (Zolezzi and Seminara, 2001) theory, the development of steady bars upstream the obstacle have been observed, under super-resonant conditions, by the numerical experiments of Siviglia et al. (2013).

Numerical models of river morphodynamics provide a fully nonlinear description of the evolution through time. On the other hand analytical theories

6.2. Formulation of the model

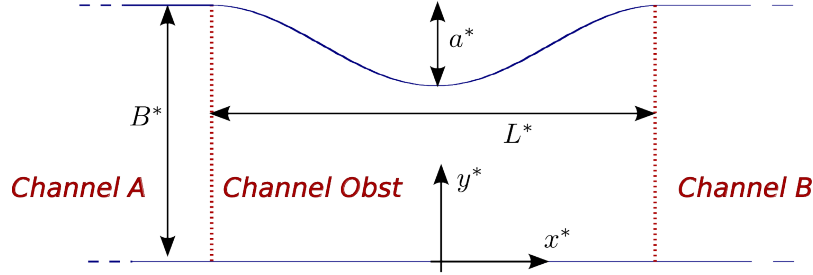


Figure 6.1: Sketch of the planimetric configuration.

based on perturbation approaches, despite being limited to a small range of parameters, allow for a complete control of the solution, which often leads to a better understanding of the mechanical processes underlying the observed morphological response.

For modelling the morphological effect of a localised restriction of a gravel-bed channel no analytical solutions exist in the literature. Aim of this work is to fill this gap by deriving a solution for a small sinusoidal obstacle; in addition we intend to study the effect of different hydraulic conditions, the role of secondary circulations and the impact of the presence of different boundary conditions.

The analytical derivation follows a perturbation approach, starting from the work of Repetto et al. (2002), who solved the linear problem for the case of a periodic variation of the channel width. The study is completed with the analysis of the boundary conditions required by the time-dependent model and with the direct comparison between the linear solution and numerical simulations obtained with the *Delft3D* numerical model.

6.2 Formulation of the model

We refer to an infinitely-long, rectangular channel of width B^* with a small, sinusoidal-shape, obstacle of amplitude a^* and length L^* (see figure 6.1), frictionless walls and well-sorted bed material with median grain size d_s^* . We placed the origin of the cartesian system of reference (x^*, y^*) at the right bank, in correspondence to the narrower section. We adopted a two-dimensional, mobile-bed, depth-averaged shallow water model, with the Engelund and Fredsoe (1982) formula for flow resistance, the Parker (1990) closure for the bed load intensity and the Ikeda (1981) relation for the effect of bottom slope on the direction of the sediment flux (i.e. Colombini et al., 1987; Crosato et al., 2011; Siviglia et al., 2013).

This model can be written as a nonlinear differential system of four equations in the four dependent variables η^*, U^*, V^*, D^* (bottom elevation, longitudinal and transverse velocity and water depth respectively, see figures 6.1 and 6.2) in the three independent variables x^*, y^*, t^* , the latter indicating the time.

6.2. Formulation of the model

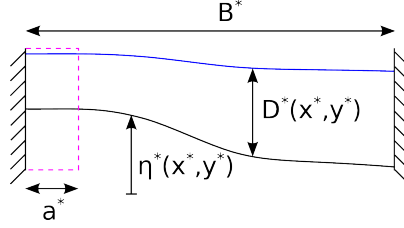


Figure 6.2: Sketch of the notation. The dashed magenta line represents the obstacle at $x = 0$.

These quantities can be made dimensionless as follows

$$\begin{cases} \{x, y\} := \frac{\{x^*, y^*\}}{B^*} \\ \{U, V\} := \frac{\{U^*, V^*\}}{U_0^*} \\ D := \frac{D^*}{D_0^*} \quad \eta := \frac{\eta^*}{D_0^*} \quad t := \frac{t^*}{T^*} \end{cases} \quad (6.1)$$

where ρ is the water density, B^* is the channel width, U_0^* , D_0^* , qs_0^* are the reference values of velocity, depth and specific solid discharge, which are assumed equal to the uniform flow conditions in the straight ($a = 0$) channel.

In addition we need to define the dimensionless values of the stress vector $\{\tau_x^*, \tau_y^*\}$, the unit bedload vector $\{qs_x^*, qs_y^*\}$ and the representative grain size d_s^* , namely

$$\{\tau_x, \tau_y\} := \frac{\{\tau_x^*, \tau_y^*\}}{\rho U_0^{*2}} \quad \{qs_x, qs_y\} := \frac{\{qs_x^*, qs_y^*\}}{qs_0^*} \quad d_s = \frac{d_s^*}{D_0^*} \quad (6.2)$$

Time is scaled using the Exner timescale, which is defined as

$$T^* := \frac{D_0^* B^* (1-p)}{qs_0^*} \quad (6.3)$$

where p is the porosity of the bed material.

The dimensionless position of the left bank, represented in figure 6.1, can be expressed as

$$\begin{cases} y^B = 1 & x < L/2 \\ y^B = 1 - \frac{a}{2} \left[1 + \cos\left(2\pi \frac{x}{L}\right) \right] & -L/2 < x < L/2 \\ y^B = 1 & x > L/2 \end{cases} \quad (6.4)$$

where $L = L^*/B^*$ and $a = a^*/B^*$ are the dimensionless obstacle length and amplitude respectively (figure 6.2).

6.2. Formulation of the model

The conservation of momentum, liquid and solid mass can be written in dimensionless form as

$$\begin{cases} T_w \beta \frac{\partial U}{\partial t} + U \frac{\partial U}{\partial x} + V \frac{\partial U}{\partial y} + \frac{1}{Fr_0^2} \frac{\partial}{\partial x} (\eta + D) + \beta \frac{\tau_x}{D} = 0 \\ T_w \beta \frac{\partial V}{\partial t} + U \frac{\partial V}{\partial x} + V \frac{\partial V}{\partial y} + \frac{1}{Fr_0^2} \frac{\partial}{\partial y} (\eta + D) + \beta \frac{\tau_y}{D} = 0 \\ T_w \beta \frac{\partial D}{\partial t} + \frac{\partial UD}{\partial x} + \frac{\partial VD}{\partial y} = 0 \\ \frac{\partial \eta}{\partial t} + \frac{\partial qs_x}{\partial x} + \frac{\partial qs_y}{\partial y} = 0 \end{cases} \quad (6.5)$$

where the reference Froude number and aspect ratio are given by

$$Fr_0 := \frac{U_0^*}{\sqrt{gD_0^*}} \quad \beta := \frac{B^*}{2D_0^*} \quad (6.6)$$

and the hydrodynamic timescale is defined as follows

$$T_w^* := D_0^*/U_0^* \quad T_w = T_w^*/T^* \quad (6.7)$$

The differential system of Eq. 6.5 needs closure equations (i.e. algebraic relations with the dependent variables) for the quantities τ_x , τ_y , qs_x , qs_y . The first two variables represent the bottom friction, whose magnitude can be estimated by the Chézy formula and the direction of the velocity vector, which leads to

$$\{\tau_x, \tau_y\} = \{U, V\} \frac{|\vec{U}|}{C^2} \quad (6.8)$$

where the dimensionless Chézy coefficient can be determined as (Engelund and Fredsoe, 1982)

$$C = 6 + 2.5 \log \left(\frac{D}{2.5 d_s} \right) \quad (6.9)$$

or alternatively, by adopting the Gauckler-Strickler formula (Strickler, 1923)

$$C = \frac{k_s}{\sqrt{g} d_s^{*1/6}} D^{1/6} = 6.74 D^{1/6} \quad (6.10)$$

Assuming, as common for gravel bed rivers, the bedload as the dominant form of sediment transport we can express the magnitude of the solid discharge as

$$|\vec{q}_s|^* = \Phi(\theta) \sqrt{g \Delta d_s^{*3}} \quad (6.11)$$

where Δ is the relative submerged weight of the sediment and the Shields parameter θ is defined as

$$\theta = \frac{\tau^*}{\rho g \Delta d_s^*} = Fr_0^2 \frac{|\vec{\tau}|}{\Delta d_s} \quad (6.12)$$

6.2. Formulation of the model

If we consider the bedload formula of Parker (1990) we can determine the function Φ as follows

$$\Phi(\theta) = 0.002181 G(\xi) \theta^{3/2} \quad (6.13)$$

where G is a function of $\xi := \theta/0.0386$, namely

$$\begin{cases} G(\xi) = \xi^{14.2} & \xi \leq 1 \\ G(\xi) = \exp [14.2(\xi - 1) - 9.28(\xi - 1)^2] & 1 < \xi \leq 1.59 \\ G(\xi) = 5474 \left(1 - \frac{0.853}{\xi}\right)^{4.5} & \xi > 1.59 \end{cases} \quad (6.14)$$

Remembering Eq. 6.1 the dimensionless sediment flux can thus be expressed as

$$|\vec{q}_s| = \frac{\Phi(\theta)}{\Phi_0} \quad \Phi_0 := \Phi(\theta_0) \quad (6.15)$$

The direction of the bedload can be estimated (Ikeda, 1981; Talmon et al., 1995) as a sum of two angles: the one formed by the velocity vector (with respect to the x-axis), given by

$$\gamma_q = \tan\left(\frac{V}{U}\right) \quad (6.16)$$

and the correction due to the bottom gradient in the direction \hat{n}_q orthogonal to the velocity vector, which can be expressed as

$$\gamma_g = -\frac{r}{\beta\sqrt{\theta}} \frac{\partial\eta}{\partial\hat{n}_q} \quad (6.17)$$

The two components of the solid discharge can be easily calculated as

$$\{qs_x, qs_y\} = \{\cos(\gamma_q + \gamma_g), \sin(\gamma_q + \gamma_g)\} \frac{\Phi(\theta)}{\Phi_0} \quad (6.18)$$

which completes the set of closure relations needed to complete the mathematical description of the differential system. For more details about the formulation see Colombini et al. (1987); Zolezzi and Seminara (2001).

Once the four closure relations are specified, we can complete the mathematical formulation by specifying the initial and boundary conditions.

The *BCs* at the two banks can be specified by considering impermeable walls, which implies the tangency of the solid discharge and velocity, namely

$$\begin{cases} qs_y(x, y^B) = qs_x(x, y^B) \frac{dy^B}{dx} & qs_y(x, 0) = 0 \\ V(x, y^B) = U(x, y^B) \frac{dy^B}{dx} & V(x, 0) = 0 \end{cases} \quad (6.19)$$

In addition, if we intend to model a channel of finite length, we must impose suitable conditions at the open boundaries; we will address this problem within sections 6.5.2 and 6.7.

6.3. The perturbation approach

6.3 The perturbation approach

In order to derive an analytical solution of this differential model we adopt a perturbation approach. For a straight ($a^* = 0$) channel a well-know solution is the simple uniform flow; if we consider this as a basic state and we expand the general solution in Taylor series for the parameter a we obtain

$$\begin{cases} \eta = -S_0\beta x + a \eta_1(x, y, t) + \mathcal{O}(a^2) \\ U = U_0 + a U_1(x, y, t) + \mathcal{O}(a^2) \\ V = V_0 + a V_1(x, y, t) + \mathcal{O}(a^2) \\ D = D_0 + a D_1(x, y, t) + \mathcal{O}(a^2) \end{cases} \quad (6.20)$$

where the subscripts $_0$ and $_1$ indicate the basic solution and the first order approximation respectively.

Without any loss of generality we can choose the scaling parameter U_0^* , D_0^* in order to have an uniform flow solution of the form

$$\{\eta_0, U_0, V_0, D_0\} = \{-S_0\beta x, 1, 0, 1\} \quad (6.21)$$

where S_0 is the bottom slope.

If we substitute this expansion into Eq. 6.5 we obtain the following uniform flow relations

$$\theta_0 = \frac{S_0}{\Delta d_s} \quad Fr_0^2 = S_0 C_0^2 \quad (6.22)$$

which allows an unique definition of the basic flow once that two independent parameters (usually θ_0 and d_s) are specified.

Let us consider a small obstacle (formally the limit of $a \rightarrow 0$); this enables to assume that the perturbation we introduce is small with respect to the basic, uniform flow. Consequently we can neglect the higher order terms $\mathcal{O}(a^2)$ which leads to a linear differential system in the variable a .

If we are interested in determining the (if any) steady state configuration we can neglect the time derivative of the variables and consider the stationary model. Consequently the mathematical nature of the differential problem changes and the knowledge of initial conditions is not needed.

If we substitute the expansion of Eq. 6.20 into the differential system of Eq. 6.5 and collect the terms the order $\mathcal{O}(a)$ we obtain the following linear system

$$\begin{cases} \frac{\partial U_1}{\partial x} + \frac{1}{Fr_0^2} \frac{\partial(D_1 + \eta_1)}{\partial x} + \frac{\beta}{C_0^2} [2U_1 - D_1(1 + C_D)] = 0 \\ \frac{\partial V_1}{\partial x} + \frac{1}{Fr_0^2} \frac{\partial(D_1 + \eta_1)}{\partial y} + \frac{\beta}{C_0^2} V_1 = 0 \\ \frac{\partial D_1}{\partial x} + \frac{\partial U_1}{\partial x} + \frac{\partial V_1}{\partial y} = 0 \\ \frac{\partial V_1}{\partial y} - \frac{r}{\beta\sqrt{\theta_0}} \frac{\partial^2 \eta_1}{\partial y^2} + 2\Phi_T \frac{\partial U_1}{\partial x} - 2\Phi_T C_D \frac{\partial D_1}{\partial x} = 0 \end{cases} \quad (6.23)$$

6.3. The perturbation approach

where we have defined the following coefficients

$$\Phi_T := \frac{\theta_0}{\Phi_0} \frac{\partial \Phi}{\partial \theta} \Big|_{\theta=\theta_0} \quad C_D := \frac{D_0}{C_0} \frac{\partial C}{\partial D} \Big|_{D=D_0} \quad (6.24)$$

which embody the dependence of bedload intensity and Chèzy coefficient on Shields stress and water depth respectively.

The analytical solution of Eq. 6.23 is not straightforward but requires a specific strategy that is briefly introduced here and developed in more details in the following sections. First of all, we divide the domain in three regions which, as sketched in figure 6.1 are defined as follows:

- channel A: upstream channel, from $x = -\infty$ to $x = -L/2$;
- channel Obst: region of the width variation, ranging from $x = -L/2$ to $x = +L/2$;
- channel B: downstream part, from $x = +L/2$ to $x = +\infty$.

Secondly, we write a general solution for each region. For the channels A and B it can be obtained by separating the variables and expressing the solution as a linear superposition of Fourier modes as in Zolezzi and Seminara (2001). For the central part, where the obstacle is placed, the solution is different due to the presence of a non-straight bank. From a linear point of view, it is possible to express the general solution as the sum of this particular result and the general solution for the straight channels (the same as in channels A and B); the particular solution can be found following Repetto et al. (2002), who tackled the problem of a channel with periodically varying width.

Finally, we can make the solutions compatible by imposing a matching of the four values at the boundaries we artificially introduced in order to separate the three regions.

In this way we obtain a unique solution expressed as a sum of a (theoretically infinite) number of Fourier components.

6.3.1 General solution for the straight channel A and B

Both the upstream and the downstream channels of figure 6.1 are straight and rectangular, thus admitting the steady two-dimensional solution described by Zolezzi and Seminara (2001).

Specifically, for each transverse Fourier mode $m \geq 1$, it is possible to find a solution of the linear problem which can be written as a sum of four complex

6.3. The perturbation approach

exponentials in x , namely

$$\left\{ \begin{array}{l} \{\eta_1, U_1, D_1\} = \cos(m\pi y) \sum_{j=1}^4 \{\hat{\eta}_{mj}, \hat{U}_{mj}, \hat{D}_{mj}\} \exp(\lambda_{mj}x) \\ V_1 = \sin(m\pi y) \sum_{j=1}^4 \hat{V}_{mj} \exp(\lambda_{mj}x) \end{array} \right. \quad (6.25)$$

The (complex) coefficients denoted with the *hat* (i.e. \hat{U}) are determined by the following relation

$$\{\hat{\eta}_{mj}, \hat{U}_{mj}, \hat{V}_{mj}, \hat{D}_{mj}\} = \tilde{\eta}_{mj} \{1, \phi_{mj}, \delta_{mj}, \xi_{mj}\} \quad (6.26)$$

where the coefficients $\{1, \phi_{mj}, \xi_{mj}, \delta_{mj}\}$ and the wavenumbers λ_{mj} depend on the basic flow and $\tilde{\eta}_{mj}$ are independent parameters. Notice that, although the results of Eq. 6.26 is a complex number, only the real part is physically significant.

As highlighted by Zolezzi and Seminara (2001) the sign of $real(\lambda_{mj})$ is of great importance; indeed if we consider a semi-infinite channel such as channel A, solutions with $real(\lambda_{mj}) < 0$ are exponentially growing in the upstream direction and consequently not compatible with the (finite) upstream boundary conditions. The behaviour of λ_j (for the first mode $m = 1$) as a function of the aspect ratio is reported in figure 6.3. We can notice that for $\beta < \beta_R$ (sub-resonant conditions) three of the four eigenvalues λ are negative, so that only the fourth solution is compatible; since the correspondent eigenvalue λ_4 is relatively large this solution rapidly decays and only a local upstream influence is possible. Conversely in the super-resonant case $\beta > \beta_R$ three eigenvalues are positive and significant upstream influence occurs.

A mirrored response can be found for the channel B, which shows significant downstream influence only in the sub-resonant case, whereas for $\beta > \beta_R$ the boundary condition is able to exert only a short, rapidly decaying influence.

If we assume that $\beta < 2\beta_R$, the higher modes $m \geq 2$ follow always a sub-resonant behaviour, in the sense that three negative eigenvalues occurs, so that three independent solutions are possible in the downstream channel B and only one in the upstream channel A.

Figure 6.4 illustrates, for each Fourier mode, the list of the compatible eigenvalues, depending on the super/sub resonant character of the channel. For a more comprehensive description of the phenomena, see Zolezzi and Seminara (2001).

Differently from most of the other analytical models of river morphodynamics (i.e. Colombini et al., 1987; Zolezzi and Seminara, 2001) we can not neglect, besides the 2D solution presented above, the presence of the one-dimensional component. A stationary 1D perturbation of the basic flow can be seen as a

6.3. The perturbation approach

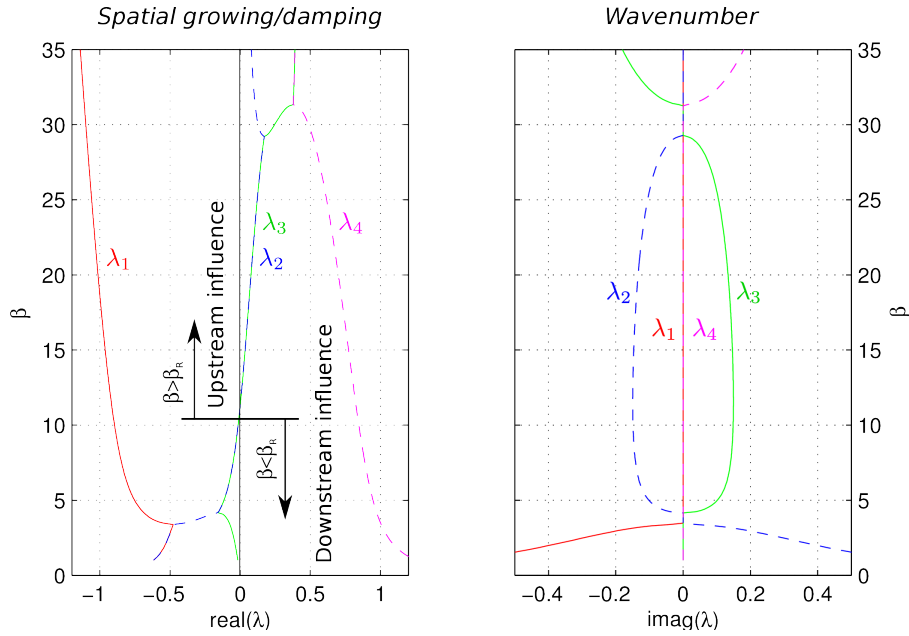


Figure 6.3: Eigenvalues λ_j for the first ($m = 1$) mode. $d_s = 0.05$, $\theta_0 = 0.1$, $r = 0.5$ are adopted as parameters of the basic flow.

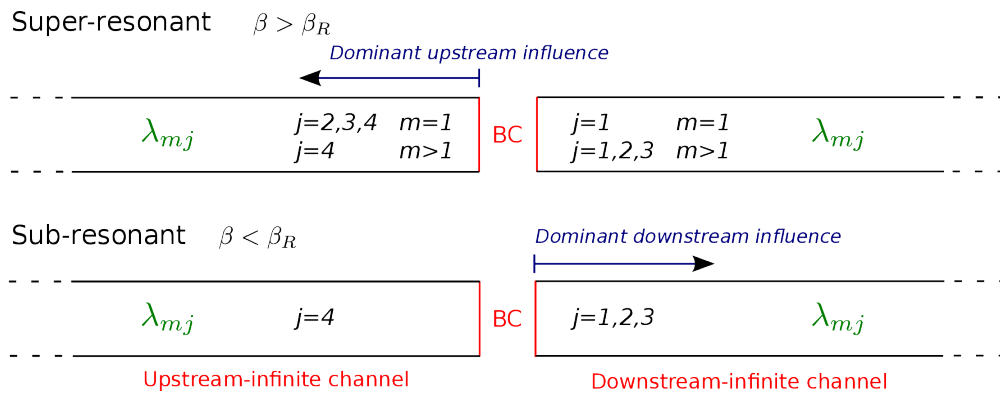


Figure 6.4: Structure of the solution for upstream and downstream semi-infinite channels in super and sub-resonant cases; the red line represent the section at which the boundary condition is applied.

6.3. The perturbation approach

uniform variation of the flow due to a (small) change of slope, discharge and the reference of the elevation, namely

$$\{\eta_1, U_1, D_1\} = \underbrace{\tilde{\eta}_0 \{1, 0, 0\}}_{\eta \text{ reference variation}} + \underbrace{\tilde{Q}_0 \{0, \gamma_1, \gamma_2\}}_{\text{Discharge perturbation}} + \underbrace{S_1 \{-\beta x, \gamma_3, -\gamma_3\}}_{\text{Slope variation}} \quad (6.27)$$

where $\tilde{\eta}_0$, S_1 , \tilde{Q}_0 are independent parameters and the coefficients γ are defined as follows

$$\gamma_2 := \frac{2}{3 + 2C_D} \frac{1}{S_0} \quad \gamma_1 := 1 - \gamma_2 \quad \gamma_3 := \frac{1}{S_0} \frac{\gamma_2}{2} \quad (6.28)$$

For a more complete description of the 1D solution, see *Chapter 7*, section 7.4.

6.3.2 General solution for the central channel Obst

For the central region the solution proposed for the straight channels A and B is not valid, because it does not satisfy the boundary condition at the left bank, which introduces a forcing effect in the differential problem. Indeed, if we express Eq. 6.19 in the primitive variables and we expand in Taylor series we obtain, for the left ($y = 1$) bank

$$\left\{ \begin{array}{l} \frac{d\eta_1}{dy}(x, 1) = 0 + \mathcal{O}(a^2); \\ V_1(x, 1) = \frac{dy^B}{dx} + \mathcal{O}(a^2) \end{array} \right. \quad (6.29)$$

which is not satisfied by Eq. 6.26, for which $V_1 = 0$ (straight bank) at both $y = 0$ and $y = 1$.

In order to determine a solution of the linear problem (Eq. 6.23) with the non-homogeneous lateral boundary condition specified by Eq. 6.29 we can proceed as follows. First of all, we can notice that in complex notation Eq. 6.19 can be written in the exponential form, namely

$$y^B = 1 - \frac{a}{2} \left(1 + e^{2\pi i x/L} \right) \quad (6.30)$$

Since only the real part has a physical meaning, we should equip all of the expression involving physical variables with the symbol *real()*. However, for the sake of notation compactness we preferred, as common in complex analysis, to omit the symbol *real()*, but keeping in mind that only the real part of the resulting solution is actually meaningful.

A similar lateral boundary condition was considered by Repetto et al. (2002), who solved a differential system analogous to Eq. 6.23 for an infinite channel with sinusoidal perturbation of the width; they tackled this problem by separating the variables and considering longitudinal variations having the same

6.3. The perturbation approach

structure of Eq. 6.30. However, differently from the present case, they studied a symmetric channel with sinusoidal variations of the position of both the banks; it is easy to see that the solution we are looking for correspond to the Repetto et al. (2002) if we consider only half of the domain $y \in [0, 1]$. In addition our position, instead of varying from -2δ to 2δ as in Repetto et al. (2002) ranges from 0 to $-a$.

Considering these minor differences we can follow the same approach and seek for a solution of the form

$$\begin{cases} \eta_1^F(x, y) = -\frac{1}{2} \underline{\eta}^F(y) \exp(-2\pi i x/L) \\ U_1^F(x, y) = -\frac{1}{2} \underline{U}^F(y) \exp(-2\pi i x/L) \\ V_1^F(x, y) = -\frac{1}{2} \underline{V}^F(y) \exp(-2\pi i x/L) \\ D_1^F(x, y) = -\frac{1}{2} \underline{D}^F(y) \exp(-2\pi i x/L) \end{cases} \quad (6.31)$$

If we substitute these functions into the linearised system of equation we obtain a first order ordinary differential system of four dependent variables, which leads to the following 4th order scalar problem in \underline{V}^F

$$\frac{d^4 \underline{V}^F}{dy^4} + \Gamma_1 \frac{d^2 \underline{V}^F}{dy^2} + \Gamma_2 \underline{V}^F = 0 \quad (6.32)$$

with the following boundary conditions given by substituting Eq. 6.30 into Eq. 6.29

$$\begin{cases} \underline{V}(1)^F = 2\pi i x/L & \underline{V}(0)^F = 0 \\ \frac{d^2 \underline{V}(1)^F}{dy^2} = 2\Gamma_3 \pi i x/L & \frac{d^2 \underline{V}(0)^F}{dy^2} = 0 \end{cases} \quad (6.33)$$

where the expression of Γ_j is given by Repetto et al. (2002).

By solving Eq. 6.32 and substituting the result into the ordinary system it is possible to determine the functions representing the transverse structure, namely

$$\begin{cases} \underline{\eta}^F = \xi_1^F \cosh(k_1 y) + \xi_2^F \cosh(k_2 y) \\ \underline{U}^F = \phi_1^F \cosh(k_1 y) + \phi_2^F \cosh(k_2 y) \\ \underline{V}^F = \gamma_1^F \sinh(k_1 y) + \gamma_2^F \sinh(k_2 y) \\ \underline{D}^F = \delta_1^F \cosh(k_1 y) + \delta_2^F \cosh(k_2 y) \end{cases} \quad (6.34)$$

in which the coefficients $k_{1/2}$ are expressed as

$$k_1 = \sqrt{\frac{1}{2} \left(-\Gamma_1 + \sqrt{\Gamma_1^2 - 4\Gamma_2} \right)} \quad k_2 = \sqrt{\frac{1}{2} \left(-\Gamma_1 - \sqrt{\Gamma_1^2 - 4\Gamma_2} \right)} \quad (6.35)$$

6.3. The perturbation approach

We defined the coefficients $\xi_{1/2}$ as follows

$$\xi_{1/2}^F = \theta_{1/2}^F Fr_0^2 - \delta_{1/2} \quad (6.36)$$

while the coefficients $\xi^F, \phi^F, \gamma^F, \delta^F$ are functions of the basic flow parameters as reported (without the superscript F) by Repetto et al. (2002).

Since, differently from Repetto et al. (2002) we considered a variation of the bank position (Eq. 6.30) around a non-zero, namely $-a/2$, the solution of Eq. 6.31 embeds also a variation of the discharge, which can be computed as follows

$$Q_1 = \int_0^{+1} (U_1^F + D_1^F) dy = -1 \quad @x = \pm L/2 \quad (6.37)$$

This is not an issue because at this stage we are looking for a particular solution of the problem for the channel Obst which does not necessarily satisfy the conditions at the open boundaries; the correct discharge will be fixed in the following when we will impose the matching conditions between the three channels and in particular when we will match the one-dimensional component (section 6.3.4).

The result of Eq. 6.31 represents a particular solution for the central region; however it is easy to prove that, due to the linearity of Eq. 6.29 it is possible to obtain a general solution by summing to Eq. 6.31 the result for the straight channel (Eq.6.25, which can be expressed as a linear combination of the (infinite) Fourier modes. Thereby we can express the general solution for channel Obst as follows

$$\{\eta_1^{obst}, U_1^{obst}, V_1^{obst}, D_1^{obst}\} = \underbrace{\{\eta_1^{obst,H}, U_1^{obst,H}, V_1^{obst,H}, D_1^{obst,H}\}}_{\text{Straight channel component}} + \underbrace{\{\eta_1, U_1, V_1, D_1\}^F}_{\text{“Forced“ solution}} \quad (6.38)$$

where the superscript H indicated the homogeneous component of the solution.

At this point the a natural question which may arise is why we need a general solution and not simply the forced component. The answer is that considering only the forced component, which is uniquely fixed by the obstacle geometry, it would be impossible to match the solution at the two boundaries. Consider for example the *bnd 1*: the matching can be ensured by decomposing the forced solution in Fourier series for each of the four variables η, U, V, D and imposing that each mode in channel A is equal across the boundary. However, since only one (or three for $m = 1$ in super-resonant conditions) independent solution a matching of four variables is impossible.

Including the homogeneous part introduces four more degrees of freedom for each Fourier mode which, as we will see in the following section, will make the problem of matching well posed.

6.3.3 The matching condition

So far we simply derived the analytical solution of the steady problem for the three regions (channels A, B, Obst) by following known methods and adapting them to the slightly different formulation we adopted.

The result we obtained is not unique, but composed by an infinite number of linearly independent solutions, and in particular 10 for each Fourier mode (except for the 1D component ($m = 0$), which is formed by a combination of 9 independent components). Among this wide spectrum of results we want to find the solution of the entire domain, in the sense that satisfy not only the problem within the three channels, but also the matching conditions at the two boundaries *bnd 1* and *bnd 2* (see figure 6.1). As we will see, this leads to a unique solution once the water and sediment fluxes (Q_1, Q_{s1}) and a reference value of the bottom elevation (η_1) are specified.

For each of the two boundaries ($x = \pm L/2$) we must impose the matching the four dependent variables. Since the procedure is similar for *bnd 1* and *bnd 2*, we will detail the procedure only with reference to the the first boundary. Specifically, we will express the solution in both the adjacent channels in Fourier series and imposing the equality of the coefficients for each mode; in this way we will derive the relations between the different components needed to satisfy the matching of the four dependent variables.

Solution for channel A at the *bnd 1*

The solution for channel A can be expressed by summing N Fourier components of Eq. 6.25 and can be evaluated at $x = -L/2$ as follows

$$U_1^a(-L/2, y) = \sum_{m=0}^{N-1} \bar{U}_m^a \cos(m\pi y) \quad (6.39)$$

where the amplitude of each cosine is a linear combination of one or three components depending on the sub or super-resonant conditions, namely

$$\begin{cases} \bar{U}_m^a = \sum_{j=2}^4 \hat{U}_{mj}^a \exp(-\lambda_{mj}L/2) & \text{if } \beta > \beta_R \text{ and } m = 1 \\ \bar{U}_m^a = \hat{U}_{m4}^a \exp(-\lambda_{mj}L/2) & \text{if } \beta < \beta_R \text{ or } m \geq 2 \end{cases} \quad (6.40)$$

Solution for channel Obst at the *bnd 1*

The solution for obstacle region channel Obst of Eq. 6.38 at the *bnd 1* reads

$$U_1^{obst}(-L/2, y) = U_1^{obst,H}(-L/2, y) + U_1^F(-L/2, y) \quad (6.41)$$

6.3. The perturbation approach

The homogeneous part can be expressed, analogously to 6.39, as

$$U_1^{obst,H}(-L/2, y) = \sum_{m=0}^{N-1} \bar{U}_m^{obst,H} \cos(m\pi y) \quad (6.42)$$

with the important difference that, being, channel Obst of finite length, there is no reason to exclude any eigenvalue, so that the linear combination of the four independent solutions can be used. Therefore the coefficients of Eq. 6.49 can be written as follows

$$\bar{U}_m^{obst,H} = \sum_{j=1}^4 \hat{U}_{mj}^{obst} \exp(-\lambda_{mj}L/2) \quad (6.43)$$

The forced component Eq. 6.31 evaluated at $x = -L/2$ gives, remembering that $\exp(\pm\pi i) = -1$

$$U_1^F(-L/2, y) = \frac{1}{2} \underline{U}^F(y) \quad (6.44)$$

In order to compare the solutions across the boundary we must expand also the forced component in Fourier cos series; in particular we consider the approximated N modes expansion, namely

$$U_1^F(-L/2, y) \simeq \sum_{m=0}^{N-1} \bar{U}_m^F \cos(m\pi y) \quad (6.45)$$

where the latter terms can be written on the basis of Eq. 6.34

$$\bar{U}_m^F = \frac{1}{2} \left(\phi_1^F C_{1m}^{\cosh} + \phi_2^F C_{2m}^{\cosh} \right) \quad (6.46)$$

C_{1m}^{\cosh} and C_{2m}^{\cosh} are the expansion coefficients of the hyperbolic cosine, which for $m \geq 2$ can be computed as follows

$$C_{jm}^{\cosh} = 2 \int_0^1 \cosh(k_j y) \cos(m\pi y) dy = \frac{2(-1)^m k_2}{k_j^2 + m^2 \pi^2} \sinh(k_j) \quad (6.47)$$

The definition of coefficients is different for the first mode $m = 1$, namely

$$C_{j0}^{\sinh} = 0 \quad C_{j0}^{\cosh} = \int_0^1 \cosh(k_j y) dy = \frac{1}{k_2} \sinh(k_j) \quad (6.48)$$

Since Eq. 6.45 furnishes only an approximation of the forced solution at the boundary the N -modes solution we obtain is exact only in the limit $N \rightarrow \infty$. However it can be seen that, since the coefficients C_{jm} tend to rapidly decay with m a rather small number of components is sufficient to obtain a sufficiently accurate solution.

By summing Eq. 6.42 and Eq. 6.45 we obtain the general solution of the channel Obst evaluated at *bnd 1* and expressed as a Fourier series

$$U_1^{obst}(-L/2, y) = \sum_{m=0}^{N-1} \left(\bar{U}_m^{obst,H} + \bar{U}_m^F \right) \cos(m\pi y) \quad (6.49)$$

Matching condition at the *bnd 1*

The equality between Eq. 6.39 and Eq. 6.49 is ensured if each Fourier component has the same coefficient across the *bnd 1*.

Specifically, if we considered, in an approximate way, the first N modes, we must impose

$$\bar{U}_m^a = \bar{U}_m^{obst,H} + \bar{U}_m^F \quad \forall m \in [0, N - 1] \quad (6.50)$$

which represents a set of N conditions.

As one may expect an identical procedure can be followed in order to determine the matching of the variables η and D , which reads

$$\begin{cases} \bar{\eta}_m^a = \bar{\eta}_m^{obst,H} + \bar{\eta}_m^F & \forall m \in [0, N - 1] \\ \bar{D}_m^a = \bar{D}_m^{obst,H} + \bar{D}_m^F & \forall m \in [0, N - 1] \end{cases} \quad (6.51)$$

Matching condition for the transverse velocity V

Slightly different is the derivation for the velocity V which have a different transverse structure; indeed the general solution in the main channel is in this case formed by a series of sines, namely

$$U_1^a(-L/2, y) = \sum_{m=0}^{N-1} \bar{U}_m^a \cos(m\pi y) \quad (6.52)$$

On the other side of *bnd 1* the Fourier sin transform of the solution in the obstacle region in this case gives

$$\bar{V}_m^{obst} = \bar{V}_m^{obst,H} + \bar{V}_m^F \quad (6.53)$$

where the latter terms is the expansion of Eq. 6.34, which reads

$$\bar{V}_m^F = a \left(\gamma_1^F C_{1m}^{\sinh} + \gamma_2^F C_{2m}^{\cosh} \right) \quad (6.54)$$

where C_{1m}^{\sinh} and C_{2m}^{\sinh} are the coefficients of the Fourier sin series expansion of the hyperbolic sine functions, namely

$$C_{jm}^{\sinh} = 2 \int_0^1 \sinh(k_j x) \sin(m\pi x) = -\frac{2(-1)^m m\pi}{k_j^2 + m^2\pi^2} \sinh(k_j) \quad (6.55)$$

The equality between Eq. 6.52 and Eq. 6.53 is ensured if

$$\bar{V}_m^a = \bar{V}_m^{obst,H} + \bar{V}_m^F \quad \forall m \in [1, N - 1] \quad (6.56)$$

Eqs. 6.50, 6.51 and 6.56 represent a set of four matching conditions for each Fourier mode m , except for $m = 0$ for which only three conditions are

6.3. The perturbation approach

needed. An identical number of constraints, which can be derived following the same matching procedure, occurs at the second boundary *bnd 2*. Since these conditions involve each mode separately we can solve an independent problem for each m , starting from the $1D$ component $m = 0$, introducing then the first $2D$ approximation $m = 1$ and ultimately refining more and more the solution by including the higher modes. This procedure is detailed in the following two subsections.

6.3.4 Matching of the one-dimensional ($m = 0$) component

For the $1D$ component we must impose the six matching conditions, while a total of nine degrees of freedom ($\tilde{\eta}_0, \tilde{D}_0, S_1$ for each of the three regions) is available. For this reason the problem is underdetermined and admits an infinite number of solutions. In order to fix this problem we must specify three additional conditions; from a physical point of view it is clear that the solution will depend on the discharge, on the sediment flux and to an arbitrary constant that fixes the bottom elevation with respect to the system of reference. Once that these three quantities are specified the problem is correctly posed and a unique solution can be found. Because we are not studying the effect of variations of the total water and sediment flux we can fix $Q_1 = 0$ and $Q_{s1} = 0$; in addition we can assume that cross-section averaged perturbation of the bottom elevation in channel A is zero, which can be practically obtained by fixing the bed or the free surface level at the downstream boundary.

The first two conditions $Q_1 = 0$ and $Q_{s1} = 0$, if applied for the channel A at the *bnd 1* can be easily translated in a condition on the velocity and depth, namely

$$\bar{U}_0^a(-L/2) = 0 \quad \bar{D}_0^a(-L/2) = 0 \quad (6.57)$$

which, as one expects, involves only the one-dimensional component.

On the basis of Eq. 6.27 we can say that Eq. 6.57 is satisfied if

$$\tilde{Q}_0^a = 0 \quad S_1^a = 0 \quad (6.58)$$

which means undisturbed discharge and slope. Similarly the continuity of water and sediment mass at the *bnd 2* implies that also the downstream channel has a vanishing perturbation of slope and water discharge, namely

$$\tilde{Q}_0^b = 0 \quad S_1^b = 0 \quad (6.59)$$

In addition from the matching condition at the *bnd 1* (Eq. 6.50) we have

$$\bar{U}_0^{obst,H}(-L/2) + \bar{U}_0^F = 0 \quad \bar{D}_0^{obst,H}(-L/2) + \bar{D}_0^F = 0 \quad (6.60)$$

6.3. The perturbation approach

which enables to compute $\bar{U}_0^{obst,H}$ and $\bar{D}_0^{obst,H}$. Thereby considering Eq. 6.27 we can determine the parameters \tilde{Q}_0^{obst} and S_1^{obst} as follows

$$\begin{cases} \tilde{Q}_0^{obst} = \frac{\bar{U}_0^{obst,H} + \bar{D}_0^{obst,H}}{\gamma_1 + \gamma_2} \\ S_1^{obst} = \frac{(\gamma_2 \tilde{Q}_0^{obst} - \bar{D}_0^{obst,H})}{\gamma_3} \end{cases} \quad (6.61)$$

The third condition can be fixed assuming that the cross sectional average of the channel B is zero at any location x . For instance we can assume

$$\int_0^1 \eta_1^b(x, y) dy = \tilde{\eta}_0^b = 0 \quad (6.62)$$

In this case the matching at the *bn*d 2 simply gives

$$\tilde{\eta}_0^{obst} = -\bar{\eta}_0^F \quad (6.63)$$

whereas is it easy to prove that the condition at the *bn*d 2 implies

$$\tilde{\eta}_0^a = S_1^{obst} \beta L \quad (6.64)$$

which completes the 1D (averaged across the section) solution.

6.3.5 Matching of the two-dimensional ($m \geq 1$) components

When we impose the matching for the two-dimensional components we must distinguish between the first mode (corresponding to alternate bars) and the higher harmonics (multiple bars).

The behaviour of the first Fourier mode ($m = 1$) depends upon the super or sub-resonant channel condition; indeed the number of linearly independent solutions for the two straight channels A and B changes between the two cases (see for example Eq. 6.40).

Let us start from the sub-resonant case and consider, as an example, the longitudinal velocity; for any $m \geq 1$ (2D components) the amplitudes \bar{U}_m^a and \bar{U}_m^b are composed by a linear combination of one and three variables respectively

$$\bar{U}_m^a(-L/2) = \hat{U}_{m4}^a \exp(-\lambda_{m4}L/2) \quad \bar{U}_m^b(+L/2) = \sum_{j=1}^3 \hat{U}_{mj}^b \exp(\lambda_{mj}L/2) \quad (6.65)$$

whereas in the central region all the four eigenvalues are compatible (Eq. 6.43)

$$\bar{U}_m^{obst,H}(\pm L/2) = \sum_{j=1}^4 \hat{U}_{mj}^{obst} \exp(\pm \lambda_{mj}L/2) \quad (6.66)$$

6.4. Results

If we remember Eq. 6.26 we can notice that the solution at the boundaries can be expressed (not only for U but also for η , V , D) as a function of the following eight independent parameters

$$\begin{cases} \tilde{\eta}_{m4}^a \\ \tilde{\eta}_{mj}^b & j = \{2, 3, 4\} \\ \tilde{\eta}_{mj}^{obst} & j = \{1, 2, 3, 4\} \end{cases} \quad (6.67)$$

Under super super-resonant conditions noting changes, for all the modes $m \geq 2$, with respect to the $\beta < \beta_R$ case; the situation is different for the first Fourier mode $m = 1$, whose coefficients for the two straight channels A and B are a linear combination of three and one independent solutions respectively, namely

$$\bar{U}_1^a(-L/2) = \sum_{j=2}^4 \hat{U}_{1j}^b \exp(-\lambda_{1j}L/2) \quad \bar{U}_1^b(+L/2) = \hat{U}_{11}^b \exp(+\lambda_{11}L/2) \quad (6.68)$$

whereas in the channel Obst we have again the same expression of Eq. 6.66. Consequently for the first mode under super-resonant conditions the following eight independent parameters appears

$$\begin{cases} \tilde{\eta}_{1j}^a & j = \{1, 2, 3\} \\ \tilde{\eta}_{14}^b \\ \tilde{\eta}_{mj}^{obst} & j = \{1, 2, 3, 4\} \end{cases} \quad (6.69)$$

If we consider the matching conditions for the four dependent variables at $x = -L/2$ and $x = +L/2$ (Eqs. 6.50, 6.51, 6.56) we obtain, for both the super and sub-resonant cases and for each Fourier mode, a system of eight linear equations in eight unknowns which can be easily solved on order to find the N -modes solution of our problem.

Specifically, using a matrix notation we can write the linear system as

$$\mathbf{A}\vec{\eta} = \mathbf{B} \quad (6.70)$$

where the vector of the known terms \mathbf{B} contains the forcing terms $\bar{\eta}_m^F$, \bar{U}_m^F , \bar{V}_m^F , \bar{D}_m^F we defined in Eq. 6.46.

As N increases the and solution rapidly converges to the exact one; thereby truncating the Fourier series to a limited number of modes (i.e. $N = 10$) leads to minor inaccuracies which are irrelevant for most purposes.

6.4 Results

The behaviour of the solution strongly depends on the super of sub-resonant character of the channel.

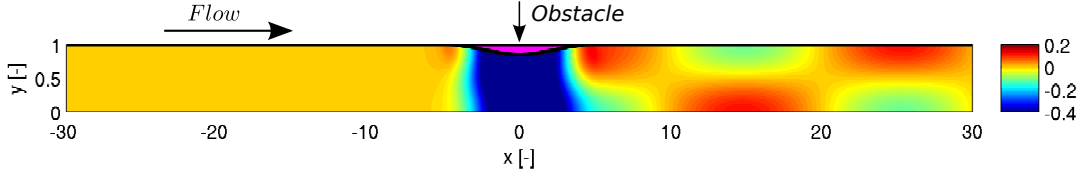


Figure 6.5: Bottom elevation map for the sub-resonant case. The length of the obstacle (small magenta bump on the left bank) is $L = 10$. $\beta = 15.7$, $\theta_0 = 0.1$, $d_s = 0.02$, $r = 0.5$, the Meyer-Peter and Müller (1948) bedload formula are adopted as parameters, which give $\beta_R = 15.80$.

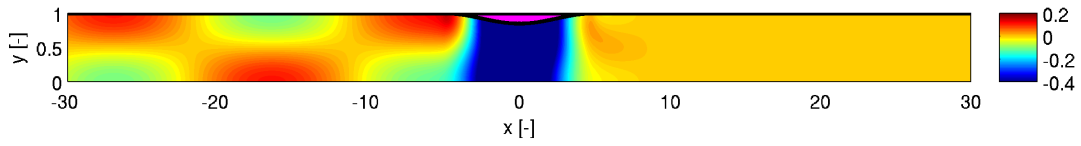


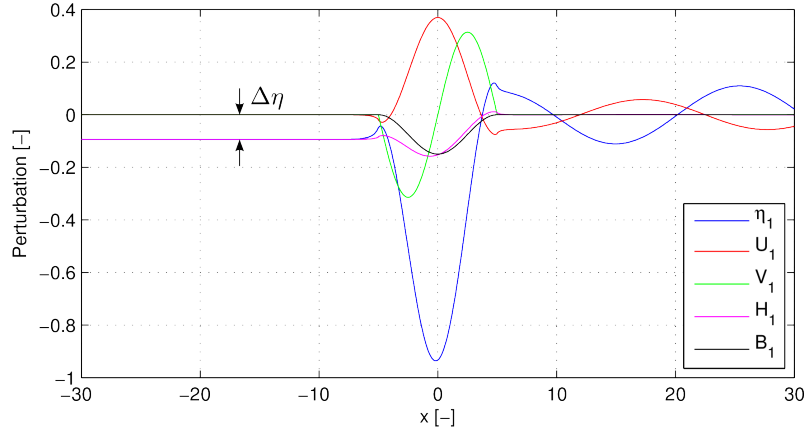
Figure 6.6: Bottom elevation map for the super-resonant case. The length of the obstacle (small magenta bump on the left bank) is $L = 10$. $\beta = 15.9$, $\theta_0 = 0.1$, $d_s = 0.02$, $r = 0.5$, the Meyer-Peter and Müller (1948) bedload formula are adopted as parameters, which give $\beta_R = 15.80$.

As an example we consider the case of a $L = 10$ obstacle placed in two different, infinitely-long rectangular channels, having $\beta_R = 15.80$ and aspect ratio slightly higher and lower than the resonant point ($\beta = 15.7$ and $\beta = 15.9$ respectively). As illustrated in figures 6.5 and 6.6, this small variation implies a dramatic change of the solution. Specifically, in agreement with the theory of the morphodynamic influence, an upstream morphological effect due to the obstacle propagates only in the super-resonant case, whereas under sub-resonant conditions the downstream influence dominates and an alternate steady bars patterns develops after the width perturbation.

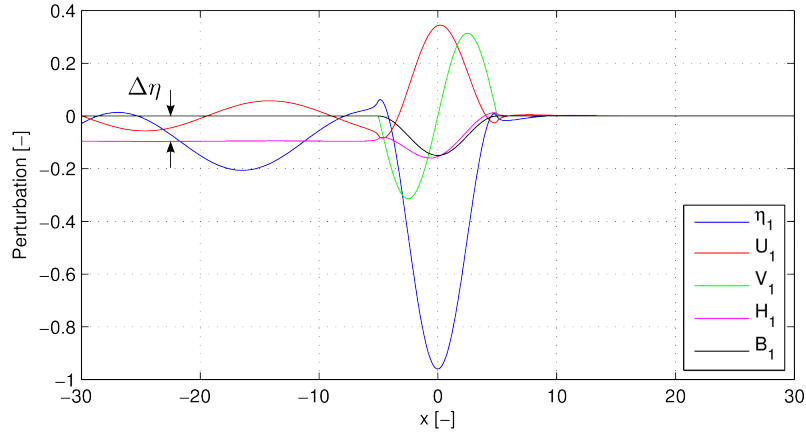
The behaviour of the different dependent variables along the domain can be seen in figure 6.7, where we report the longitudinal profiles of the solution along the left bank. Firstly, we can notice that the transverse velocity is proportional to the local angle of the bank (derivative the width perturbation B_1 represented by the black line), as required by the impermeability condition (Eq. 6.29). Secondly, the longitudinal velocity and the bottom elevation are oscillating with approximately the opposite phase in the upstream (figure 6.6) or downstream (figure 6.5) direction, depending on the super or sub-resonant character of the channel; the wavelength of the oscillations is about 20 times the width. Finally, it is also possible to see that in this specific case the oscillations of the free surface elevation are quite modest outside the obstacle region; this enables to clearly appreciate the one-dimensional effect, which leads to a positive elevation difference between the channels A and B, independently of the aspect ratio β .

Since, in both the examples, the conditions are very close to the resonant point, the damping rate of the upstream/downstream steady bars is very small,

6.4. Results



(a) Slightly sub-resonant condition ($\beta = 15.7$).



(b) Slightly sub-resonant condition ($\beta = 15.9$).

Figure 6.7: Longitudinal profiles at the left bank ($y = 1$) for the first $N = 10$ Fourier components of the analytical solution. The parameters of the basic flow are $\theta_0 = 0.1$, $d_s = 0.02$, $r = 0.5$ which leads to $\beta_R = 15.8$; the length of the obstacle is $L = 10$. $\Delta\eta$ represents the upstream scour produced by the $1D$ effects of the obstacle.

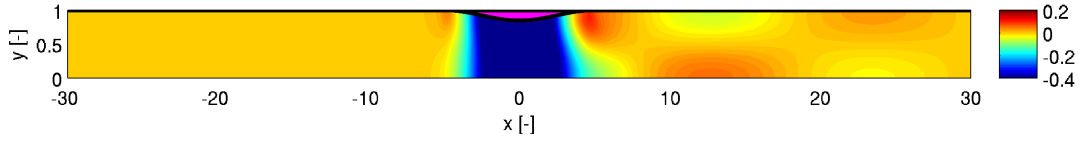


Figure 6.8: Bottom elevation map for the sub-resonant case. Same parameters as in figure 6.5 but with a smaller aspect ratio ($\beta = 12.0$), which increases the damping rate of the downstream steady bars.

so that can not be appreciated in figures 6.5, 6.6 and 6.7. However, as we can see in figure 6.3, the values of $|real(\lambda_{2/3})|$, which indicates the damping rate of the forced alternating bars, increases with the distance from β to β_R ; for example in figure 6.8 we represented the bottom elevation for $(\beta - \beta_R/\beta_R) = -0.24$; we can see that, in comparison with figure 6.5, the alternate bars are smaller and tend to rapidly decay in space.

6.5 Discussion

The perturbative approach adopted to derive the analytical solution is strictly valid in the limit of vanishing obstacle amplitude a . In spite of that, flume experiments with periodic width variation (Repetto et al., 2002) suggest that the linear scheme may be able to capture the steady-state channel morphology even for a width variations up to 50% the channel size.

It is also worth to notice that the time-dependent model shows, when the aspect ratio exceeds a critical threshold $\beta_{cr} < \beta_R$, an instability mechanism causing, in a straight channel, the formation of migrating alternate bars, which grow until an equilibrium value is attained (e.g. Colombini et al., 1987). In this case the presence of a small obstacle is expected to produce a perturbation of the migrating bars, rather than the steady configuration of figure 6.6. However laboratory and numerical experiments (e.g. Crosato et al., 2012; Siviglia et al., 2013) suggest that if the obstacle amplitude a is sufficiently large the nonlinear interaction suppresses the propagation of migrating bars. This process is similar to what described by Tubino and Seminara (1990) with reference to meandering channels, where the migrating perturbation can be annihilated by the presence of stationary point bars forced by the channel curvature. Therefore we expect that the system attains a steady-state solution, which may be qualitatively similar to the analytical but not identical because of the nonlinear terms which are not accounted by the perturbation method.

At this stage no more elements are available to go beyond these preliminary considerations about nonlinear interaction between free migrating and steady bars and about the role of the boundary conditions in this mechanism. A deeper investigation is possible through a fully nonlinear numerical scheme; in appendix 6.7.1 we will setup a two-dimensional morphodynamic model using

6.5. Discussion

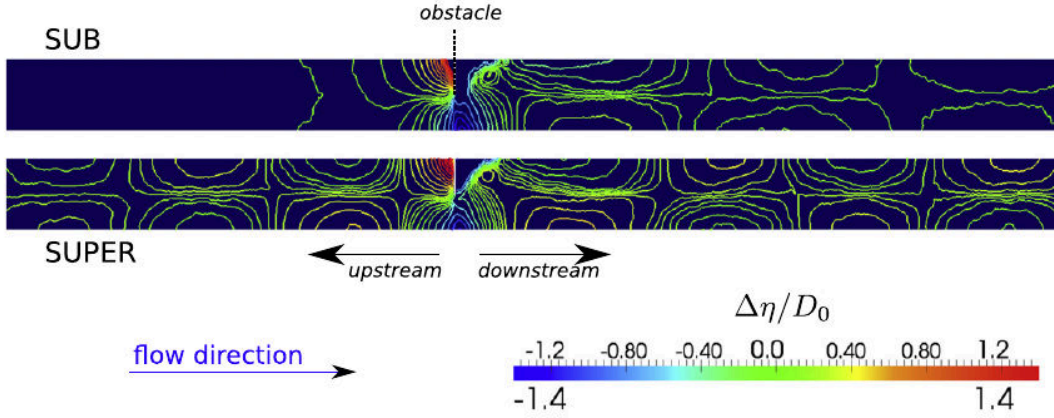


Figure 6.9: Bottom elevation map for the super-resonant case from the numerical experiments of Siviglia et al. (2013). Upper panel: sub-resonant ($\beta = 10.42$) case, lower panel: sub-resonant ($\beta = 16.72$) case. $\theta_0 = 0.1$, $d_s = 0.067$, $r = 0.3$ and the Wong and Parker (2006c) bedload formula have been adopted. The resonant point is $\beta_R = 13.28$.

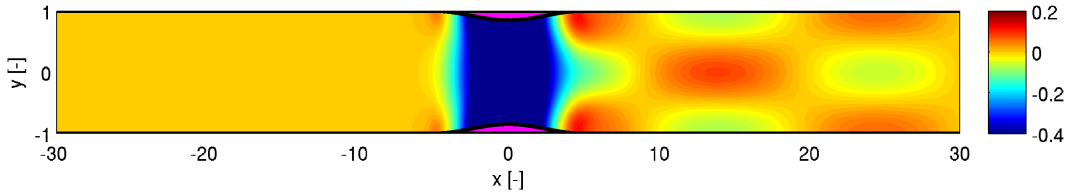


Figure 6.10: Bottom elevation map, for the symmetric obstacle under super-resonant conditions ($\beta = 28.0$, $\beta_R = 15.80$). The same parameters as in figures 6.5, 6.6 have been adopted.

the *Delft3D* code and we will present a few preliminary results.

It is interesting to observe that the solution we derived can be conveniently extended to a symmetric obstacle by simply mirroring the result across the $y = 0$ axis. For example, starting with a sub-resonant configuration ($\beta = 14$, $\beta_R = 15.8$), we can obtain the result of figure 6.10, which shows the formation of a central bars pattern downstream the restriction. The aspect ratio becomes twice the original and therefore the conditions becomes super-resonant ($\beta = 28$); despite that no upstream influence occurs until $\beta > 2\beta_R$. This is a peculiar feature of any symmetric forcing which, according to the linear model, induce the formation of central steady bars that propagates upstream only if the aspect ratio exceeds *twice* the resonant value.

6.5.1 The effect of the secondary currents

As widely assumed in river morphodynamics (e.g. Colombini et al., 1987), the 2D depth-averaged model we solved does not include any three-dimensional effect due to the curvature of the flow. However, in the case of the obstacle, we may expect relevant impact of the secondary flow on the morphology; therefore we need to explore in what extent this additional ingredient is affecting our results.

The 3D effects due to the presence of secondary currents do not significantly change the resonant point, and therefore do not affect the response in terms of direction of the morphodynamic influence.

Nevertheless the impact of the secondary flow on the forced solution is not negligible; indeed the analytical solution of the fully 3D model, as well as from laboratory experiments Repetto et al. (2002), reveal that the cross-sectional profiles are significantly influenced by the spiral flow, especially for relatively short wavelength of the width variations. Repetto et al. (2002) also noticed that a simplified closure of the spiral flow in the depth-averaged model is able to capture the more relevant effects on the equilibrium hydraulic and morphological configuration.

Following the same approach we express the transverse shear stress as

$$\tau_y = \tau'_y + \tau_H \quad (6.71)$$

where τ'_y is the stress computed on the basis of Eq. 6.8, whereas the additional component due to the spiral flow can be computed (Kalkwijk and Booij, 1986; Zolezzi and Seminara, 2001) as follows

$$\tau_H = C |\vec{U}| k_3 \frac{D U}{\beta C_0} = C |\vec{\tau}| \frac{k_3 C_0}{\beta} \quad (6.72)$$

in which we have defined the dimensionless curvature as

$$C = B^* C^* = B^* \frac{1}{R^*} \quad (6.73)$$

with R^* indicating the local radius of curvature.

The coefficient k_3 represents the ratio between bottom shear of the secondary velocity profile and the principal stress. For this reason in this section Following Kalkwijk and Booij (1986), Zolezzi and Seminara (2001) it is possible to estimate this coefficient as a function of the relative roughness d_s .

Once the expression of τ_y is known, we can simply substitute the new closure relation into Eq. 6.5, which leads to a linear system which has exactly the same structure of Eq. 6.23, but with different coefficients. This system can be solved by following exactly the same procedure and gives the result of figure 6.11, where we report the map of bottom elevation for the same basic flow with two different obstacle lengths (upper and lower panels) without (left) and with

6.5. Discussion

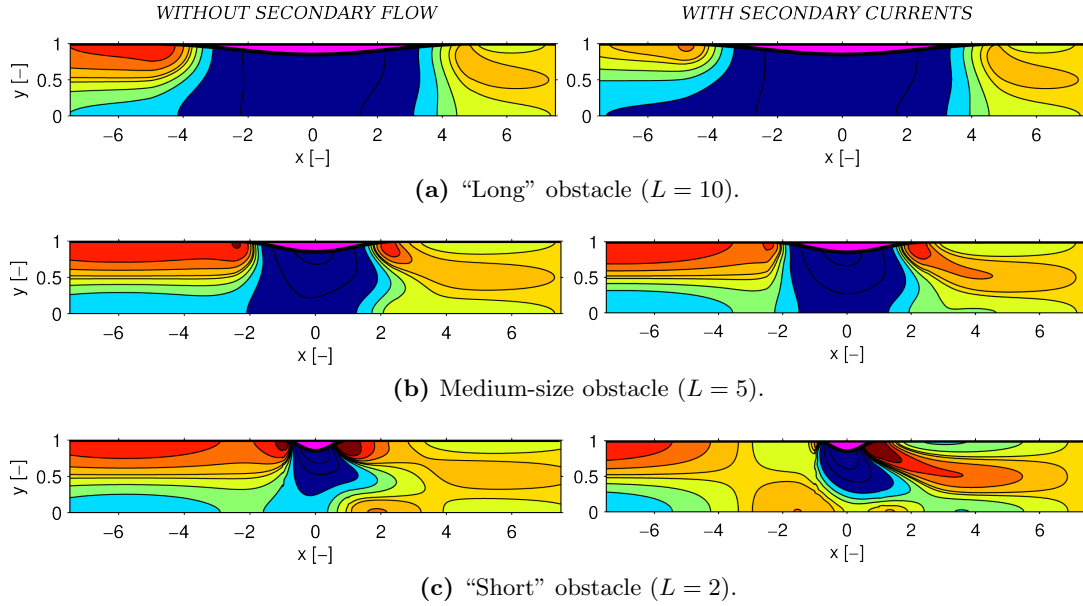


Figure 6.11: Maps of bottom elevation without (left) and with (right) secondary currents. $\beta = 15.9$, $\theta_0 = 0.1$, $d_s = 0.02$, $r = 0.5$ are adopted as parameters; the first $N = 10$ Fourier components have been considered.

(right) secondary currents. This comparison reveals that the impact of spiral flow is stronger for the shorter ($L = 2$) obstacle, where it causes deposition on the opposite side of the obstacle and increase of the height of the downstream central bars. Indeed the intensity of the spiral flow, as pictured in figure 6.12, is maximal near the obstacle apex, where the curvature induced by the bank geometry creates a positive additional stress in the y direction.

A cross-sectional view of the effect of the secondary flow on the different variables at $x = 0$ is reported in figure 6.13. As one may expect, the curvature produces a decrease of the free surface height close to the obstacle. The transverse profile of bottom elevation is less intuitive; indeed, differently from a channel curve (which typically produce external scour and internal point bar), the curvature is in this case highly variable in both x and y . This causes the reinforcement of the transverse velocity V , which compensates the effect of τ_H .

6.5.2 The role of the boundary conditions

If the domain length is finite the steady solution is always influenced by the conditions at the domain boundaries. Indeed in the long term both the one and two-dimensional information have time to propagate throughout the channel and influence the final solution.

The preconditions for studying this effect is the knowledge of how many boundary conditions we need to specify at each (upstream and downstream)

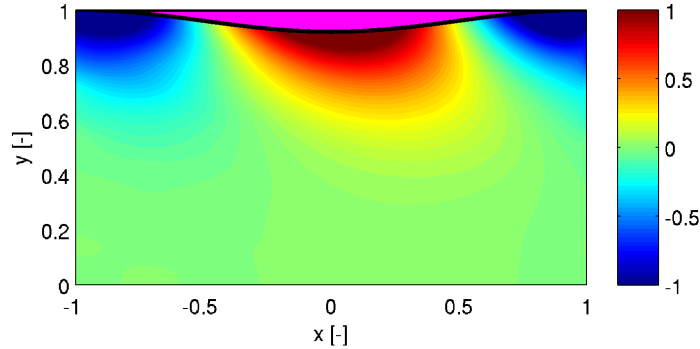


Figure 6.12: Intensity of the spiral flow τ_H/τ_0 for the $L = 2$ obstacle of figure 6.11c. Positive values indicates negative (left bending) curvature \mathcal{C} and consequently positive bottom velocities and stresses.

boundary in order to obtain a well-posed problem.

Consider the infinite-domain solution, and simply cut it at the boundaries; this expression satisfies the problem inside the domain and correspond to well defined boundary conditions. However this is not the general solution because in this case there is no reason to eliminate the eigenvalues that exponentially grow (to infinite values) as we did before (Eqs. 6.65 and 6.68) for the infinite domain.

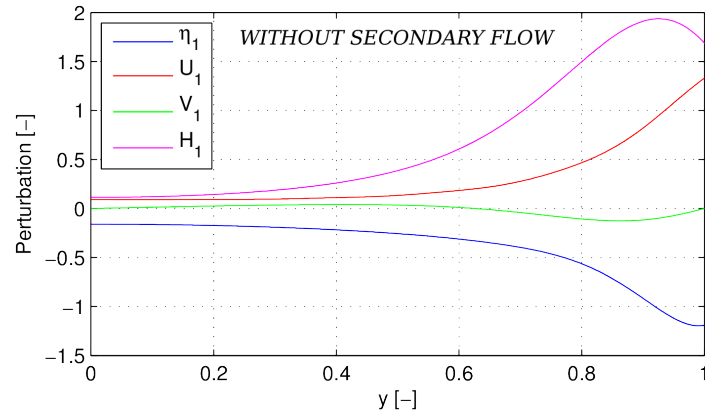
We can imagine the general solution with boundaries as the sum of the particular (infinite domain) and the general solution of a straight channel of finite length. In this perspective the question about which are the proper boundary conditions is exactly the same for a straight and for a more complex channel geometry.

As we have seen the solution for a single, straight channel is a function of four independent parameters for each Fourier mode and consequently four boundary conditions must be specified in order to fix the solution. At this point the important question is *where* the conditions must be specified, and in particular how many should be fixed upstream and how many downstream.

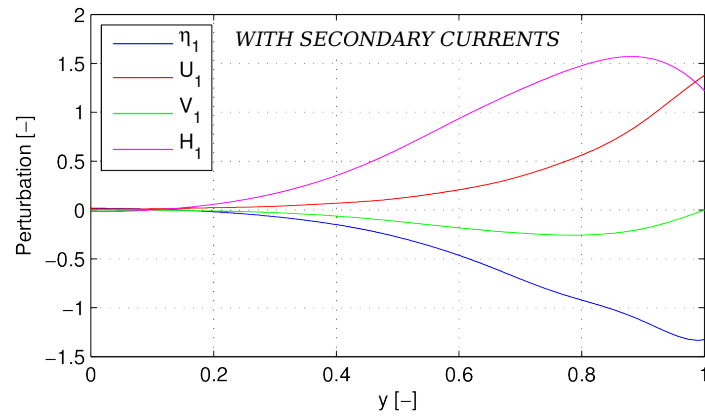
Under sub-resonant conditions three eigenvalues are downstream-dampen and one is upstream-damped, for any Fourier mode. For this reason if we specify three upstream and one downstream boundary condition we obtain a solution whose dependence on the *BCs* decreases with the distance from the domain boundary.

The situation is more trickily in the super-resonant case because the first mode $m = 1$ has a peculiar behaviour, with three positive eigenvalues which are downstream-growing. This means that if we apply three upstream *BCs* their influence increases exponentially in space; as far as the domain is finite this growth is also finite, so that if we specify three upstream conditions we obtain a solution which, from a linear point of view, is acceptable. However, when

6.5. Discussion



(a) Solutions without spiral flow.



(b) Solution with a simplified closure for secondary currents ($k_3 = -0.908$).

Figure 6.13: Cross sectional profiles of the solution at $x = 0$ for a relatively short $L = 2$ obstacle. $\beta = 15.9$, $\theta_0 = 0.01$, $d_s = 0.02$, $r = 0.5$ are adopted as parameters; the first $N = 10$ Fourier components have been considered.

the solution becomes relatively big, although finite, the hypothesis of small variations which is the basis of the perturbation approach is not valid. Specifically, if the domain is relatively long (and $\beta > \beta_R$) even very small upstream disturbances eventually grow enough to break the assumption of small perturbations. The morphological response in the region where the linear model fails can be explored thanks to the weakly non-linear approach proposed by Seminara and Tubino (1992). If the parameter $\epsilon = (\beta - \beta_R)/\beta_R$ is relatively small we can study the spatial growth of the steady perturbation are affected by the non-linear effects. Indeed according to Seminara and Tubino (1992) for $\epsilon \rightarrow 0$ the spatial development of the two complex conjugate solutions is not exponential as predicted by the linear theory but is limited by the non-linear ($O(\epsilon^{3/2})$) terms which reduce the growth rate with the wave amplitude. Figure 6.17 illustrates the longitudinal variation of the amplitude (absolute value) of the complex-conjugate solution in the super-resonant case, resulting from the Landau-Stuart equation as derived by Seminara and Tubino (1992). Initially the curves follow the exponential growth but, as far as the solution becomes sufficiently large, the growth rates decreases and ultimately the amplitude reaches a constant (equilibrium) value which depends on ϵ . It is worth to notice that the x-axis of figure 6.17 represents the longitudinal coordinate multiplied by the growth rate $real(\lambda)$ which is proportional to ϵ ; this mean that the distance at with the non-linearity is felt increases as far as the aspect ratio approaches the resonant value.

From the two-dimensional point of view there is not a preferred *type* of boundary we should specify. However from the analysis of the 1D component it is clear that we can not impose the boundary conditions in an arbitrary way; indeed we must avoid redundant information which leaves other condition unspecified and which can violate the compatibility conditions imposed by the conservation principles. If for example we fix U, V, D upstream and U downstream the problem is clearly not well-posed for two reasons:

- We are not fixing any reference for the elevations; for this reason we can add any arbitrary constant to the solution without violating the *BCs*, thus obtaining, formally speaking, an infinite number of solutions.
- Imposing a different 1D component of velocity upstream and downstream does not allow to find a balanced sediment transport.

in order to obtain a well-posed problem the following conditions must be satisfied:

1. one of the four variables is the bottom elevation;
2. the transverse velocity is specified at once but not more than once.

This behaviour, mathematically rather weird but physically obvious, can be easily explained by studying the behaviour of the 1D component of the solution. Indeed in order to fix a reference elevation one of the four *BCs* has to be the

6.6. Conclusions

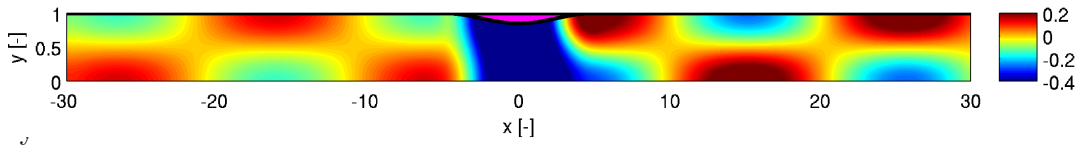


Figure 6.14: Bottom elevation map for the super-resonant case after imposing a sinusoidal perturbation of the transverse velocity at the upstream boundary. $L = 10$, $\beta = 15.9$, $\theta_0 = 0.1$, $d_s = 0.02$, $r = 0.5$, the Meyer-Peter and Müller (1948) bedload formula are adopted as parameters, while the amplitude of the upstream perturbation is of 0.1δ .

bottom elevation (or any combination of it, such as the free surface level $\eta + D$). In addition one BC must involve V because otherwise we should impose four conditions to the $1D$ solution which has only three degrees of freedom; for the same reason the V can not be fixed simultaneously upstream and downstream (it would lead to an undetermined $1D$ system in which only two $1D$ conditions are fixed).

This brief and informal explanation enables to understand that if we specify three upstream and one downstream boundary conditions the problem becomes well-posed, in the sense that for any arbitrary boundary configuration (expressed as functions of y) we can find an unique solution, independently of the sub or super-resonant character of the channel (see illustration of figure 6.15).

This correspond to the number of boundary conditions needed by the time-dependent problem, which implies that for *any* steady boundary configuration the (linear) time-dependent system admits a stationary solution.

The presence of a boundary can significantly change the steady state solution; for example if we impose a sinusoidal perturbation of the transverse velocity V and a zero perturbation of the longitudinal velocity and water depth we obtain, in the super-resonant case, a configuration in which steady alternate bars appears also downstream the obstacle (see figure 6.14).

6.6 Conclusions

Within this work we derived an analytical solution of the steady shallow water morphodynamic model for a local, sinusoidal obstacle placed in a straight channel with rectangular cross-section. This solution, expressed in terms of Fourier series, is exact in the limit small amplitude obstacle ($a \rightarrow 0$).

The analytical approach allows to study the long-term morphological response of a gravel-bed channel in different conditions; in particular it enables to determine both the local effect near the obstacle region and the morphological influence exerted on the upstream and downstream branches.

The analysis of the analytical solution confirms the importance of the reso-

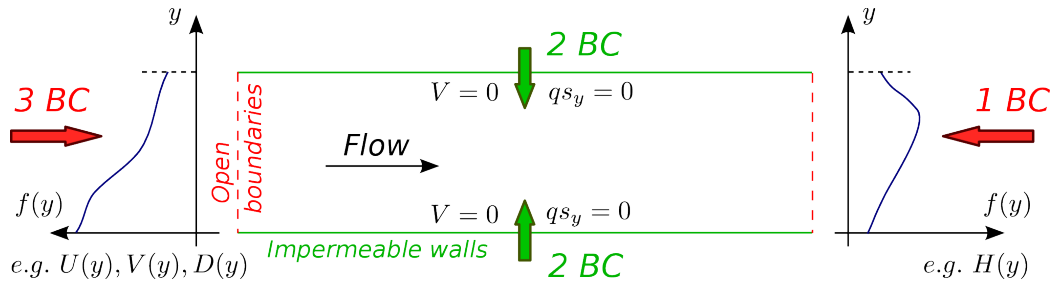


Figure 6.15: Schematic picture of the boundary conditions required by both the steady and the time-dependent models. The arrows indicates the direction of propagation of the boundary information whereas flow is from left to right. $f(y)$ indicates a generic function of the transverse coordinate.

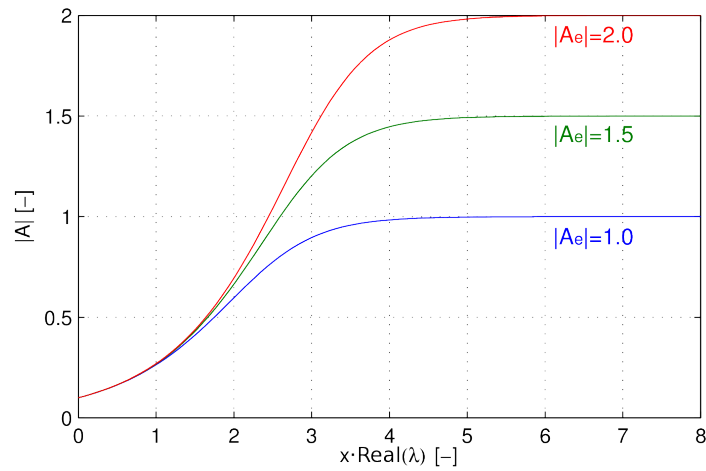


Figure 6.16: Spatial development of the amplitude of the complex-conjugate solution in super-resonant conditions according to the weakly non-linear theory of Seminara and Tubino (1992). $\text{real}(\lambda)$ represents the initial (linear growth rate); the initial amplitude has been arbitrary fixed to 0.1, whereas the asymptotic equilibrium $|A_e|$ depends on the basic flow (different values are here represented by different colours).

6.7. Appendix: Eigenstructure of the linear, coupled, time-dependent problem

nance phenomenon (as defined by Blondeaux and Seminara (1985)) for determining the dominant direction of morphodynamic influence. Specifically, as also predicted by the numerical experiments of Siviglia et al. (2013), an upstream propagation of two-dimensional disturbances occurs under super-resonant conditions, whereas only downstream influence can be observed on the narrower, sub-resonant, case.

We have also seen that, including the secondary effects of the spiral flow, causes a minor impact on the results in terms of the direction of morphodynamic influence. However, especially if the obstacle is relatively short small, the secondary currents produce a significant variation of the morphology in the region near the obstacle.

The analytical model also enables to explore the role of the boundary conditions, showing that an unique steady solution can be found once three upstream and one downstream *BCs* are specified. Although this is valid in both the super and sub resonant conditions, the influence of the boundaries can significantly differ in the two regimes. For $\beta > \beta_R$ the effect of the upstream boundary is growing along the channel and, if the domain is long enough, it attains an amplitude which violates the basic assumption of small perturbation; therefore the nonlinear effects play an important role and in particular, as predicted by the weakly nonlinear theory of Seminara and Tubino (1992), they reduce the growth rate and lead to a bounded solution.

Finally, from the analysis of the eigenstructure of the differential model, it is possible to prove that the number of boundary conditions of the time-dependent linear model are the same as in the stationary case, which suggests that a steady solution may exist for any steady boundary configuration.

6.7 Appendix: Eigenstructure of the linear, coupled, time-dependent problem

In order to determine the solution of a differential system for a general boundary configuration we must know what “general” means, and in particular how many upstream, downstream and lateral (at the fixed walls) conditions must be independently specified in order to have a well-posed mathematical problem.

In general this is not straightforward and requires a deep knowledge of the theory of partial differential equations. However, for a specific class of problems, namely the hyperbolic differential systems, the question can be addressed by performing the well-known analysis of the (bi)characteristics (e.g. Wesseling, 2001), as already done for *1D* shallow water morphodynamic model (de Vries, 1965) as well as *2D* models, both fixed-bed (e.g. Abbott, 1979) and mobile-bottom (e.g. Vriend, 1987).

The study of characteristics is important not only for what concerns the boundary conditions, but more in general to explore the direction of prop-

6.7. Appendix: Eigenstructure of the linear, coupled, time-dependent problem

agation of the information. For example this may give some insight to the discussion of Mosselman et al. (2006), who argued that “a deeper analysis of the characteristics may reveal that the upstream influence is actually related to supercritical flow” rather than the super-resonant condition.

In the present section we investigate the properties of the present two-dimensional linear model. Specifically, we consider the linearized form of the Eq. 6.5, which is similar to the linear system of Eq. 6.23, but with the incorporation of the time derivatives.

For the numerical analysis the resulting system is often treated as hyperbolic (e.g. Siviglia et al., 2013). However, from a formal point of view, such an assumption is not possible; indeed the effect of the gravity on the sediment transport leads to a diffusive term in the Exner equation (e.g. Cordier et al., 2011), and consequently to a mixed hyperbolic-parabolic system which can not be studied using the method of the characteristics. In order to bypass this issue we perform a little trick, changing the formulation for the gravity effect in order to obtain an hyperbolic model. This can be done by substituting the algebraic closure of Ikeda (1981) with a differential formulation. Specifically, we assume that the direction of the sediment transport does not respond instantaneously to the variation of the bottom gradient, but it adapts asymptotically to the equilibrium value following a simple differential law

$$\frac{d\gamma_g}{dt^*} = -\frac{1}{T_s^*} (\gamma_g - \gamma_{g,eq}) \quad (6.74)$$

where $\gamma_{g,eq}$ is the angle assumed in the algebraic closure

$$\gamma_{g,eq} = -\frac{r}{\sqrt{\theta_0}} \frac{\partial \eta_1}{\partial y} \quad (6.75)$$

and T_s is the temporal scale of the adaptation (sometimes called relaxation parameter). In dimensionless form Eq. 6.74 becomes

$$\frac{d\gamma_g}{dt} = -\frac{1}{T_s} (\gamma_g - \gamma_{g,eq}) \quad T_s = T_s^*/T^* \quad (6.76)$$

If T_s is sufficiently small the adjustment to equilibrium becomes very fast and, in the limit $T_s \rightarrow 0$ the original model is retrieved, in the sense described by Nagy et al. (1994) about the convergence of the hyperbolic heat equation to the classic diffusive model.

As one may imagine, there may be some physical reasons for choosing a differential formulation for the non-equilibrium transport rate; however, at this level, we can simply see the new closure as a different formation that converges to the original algebraic curve when $T_s \rightarrow 0$. The advantage of this approach from the mathematical point of view is that enables to obtain a two-dimensional hyperbolic system of five differential equations in five unknowns; if we expand

6.7. Appendix: Eigenstructure of the linear, coupled, time-dependent problem

the variables in Taylor series around a known basic state (the simple uniform flow), as in Eq. 6.20, and we assume relatively small perturbations, we obtain a linear differential system which can be written in the following form

$$T_w \frac{d\vec{Q}}{dt} + \mathbf{A}_x \frac{1}{\beta} \frac{d\vec{Q}}{dx} + \mathbf{A}_y \frac{1}{\beta} \frac{d\vec{Q}}{dy} = \vec{S} \quad (6.77)$$

where \vec{S} represents the source vector, which contains the non-differential terms. The vector of the unknowns is defined as

$$\vec{Q} = [\eta_1, U_1, V_1, D_1, \gamma_g]^T \quad (6.78)$$

with T indicating the matrix transpose.

The matrix \mathbf{A}_x contains the coefficients of the x -derivative, which reads

$$\mathbf{A}_x = \begin{bmatrix} \frac{1}{Fr_0^2} & 1 & 0 & \frac{1}{Fr_0^2} & 0 \\ 0 & 0 & 1 & 0 & 0 \\ 0 & 1 & 0 & 1 & 0 \\ 0 & 2\Phi_T \beta T_w & 0 & -2C_D \Phi_T \beta T_w & -\frac{r T_w}{\sqrt{\theta_0}} \\ 0 & 0 & 0 & 0 & 0 \end{bmatrix} \quad (6.79)$$

whereas the matrix of the y -derivatives coefficients is written as

$$\mathbf{A}_y = \begin{bmatrix} 0 & 0 & 0 & 0 & 0 \\ \frac{1}{Fr_0^2} & 0 & 0 & \frac{1}{Fr_0^2} & 0 \\ 0 & 0 & 1 & 0 & 0 \\ 0 & 0 & \beta T_w & 0 & -\frac{r T_w}{\sqrt{\theta_0}} \\ -\frac{\beta T_w}{T_s} & 0 & 0 & 0 & 0 \end{bmatrix} \quad (6.80)$$

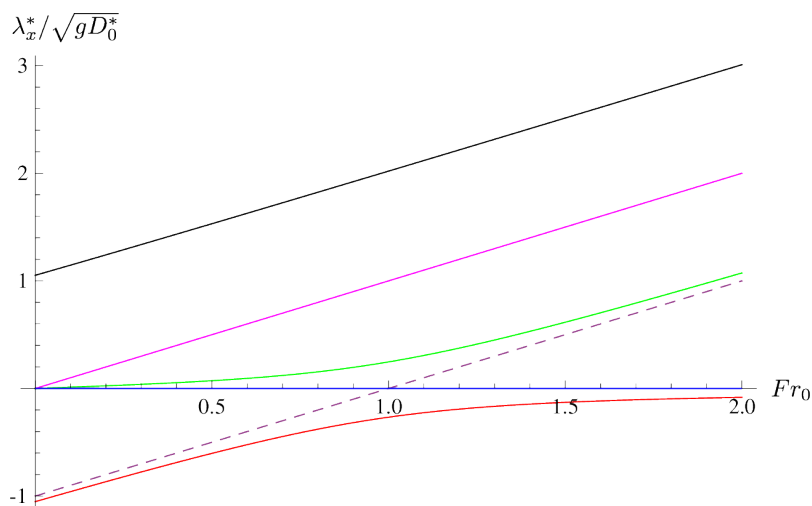
If we compute the eigenvalues of the matrix \mathbf{A}_x we obtain the five roots reported in figure 6.17a. The first one is zero, the second represents a wave travelling with longitudinal speed ($\lambda^* = U_0^*$) and the remaining three are the classic eigenvalues of the 1D mobile-bed model (de Vries, 1965; Sieben, 1997).

If the Exner timescale becomes relatively small, compared with the hydrodynamic one (low-transport conditions, figure 6.17b), one of the eigenvalues becomes much smaller (decoupled problem), except in the region close to the unitary Froude number.

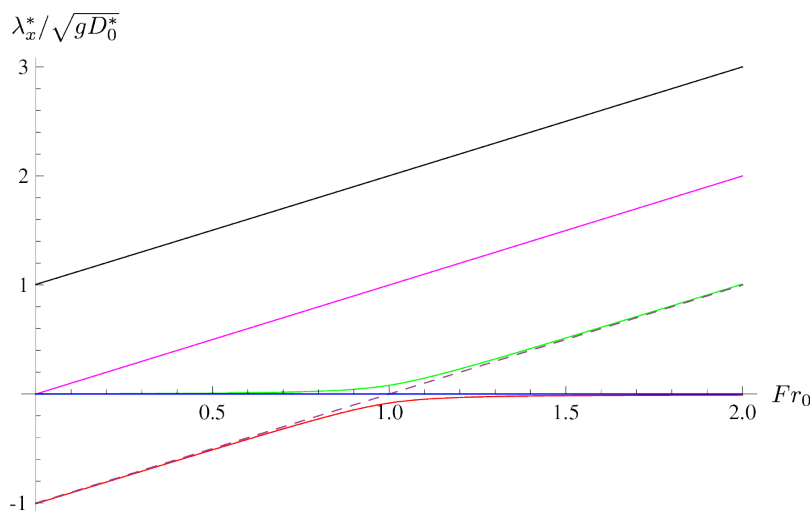
Is it easy to prove that the the eigenvalues in the y -direction can be conveniently scaled in order to find the following functional dependence

$$\frac{\lambda_{4/5}^*}{\sqrt{gD_0^*}} = \lambda_{4/5} Fr_0 = fct \left(\beta T_w, \sqrt{\frac{\beta r}{\sqrt{\theta_0}}} \frac{T_w}{\sqrt{T_s}} Fr_0 \right) \quad (6.81)$$

**6.7. Appendix: Eigenstructure of the linear, coupled,
time-dependent problem**



(a) $T_w^* = 10^{-2} T^* / \beta$. For a relatively wide range of Fr_0 numbers the celerity of the four waves has the same order of magnitude, so that the morphological timescale is comparable with the hydrodynamic one.



(b) $\beta T_w^* = 10^{-3}$. In this case the morphodynamic and the hydrodynamic problem can be considered as decoupled, except for the relevant case of trans-critical ($Fr_0 \simeq 1$) flow.

Figure 6.17: Eigenvalues of the hyperbolic problem in the x -direction for different values of the hydrodynamic timescale T_w . $\theta_0 = 0.1$ are adopted as parameter; the dashed line represent the function $\lambda = -1 + Fr_0$.

6.7. Appendix: Eigenstructure of the linear, coupled, time-dependent problem

where fc indicates a generic function.

Figure 6.18 shows that one eigenvalue is zero, two are positive and the remaining two can be found by the symmetry of the problem across $y = 0$. Having two positive and two negative eigenvalues, we need to impose two boundary conditions, both on the left and on the right sides. Specifically, it is rather natural, from a physical point of view, to fix at the lateral walls the impermeability of both the liquid and solid discharge ($V_1 = 0$ and $\gamma_g = 0$).

The first panel (figure 6.18a) illustrates how, as far as $T_w \rightarrow 0$, the eigenstructure becomes very simple, whereas if T_w is larger a wide region with curved lines appears. For relatively small values of T_s , the combination of parameters on the x-axis increases and two eigenvalues become very large; this indicates that information associated with the adaptation of the transverse slope to the hydraulic conditions is fast, so that model tends to the “classic” one, in which the gravitational effect on the bedload leads to a diffusive term.

From this analysis we can conclude that the present time-dependent linear problem needs three upstream and only one downstream *BCs*. Formally we proved this only for the hyperbolic and fully-decoupled system; however we can imagine that similar boundary conditions may be required by the system of Eq. 6.23, which can be obtained as a limit of the hyperbolic model for low transport rate and fast adaptation of the bedload direction. This is consistent with the analysis of section 6.5.2 about the boundary conditions needed to obtain an (unique) solution of the stationary problem.

6.7.1 Appendix 2: Numerical modelling

In this section we study the problem of the obstacle through a morphodynamical numerical model. This allows for investigating the role of the two main ingredients we are missing in the analytical approach, namely the non-linearity of the system and the temporal evolution of the solution for a given initial condition. In particular the nonlinear effects are relevant when the magnitude of the perturbation is relatively big, which may occur because of the non-small amplitude a or because of the spontaneous growth of migrating bars.

The main purposes of the present section are the following:

1. assess which is the capability to the simple linear approach, in terms of prediction of the long-term morphological and hydraulical configuration;
2. study the behaviour of the time-dependent solution and assess in which condition it attains a steady state.

A secondary objective is to test of the accuracy provided by the numerical scheme in the cases in which the analytical solution is expected to be exact.

We adopted in particular the *Delft3d* software in *2D* mode which enables, once a proper setting of the parameters is provided, to resolve a differential

6.7. Appendix: Eigenstructure of the linear, coupled, time-dependent problem

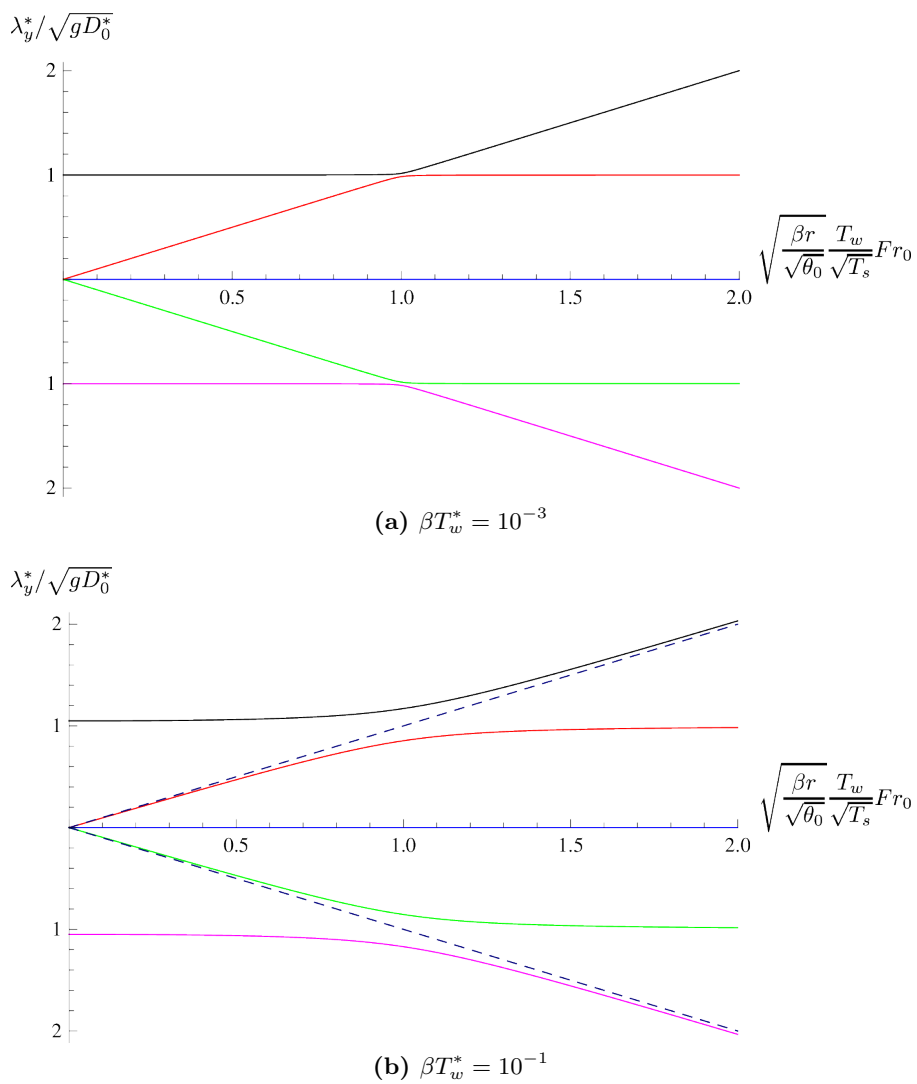


Figure 6.18: Eigenvalues of the hyperbolic problem for different hydrodynamic timescales T_w . The dashed lines have a unitary (± 1) slope.

6.7. Appendix: Eigenstructure of the linear, coupled, time-dependent problem

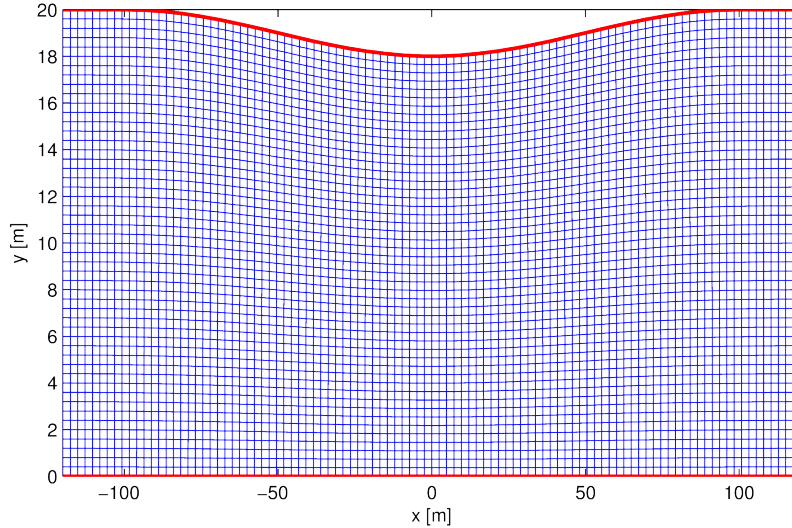


Figure 6.19: Rectangular mesh adopted for the numerical simulations. Only the obstacle region is here represented.

system which is equivalent, from a linear point of view, to the formulation we consider for our analytical derivation.

Geometry and computational grid

We adopted a $B^* = 20$ m wide channel, a sinusoidal obstacle having length $L^* = 200$ m and amplitude $a^* = 2$ m, and equal upstream and downstream channel $L_a^* = L_b^* = 500$ m, for a total domain length of 1200 m.

We built a rectangular mesh with 500 cells in the longitudinal direction and 50 in the transverse one, so that the average grid spacing is $dx = 1.2$ m and $dy = 0.4$ m respectively (figure 6.19).

In addition we constructed a second mesh having similar features but describing a wider ($a^* = 8$ m) obstacle which occupies 40 % of the channel section.

Experimental setup

In order to compare the analytical theory with numerical simulations it is important to consider an identical formulation and the same closure equations and parameters. The numerical model *Delft3d* allows the choice between different transport formulas, in particular the so-called “general formula” can reproduce, once a proper choice of the parameters is made, the Wong and Parker (2006a) relation. Similarly a proper choice of the formulation Eq. 6.17 for the bed slope can be obtained by selecting the Ikeda et al. (1982) option of the model, with

6.7. Appendix: Eigenstructure of the linear, coupled, time-dependent problem

<i>Parameter</i>	<i>Symbol</i>	<i>Value</i>
Transport formula		Wong and Parker (2006a)
Horizontal eddy viscosity	ν_H	$0 \text{ m}^2 \text{ s}^{-1}$
Secondary currents parameter	β_c	0
Gravitational acceleration	g	9.81 m s^{-2}
Time step	dt^*	6 s
Morphological factor		$5 \div 10$
Transverse slope coefficient	α_{bn}	2.306
Longitudinal slope coefficient	α_{bs}	0

Table 6.1: Most important settings of the numerical model.

<i>Parameter</i>	<i>Symbol</i>	<i>Value</i>
Shield stress	θ	0.080
Relative roughness	d_s	0.010
Slope	S	0.134 %
Resonant β	β_R	11.24
Critical β	β_{cr}	8.00
Froude number	Fr	0.53

Table 6.2: Common parameters between the different experiments.

the following coefficient

$$\alpha_{bn} = \frac{r}{\sqrt{\theta_{cr}}} = \frac{0.5}{\sqrt{0.047}} = 2.306 \quad (6.82)$$

For the hydraulic resistance we adopted the Manning formula (Eq. 6.10); we selected zero horizontal viscosity and did not consider the effect of secondary currents. Since we are here interested only in the stationary phase we do not expect the morphological factor to play an important role; therefore we adopted (Crosato et al., 2011) a factor 10. A summary of the parameters of the numerical model are reported in table 6.1.

In order to investigate the response of the system under different conditions we considered four experiments having same width, slope, Shields stress and relative roughness (table 6.2) but a different aspect ratio, which can be obtained by varying simultaneously the discharge the grain size as detailed in table 6.2.

The resonant values, as well as the critical aspect ratio for the development of migrating bars (Colombini et al., 1987), do not vary because they depend only on θ and d_s (which are constant in our simulations). For this reason the values of β obtained by varying both discharge and roughness can be easily chosen in order to reproduce super/sub resonant conditions and super/sub critical values.

6.7. Appendix: Eigenstructure of the linear, coupled, time-dependent problem

<i>Parameter</i>	<i>Super</i>	<i>Super 2</i>	<i>Sub</i>	<i>Sub 2</i>
β	12.0	15.0	10.5	7.0
D^* [m]	0.833	0.667	0.952	1.429
d_s^* [mm]	8.33	6.67	9.52	14.29
ks [$m^{1/3}s^{-1}$]	46.9	48.6	45.8	42.8
Q^* [m^3s^{-1}]	25.13	17.98	30.70	56.40
U^* [ms^{-1}]	1.51	1.35	1.61	1.97
Qs^* [ls^{-1}]	1.286	0.920	1.571	2.887

Table 6.3: Hydraulic parameters of the different experiments.

Preliminary results

In most of the numerical simulations the interaction between the migrating bars and the steady solution makes the analysis more complex and interesting at the same time. However in this preliminary analysis we limit our attention to the simple direct comparison between numerical and analytical outcomes.

This is possible for the *Sub 2* experiment because in that configuration the aspect ratio is sufficiently small to prevent formation of migrating alternate bars ($\beta < \beta_{cr}$); therefore we do not expect the growth of free bars but simply the development of the steady configuration as predicted by the analytical derivation.

In figure 6.20 we report the comparison between analytical and numerical solutions for a long-term simulation (40 d) in the case of a relatively small $a = 2 m$ a bigger $a = 8 m$ obstacle. We can notice that the morphological pattern is qualitatively correctly reproduced, as well as the approximate height of the steady bars and the elevation difference between the upstream and downstream branches.

However also significant differences occur; in particular figure 6.20b shows that even for relatively small obstacle there is a significant difference between numerical and analytical results. In order to understand whether this is related to the limited grid resolution, small differences in the formulation or differences sources further investigations are needed.

The solution is rather similar for the big obstacle of figure 6.20c which confirms the limited impact of the nonlinear effect even for relatively large perturbation observed in Repetto et al. (2002) experiments with periodic width variation.

6.7.2 List of symbols and acronyms

Subscripts and superscripts

0	Parameter of the basic flow;
R	Referred to resonant condition;

6.7. Appendix: Eigenstructure of the linear, coupled, time-dependent problem

$*$	Dimensional quantity;
F	Forced component;
H	Homogeneous component;
T	Matrix transpose;
a	Refers to the upstream channel;
b	Refers to the downstream channel;
$obst$	Refers to the central region, where the obstacle is located;

Latins

BC		Boundary condition;
\cosh		Hyperbolic cosine;
\sinh		Hyperbolic sine;
d_s^*	$[l]$	Sediment size;
m	$[-]$	Fourier mode;
g	$[lt^{-2}]$	Gravitational acceleration;
i	$[-]$	Imaginary unit;
$k_{1/2}$	$[-]$	Coefficients of the obstacle solution;
k_3	$[-]$	Coefficients of the spiral flow;
k_s	$[l^{1/3}t^{-1}]$	Gauckler-Strickler coefficient;
r	$[-]$	Coefficient of the Ikeda (1981) formula;
x^*	$[l]$	Longitudinal coordinate;
y^*	$[l]$	Transverse coordinate;
y^B	$[-]$	Dimensionless bank position;
A_m	$[-]$	Expansion of a linear function in Fourier sin series;
\mathbf{A}	$[-]$	Matrix of coefficients of the linear system;
\mathbf{B}	$[-]$	Matrix of known terms of the linear system;
\mathbf{A}_x	$[-]$	Matrix of coefficients of the x -derivatives (hyperbolic system);
\mathbf{B}_y	$[-]$	Matrix of coefficients of the y -derivatives (hyperbolic system);
A_m	$[-]$	Expansion of a linear function in Fourier sin series;
B	$[-]$	Channel width;
C_{jm}^{\cosh}	$[-]$	Coefficients of the Fourier expansion of the hyperbolic cosine;
C_{jm}^{\sinh}	$[-]$	Coefficients of the Fourier expansion of the hyperbolic sine;
C	$[-]$	Dimensionless Chézy coefficient;
C_D	$[-]$	Variation of the Chézy coefficient with the water depth;
C^*	$[l^{-1}]$	Channel curvature;
D^*	$[l]$	Water depth;
E_{mj}	$[-]$	Longitudinal variation of the eigenvalue j of the component m ;
Fr	$[-]$	Froude number;
H	$[l]$	Free surface height;
N	$[-]$	Number of Fourier modes;
\vec{Q}	$[-]$	Vector of the unknown;
Q^*	$[l^3t^{-1}]$	Water discharge;
Q_s^*	$[l^3t^{-1}]$	Solid discharge;
R^*	$[l]$	Radius of curvature;
S	$[-]$	Channel slope;
\vec{S}	$[-]$	Source term of the hyperbolic system;

6.7. Appendix: Eigenstructure of the linear, coupled, time-dependent problem

T^*	$[t]$	Exner time scale;
T_w^*	$[t]$	Time scale of the hydrodynamics;
T_s^*	$[t]$	Time scale of the adaptation of the bedload direction;
U^*	$[lt^{-1}]$	Longitudinal (along x -direction) component of velocity;
\vec{U}^*	$[lt^{-1}]$	Vector of dependent variables in the hyperbolic system;
V^*	$[lt^{-1}]$	Transverse (along y -direction) component of velocity;

Greeks

α	$[rad]$	Bifurcation angle;
β	$[-]$	Aspect ratio;
β_{cr}	$[-]$	Critical aspect ratio for formation of migrating alternate bars;
γ_g	$[-]$	Deviation of bedload transport due to the gravitational effect;
$\gamma_{g,eq}$	$[-]$	γ_g according to the algebraic closure Ikeda (1981);
$\gamma_{1/2}^F$	$[-]$	Coefficients of the transverse velocity in the obstacle solution;
$\Gamma_{1/2}$	$[-]$	Coefficients of the forced solution;
δ	$[-]$	Amplitude of the width variation;
$\delta_{1/2}^F$	$[-]$	Coefficients of the water depth in the obstacle solution;
Δ	$[-]$	Relative submerged density of sediment;
ΔS	$[-]$	Relative variation of channel slope;
η	$[-]$	Bottom elevation;
$\vec{\eta}$	$[-]$	Vector of the unknowns;
λ	$[-]$	(Complex) spatial growth;
λ_x^*	$[lt^{-1}]$	Eigenvalues of the hyperbolic system in longitudinal direction;
λ_y^*	$[lt^{-1}]$	Eigenvalues of the hyperbolic system in transverse direction;
θ	$[-]$	Shields parameter;
τ^*	$[Ml^{-1}t^{-2}]$	Shear stress;
τ_H^*	$[Ml^{-1}t^{-2}]$	Transverse shear stress due to secondary currents;
$\theta_{1/2}^F$	$[-]$	Coefficients of the water depth in the obstacle solution;
$\xi_{1/2}^F$	$[-]$	Coefficients of the bottom elevation in the obstacle solution;
$\Phi_{1/2}^F$	$[-]$	Coefficients of the longitudinal velocity in the obstacle solution;

6.7. Appendix: Eigenstructure of the linear, coupled, time-dependent problem

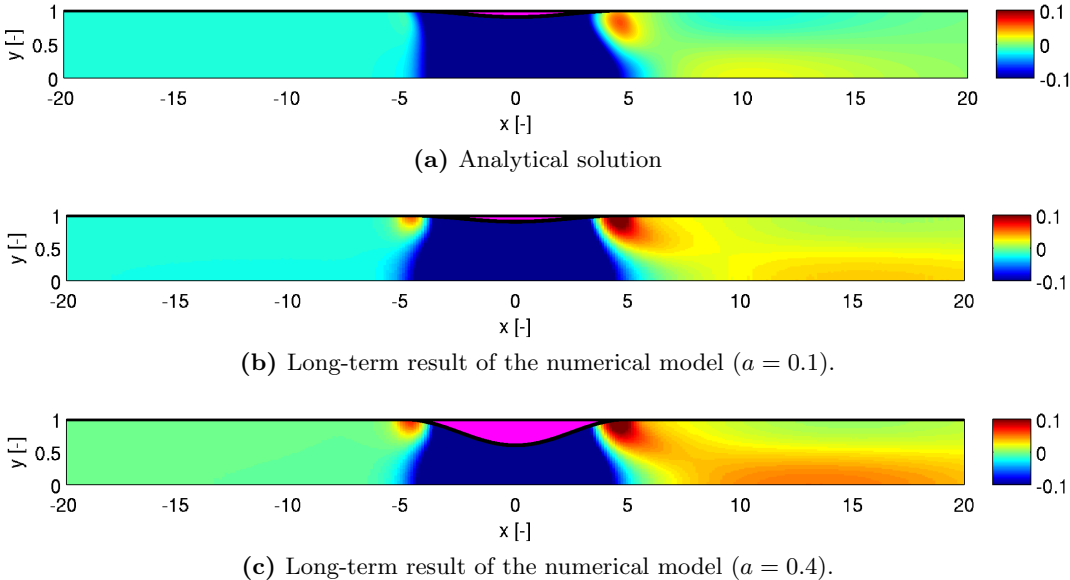


Figure 6.20: Steady bottom configuration of the Sub 2 experiment.

**6.7. Appendix: Eigenstructure of the linear, coupled,
time-dependent problem**

Chapter 7

Perturbative solution of the 2D model for gravel-bed river bifurcations

7.1 Introduction

Bifurcations are fundamental processes in the dynamics of many river systems like alluvial fans, braided and anastomosing rivers, fluvial lowland plains and deltas (Kleinhans et al., 2013).

Understanding the control on their morphodynamics and how they evolve in time is therefore key to increase the present knowledge on a vast class of fluvial systems.

Many observation in both natural and laboratory gravel-bed rivers (Mosley, 1983; Federici and Paola, 2003; Zolezzi et al., 2006) show the tendency of bifurcations in these systems to develop an unbalanced configuration, with one branch carrying most of the coming discharge. Such asymmetric behaviour can be geometrically forced, like in the presence of channel curvature or of a slope advantage of one of the distributaries, but can arise even in symmetrical configurations (Bertoldi and Tubino, 2007).

Despite the flow being strongly three-dimensional several properties of bifurcation systems have been modelled by matching a simple one-dimensional scheme for the morphodynamics of each channel with a suitable nodal condition. Following this approach Wang et al. (1995) proposed an empirical relation for the partition of the sediment flux, showing how an uneven sediment and water distribution may occur even in a symmetrical planform configuration. A more physically-based nodal condition has been proposed by Bolla Pittaluga et al. (2003) who introduced a simplified process description based on two rectangular cells located just upstream the bifurcation, which mutually exchange water and sediment flows depending on the transverse bottom gradient. This approach

7.1. Introduction

allows for including further ingredients, like the secondary flow developing in a curved channel (Kleinhans et al., 2008). The experimental observations of Bertoldi and Tubino (2007) confirmed the capability of the Bolla Pittaluga et al. (2003) model to distinguish between balanced and unbalanced cases

The main limitations of the above models lie in the need to calibrate some parameter. In the Bolla Pittaluga et al. (2003) approach this is mainly represented by the longitudinal size of the rectangular cells measuring the upstream reach length that controls the partition of sediment and water fluxes in the distributaries. As typical of simplified closure relations, this fundamental problem reflects a limitation in the physical description of the complex processes masked by the calibration parameters. Moreover, analysis of the experimental findings of Bertoldi and Tubino (2007) point out a particular intriguing finding, whereby the optimal length of these cells is closely related to the distance between the local hydraulic conditions and the so-called resonant point (Blondeaux and Seminara, 1985). In the $2D$ morphodynamics of single thread river channels, resonance represents a fundamental theoretical condition discriminating between different models of planform evolution of meandering rivers (Seminara et al., 2001; Lanzoni and Seminara, 2006; Frascati and Lanzoni, 2009; Zolezzi et al., 2009) and setting the threshold between prevailing upstream or downstream propagation of $2D$ information of morphological change (Zolezzi and Seminara, 2001; Mosselman et al., 2006).

On the basis of such finding Bertoldi and Tubino (2007) proposed a new interpretation of bifurcation instability founded on the theory of (Zolezzi and Seminara, 2001), showing that the distance from the resonant conditions is clearly correlated with the response of the bifurcation in terms of discharge partition and secondary channels elevation. In more detail Bertoldi and Tubino (2007) suggested that the upstream influence exerted by the bifurcation under super-resonant conditions leads to the formation of a steady alternate bar in the upstream reach, which is the primary topographic cause of flow diversion towards one of the two distributaries and consequent development of an asymmetrical configuration.

This concept brings a fascinating theoretical legacy between bifurcation dynamics, mostly studied within one dimensional approaches, and the framework of morphodynamic theories for river bars and meandering. Such legacy clearly emerges from experimental observations but it hasn't been given a rigorous theoretical explanation so far.

In this work we aim at developing a theoretical explanation of the linkage between the phenomenon of resonance in single thread channels and the dynamics of channel bifurcations. This is achieved by solving analytically the depth-averaged shallow water morphodynamic model through a perturbation approach, with reference to a bifurcating channel domain.

The solution is found by imposing a matching of the solution at the bifurcation node which ensures the continuity of all the variables across the three

7.2. Gravel bed rivers bifurcations and morphodynamic influence

channels.

The proposed solution refers to the commonly investigated geometrically symmetrical bifurcation configuration, and is initially developed with reference to the idealised case of two parallel branches separated by a thin wall and is afterwards extended to the more realistic case of a non-vanishing bifurcation angle. It can be viewed as the exact analytical solution for the “free” bifurcation problem, i.e., which doesn’t consider external forcing effects such as channel curvature or slope advantages which are out of the scope of the present work and can be studied using the free solution as the starting point.

7.2 Gravel bed rivers bifurcations and morphodynamic influence

The key point of this work is to model the bifurcation dynamics in the framework of $2D$ steady bar theory and morphodynamic influence. It is convenient to briefly recall the fundamental theoretical background of morphodynamic influence and bifurcation dynamics which sustain the basic idea of the present work.

7.2.1 The theory of the morphodynamic influence

Two-dimensional morphodynamic influence can be defined as the process whereby the presence of a local persistent perturbation in channel geometry is felt downstream and/or upstream through a series of steady bed waves typically taking the form of alternate bars (Zolezzi and Seminara, 2001). Theoretically this emerges from the linear theory of non-migrating bars in straight channels with a non-uniform boundary condition at one end of the channel, which translates into mathematical terms the mathematical discontinuity. The phenomenon is known since decades to occur downstream of the local perturbation (Struiksmas et al., 1985; Struiksmas and Crosato, 1989) through the discovery that under special conditions morphodynamic influence can be felt also upstream of the geometrical perturbation is more recent (Zolezzi and Seminara, 2001). Such phenomenon has been experimentally verified (Zolezzi et al., 2005) and numerically reproduced (Van der Meer et al., 2011; Siviglia et al., 2013), and has been mostly associated with the effect of a local narrowing in a straight channel or with a discontinuity in channel curvature in a stream of constant width.

A crucial parameter of this theory is the bar-forming channel aspect ratio β , defined as the (half) width to depth ratio, and in particular the so-called resonant value β_R which can be computed as

$$\beta_R = f(\theta, d_s) \tag{7.1}$$

where f indicates a function of the Shields stress θ and d_s is the relative roughness.

7.2. Gravel bed rivers bifurcations and morphodynamic influence

It's now broadly agreed (Mosselman et al., 2006) that 2D morphodynamic influence can occur upstream of the geometrical perturbation only if $\beta \geq \beta_R$ with only downstream influence occurring in the opposite case.

Though not being fully rigorous, an analogy has been suggested between the role of the aspect ratio β in two (x, y) dimensions and the Froude number Fr in one dimension, being β_R the analogue of unity, which distinguish the prevailing direction of propagation of information of 1D morphological change at the reach level.

The legacy between morphodynamic influence and bifurcation dynamics can be understood when viewing the bifurcation node as a localised persistent perturbation located at the downstream end of the bifurcating channel and at the upstream ends of the two downstream bifurcates.

7.2.2 Channel bifurcations: simplified modelling and morphodynamic influence

Modelling of channel bifurcation morphodynamics has been proposed in the last three decades through simplified 1D approach for each of the three distributaries, plus suitable boundary conditions to be imposed at the upstream end of the bifurcating channel, at the downstream ends of the bifurcates and at the bifurcation node. Namely, adopting a 1D mobile-bed model for every channel requires to specify 2 upstream conditions at the upstream end of each distributary and 1 condition at the downstream end of the inlet channel, for a total of 5 nodal relations (Bolla Pittaluga et al., 2003). In addition to the conservation of water and sediment mass (2 conditions) many models (Wang et al., 1995; Bolla Pittaluga et al., 2003; Miori et al., 2006) assume the conservation of specific energy from the main channel to the two branches (2 conditions); the fifth relation is more delicate because it needs to take into account the complex flow field and sediment transport near the bifurcation node. The type of these boundary conditions and the values of the involved parameter are key to discriminate between contrasting types of bifurcation behaviours. Moreover, the nodal condition is nearly the only opportunity of incorporating 2D information related to water and sediment partition by the bifurcation within a 1D modelling approach.

The first attempt to close a 1D model with a suitable nodal relation has been proposed by Wang et al. (1995), who adopted a simple power law which links the partition of the sediment flow with the water discharge ratio, namely

$$\frac{qs_b^*}{qs_c^*} = \left(\frac{q_b^*}{q_c^*} \right)^k \quad (7.2)$$

where q and qs are respectively the liquid and solid specific (per unit width) discharges in the two distributaries (referred as b and c) and the superscript $*$ indicates dimensional quantities. According to this model, a threshold k

7.2. Gravel bed rivers bifurcations and morphodynamic influence

value of $n/3$ separates two drastically different bifurcation behaviours, where n indicates the dependency of the sediment flux to the velocity (through the power law $qs \propto U^n$). Indeed when k is smaller than $n/3$ the balanced solution is unstable and one of the two distributaries dominates, and viceversa for k larger than $n/3$.

In spite of the empirical nature of Eq. 7.2 this simple model has the advantage to show which are the conditions for which an instability arises. In particular if the partition of solid flow is highly dependent on the discharge ratio (high k) a slightly more elevated channel would receive less sediment than its transport capacity, erode its bottom and return to the balanced state; on the other hand if k is small a more elevated channel would receive almost the same quantity of material, which can be higher than the transport capacity and consequently would lead to an increasingly unbalanced configuration.

A more physically-based nodal condition has been proposed by Bolla Pittaluga et al. (2003) who introduced a simple two-cells description of the $2D$ processes at the bifurcation node (see figure 7.1). This condition is based on considering two cells of length proportional to the width of the inlet channel by a parameter α which measures upstream reach length affected by the bifurcation; Bolla Pittaluga et al. (2003) assumed a uniform flow entering the cells from upstream and have allowed three different values of the average bed elevation in both the two cells (η_b and η_c) and in the upstream section of the inlet channel (η_a). It is worth noting that η_b and η_c also coincide with the bed level of the upstream end section of the two downstream bifurcates.

The key $2D$ information is related to the lateral sediment flux which is allowed between the two cells and is due to the transverse flow component related to the exchange of water between the cells and to the gravity effect related to the lateral bed elevation gap between the two cells. Such condition can be formalised through the following expression

$$qs_y^* = qs_a^* \left[\frac{Q_y^* D_a^*}{Q_a^* \alpha D_{abc}^*} - \frac{2r}{\sqrt{\theta_a}} \frac{\eta_b^* - \eta_c^*}{B_b^* + B_c^*} \right] \quad (7.3)$$

where Q represents the water flux, D the depth, B the channel width and r the Ikeda (1981) parameter; D_{abc} indicates the average depth of the three branches and Q_y the exchange of water from cell c to cell b .

The analysis of this model suggests that if the aspect ratio of the inlet channel β_a is higher than a critical value β_{cr} the balanced solution is unstable and an uneven configuration arises. In particular such critical value is a function of the channel-forming value of the Shields stress θ_a and the relative roughness d_{sa} of the inlet channel, namely

$$\frac{\beta_{cr}}{r\alpha} = \mathcal{G}(\theta, d_s) \quad (7.4)$$

where \mathcal{G} represent a generic function.

7.2. Gravel bed rivers bifurcations and morphodynamic influence

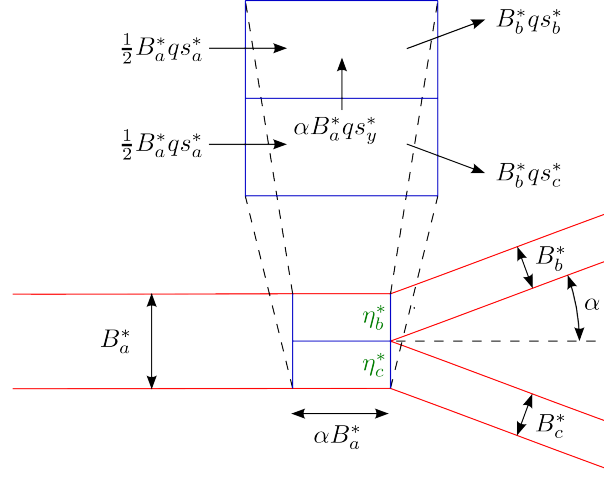


Figure 7.1: Sketch of the two-cells model of Bolla Pittaluga et al. (2003). Arrows indicate sediment fluxes across the cells boundaries.

This simple model is able to capture important bifurcation properties observed both in laboratory physical models and in the field (Ferguson et al., 1992; Zolezzi et al., 2006), and in particular the development, in the case of relatively low Shields stress θ_a and large aspect ratio β_a , of an unbalanced bifurcation configuration.

The main disadvantage of this quasi-2D approach is that a nodal relation of general validity is difficult to formulate; in particular the calibration of the parameter α often yields rather different values (1 in Bolla Pittaluga et al. (2003), 2.5 in Siviglia et al. (2013), 3 in Kleinhans et al. (2008), 6 in Bertoldi and Tubino (2007)). For example in figure 7.2 we report results from the flume experiments of Bertoldi and Tubino (2007) and from the numerical simulations of Siviglia et al. (2013): it clearly appear that a unique curve is not able to discriminate between stable and unstable points and consequently different values of α must be adopted.

The clearest and perhaps most intriguing indication of the most likely controlling factor of the length of the bifurcation-affected upstream channel reach (equal to αB_a) came from the experimental analysis of Bertoldi and Tubino (2007) who observed that the value of the parameter α which yields the best matching with the measured discharge partition is highly correlated with the difference between the channel-forming value of the inlet channel aspect ratio β and its resonant threshold β_R , an observation which sets the connection between the dynamics of bifurcations and the theory of 2D morphodynamic influence. In particular, as reported in figure 12 of Bertoldi and Tubino (2007) the optimal cell size α increases in near-resonant conditions; this is consistent with the theory of the morphodynamic influence which predicts the spatial damping of the upstream influence to vanish at the resonant point. In addition they

7.3. Formulation of the problem

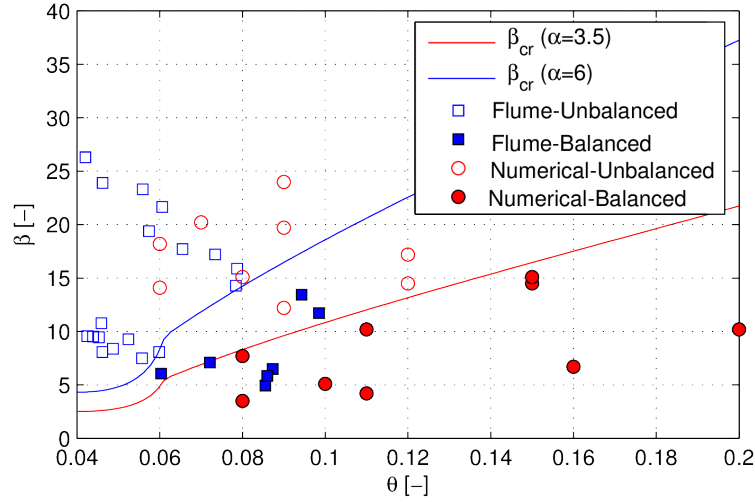


Figure 7.2: Laboratory experiments Bertoldi and Tubino (2007) and numerical simulation of Siviglia et al. (2013), and theoretical curves of Bolla Pittaluga et al. (2003). The Manning resistance law, Parker (1990) transport formula and $r = 0.5$ have been adopted.

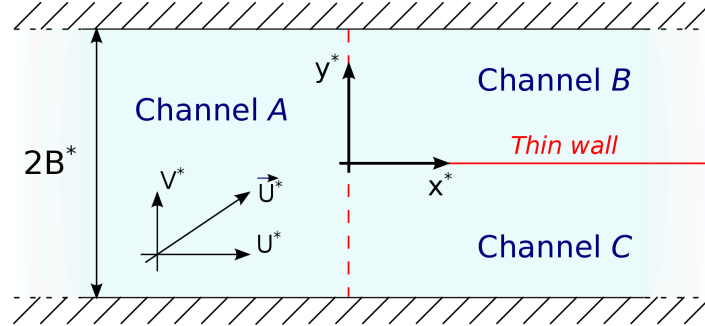
noticed that the final configuration crucially depends on the distance from the resonant conditions; indeed the inlet step (see figures 7 and 10 of Bertoldi and Tubino (2007) as well as the discharge ratio turns out to be well correlated with $(\beta - \beta_R)/\beta_R$ than to the aspect ratio itself.

More specifically, two main findings support this legacy. First, the two typical indicators of bifurcation asymmetry show a strong correlation with the scaled difference $(\beta - \beta_R)/\beta_R$, rather than with the aspect ratio itself (figures 5 and 7 of Bertoldi and Tubino (2007)). These two indicators are the discharge ratio r_Q between the downstream anabranches and the so called “inlet step”, i.e. the normalised elevation difference between the upstream end sections of the same anabranches $(\eta_b - \eta_c)/D_a$. Second, the value of α that provides the best match between model predictions and experimental observations is also correlated with the same difference $(\beta - \beta_R)/\beta_R$, and shows its peak under near-resonant conditions, i. e. when such difference almost vanishes (Figure 12 of Bertoldi and Tubino (2007)).

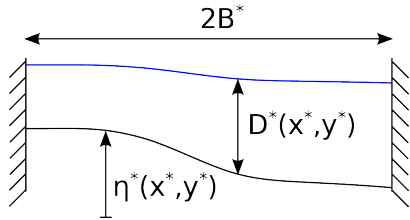
7.3 Formulation of the problem

The study refers to the channel configurations illustrated in Figure 3, consisting of one upstream channel “A” and two downstream bifurcates (“B” and “C”) separated by a thin wall. The channels have erodible bed, fixed and frictionless banks and are assumed to be indefinitely long far from the bifurcation node. The width of the channel A is assumed to be twice than the width of B and C.

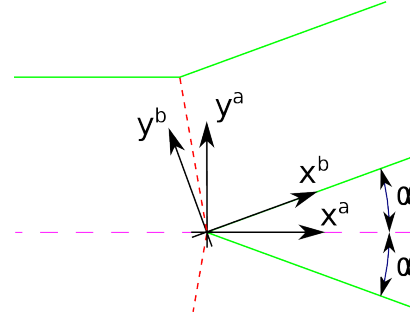
7.3. Formulation of the problem



(a) Planimetric view of the simple geometrical configuration. The red line represent a thin and impermeable barrier, the dashed line the (imaginary) boundary we defined for separating the three regions called *channel A, B, C*.



(b) Cross-sectional view of the main *channel A* and notation.



(c) Geometry and system of reference adopted in the case of non-zero angle α .

Figure 7.3: Geometrical configuration and notation.

A two-step analysis is proposed, whereby the idealized configuration of figure 3a is initially investigated (vanishing bifurcation angle) and the more realistic layout with bifurcates diverging by an angle 2α is successively examined.

Indeed many laboratory and fields analysis adopted values of the angle between the distributaries (2α in the notation of figure 7.3c) ranging from 35° to 60° (Federici and Paola, 2003; Bertoldi and Tubino, 2005; Burge, 2006; Thomas et al., 2011; Hardy et al., 2011; Bertoldi, 2012). In particular the laboratory an numerical experiments of figure 7.2 Bertoldi and Tubino (2007); Siviglia et al. (2013) adopted an angle of 30° .

In Section 7.3.1 the complete two-dimensional model is formulated in dimensionless form, Section 7.3.2 describes the perturbation approach used to find the linear steady solution, which is illustrated in Section 7.3.3. The reader will note that the linear solution in this case is obtained as the sum of a one-dimensional and a two-dimensional component, which represents a specificity of the bifurcation problem that requires matching of linear solutions separately derived for channels A, B and C having different width. Section 7.3.4 then illustrates how

7.3. Formulation of the problem

the steady linear bifurcation solution can be obtained when considering two diverging bifurcates by an angle 2α and Section 7.3.5 reviews the fundamental linkage between the eigenvalues of the steady linear system derived in Section 7.3.3. and the phenomenon of $2D$ morphodynamic influence.

7.3.1 The two-dimensional model

We adopt a cartesian system of coordinates $\{x^*, y^*\}$ and we call U^* and V^* the longitudinal and cross components of the velocity vector. We also define $\{\tau_x^*, \tau_y^*\}$ and $\{qs_x^*, qs_y^*\}$ as the components of the bottom friction and the specific solid discharge respectively. In addition we use the symbols D^* for the water depth, η^* for the bottom elevation, d_s^* for the grain size and t^* for the time.

These quantities can be made dimensionless as follows

$$\left\{ \begin{array}{l} \{x, y\} := \frac{\{x^*, y^*\}}{B^*} \quad \{U, V\} := \frac{\{U^*, V^*\}}{U_0^*} \\ \{\tau_x, \tau_y\} := \frac{\{\tau_x^*, \tau_y^*\}}{\rho U_0^{*2}} \quad \{qs_x, qs_y\} := \frac{\{qs_x^*, qs_y^*\}}{qs_0^*} \\ D := \frac{D^*}{D_0^*} \quad \eta := \frac{\eta^*}{D_0^*} \quad d_s = \frac{d_s^*}{D_0^*} \quad t := \frac{t^*}{T^*} \end{array} \right. \quad (7.5)$$

where ρ is the water density, B^* is the horizontal length scale, taken to coincide with the width of the bifurcates, U_0^* , D_0^* , qs_0^* are the reference values for velocity, depth and solid discharge respectively.

The morphological timescale is defined from the sediment continuity equation and reads

$$T^* := \frac{D_0^* B^* (1-p)}{qs_0^*} \quad (7.6)$$

where qs_0^* is the reference value of the unit bedload transport capacity and p denotes the porosity of the bed material.

Assuming the morphological evolution to be much slower compared to the hydrodynamic timescale allows to neglect the local time derivatives in the momentum equations; under this approximation the two-dimensional conservation of x -momentum, y -momentum, water mass and sediment mass can be expressed through the following set of partial differential equations

$$\left\{ \begin{array}{l} U \frac{\partial U}{\partial x} + V \frac{\partial U}{\partial y} + \frac{1}{Fr_0^2} \frac{\partial}{\partial x} (\eta + D) + \beta \frac{\tau_x}{D} = 0 \\ U \frac{\partial V}{\partial x} + V \frac{\partial V}{\partial y} + \frac{1}{Fr_0^2} \frac{\partial}{\partial y} (\eta + D) + \beta \frac{\tau_y}{D} = 0 \\ \frac{\partial UD}{\partial x} + \frac{\partial VD}{\partial y} = 0 \\ \frac{\partial \eta}{\partial t} + \frac{\partial qs_x}{\partial x} + \frac{\partial qs_y}{\partial y} = 0 \end{array} \right. \quad (7.7)$$

7.3. Formulation of the problem

where the Froude number and aspect ratio are defined as follows

$$Fr_0 := \frac{U_0^*}{\sqrt{gD_0^*}} \quad \beta := B^*/D_0^* \quad (7.8)$$

In order to close the problem we need to specify, if we consider U, V, D, η as primitive variables, an expression for $\tau_x, \tau_y, qs_x, qs_y$.

This is achieved through a “local equilibrium” approximation whereby closure relation for near bed Shields stress and bedload rates can be evaluated through uniform flow relations using the local values of the primitive variables.

The magnitude of the bottom friction can be estimated by considering the Chèzy formula and the direction of the velocity vector, which leads to

$$\{\tau_x, \tau_y\} = \{U, V\} \frac{|\vec{U}|}{C^2} \quad (7.9)$$

where the dimensionless Chèzy coefficient can be estimated as (Engelund and Fredsoe, 1982) or, alternatively, by adopting the Manning formula, namely

$$C = 6 + 2.5 \log \left(\frac{D}{2.5 d_s} \right) \quad C = \frac{1}{n\sqrt{g}} \left(\frac{D}{d_s} \right)^{\frac{1}{6}} \quad (7.10)$$

As typical of gravel-bed bifurcations we assume bedload as the dominant model of sediment transport; bedload rate therefore reads

$$|\vec{q}\vec{s}|^* = \Phi(\theta) \sqrt{g\Delta d_s^{*3}} \quad (7.11)$$

where the Shields parameter θ is defined as

$$\theta = \frac{\tau^*}{\rho g \Delta d_s^*} = Fr_0^2 \frac{|\vec{\tau}|}{\Delta d_s} \quad (7.12)$$

The dimensionless bedload rate can be consequently expressed as

$$|\vec{q}\vec{s}| = \frac{\Phi(\theta)}{\Phi_0} \quad (7.13)$$

where we compute $\Phi(\theta)$ using the bedload formula of Parker (1990).

The bedload rate vector is assumed to deviate from the local velocity vector γ_q by a correction γ_g (Ikeda, 1981; Talmon et al., 1995) due to the bottom gradient in the direction normal to the velocity, namely

$$\gamma_q = \tan \left(\frac{V}{U} \right) \quad \gamma_g = -\frac{r}{\sqrt{\theta}} \frac{\partial \eta}{\partial \hat{n}_q} \quad (7.14)$$

The dimensionless bedload discharge is finally given by

$$\{qs_x, qs_y\} = \frac{\Phi(\theta)}{\Phi_0} \{\cos(\gamma_q + \gamma_g), \sin(\gamma_q + \gamma_g)\} \quad (7.15)$$

7.3.2 Perturbation approach

The governing mathematical model we obtain is formed by a system of four non-linear partial differential equations in two space dimensions (Eq. 7.7) whose initial-boundary problem can be fully solved only through numerical approximation.

Nevertheless under the hypothesis of relatively small perturbations with respect to a known basic solution it is possible to linearize the problem; this enables, for some particular geometrical and boundary configurations, to obtain an analytical solution, which has the main advantage of allowing to easily detect the main controlling parameters and efficiently explore the system behaviour within a broad range of controlling factors.

Referring to the basic straight channel of width $2B^*$ solution is usually taken as the uniform flow that would occur on a flat-bottom sloping channel, and has constant values of depth D_0 and velocity U_0 , namely

$$\{\eta, U, V, D\} = \{\eta_0 = -S_0\beta x, U_0, 0, D_0\} \quad (7.16)$$

where S_0 is the longitudinal slope.

A perturbation solution of Eq. 7.7 is obtained by expanding the four unknowns (η, U, V, D) around the basic state as follows

$$\begin{cases} \eta = -S_0\beta x + \epsilon \eta_1(x, y, t) + \mathcal{O}(\epsilon^2) \\ U = U_0 + \epsilon U_1(x, y, t) + \mathcal{O}(\epsilon^2) \\ V = V_0 + \epsilon V_1(x, y, t) + \mathcal{O}(\epsilon^2) \\ D = D_0 + \epsilon D_1(x, y, t) + \mathcal{O}(\epsilon^2) \end{cases} \quad (7.17)$$

where the small parameter ϵ measures the order of magnitude of the perturbations and $\mathcal{O}(\epsilon^2)$ indicates quadratic and higher order terms as far as the perturbations are sufficiently small to ensure that the non-linear effects are weak.

The scaling parameters U_0^* , D_0^* can be conveniently selected in order to obtain

$$\{\eta_0, U_0, V_0, D_0\} = \{-S_0\beta x, 1, 0, 1\} \quad (7.18)$$

while a proper choice of the scaling flux Φ_0 gives, without any loss of generality

$$qs_0 = \frac{\Phi(\theta_0)}{\Phi_0} = 1 \quad (7.19)$$

Substituting this expansion into Eq. 7.7 we obtain the following uniform flow relations

$$\theta_0 = \frac{S_0}{\Delta d_s} \quad Fr_0^2 = S_0 C_0^2 \quad (7.20)$$

where C_0 is the Chézy coefficient of the uniform flow. This relations allow for an univocal definition of the basic flow once that three independent parameters (typically β , θ_0 , d_s) are fixed.

7.3. Formulation of the problem

7.3.3 The steady linear solution

The complete linear solution for the free bifurcation requires to separately solve the 2D linear morphodynamic problem for each of the three separate channels A, B, C and then match them through suitable nodal conditions. Matching the solutions for the three channels also implies that every solution is obtained referring to the same cartesian coordinate system (x, y) displayed in figure 7.3. This means that the origin of the y -axis is located on the centerline of channel A , on the right bank of channel B and on the left bank of channel C .

In this section we derive the steady linear solution for the channel B ; this is analogous to Colombini et al. (1987), except for a different choice of the width ($2B^*$ in that case). Obtaining the solution for channels A and C is straightforward and only requires to shift the location of the streamwise axis x with respect to the lateral channel boundaries (see Sections 7.4.1 and 7.4.2 for more details).

The linear approximation of the system of Eq. 7.7, at the order $O(\epsilon)$, reads

$$\begin{cases} \frac{\partial U_1}{\partial x} + \frac{1}{Fr_0^2} \frac{\partial(D_1 + \eta_1)}{\partial x} + \frac{\beta}{C_0^2} [2U_1 - D_1(1 + 2C_D)] = 0 \\ \frac{\partial V_1}{\partial x} + \frac{1}{Fr_0^2} \frac{\partial(D_1 + \eta_1)}{\partial y} + \frac{\beta}{C_0^2} V_1 = 0 \\ \frac{\partial D_1}{\partial x} + \frac{\partial U_1}{\partial x} + \frac{\partial V_1}{\partial y} = 0 \\ \frac{\partial \eta_1}{\partial t} + \frac{\partial V_1}{\partial y} - \frac{r}{\beta\sqrt{\theta_0}} \frac{\partial^2 \eta_1}{\partial y^2} + 2\Phi_T \frac{\partial U_1}{\partial x} - 2\Phi_T C_D \frac{\partial D_1}{\partial x} = 0 \end{cases} \quad (7.21)$$

where Φ_T and C_D account for the dependence of bedload and flow resistance on Shields stress and depth respectively, and read

$$\Phi_T := \frac{\theta_0}{\Phi_0} \frac{\partial \Phi}{\partial \theta} \Big|_{\theta=\theta_0} \quad C_D := \frac{D_0}{C_0} \frac{\partial C}{\partial D} \Big|_{D=D_0} \quad (7.22)$$

which represent how bedload and flow resistance depends on Shields stress and depth respectively.

The first order linear system of Eq. 7.21 can be solved by Fourier analyzing the unknowns in the transverse (y) direction, thus obtaining a cascade of partial differential problems in the independent variables (x, t) for each Fourier mode m . The linearity of Eq 7.21 allows to solve the differential problem for each m separately, which also reduce to ordinary differential problems when the steady solution is of interest, like in our case. Without loss of generality, the assumption of semi-infinite length of each channel that are only bounded at their node end enables to assume a periodic structure of the unknowns also in the streamwise direction x .

7.3. Formulation of the problem

The Fourier expansion has the following structure

$$\begin{aligned} \{\eta_1, U_1, D_1\} &= \{\hat{\eta}_m, \hat{U}_m, \hat{D}_m\} \cos(m\pi y) \exp(\lambda_m x + \omega t) \\ V_1 &= \hat{V}_m \sin(m\pi y) \exp(\lambda_m x + \omega t) \end{aligned} \quad (7.23)$$

where λ_m is the (complex) wavenumber, ω the (complex) frequency and $(\hat{\eta}_m, \hat{U}_m, \hat{V}_m, \hat{D}_m)$ are complex constants.

It is worth to notice that, being m an integer number, Eq. 7.23 automatically satisfies the condition of zero water and sediment flux across the lateral walls, namely

$$V_1 = 0 \quad \frac{\partial \eta_1}{\partial y} = 0 \quad @ \ y = \{0, 1\} \quad (7.24)$$

On substituting Eq. 7.23 into Eq. 7.21 we obtain an homogeneous algebraic linear system, which admits a nontrivial solution provided the following solvability condition holds

$$f_m(\omega, \lambda_m, \beta, d_s, \theta_0) = 0 \quad (7.25)$$

for given ω and uniform flow parameters $\{\beta, d_s, \theta_0\}$, f_m is a 4th order polynomial in λ which admits four eigenvalues λ_{mj} ($j = 1, \dots, 4$) that are the key to explain the phenomenon of morphodynamic influence (see section 7.3.5).

Differently from the classical solution of steady bars in straight channels (e.g. Struiksma and Crosato, 1989; Seminara and Tubino, 1992) in the case of the bifurcation problem the solution of Eq. 7.23 has to be obtained as the sum of a 1D $((\eta_1, U_1, D_1)^{1D}$: transverse mode $m = 0$) and a 2D $((\eta_1, U_1, D_1)^{2D}$: transverse modes $m \geq 1$) linear steady solutions.

The steady 1D solution can not be straightforwardly derived by fixing $m = 0$ and $\omega = 0$ in Eq. 7.23; indeed as detailed in appendix 7.9.2 a singularity appears for $\omega \rightarrow 0$. However we can easily solve the problem by considering the water and sediment continuity (third and fourth lines of Eq. 7.21), which imply that any steady solution is uniform, namely

$$U_1 = \text{const} \quad D_1 = \text{const} \quad (7.26)$$

Substituting these value into the x -momentum equation (first line of Eq. 7.21) and remembering Eq. 7.20 gives

$$\eta_1 = -\beta S_1 x + \tilde{\eta}_0 \quad S_1 = S_0 [2 U_1 - D_1 (1 + 2 C_D)] \quad (7.27)$$

where the integration constant $\tilde{\eta}_0$ indicates an uniform variation of the bottom elevation whereas S_1 represents a variation of the bed slope. An unique solution can therefore be determined once that the three constants $\tilde{D}_0, \tilde{D}_0, \tilde{\eta}_0$ are fixed.

7.3. Formulation of the problem

In order to make the variation of the discharge and slope explicit we prefer to adopt \tilde{Q}_0, S_1 , which gives

$$\{\eta_1, U_1, D_1\}^{1D} = \underbrace{\tilde{\eta}_0 \{1, 0, 0\}}_{\text{Uniform } \eta \text{ perturbation}} + \underbrace{\tilde{Q}_0 \{0, \gamma_1, \gamma_2\}}_{\text{Discharge perturbation}} + \underbrace{S_1 \{-\beta x, \gamma_3, -\gamma_3\}}_{\text{Slope variation}} \quad (7.28)$$

where $\tilde{\eta}_0, S_1, \tilde{Q}_0$ are independent parameters and the coefficients $\gamma_1, \gamma_2, \gamma_3$ are defined in appendix 7.9.2 (Eqs. 7.88 and 7.88).

The 1D solution of Eq. 7.28 is a constant value in the transverse direction and physically expresses the lowest-order ($m = 0$) channel response felt by a variation in the flow discharge (term proportional to \tilde{Q}_0) or and adjustment of the slope (term proportional to S_1) or by a uniform variation of the bottom elevation $\tilde{\eta}_0$.

In the case of the 2D solution ($m \geq 1$), for each wavenumber λ_{mj} the following relation between the amplitudes (and phases) of the different dependent variables can be determined

$$\{\hat{\eta}_{mj}, \hat{U}_{mj}, \hat{V}_{mj}, \hat{D}_{mj}\} = \tilde{\eta}_{mj} \{1, \phi_{mj}, \delta_{mj}, \xi_{mj}\} \quad j = 1..4 \quad (7.29)$$

where $\tilde{\eta}_{mj}$ is an arbitrary (complex) constant and the coefficients ϕ, δ, ξ depends on the basic flow.

In this way for each Fourier mode m we obtain four solutions of the form given by Eq. 7.23 each one proportional to $\tilde{\eta}_{mj}$; due to the linearity of the problem the complete 2D steady solution is obtained by simply adding the solution for each mode m , namely

$$\begin{aligned} \{\eta_1, U_1, D_1\} &= \cos(m\pi y) \sum_{j=1}^4 \tilde{\eta}_{mj} \{1, \phi_{mj}, \xi_{mj}\} E_{mj} \\ V_1 &= \sin(m\pi y) \sum_{j=1}^4 \tilde{\eta}_{mj} \delta_{mj} E_{mj} \end{aligned} \quad (7.30)$$

where we have defined

$$E_{mj} = \exp(\lambda_{mj}x + \omega t) \quad (7.31)$$

The complete linear steady solution for a straight channel can be expressed by simply summing the two dimensional 7.30 and one-dimensional 7.28 components. Specifically, considering a finite sum of the first N Fourier modes the

7.3. Formulation of the problem

solution reads

$$\begin{aligned}
\{\eta_1, U_1, D_1\} &= \{\eta_1, U_1, D_1\}^{1D} + \{\eta_1, U_1, D_1\}^{2D} \\
&= \sum_{m=1}^{N-1} \left[\sum_{j=1}^4 \tilde{\eta}_{mj} \{1, \phi_{mj}, \xi_{mj}\} E_{mj} \right] + \\
&\quad + \tilde{\eta}_0 \{1, 0, 0\} + \tilde{Q}_0 \{0, \gamma_1, \gamma_2\} + S_1 \{-\beta x, \gamma_3, -\gamma_3\} \\
V_1^{2D} &= \sum_{m=1}^{N-1} \left[\sum_{j=1}^4 \tilde{\eta}_{mj} \delta_{mj} E_{mj} \right]
\end{aligned} \tag{7.32}$$

A fundamental property of the obtained linear solution, representing the key mathematical ingredient that links the "free" bifurcation stability with morphodynamic influence, is the number of degrees of freedom for the solution in each channel, in other words the number of complex constants that can be chosen arbitrarily. The solution of Eq. 7.32, which refers to the left downstream bifurcate (channel B) represents a linear combination of the following $3 + 4N - 4 = 4N - 1$ parameters

$$\begin{array}{ll}
\tilde{\eta}_1, \tilde{Q}_0, S_1 & 3 \text{ parameters} \\
\tilde{\eta}_{m1}, \tilde{\eta}_{m2}, \tilde{\eta}_{m3} \quad \forall m = 1..N-1 & 4N - 4 \text{ parameters}
\end{array} \tag{7.33}$$

As we pointed out before in a semi-infinite channel only a subset of these components is acceptable with the condition of a bounded solution.

7.3.4 Linear solution for the small-angle divergent bifurcation

Let us consider a bifurcation with an angle 2α between the two distributaries, each of them having the same width B^* .

We model the effect of the angle α as producing a perturbation of the basic uniform flow that can be expanded the Taylor series in the parameter α , namely

$$\begin{cases}
\eta = -S_0 \beta x + \alpha \eta_1(x, y) + \mathcal{O}(\alpha^2) \\
U = U_0 + \alpha U_1(x, y) + \mathcal{O}(\alpha^2) \\
V = V_0 + \alpha V_1(x, y) + \mathcal{O}(\alpha^2) \\
D = D_0 + \alpha D_1(x, y) + \mathcal{O}(\alpha^2)
\end{cases} \tag{7.34}$$

Under the hypothesis of relatively small angle only linear terms $\mathcal{O}(\alpha)$ are retained.

Referring to figure 7.3c), and considering a rotated coordinate system in channels B and C , a linear problem is obtained for each of the three channels, which is formally identical to the one solved in the previous section.

The main differences compared to the bifurcation with vanishing angle lies in the matching condition that contains in this case a symmetric forcing

7.3. Formulation of the problem

term which leads to a well defined symmetric solution for the four variables η_1, U_1, V_1, D_1 which depends on the basic flow only. It is worth to notice that because of the symmetry this solution does not affect the water and sediment distribution, which remains perfectly balanced.

Eq. 7.34 represents only the particular solution of the problem forced by the bifurcation angle and it vanishes for $\alpha = 0$. The linearity of the problem allows to construct a general solution as the sum of the forced $\mathcal{O}(\alpha)$ symmetric component and the free $\mathcal{O}(\epsilon)$, anti-symmetric part.

7.3.5 Morphodynamic influence and its relation to the eigenvalues of the linear system

According to the theory of (Zolezzi and Seminara, 2001) the sign of $real(\lambda_{1j})$ (spatial growth rate of each solution) plays a key role in determining the dominant direction of morphological influence. This result can be explored by considering the first ($m = 1$) transverse mode only: for this reason we will omit, for the sake of notation compactness, the index m .

Figure 6.3 illustrates the dependency of the four eigenvalues λ_{1j} ($j = 1, \dots, 4$) for the 2D steady ($\omega = 0$) solution on the channel aspect ratio β . Specifically, the left panel shows that the sign of the two complex conjugate eigenvalues $real(\lambda_2, \lambda_3)$ changes with the aspect ratio β ; the point at which they vanish is called (after Blondeaux and Seminara (1985)) resonance aspect ratio and identified with the symbol β_R .

On the basis of the channel aspect ratio with respect to this particular values two cases can be identified:

- super-resonant ($\beta > \beta_R$); in this case $real(\lambda_j) > 0$ for three eigenvalues ($j = 2, 3, 4$) and the upstream influence is dominant;
- sub-resonant ($\beta < \beta_R$): only one the eigenvalue λ_4 is positive and the dominant influence occurs downstream;

In order to understand the connection between resonance and upstream influence we can consider a semi-infinity rectangular channel extending to $-\infty$ (left part of figure 6.4); if we look for bounded (i.e. limited) solutions having the form of Eq. 7.23 we must reject the solutions associated with the eigenvalues $\lambda_j < 0$ which are exponentially growing in the upstream (negative x) direction.

Under super-resonant conditions three independent solution are acceptable, included the two associated with the two complex conjugate eigenvalues λ_2 and λ_3 which, having a smaller real part, lead to a relatively small damping rate; this means that any perturbation can influence the morphodynamics relatively far upstream..

On the other hand, under sub-resonant conditions, the only acceptable solution which correspond is rapidly damping because is associated with a relatively large eigenvalue $real(\lambda_4)$; consequently only a marginal, local upstream influence occurs.

7.4. Free steady solution for a channel bifurcation

Completely opposite is the behaviour of the semi-infinite channel which extends towards $+\infty$ (right side of figure 6.4): in this case the downstream influence is possible under sub-resonant conditions (when the two small, negative λ_2 and λ_3 are acceptable), whereas if $\beta > \beta_R$, the only possible solution (associated with λ_1) is rapidly damping, thus producing only a short and limited downstream influence.

The solution plotted in figure 6.3 represents the first ($m = 1$) Fourier mode only; however it is easy to prove that the eigenvalues for the higher modes correspond simply to the λ for the first mode in a channel having an aspect ratio reduced by a factor m . More precisely the following relation between different modes holds

$$f_m(\omega, \lambda_{mj}, \beta, d_s, \theta_0) = f_1(\omega, \lambda_{1j}m, \beta/m, d_s, \theta_0) \quad (7.35)$$

so that, once f_1 is known, the entire set of eigenvalues (including those relative to $m > 1$) can be determined.

According to Eq. 7.35 if $\beta < 2\beta_R$ there are three negative eigenvalues for all $m > 1$; this means that for the higher modes $m \geq 2$ there are always three linearly independent solutions in the downstream infinite channel and one in the upstream infinite channel (see figure 6.4).

7.4 Free steady solution for a channel bifurcation

Once the solution for a single semi-infinite channel is known we can move towards the more complex case of the bifurcation composed with three straight, semi-infinite channels which join together at the bifurcation node, as illustrated in figure 7.3a.

This section starts by considering the zero-angle bifurcation, whereas the more general case of symmetrically divergent distributaries is studied in the following.

Similarly to the solution for a localised channel curve (Zolezzi and Seminara, 2001) or for an obstacle in a straight channel (*Chapter 7* of the present thesis), the solution for the domain which represents a bifurcation, can be determined by imposing the matching of the four primary variables across the three different channels. However, with respect to the previous works we just mentioned, the procedure to derive a solution for the bifurcating channel shows importance differences both from a formal and a substantial point of view, namely:

- In the case of Zolezzi and Seminara (2001) (or the present *Chapter 7*), the formation of the steady bars pattern is due to the forcing effect exerted by the curve (obstacle) itself; consequently the solution of the linear problem is fixed by the intensity of the geometrical perturbation (curvature or obstacle width respectively). For the zero-angle bifurcation no forcing effects occurs, but the steady configuration we can determine is the result

7.4. Free steady solution for a channel bifurcation

of a instability which arises under certain (namely super-resonant) conditions as a free response of the system. From a linear point of view, any multiplication of the solution with a (complex) constant furnish again a solution of the problem; therefore in cases where not forcing effects exist the amplitude (and phase) of the final solution remains undetermined.

- Due to different width of the main and secondary branches, a different representation of the Fourier modes is needed. From a formal point of view, this slight difference makes the matching much more complicate; indeed we do not have a straightforward correspondence of each Fourier mode, but the expansion of the single component in the main channel induces an infinite number of modes in the distributaries. Consequently, the Fourier components can not be treated independently but must be solved together through an unique linear system which leads to a N -modes approximation of the exact solution.

Firstly, it is worth to consider that the linear solution can be decomposed, without any loss of generality, in symmetric and in anti-symmetric components, where in the previous the functions are even in y (except for V which is odd), namely

$$\begin{aligned} \{\eta^{sym}(y), U^{sym}(y), D^{sym}(y)\} &= \{\eta^{sym}(-y), U^{sym}(-y), D^{sym}(-y)\} \\ V^{sym}(y) &= -V^{sym}(-y) \end{aligned} \quad (7.36)$$

which indicates a solution mirrored across the x -axis. The remaining anti-symmetric part satisfy the property

$$\begin{aligned} \{\eta^{asym}(y), U^{asym}(y), D^{asym}(y)\} &= -\{\eta^{asym}(-y), U^{asym}(-y), D^{asym}(-y)\} \\ V^{asym}(y) &= V^{asym}(-y) \end{aligned} \quad (7.37)$$

and represent a solution which changes sign across the main channel axis.

Finding the symmetric part of the solution is quite easy at this point; indeed the result we would obtain by considering the three channels and imposing the matching, can be also obtained, in a more straightforward way, by following a simple physical argument. Indeed if we consider the general symmetric solution, which is composed by a sum of all the even modes of Eq. 7.32, we can notice that it does not include any flux of water, sediment and momentum across the symmetry axes. Therefore solution will not be affected by the presence of any frictionless barrier at the channel axes; consequently the symmetric component for the zero-angle bifurcation correspond to the solution for a straight channel (of width B^*) formed by the left half of channel A and the channel B. Specifically, the only possible steady solution is the basic unperturbed flow (as predicted by Zolezzi and Seminara, 2001)), whereas if we seek for migrating disturbances we expect to find the migrating central bars predicted by Colombini et al. (1987). These migrating bars arises when β is larger than $2\beta_{cr}$, which

7.4. Free steady solution for a channel bifurcation

is in any case higher than the resonance value; this symmetric disturbance will not affect the balance of the bifurcation because, due to the symmetry, induce an even partition of the discharge between the distributaries. The solution in the remaining part of the domain (right half of channel A and channel C) can be determined by symmetry (Eq. 7.36).

Conversely, the presence of an anti-symmetric component can produce a non-balanced discharge ratio as well as an inlet step between secondary branches which has been observed in laboratory scale bifurcations even in the case of a symmetrical geometrical configuration. The behaviour of the anti-symmetric part is more tricky because the odd Fourier modes for a single channel are not a solution of the problem any more. Aim of this section is to prove that in some conditions an anti-symmetric solution exists.

In the following derivation we assume that $\beta < 2\beta_R$; this is the case of most study cases reported in the literature Bolla Pittaluga et al. (2003); Miori et al. (2006); Bertoldi and Tubino (2007); Kleinhans et al. (2008); this implies that the secondary channels A and B, having half of the main channel width, are always in sub-resonant condition.

7.4.1 Solution for the downstream branches

The solution of the secondary channel can be directly obtained from the result of Eq. 7.32; however we must consider that, as described in section 7.3.5, in a semi infinite-channel not all the components are compatible. Specifically, since we assumed that the distributaries are always in sub-resonant conditions, we must exclude, from all the $2D$ modes, the $4th$ positive eigenvalue (see figure 6.4).

A similar consideration must be applied to the $1D$ component; indeed any change of the slope S_1 produce a variation of the bottom level which becomes infinite when $x \rightarrow \infty$, and is therefore not acceptable. In order to better understand, from a physical point of view, why this component must be rejected, we can imagine a channel with finite length, whose downstream boundary condition is, for example, a fixed water surface elevation; as far as the perturbation of this boundary condition is finite, the slope variation decreases with the channel length L_b and eventually becomes negligible ($S_1 = 0$) for $L_b \rightarrow \infty$.

Following these considerations we can express the solution for the (semi-infinite) secondary branches as

$$\begin{aligned} \{\eta_1^b, U_1^b, D_1^b\} &= \sum_{m=1}^{N-1} \left[\sum_{j=1}^3 \tilde{\eta}_{mj}^b \{1, \phi_{mj}^b, \xi_{mj}^b\} E_{mj}^b \right] + \tilde{\eta}_0^b \{1, 0, 0\} E_{0j}^b + \tilde{Q}_0^b \{0, \gamma_1^b, \gamma_2^b\} \\ V_1^b &= \sum_{m=1}^{N-1} \left[\sum_{j=1}^3 \tilde{\eta}_{mj}^b \delta_{mj}^b E_{mj}^b \right] \end{aligned} \tag{7.38}$$

7.4. Free steady solution for a channel bifurcation

This solution is a combination of $3N - 1$ linearly independent components, whose individual amplitude is defined by the following parameters

$$\begin{cases} \tilde{Q}_0^b, \tilde{\eta}_0^b & 2 \text{ param} \\ \tilde{\eta}_{m1}^b, \tilde{\eta}_{m2}^b, \tilde{\eta}_{m3}^b & \forall m = 1..N-1 \quad 3N - 3 \text{ param} \end{cases} \quad (7.39)$$

which represents the degrees of freedom of the solution for the distributaries.

7.4.2 Solution for the main channel

In order to determine the solution for the main channel we must firstly notice that, being the channel of width $2B^*$ and the system of reference placed at the channel centre (instead than on the left bank), it is not possible to express the solution in the form of Eq. 7.32, because a translation and scaling of the y axis with respect to the previous results is needed.

The solution can be simplified by considering the symmetry, which enables to exclude all the even modes and the $1D$ component.

Differently from the distributaries, the main channel may be either super or in sub-resonant; therefore the number of linearly independent solutions for the first Fourier mode depends on the aspect ratio with respect to β_R , and a different expression of general solution arises. For this reason the two cases and will be tackled separately in the two following sections.

Sub-resonant case

As mentioned in section 7.3.1, under sub-resonant conditions only the $j = 4$ solution is compatible with the semi-infinite length of the channel, regardless the mode m .

For this reason, we can write the general, anti-symmetric solution as the following linear combination of the N , independent components $\tilde{\eta}_{m4}$

$$\begin{aligned} \{\eta_1^a, U_1^a, D_1^a\} &= \underbrace{\tilde{\eta}_{04}^a \{1, \phi_{04}^a, \xi_{04}^a\} \sin\left(\frac{\pi y}{2}\right) E_{04}^a}_{\text{First mode}} + \underbrace{\sum_{i=1}^{N-1} \tilde{\eta}_{i4}^a \{1, \phi_{i4}^a, \xi_{i4}^a\} \sin\left(\frac{n\pi y}{2}\right) E_{i4}^a}_{\text{Higher modes}} \\ V_1^a &= \underbrace{\tilde{\eta}_{04}^a \delta_{04}^a \cos\left(\frac{\pi y}{2}\right) E_{04}^a}_{\text{First mode}} + \underbrace{\sum_{i=1}^{N-1} \tilde{\eta}_{i4}^a \delta_{i4}^a \cos\left(\frac{n\pi y}{2}\right) E_{i4}^a}_{\text{Higher modes}} \quad n := 2i + 1 \end{aligned} \quad (7.40)$$

where N indicates the number of Fourier modes taken into account. Notice that, in comparison with Eq. 7.32, each individual component has half periodicity ($n\pi/2$) (because of the double width) and \sin and \cos are exchanged (because of the translation of the system of reference).

The number of independent parameters ($\tilde{\eta}_{m4}$) in this case equals N .

7.4. Free steady solution for a channel bifurcation

Super-resonant case

For $\beta > \beta_R$ the first ($i = 1$) harmonic admits three linearly independent solutions compatible with the semi-infinite domain length.

For this reason the general N -modes solution has two more degrees of freedom compared with Eq. 7.40, and can be written as

$$\begin{aligned}
 \{\eta_1^a, U_1^a, D_1^a\} &= \underbrace{\sum_{j=1}^3 \tilde{\eta}_{0j}^a \{1, \phi_{0j}^a, \xi_{0j}^a\} \sin\left(\frac{\pi y}{2}\right) E_{0j}^a}_{\text{First mode}} + \underbrace{\sum_{i=1}^{N-1} \tilde{\eta}_{i4}^a \{1, \phi_{i4}^a, \xi_{i4}^a\} \sin\left(\frac{n\pi y}{2}\right) E_{i1}^a}_{\text{Higher modes}} \\
 V_1^a &= \underbrace{\sum_{j=1}^3 \tilde{\eta}_{0j}^a \delta_{0j}^a \cos\left(\frac{\pi y}{2}\right) E_{0j}^a}_{\text{First mode}} + \underbrace{\sum_{i=1}^{N-1} \tilde{\eta}_{i4}^a \delta_{i4}^a \cos\left(\frac{n\pi y}{2}\right) E_{i1}^a}_{\text{Higher modes}} \quad n := 2i + 1
 \end{aligned} \tag{7.41}$$

which, if compared with the sub-resonant case, shows two additional degrees of freedom $\tilde{\eta}_{02}$ and $\tilde{\eta}_{03}$, for a total of $N + 2$ independent components.

7.4.3 The matching procedure

The general N -modes solution we derived for each channel is a combination of many linearly independent components whose amplitude can be independently chosen. Among this wide spectrum of possibilities, we are now interested in the solutions which satisfy not only the differential problem within each channel, but also the matching condition across the boundary between inlet channel and distributaries.

As we have seen in the previous sections, the general solution in the secondary channel B is a linear function of $3N - 1$ independent parameters, while in the main channel A is a combination of N or $N + 2$ parameters in sub and super-resonant conditions respectively (see table 7.1).

	Channel A		Channel A		Total
	$i = 0$	$i \geq 1$	$m = 0$	$m \geq 1$	
Sub-resonant $\beta < \beta_R$	1	$N - 1$	2	$3N$	$4N - 1$
Super-resonant $\beta > \beta_R$	3	$N - 1$	2	$3N$	$4N + 1$

Table 7.1: Number of degrees of freedom (linearly independent solutions) for each channel, under sub and super-resonant conditions.

As matching conditions we impose that the N -modes expansion of the main channel solution at $x = 0$ is equal, within the range $y \in (0, 1)$, to the solution at $x = 0$ if the channel B. This condition can be ensured by expanding V^a in Fourier sine series and the other three variables in cosine series.

Due to the different width of the channels the procedure is not as straightforward as it may appear: for example if we expand the function $\sin(\pi y/2)$ in

7.4. Free steady solution for a channel bifurcation

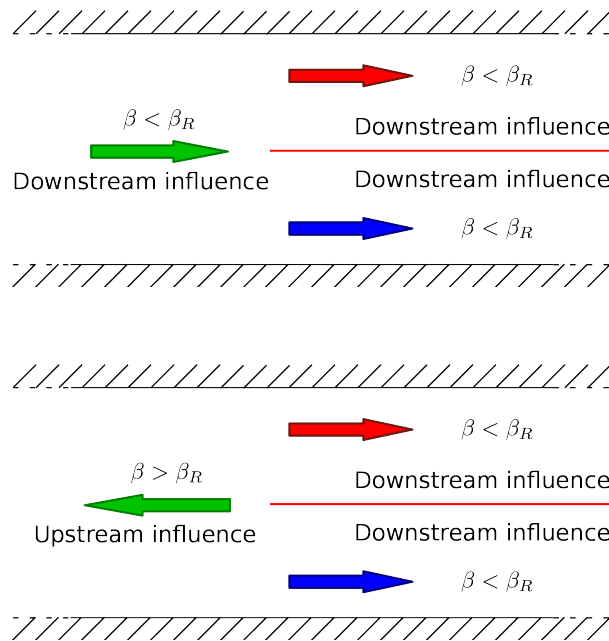


Figure 7.4: Morphodynamic influence in the different branches when the main channel is in super-resonant conditions. Because upstream and downstream influence can occur simultaneously, the bifurcation node acts like a control section and can lead to an unbalanced solution.

7.4. Free steady solution for a channel bifurcation

the interval $y \in (0, 1)$ we do not obtain a single component but the following expression

$$\sin(n\pi y/2) \simeq \sum_{m=0}^{N-1} C_{mi} \cos(m\pi y) \quad (7.42)$$

Considering the matching of the four primitive variables η, U, V, D we obtain, as detailed in section 7.9.1, a set of $4\mathbf{N} - \mathbf{1}$ matching conditions, which can be expressed as an homogeneous system of linearly independent equations.

For $\beta < \beta_R$ the number of equations equals the number of unknowns, and consequently the only solution is the banal one, which correspond to vanishing perturbation (uniform flow).

The situation is different in the super-resonant configuration, because two more degrees of freedom exist; therefore the system of equation admits ∞^2 solution or, in other words, an unique solution once two complex constants are independently fixed. In practice, since from a physical point of view only the real component of the solution is meaningless, all the possible solutions can be obtained by varying a single complex constant A regardless the value of the second constant, which can be set to zero without any loss of generality.

7.4.4 Solution for the small-angle bifurcation

If the distributaries are divergent we expect that a non-banal solution arises independently of the channel condition, included the sub-resonant regime. If the angle α is relatively small the problem can be treated in a linear way, so that a general solution can be obtained by simply summing the free part we derived above with the forced part due to the channels divergence. The presence of an angle does not affect the result in terms of bifurcation instability but simply adds a symmetric component proportional to α .

It is worth to notice that, because of the symmetrical geometry, we can seek for a solution for the upper half of the domain and then simply mirror it (following Eq. 7.36) with respect to the symmetry axes $x^a = 0$. For this reason if we insert a thin wall at $y = 0$ we do not affect the solution; therefore we can consider the channel A to have width B^* , ranging from $y = 0$ to $y = B^*$.

As we mentioned before we adopt for each of the two branches a different system of cartesian coordinates, as reported in figure 7.3c. In the rotated coordinate system the Eq. 7.34 solution at the order $\mathcal{O}(\alpha)$ for each channel is formally identical to the one at $\mathcal{O}(\epsilon)$ we derived in section 7.3.3; consequently the N mode solution of channel B can be expressed as in Eq. 7.38 (without the $1D$ component) whereas for the channel A we have only the eigenvalue $j = 4$

7.4. Free steady solution for a channel bifurcation

(figure 6.4, sub-resonant case)

$$\begin{aligned} \{\eta_1^a, U_1^a, D_1^a\} &= \sum_{m=1}^N \{\hat{\eta}_{mj}^a, \hat{U}_{mj}^a, \hat{D}_{mj}^a\} \cos(m\pi y) E_{m4} \\ V_1^a &= \sum_{m=1}^N \hat{V}_m^a \sin(m\pi y) E_{m4} \end{aligned} \quad (7.43)$$

In this framework the effect of the variation in the channel direction is felt in the matching conditions; indeed at the bifurcation node ($x = 0$) we must in this case ensure the matching of depth, bottom elevation and of the depth-averaged velocity vector. Due to the different systems of reference adopted for the two branches this can not be simply ensured by imposing the matching of the component U and V .

Indeed the components of the velocity vector \mathbf{V} can be expressed in the two systems of references as

$$\mathbf{V} = \{U^a, V^a\} = \{U^b, V^b\} \quad (7.44)$$

where the rotated components satisfy the following relation

$$\begin{cases} U^a = U^b \cos(\alpha) - V^b \sin(\alpha) \\ V^a = U^b \sin(\alpha) + V^b \cos(\alpha) \end{cases} \quad (7.45)$$

If we substitute Eq. 7.34 into Eq. 7.45 and, under the hypothesis of relatively small angles α , we neglect the higher order term we obtain

$$\begin{cases} U_1^a(0, y^a) = U_1^b(0, y^b) + \mathcal{O}(\alpha^2) \\ V_1^a(0, y^a) = V_1^b(0, y^b) + U_0 + \mathcal{O}(\alpha^2) \end{cases} \quad (7.46)$$

The term U_0 represent a forcing effect which appears because of the small deviation of the basic flow direction. This effect produces an inhomogeneity of the boundary condition, so that the uniform flow is not a solution of the differential problem any more.

Substituting Eqs. 7.43 and 7.38 into Eq. 7.46, expanding the constant term U_0 in Fourier cosine series and neglecting the higher order terms we obtain

$$\begin{aligned} \sum_{m=0}^N \{\bar{\eta}_m^a, \bar{U}_m^a, \bar{D}_m^a\} \cos(m\pi y) &= \sum_{m=0}^N \{\bar{\eta}_m^b, \bar{U}_m^b, \bar{D}_m^b\} \cos(m\pi y) \\ \sum_{m=0}^N \bar{V}_m^a \sin(m\pi y) &= \sum_{m=0}^N \bar{V}_m^b \sin(m\pi y) + U_0 \sum_{m=1}^N B_m \sin(m\pi y) \end{aligned} \quad (7.47)$$

where the overbar indicates the sum of the amplitude of each independent solution of each mode m (one upstream and three downstream) as defined in

section 7.9.1; the Fourier expansion coefficients can be computed as

$$B_m := 2 \int_0^1 \sin(m\pi y) = \begin{cases} 4/(m\pi) & \text{if } m \text{ is odd} \\ 0 & \text{if } m \text{ is even} \end{cases} \quad (7.48)$$

It is easy to see that the equation set (7.47) is satisfied if each term of the sums satisfy the two equations, namely if $\forall m$ the following relation holds

$$\begin{aligned} \{\bar{\eta}_m^a, \bar{U}_m^a, \bar{D}_m^a\} &= \{\bar{\eta}_m^b, \bar{U}_m^b, \bar{D}_m^b\} \\ \bar{V}_m^a &= \bar{V}_m^b + U_0 B_m \end{aligned} \quad (7.49)$$

where, according to our formulation, $U_0 = 1$.

The solution of this problem is much simpler than for the free, anti-symmetric case; indeed now each Fourier component does not interact with the other and can be computed separately.

Specifically, for each mode m we have a set of four matching conditions (Eq. 7.49) and the four unknowns $\tilde{\eta}_{m1}^a, \tilde{\eta}_{m2}^a, \tilde{\eta}_{m3}^b, \tilde{\eta}_{m4}^a$. The solution of the resulting 4×4 linear system is banal (equal to zero) for the even modes (no forcing effect) and easy to determine for the odd m components.

7.5 Results

This section shows the most relevant outcomes of the present work. First of all, we will consider the simple possible approximation formed by the first ($N = 1$) Fourier approximation, which allows for better understanding the reason why a non-balanced steady solution can be found only under super-resonant conditions. We will then analyse the more complete ($N \gg 1$) solution and, finally, we will compare the analytical results with previous laboratory and numerical outcomes.

7.5.1 Example: first $N = 1$ approximation

As a first approximation, we can solve the problem by considering only a single Fourier component; in this case the flow in the secondary branches is treated with a $1D$ model, whereas in the main channel only the first harmonic is accounted (sinusoidal variation of the variables in y). The matching condition is therefore very simple, and requires that the integral values of η , U , D at the bifurcation node are the same in (half) channel A and in channel B; equivalently we could say that we are imposing the conservation of the liquid and solid fluxes, as well as the energy, between the (half) inlet channel and the secondary branches.

The analysis of the previous section suggests that in the sub-resonant bifurcations the only possible steady solution is the trivial one, which correspond

7.5. Results

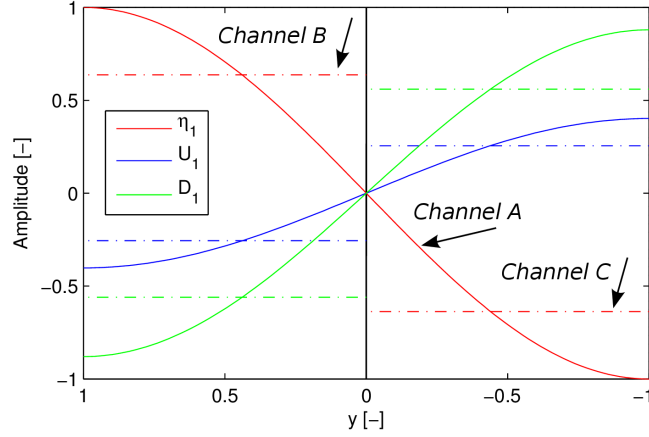


Figure 7.5: Solution at $x = 0$ in super-resonant conditions according to the first $N = 1$ approximation. Continuous line: main channel; dashed line: secondary channels. The parameters of the basic flow are $d_s = 0.05$, $\theta = 0.08$, $r = 0.5$; the aspect ratio is $\beta = 16$.

to the uniform flow. In order to better understand the reason of this behaviour we can consider the only possible steady solution in the main channel, given by the component with eigenvalue λ_4 , which represents simply as $\sin(\pi y/2)$ (\cos for the transverse velocity V) function, exponentially growing in x . In order to ensure the matching the correspondent $1D$ solution in the secondary channels should satisfy the three matching conditions described above. If we impose two of them, for example conservation of energy and liquid discharge, and we compute the ($1D$) response of the downstream branches we obtain a transport capacity which is different from the sediment flux arriving from upstream; for this reason such a configuration can not be sustained and no non-banal steady solutions exist.

Things are remarkably different under super-resonant conditions; indeed the solution of the main channel has two more degrees of freedom, so that we can linearly combine the two possible, linearly independent, solutions for the channel A in order to satisfy at the same time the three matching conditions. Figure 7.5 shows the result at the bifurcation node $x = 0$; we can see that the matching of η , U , D is ensured, which implies the conservation of energy, sediment flux and water discharge simultaneously.

7.5.2 The complete solution

The approximate solution we presented above satisfies the conservation of mass and momentum at the bifurcation node; however if we want a more accurate matching we need to increase the number of modes adopted to describe the solution.

In figure 7.6 we report the bed elevation η , obtained with $N = 50$ modes,

in both the super and sub-resonant case. If $\beta < \beta_R$ only the banal, uniform solution is possible; conversely super-resonant conditions lead to a steady configuration, where the formation of an alternate bar pattern upstream the bifurcation forces an asymmetrical discharge partition and produces an elevation difference (called inlet-step) between the distributaries.

As pointed out before, the non-banal, $\beta > \beta_R$ solution is not unique, because all the dependent variables are proportional to a complex constant A which can be arbitrary chosen; in particular the module $|A|$ define the amplitude of the solution, whereas the argument $\arg(A)$ defines the phase of the stationary bars which develops upstream (and consequently the “shape” of the solution).

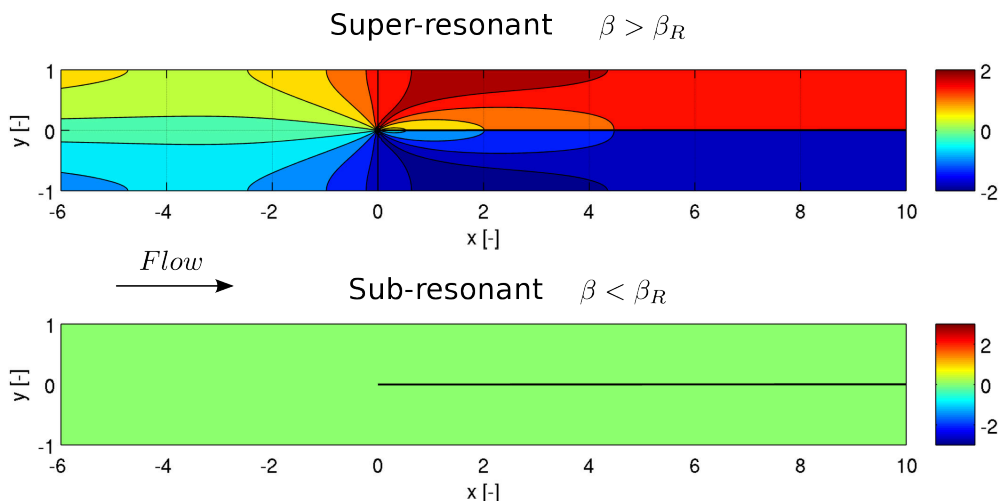


Figure 7.6: Example of bottom elevation obtained by considering $N = 50$ modes. Upper panel: super-resonant ($\beta = 15$) solution; lower panel: sub-resonant solution. $d_s = 0.05$, $\theta = 0.1$, $r = 0.5$, $\beta = 0.015$ are adopted as parameters, which leads to $\beta_R = 11.3$.

7.5.3 Comparison with numerical results and laboratory experiments

As discussed above, the laboratory experiments of Bertoldi and Tubino (2007) reveal a strong correlation between the distance from the resonance point and the bifurcation unbalancing.

Besides these laboratory results, in this section we also analyse the recent numerical outcomes of Siviglia et al. (2013), obtained by solving, in a nonlinear and fully-coupled way, the two-dimensional, shallow water morphodynamical model. Specifically, they consider a bifurcation with angle of 30° between the $1.3 B^*$ -wide branches and they chose the basic flow parameters reported in table 7.2. The authors assessed the “stable” or “unstable” character of the

7.5. Results

Parameters range	Bertoldi and Tubino (2007)	Siviglia et al. (2013)
β	4.9 ÷ 26.3	3.5 ÷ 24
θ	0.042 ÷ 0.099	0.06 ÷ 0.20
d_s	0.017 ÷ 0.092	0.015 ÷ 0.043

Table 7.2: Range of the dimensionless parameters of the basic flow within the laboratory and numerical experiments of Bertoldi and Tubino (2007) and Siviglia et al. (2013) respectively.

bifurcation by monitoring the temporal evolution of the discharge partition between the distributaries.

Before looking at the results, it is worth to recall the definition of the discharge ratio which, at the first order of approximation, gives

$$r_Q = \frac{Q^b}{Q^c} = \frac{1 + \epsilon Q_1^b + \mathcal{O}(\epsilon^2)}{1 - \epsilon Q_1^b + \mathcal{O}(\epsilon^2)} = 1 + 2\epsilon Q_1^b + \mathcal{O}(\epsilon^2) \quad r_{Q1} = 2Q_1^b \quad (7.50)$$

For each numerical and laboratory experiment, we computed the resonance point; in addition we classified the Bertoldi and Tubino (2007) runs on the basis of the discharge ratio (considering “stable” the experiments having $r_Q > 0.8 \div 0.9$). The results of figure 7.7 confirms that the aspect ratio relative to the resonance point, is correlated with the bifurcation stability; indeed most of the stable points lie in the sub-resonant region, whereas the unstable cases are located in the super-resonant domain. Within the range of explored experimental conditions this outcome is, as predicted by the theory, independent of both the Shields stress and the relative roughness.

7.5.4 The small-angle bifurcation

As we noticed in section 7.4.4, the bifurcation divergence induces a symmetric component of the solution which, under the hypothesis of relatively small angle can be analytically determined.

We have also seen that the linearity of the problem at the first order of approximation enables to express the general solution as a sum of the forced component (due to the angle) and the free component (instability of the straight bifurcation). In this section we will consider only the forced, symmetric part; however we must keep in mind that, under super-resonant conditions, an additional steady solution due to the bifurcation instability arises.

In figure 7.9b we report the resulting maps for the different quantities. As one may expect, a scour develops at the bifurcation mouths, whereas a deposition occurs at the external sides; in addition a steady bar, with internal scour and external deposition, develops at a distance of few widths from the bifurcation. Conversely, within the inlet channel only a local effect appears, without any upstream propagation of steady disturbances; this is consistent with the result of Eq. 6.10, which shows that an aspect ratio larger than twice

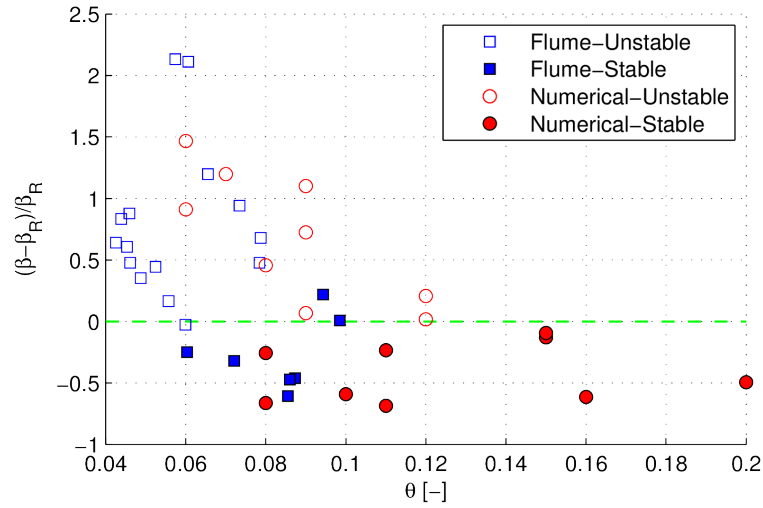


Figure 7.7: Stability of flume and laboratory bifurcation (Bertoldi and Tubino, 2007; Siviglia et al., 2013) and distance between the aspect ratio β and the resonant value β_R , for different values of the Shields stress. The green, dashed line indicates the resonant conditions.

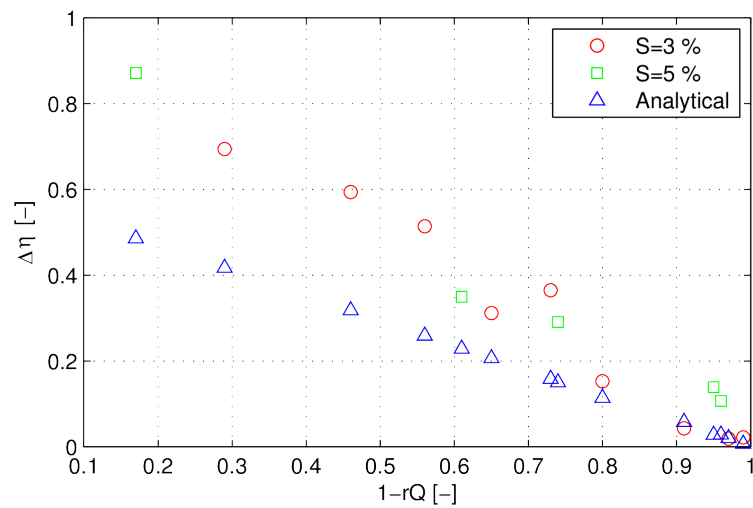


Figure 7.8: Discharge ratio and inlet step of (Bertoldi and Tubino, 2007) and inlet step computed from the analytical model correspondent to the measured r_Q .

7.5. Results

the resonant value $\beta > 2\beta_R$ is needed for the upstream propagation of steady symmetric (i.e. central) bars.

This result is from a formal point of view, an exact solution of the $2D$ model in the limit for small $\alpha \rightarrow 0$ angle. Despite its simplicity, the analytical model is able to reproduce some features observed in the solution of more complicate fully nonlinear and three-dimensional numerical models.

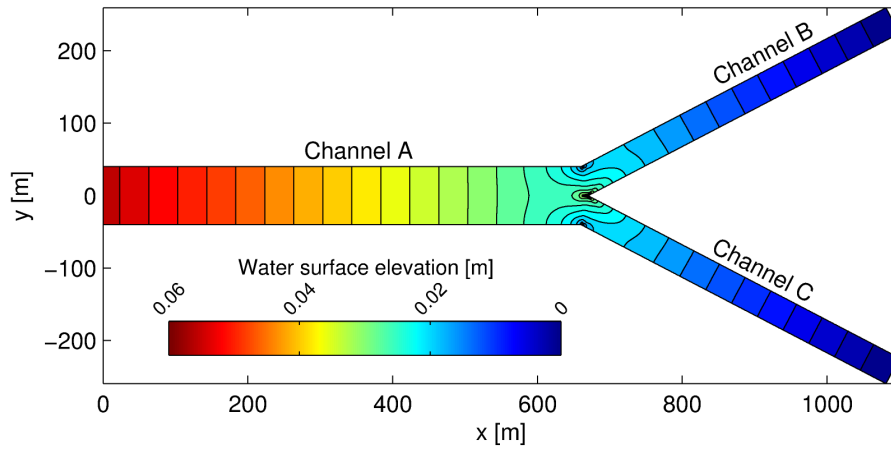
Indeed the result of figure 7.9b is in agreement with the numerical simulations of Edmonds and Slingerland (2008), who solved the $3D$ shallow water model with a k - ϵ closure for the turbulent flow. In particular we can recognise the following common features:

- small super-elevation of the water surface at the bifurcation node associated with a depression near the external bank;
- significant deposition at the bifurcation with a scour on the other side;
- deposition of an alternate bar in the distributaries, with negligible effect on the free-surface level;
- limited extension of the upstream influence.

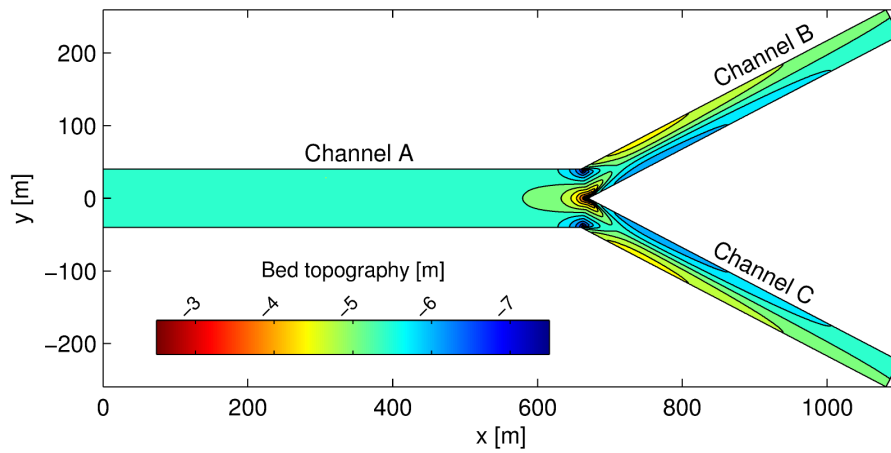
From a quantitative point of view it is worth to notice that, despite the relatively large angle adopted in the numerical simulations, the linear model is able to capture the intensity of the scour at the bifurcation vertex. Also length and position of the alternate bar in the distributaries are correctly reproduced, whereas the height is evidently underestimated by the analytical solution; this is probably because we are neglecting the secondary currents: indeed if we account for the spiral flow using a simplified algebraic closure (see appendix 7.9.3) we obtain the result of figure 7.9, where we can notice the increase of the alternate bar height in the distributaries, and better agreement with the numerical outcomes.

The simple analytical approach allows for investigating the mechanisms producing this configuration; for example the development of a mid channel bar, observed at the node of river bifurcations (e.g. Burge, 2006; Edmonds and Slingerland, 2008) can be interpreted as follows: the channel deviation produces a transverse velocity V and consequently a divergence of the flow close to the bifurcation vertex which, because of water mass continuity, causes a decrease of the velocity U (i.e. Hardy et al., 2011); this induces a decrease of the longitudinal bedload which, in order to maintain equilibrium, must be compensated by a (positive) transverse sediment flux. This flux can be sustained either by a positive V or by a negative bed gradient; due to the strong nonlinearity of the $qs(U)$ relation the first is term is not sufficient, so that deposition occurs until the lateral bed gradient is large enough to ensure equilibrium.

On the other side, close to the outer bank the flow converges, causing an increase of the longitudinal velocity and ultimately a local scour.



(a) Free surface level $(\eta_1 + D_1)\alpha$. Contours interval is 0.02 m.



(b) Bottom elevation $\eta_1\alpha$. Contours interval is 0.33 m

Figure 7.9: Analytical solution for the diverging bifurcation. Elevations are expressed in [m]; $\theta_0 = 1.3$, $d_s = 2.52 \cdot 10^{-5}$, $\beta = 16$, $r = 0.5$, $C_0 = 12.5$, $B^* = 40$ m, $\alpha = 27.5^\circ$ are adopted as parameter, the first $N = 10$ harmonics have been considered. The angle adopted for these maps is not to scale.

7.5. Results

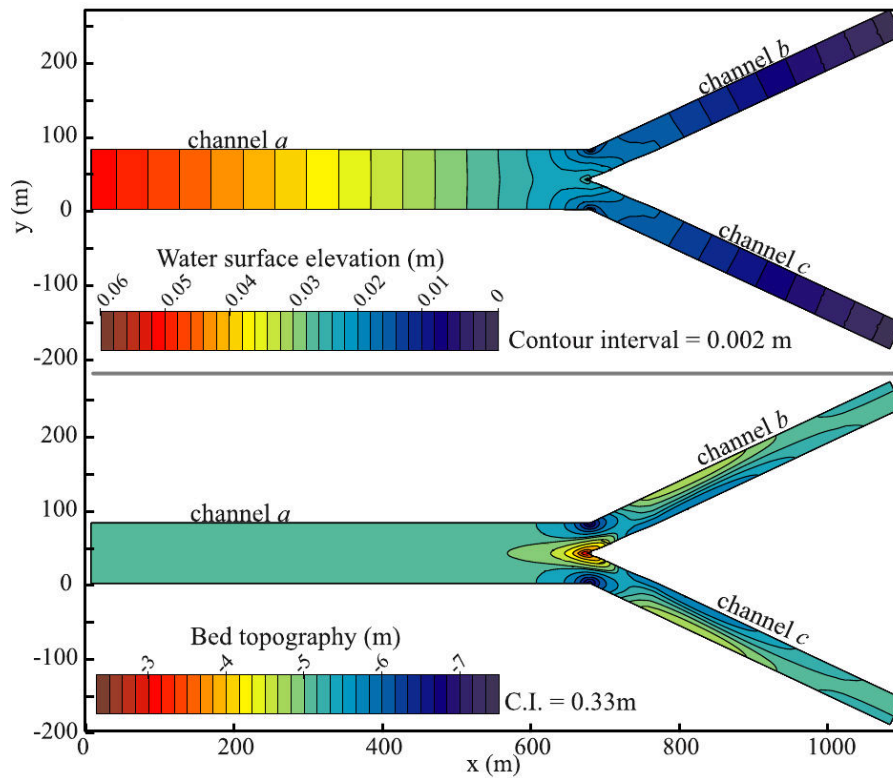


Figure 7.10: Water surface and bottom elevation in a symmetric bifurcation, according to the numerical depth-averaged model of Edmonds and Slingerland (2008). The angle between distributaries is $2\alpha = 55^\circ$. $\beta \simeq 16$, $C \simeq 12.5$, $\theta \simeq 1.3$, $d_s = 2.5 \cdot 10^{-5}$ are the parameters of the main channel flow.

7.6 Discussion

The linear analysis we propose is based on a fully two-dimensional model; for this reason, with respect to the existing theoretical models, it provides a more complete description of the mechanisms governing the bifurcation morphodynamics. Therefore, the present model does not require the introduction of a nodal point relation as simplified closure of the $2D$ processes, and consequently does not need the calibration of any ad-hoc parameter. Indeed the more relevant parameter of the $2D$ model, namely the Ikeda r coefficient, has a clear physical meaning and can be estimated on the basis of both direct and indirect (e.g. alternate bar length) observations. This is not the case for the Bolla Pittaluga et al. (2003) model; indeed the additional parameter α , despite having a well-defined physical meaning, depends (in an unknown way) on the channel conditions so that its calibration is needed.

The $2D$ formulation also allows for exploring the role of other effects, namely secondary currents, channel curvature and secondary channel angles, as well as the interaction between migrating bars and the bifurcation node. Nevertheless, being based on a merely linear approach the present theory does not allow to determine amplitude and phase of the super-resonant solution and, consequently the inlet step and the discharge ratio.

The solution we presented, being restricted to steady case, does not enable to explore the possible temporally varying solutions. However a very similar approach can be followed to study solutions which oscillates through time; the result reveals that, even under sub-resonant conditions, non-banal solutions can be found if $\beta > \beta_{cr}$, where the latter indicates the critical aspect ratio for the formation of alternating bars (Colombini et al., 1987). This solution shows an oscillating discharge ratio due to the migration of the alternate bars in the main channel, similarly to what observed in the laboratory experiments of Bertoldi et al. (2009c).

Some discussion is needed about the role of the three-dimensional effect, which are not accounted in our formulation. In the case of the straight channel we do not expect, due to the relatively small curvature of the flow, a strong effect of the secondary current on the bifurcation instability; indeed a linear analysis with a simplified closure for the secondary currents shows only a small variation of the resonant point (figure 7.12). Consequently the capability of the inlet channel to exert an upstream influence is poorly affected by the presence of a bifurcation angle. For a diverging bifurcation the role of the secondary currents is expected to be important, at least in determining the local morphology at the bifurcation node (figure 7.13 and in the distributaries, whereas the $3D$ effects appears to be limited in the main channel, as confirmed by the laboratory observations of Thomas et al. (2011).

As we have seen above, the presence of an angle between the secondary branches does not change the distribution of the flow; however it produces a

7.7. Conclusions

symmetrical morphological configuration which can be often observed in gravel-bed river bifurcations and enabled to explore the mechanism which leads to the observed scour and deposition pattern. Similarly, any symmetric perturbation, such an even variation of the slope of the distributaries or an equal variation of the downstream boundary condition (in the case of finite length distributaries), does not affect neither the equal partition of the flow in sub-resonant conditions nor the instability which arises when $\beta > \beta_R$. For example if we set an equal perturbation of the water level at the downstream boundaries, or we fix the same stage-discharge curve in channels B and C, or, more in general, any relation that does not advantage one of the two distributaries (such a perfectly symmetrical confluence) we do not expect, according to our analytical model, any modification of the discharge ratio.

On the other hand, if the geometrical configuration or the boundary conditions are asymmetrical an unbalanced morphology and an unequal discharge develops even in the stable, sub-resonant regime. For example a curvature of the main channel can force more water and sediment to flow into the outer channel; similarly if one of the tributaries is steeper or if it has a different boundary conditions it induces an asymmetry of the problem and consequently an unbalanced discharge ratio (e.g. Kleinhans et al., 2008).

On the basis of these considerations, we claim that a clear distinction should be made between the unbalanced configuration resulting from a free instability and the unbalance solution which is driven by an “external” forcing such as a slope advantage or a channel curvature.

The hypothesis of fixed banks, which is equivalent to assume that the timescale of the lateral variations is much higher than the timescale of the bed evolution, is often not fulfilled in braided rivers. For this reason Miori et al. (2006) included the effect of the bank erosion in the two-cells model, showing the tendency of a gravel bed river bifurcation to eventually reach an unbalanced flow distribution. In the perspective of the present theory a similar conclusion comes from Zolezzi et al. (2009), who observed the tendency of gravel bed rivers at low Shield stresses to behave super-resonantly.

7.7 Conclusions

Within this work we have solved analytically the shallow-water mobile-bed 2D model for a geometrically symmetrical bifurcation. In particular, under the hypothesis of small variations with respect to the basic configuration, we found a solution which: a) is valid within each of the three branches; b) satisfies suitable matching conditions which ensure the continuity of all the variables across the channels.

The analytical model shows that a non-banal, steady solution can be found if, and only if, the main channel belongs to super-resonant conditions (as defined by Blondeaux and Seminara, 1985). This result provides a rigorous theoretical

7.8. List of symbols and acronyms

explanation to the observations of Bertoldi and Tubino (2007) who noticed, on the basis of laboratory, a connection between the bifurcation dynamics and the theory of the morphodynamic influence proposed by Zolezzi and Seminara (2001).

An additional support to this theory comes from the numerical results of Siviglia et al. (2013), whose observations about bifurcation stability can be correctly interpreted in term of morphodynamic influence.

The solution we have derived refers to a simple, non-diverging bifurcation formed by a thin barrier which separates the two distributaries. However, the introduction of an angle between the secondary branches does not change the result in terms of bifurcation stability. Indeed, for relatively small angles we can derive again an analytical solution, which enables to reproduce the scour/deposition pattern predicted by fully-nonlinear numerical models and frequently observed in natural bifurcations. Such an analytical approach provides a deeper understanding of the fundamental mechanisms which drive the morphodynamic response of the diffuence.

The present model enables to clearly distinguish between the instability due to the free morphodynamic response and the effect driven by "external" forcing effects, such as the presence of a slope advantage between the distributaries or a curvature of the main channel, which both may result in an unbalanced bifurcation.

Overall, our work provides a more comprehensive analysis of the physical processes with respect to the pre-existing quasi-2D models. Specifically, it also provides a prediction of the threshold for the occurrence of unbalanced configuration which does not require an empirical estimate of the model coefficients. Indeed it enables to bypass the estimation of the coefficient α (Bolla Pittaluga et al., 2003), which has been observed to significantly vary depending on the experimental conditions, and for which no empirical nor theoretical expressions exist.

7.8 List of symbols and acronyms

Subscripts

0	Parameter of the basic flow;
R	Resonant conditions;

Superscripts

*	Dimensional quantity;
---	-----------------------

Latins

d_s	$[l]$	Sediment size;
C	$[-]$	Dimensionless Chézy coefficient;

7.8. List of symbols and acronyms

c_D	[–]	Variation of the Chézy coefficient with the water depth;
p	[–]	Porosity of the bed material;
r	[–]	Coefficient of the Ikeda (1981) formula;
g	$[lt^{-2}]$	Gravity acceleration;
qs_x^*	$[l^2t^{-1}]$	Solid discharge per unit width in longitudinal direction;
qs_y^*	$[l^2t^{-1}]$	Solid discharge per unit width in transverse direction;
t^*	$[t]$	Time;
x^*	$[l]$	Longitudinal coordinate;
y^*	$[l]$	Transverse coordinate;
\mathbf{A}	[–]	Matrix of coefficients of the linear system;
B^*	$[l]$	Width (or half width) of the channel;
B_m	[–]	Expansion of a constant value in Fourier sin series;
C_{mi}	[–]	m^{th} coeff. of the Fourier expansion of the channel A i^{th} component;
C_{mi}^V	[–]	C_{mi} for the transverse velocity V ;
D	[–]	Water depth;
E_{mj}	[–]	Longitudinal variation of the eigenvalue j of the component m ;
Fr	[–]	Froude number;
N	[–]	Number of Fourier modes considered;
S	[–]	Channel slope;
T^*	$[t]$	Time scale;
U^*	$[t^{-1}]$	Longitudinal (x) component of velocity;
V^*	$[t^{-1}]$	Transverse (y) component of velocity;

Greeks

α	$[rad]$	Bifurcation angle;
β	[–]	Aspect ratio;
γ_0	[–]	Ratio between velocity and depth uniform perturbations;
γ_q	[–]	Angle between the velocity vector and the x axis;
γ_g	[–]	Deviation of the bedload transport due to the gravitational effect;
Δ	[–]	Relative submerged density of sediment;
ϵ	[–]	Order of magnitude of the perturbation;
η^*	$[l]$	Bottom elevation;
$\vec{\eta}$	[–]	Vector of the unknown;
λ	[–]	(Complex) spatial growth;
ρ	$[Ml^{-3}]$	Water density;
Φ	[–]	Dimensionless solid discharge (Einstein scaling);
Φ_T	[–]	Variation of the solid discharge with the Shields stress;
θ	[–]	Shields parameter;
ω	[–]	(Complex) temporal growth rate;
τ_x^*	$[Ml^{-1}t^{-2}]$	Shear stress in longitudinal direction;
τ_y^*	$[Ml^{-1}t^{-2}]$	Shear stress in transverse direction;

7.9 Appendixes

7.9.1 The matching procedure

In section 7.4 we claimed that, in order to ensure the matching of the four dependent variable at the bifurcation node, we need to impose $4N - 1$ matching conditions, where N is the number of Fourier modes adopted for the approximate representation of the solution in both the main and the secondary channels.

In this section we derive step-by-step the number and the expression of these matching conditions we need to impose in order to ensure the continuity of the solution across the boundaries between the main and the secondary branches.

Because the dependent variable $\{\eta, U, D\}$ share the same transverse structure we can, for the sake of notation simplicity, develop the matching for only one quantity and repeat the procedure for the two remaining variables.

Specifically, with reference to the longitudinal velocity U the sub-resonant solution in the main channel (Eq. 7.40) evaluated at the bifurcation node ($x = 0$) can be written as

$$U_1^a(0, y) = \sum_{i=0}^{N-1} \hat{U}_{i4}^a \sin(n\pi y/2) = \sum_{i=0}^{N-1} \bar{U}_i^a \sin(n\pi y/2) \quad n := 2i + 1 \quad (7.51)$$

Similarly, for the distributaries we can write the longitudinal velocity at $x = 0$ as (Eq. 7.38)

$$\begin{aligned} U_1^b(0, y) &= \sum_{m=1}^{N-1} \left[\sum_{j=1}^3 \hat{U}_{mj}^b \right] \cos(m\pi y) + \hat{U}_{01} + \tilde{U}_0 \\ &= \sum_{m=0}^{N-1} \bar{U}_m^b \cos(m\pi y) \end{aligned} \quad (7.52)$$

where the symbols \bar{U}_m^a and \bar{U}_m^b (sum of the Fourier coefficients for each mode) are introduced for the sake of notation simplicity.

These two functions are different, so that it is not possible to obtain an exact matching with a finite number of Fourier modes N ; however we can impose the expansion U_1^a in a Fourier series (in the interval $y \in [0, 1]$) to be equal to U_1^b .

This condition can be ensured as follows: first of all let us consider a single component i of the main channel velocity (Eq. 7.51); we will than repeat the same procedure for all the N -components of the U_1^a . If we the take the single component of Eq. 7.51 in the interval $y \in [0, 1]$ and we expand it in a N -components Fourier cosine series we obtain

$$\bar{U}_i^a \sin(n\pi y/2) \simeq \sum_{m=0}^{N-1} \bar{U}_{mi}^b \cos(m\pi y) \quad (7.53)$$

7.9. Appendixes

where the coefficients can be found through the following integral

$$U_{mi}^b = 2 \bar{U}_i^a \int_0^1 \sin(n\pi y/2) \cos(m\pi y) dy \quad m \geq 1 \quad (7.54)$$

$$= \bar{U}_i^a \int_0^1 \sin(n\pi y/2) dy \quad m = 0 \quad (7.55)$$

Solving these integrals we can express Eq. 7.53 in the compact form $\bar{U}_{mi}^b = \bar{U}_i^a C_{mi}$ where the expansion coefficients are given by

$$C_{mi} := \frac{4n}{(n^2 - 4m^2)\pi} \quad m \geq 1 \quad (7.56)$$

$$:= \frac{2}{n\pi} \quad m = 0 \quad (7.57)$$

In the example of figure 7.11 we can observe how the expansion of the sine function (Eq. 7.53) is composed; in particular we can notice that with $N = 1$ only the average value on the range $y \in [0, 1]$ is captured, whereas for $N = 2$ a better description is obtained and for $N = 8$ it becomes difficult to distinguish between the original function and the Fourier approximation; despite that an exact matching would be ensured only with infinite N . As we pointed out before the solution on the other side (channel C) is not particularly interesting, because exactly the same except for the reversed sign (anti-symmetric solution, Eq. 7.37).

If we perform the expansion of Eq. 7.53 for each Fourier mode i we can approximate Eq. 7.51 as follows

$$U_1^a(0, y) = \sum_{i=0}^{N-1} \bar{U}_i^a \sin(n\pi y/2) \simeq \sum_{m=0}^{N-1} \left[\sum_{i=0}^{N-1} \bar{U}_i^a C_{mi} \right] \cos(m\pi y) \quad (7.58)$$

The term at the right hand side exactly equals the velocity in the secondary channel (Eq. 7.52) if the following relation holds $\forall m \in [0, N - 1]$

$$\bar{U}_m^b = \sum_{i=0}^{N-1} \bar{U}_i^a C_{mi} \quad (7.59)$$

which completes the derivation of the matching conditions for the variable U .

Similarly, if we repeat the same procedure for the bottom elevation and the water depth we obtain

$$\bar{\eta}_m^b = \sum_{i=0}^{N-1} \bar{\eta}_i^a C_{mi} \quad \bar{D}_m^b = \sum_{i=0}^{N-1} \bar{D}_i^a C_{mi} \quad (7.60)$$

The matching procedure is slightly different for the transverse velocity V , which has a different structure in both the main and the secondary channels.

Indeed the the transverse velocity in the main channel at the bifurcation node is represented as a series of cosines, namely

$$V^a(0, y) = \sum_{i=0}^{N-1} \left[\sum_{j=2}^4 \hat{V}_{ij}^a \right] \cos(n\pi y/2) = \sum_{i=0}^{N-1} \bar{V}_i^a \cos(n\pi y/2) \quad n = 2i + 1 \quad (7.61)$$

in which we have introduced the symbol \bar{V}_i^a to have a lighter notation.

In the secondary channel the velocity V is represented as a sum of sines, namely

$$V^b(0, y) = \sum_{m=1}^{N-1} \hat{V}_{m1}^b \sin(m\pi y) = \sum_{m=1}^{N-1} \bar{V}_m^b \sin(m\pi y) \quad (7.62)$$

where m starts from 1 because the sine series expansion does not contain any continuous component.

Following the same procedure as for the variable U we consider the generic component i of Eq. 7.61 and we expand it in $N - 1$ sines within the interval $y \in (0, 1)$, namely

$$\bar{V}_i^a \cos(n\pi y/2) = \sum_{m=1}^{N-1} \bar{V}_{mi}^b \sin(m\pi y) \quad (7.63)$$

where the Fourier coefficients can be found by solving the integral

$$\bar{V}_{mi}^b = 2 \bar{V}_i^a \int_0^1 \cos(n\pi y/2) \sin(m\pi y) dy = \bar{V}_i^a C_{mi}^V \quad (7.64)$$

The previous integral can be analytically solved, giving the following expression for the matching coefficients

$$C_{mi}^V := -\frac{8m}{(n^2 - 4m^2)\pi} \quad m \geq 1 \quad (7.65)$$

$$(7.66)$$

Consequently the matching of transverse velocity is ensured if

$$\bar{V}_m^b = \sum_{i=0}^{N-1} \bar{V}_i^a C_{mi}^V \quad \forall m \in [1, N - 1] \quad (7.67)$$

which complete the last set of matching conditions.

Summarising, the nodal conditions on the four variables (Eqs. ??, 7.60 and 7.60, can be re-written as follows

$$\{\bar{\eta}_m^b, \bar{U}_m^b, \bar{D}_m^b\} = \sum_{i=0}^{N-1} C_{mi} \{\bar{\eta}_i^a, \bar{U}_i^a, \bar{D}_i^a\} \quad \forall m \in [1, N - 1] \quad (7.68)$$

7.9. Appendixes

which represents the set of $4N - 1$ matching conditions.

The values of $\{\hat{\eta}_m, \hat{U}_m, \hat{D}_m, \hat{V}_m\}$ in all the channels are not independent but are a linear combination of $\tilde{\eta}_{mi}$. For example for the secondary channel the following quantities can be freely fixed (see Eq. ??)

$$\begin{aligned} & \tilde{\eta}_{01}^b, \tilde{D}_0 \\ & \tilde{\eta}_{mj}^b \quad j = 1, 2, 3 \quad m = 1, \dots, N - 1 \end{aligned} \quad (7.69)$$

If also the main channel is narrower than the resonant threshold $\beta < \beta_0$ only one eigenvalue for each mode is compatible with the upstream boundary condition; for this reason, as clear from Eq. 7.40, it is possible to fix only the following quantities

$$\tilde{\eta}_{i4}^a \quad i = 1, \dots, N \quad (7.70)$$

and we can write a $4N - 1 \times 4N - 1$ homogeneous linear system of the form

$$\mathbf{A}\vec{\eta} = \mathbf{0} \quad (7.71)$$

where the vector of unknowns is composed as

$$\vec{\eta} = \begin{bmatrix} \tilde{\eta}_{01}^b \\ \tilde{D}_0^b \\ \tilde{\eta}_{11}^b \\ \tilde{\eta}_{12}^b \\ \tilde{\eta}_{13}^b \\ \dots \\ \dots \\ \tilde{\eta}_{M1}^b \\ \tilde{\eta}_{M2}^b \\ \tilde{\eta}_{M3}^b \\ \tilde{\eta}_{04}^a \\ \tilde{\eta}_{14}^a \\ \dots \\ \dots \\ \tilde{\eta}_{M4}^a \end{bmatrix} \quad (7.72)$$

and the matrix of coefficients can be written as

$$\mathbf{A} = \begin{bmatrix}
 1 & 0 & 0 & 0 & 0 & \cdots & 0 & 0 & 0 & -C_{00} & -C_{01} & \cdots & -C_{0M} \\
 \phi_{01}^b & \gamma_0 & 0 & 0 & 0 & \cdots & 0 & 0 & 0 & -C_{00}\phi_{14}^a & -C_{01}\phi_{14}^a & \cdots & -C_{0M}\phi_{M4}^a \\
 \xi_{01}^b & 1 & 0 & 0 & 0 & \cdots & 0 & 0 & 0 & -C_{00}\xi_{14}^a & -C_{01}\xi_{14}^a & \cdots & -C_{0M}\xi_{M4}^a \\
 0 & 0 & 1 & 1 & 1 & \cdots & 0 & 0 & 0 & -C_{10} & -C_{11} & \cdots & -C_{1M} \\
 0 & 0 & \phi_{11}^b & \phi_{12}^b & \phi_{13}^b & \cdots & 0 & 0 & 0 & -C_{10}\phi_{14}^a & -C_{11}\phi_{14}^a & \cdots & -C_{1M}\phi_{M4}^a \\
 0 & 0 & \delta_{11}^b & \delta_{12}^b & \delta_{13}^b & \cdots & 0 & 0 & 0 & -C_{10}^v\delta_{14}^a & -C_{11}^v\delta_{14}^a & \cdots & -C_{1M}^v\delta_{M4}^a \\
 0 & 0 & \xi_{11}^b & \xi_{12}^b & \xi_{13}^b & \cdots & 0 & 0 & 0 & -C_{10}\xi_{14}^a & -C_{11}\xi_{14}^a & \cdots & -C_{1M}\xi_{M4}^a \\
 \cdots & \cdots & \cdots & \cdots & \cdots & \cdots & \cdots & \cdots & \cdots & \cdots & \cdots & \cdots & \cdots \\
 0 & 0 & 0 & 0 & 0 & \cdots & 1 & 1 & 1 & -C_{M0} & -C_{M1} & \cdots & -C_{MM} \\
 0 & 0 & 0 & 0 & 0 & \cdots & \phi_{M1}^b & \phi_{M2}^b & \phi_{M3}^b & -C_{M1}\phi_{14}^a & -C_{M2}\phi_{24}^a & \cdots & -C_{MM}\phi_{M4}^a \\
 0 & 0 & 0 & 0 & 0 & \cdots & \delta_{M1}^v & \delta_{M2}^v & \delta_{M3}^v & -C_{M1}\delta_{14}^a & -C_{M2}\delta_{24}^a & \cdots & -C_{MM}\delta_{M4}^a \\
 0 & 0 & 0 & 0 & 0 & \cdots & \xi_{M1}^b & \xi_{M2}^b & \xi_{M3}^b & -C_{M1}\xi_{14}^a & -C_{M2}\xi_{24}^a & \cdots & -C_{MM}\xi_{M4}^a
 \end{bmatrix} \quad (7.73)$$

where for notational compactness we have defined $M := N - 1$.

The trivial solution of the homogeneous system is simply a zero vector, which represent a uniform flow in the whole domain. By looking at the structure of the matrix it is easy to see that the determinant of the matrix can vanish only if the eigenvalues of each single mode in channel B.

By looking at the structure of the matrix A it is easy to see that it has a full rank; indeed it is not possible to express any row as a linear combination of the others as far as the coefficients ϕ , δ , ξ are linearly independent. For this reason the determinant of the matrix is never zero and there are not non-banal solutions which satisfies the nodal matching conditions.

If the system had been not homogeneous the solution of the linear system would not be zero; this is the case of we adopt a similar approach to model a bifurcation in which a forcing effect due to small variations of the geometry or of the boundary conditions exist (i.e. small-angle bifurcation of section 7.4.4). From a physical point of view this mean (as we expect) that in a more complex configuration the simple uniform flow is never a solution of the problem.

Now let us consider a bifurcation whose main channel is in super-resonant conditions. In this case for the first mode ($i = 1$) we have two more linearly independent solutions Channel a and consequently two more unknowns which lead to a linear system with a kernel of dimension two (or loosely speaking to ∞^2 solutions).

This suggest us that in this conditions an unbalanced configuration even in this very simple configuration is possible. Nevertheless the linear theory does not allow us to determine a single solution but an infinite number of possibilities characterised by different values of amplitude and phase.

7.9.2 Stationary 1D solutions

This section focuses on: a) the derivation of the time-dependent, 1D ($m = 0$) solution of the linear system of Eq. 7.21 b) solution of the steady problem as a

7.9. Appendixes

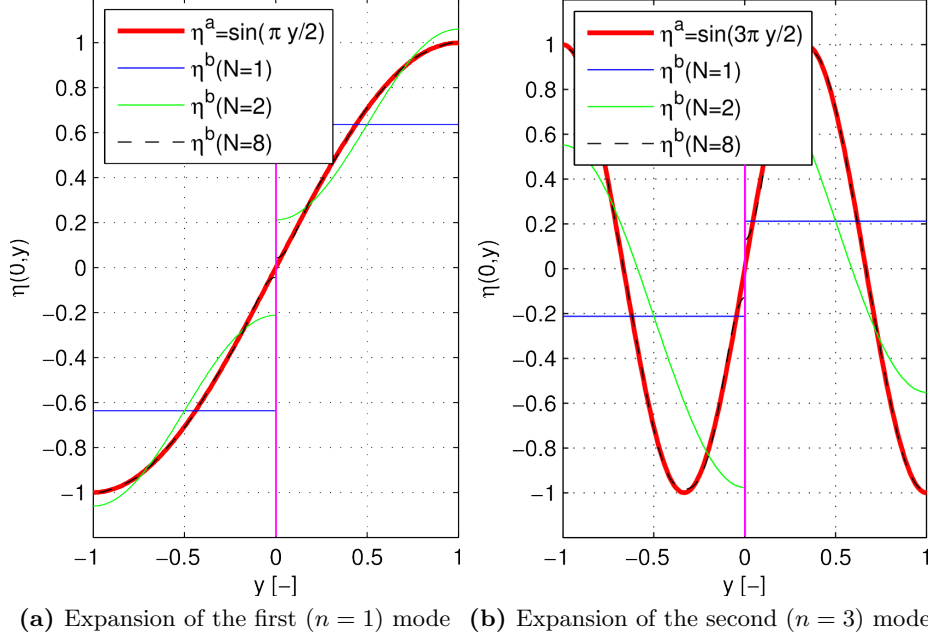


Figure 7.11: Example of the expansion of the first two modes in channel A as sum of N modes in the secondary channels.

limit, for slow time variations, of the previous time-dependent result.

As in the $2D$ problem, we can start by seeking solutions having the form of Eq. 7.23, for the particular case $m = 0$, namely

$$\begin{aligned} \{\eta_1, U_1, D_1\} &= \{\hat{\eta}_{0j}, \hat{U}_{0j}, \hat{D}_{0j}\} \exp(\lambda_0 x + \omega t) \\ V_1 &= 0 \end{aligned} \quad (7.74)$$

Substituting this expression into the linear system (Eq. 7.21), three linearly independent solutions can be found. Two of them can be written (analogously to the four $2D$ solution of Eq. 7.75) as follows

$$\{\eta_1, U_1, D_1\} = \tilde{\eta}_{0j} \{1, \phi_{0j}, \xi_{0j}\} \quad j = 1, 2 \quad (7.75)$$

where $\tilde{\eta}_{0j}$ are independent parameters, ϕ_{0j} depend on the the basic flow through θ_0 and d_s and $\phi_{0j} = \xi_{0j}$.

Hoever, at this point, a difference with the $2D$ ($m \geq 1$) arises. Indeed for $m = 0$ the third eigenvalue is zero ($\lambda_0 = 0$), thus representing an uniform perturbation. The corresponding solution represents a variation in time of the discharge without any perturbation bed elevation; therefore it can not be written in the form of Eq. 7.75, which would need infinite coefficients ϕ_{0j} and ξ_{0j} , but can be expressed as

$$\{\eta_1, U_1, D_1\} = \tilde{Q}_0 \{0, \gamma_1, \gamma_2\} \exp(\omega t) \quad (7.76)$$

where γ_1, γ_2 are the variations of velocity and depth due to a unitary perturbation of discharge and are defined as

$$\gamma_1 := \frac{1 + 2 C_D}{3 + 2 C_D} \quad \gamma_2 := \frac{2}{3 + 2 C_D} \quad (7.77)$$

The meaning of the parameter \tilde{Q}_0 is clear if we compute the discharge, which from a linear level, is given by

$$Q_1 = U_1 + D_1 = \tilde{Q}_0 \exp(\omega t) \quad (7.78)$$

By summing the three linearly independent components (Eq. 7.75 and Eq. 7.76) we obtain the full expression of the $1D$, time-dependent solution, namely

$$\{\eta_1, U_1, D_1\} = \sum_{j=1}^2 \tilde{\eta}_{0j} \{1, \phi_{0j}, \xi_{0j}\} E_{0j} + \tilde{Q}_0 \{0, \gamma_1, \gamma_2\} \exp(\omega t) \quad (7.79)$$

where $\tilde{\eta}_{0j}$ and \tilde{Q}_0 are three independent parameters.

Once the time-dependent problem has been solved we can move to the second step of this section: the derivation of the steady, $1D$ solution. Obtaining the steady solution as a limit for small temporal variations of Eq. 7.79, is more tricky than for the $2D$ problem. Indeed the limit for $\omega \rightarrow 0$ we have $\lambda_{01} = \lambda_{02} = 0$ and both the two solutions of Eq. 7.75 becomes identical, namely

$$\{\eta_1, U_1, D_1\} = \tilde{\eta}_{0j} \{1, 0, 0\} \quad j = 1, 2 \quad (7.80)$$

which represents a banal uniform variation of the bottom elevation without any perturbation on the hydrodynamics. Since two identical solution arises, only two independent components remain and one of the three degrees of freedom is lost.

In order to maintain the third solution during the limit process we must to re-scale the problem when we approach $\omega = 0$, which is possible because the linearity of the solution allows the multiplication by an arbitrary scaling factor.

Specifically, if we choose opposite coefficients $\tilde{\eta}_{02} = -\tilde{\eta}_{01}$ and we consider the sum of the two solutions of Eq 7.80 we obtain, in the limit $\omega \rightarrow 0$, a zero solution (see Eq. 7.80). However if we magnify the amplitude of the two components as follows

$$\tilde{\eta}_{01} = -\tilde{\eta}_{02} = \frac{A}{\lambda_{01}} \quad (7.81)$$

(where A is an arbitrary constant) and we substitute Eq. 7.81 into the sum of the two solutions of Eq. 7.74 we obtain

$$\eta_1 = \frac{A}{\lambda_{01}} [\exp(\lambda_{01}x) - \exp(\lambda_{02}x)] \quad (7.82)$$

7.9. Appendixes

In the limit $\omega \rightarrow 0$ it is possible to prove that $\lambda_{02} \simeq -\lambda_{01} \rightarrow 0$, so that the limit of Eq. 7.82 becomes

$$\eta_1 = 2Ax \quad (7.83)$$

The latter solution simply represents a perturbation of the slope S_1 , given by

$$S_1 = -\frac{2A}{\beta} \quad (7.84)$$

which directly links the slope perturbation S_1 and the constant A .

The water depth can be found, on the basis of Eq. 7.79 and Eq. 7.81, as follows

$$D_1 = \tilde{\eta}_{01} \phi_{01} + \tilde{\eta}_{02} \phi_{02} = \frac{A}{\lambda_{01}} (\phi_{01} - \phi_{02}) \quad (7.85)$$

It is easy to prove that the coefficients ϕ becomes, in the $\omega \rightarrow 0$ limit

$$\phi_{01} = -\phi_{02} = -\frac{\lambda_{01}}{\theta_0 \Delta d_s \beta (3 + 2 C_D)} \quad (7.86)$$

and consequently, from Eq. 7.84 we have, remembering the definition of 7.20, the following expression

$$D_1 = \eta_1 \phi_{01} = -\frac{S_1}{S_0 (3 + 2 C_D)} = -\gamma_3 S_1 \quad (7.87)$$

which simply represent the linear uniform flow relation between slope and depth in the case of a fixed discharge $Q_1 = D_1 + U_1 = 0$. The coefficient γ_3 represents the impact on depth and velocity of a variation of slope and is defined as

$$\gamma_3 := \frac{1}{S_0} \frac{1}{3 + 2 C_D} \quad (7.88)$$

Summarising, the third steady solution reads

$$\{\eta_1, U_1, D_1\} = S_1 \{-\beta x, \gamma_3, -\gamma_3\} \quad (7.89)$$

which, if combined with the other two (obtained straightforwardly as the limit $\omega \rightarrow 0$ of Eq. 7.79) leads to the general, steady, 1D solution of Eq. 7.28.

7.9.3 The role of the secondary currents

The depth-averaged model we adopted so far, does not include any three-dimensional effect due to secondary currents. This assumption is common to most analytical studies of river morphodynamics, included the bifurcation models of Bolla Pittaluga et al. (2003); Miori et al. (2006).

Nonetheless, it is evident that in some bifurcation configurations, especially for relatively large angles between the branches or when a channel curvature occurs, the spiral flow can affect the local morphology, and as well as the flow

repartition between the distributaries (e.g. Bulle, 1926). For this reason Kleinhans et al. (2008) proposed an extension of the Bolla Pittaluga et al. (2003) model which takes into account the effects of secondary circulations induced by the main channel curvature.

In this section we aim at studying the impact of secondary currents on the instability of bifurcation. This can be achieved by including the spiral flow in the 2D scheme through a simplified approach.

Zolezzi and Seminara (2001) proposed an extension of the Kalkwijk and de Vriend (1980) flow decomposition which enables to determine, in a simplified way, the structure of the spiral flow on the basis of the local conditions (depth, velocity and curvature), as well as their longitudinal derivatives (convection and shoaling effects). This approach, originally developed by taking into account only the curvature of the channel, Zolezzi and Seminara (2001) can be extended to model the secondary flow induced by the streamline curvature (Luchi et al., 2011). According to this formulation, the three dimensional flow produces additional terms in the depth-averaged model of Eq. 7.21; specifically, from a linear point of view (weak curvature), three terms appears on the left hand side of the longitudinal and transverse momentum and in the Exner equations ($f_\alpha, g_\alpha, h_\alpha$ respectively). These coefficients can be obtained by linearizing the expressions reported by Luchi et al. (2011), which leads, at the first order of approximation $\mathcal{O}(\epsilon)$, to the following formulas

$$\begin{cases} h_C = k_0 \frac{C_0}{\beta} \frac{\partial C_1}{\partial y} + k_1 \frac{C_0^2}{\beta^2} \frac{\partial C_1'}{\partial y} \\ m_C = k_0 \frac{C_0}{\beta} C_1' + k_1 \frac{C_0^2}{\beta^2} \frac{\partial C_1'}{\partial x} + k_3 \frac{1}{C_0} C_1 + k_4 \frac{1}{\beta} C_1' \\ n_C = k_3 \frac{C_0}{\beta} \frac{\partial C_1}{\partial y} + k_4 \frac{C_0^2}{\beta^2} \frac{\partial C_1'}{\partial y} \end{cases} \quad (7.90)$$

where s is the curvilinear coordinate along the streamline and \mathcal{C} is the dimensionless curvature (positive for right bends), defined as

$$\mathcal{C} = \frac{\mathcal{C}^*}{B^*} = -\frac{\partial \alpha}{\partial s} \quad (7.91)$$

with α representing the angle of the velocity vector, which can be expanded as follows

$$\alpha = \tan^{-1} \left(\frac{V}{U} \right) = \epsilon V_1 + \mathcal{O}(\epsilon^2) \quad (7.92)$$

thus allowing to express the curvature as

$$\mathcal{C} = \epsilon \mathcal{C}_1 + \mathcal{O}(\epsilon^2) \quad \mathcal{C}_1 = -\frac{\partial V_1}{\partial x} \quad (7.93)$$

The derivative of the curvature (at the linear level) is given by

$$C_1' = \frac{\partial \mathcal{C}_1}{\partial x} \quad (7.94)$$

7.9. Appendixes

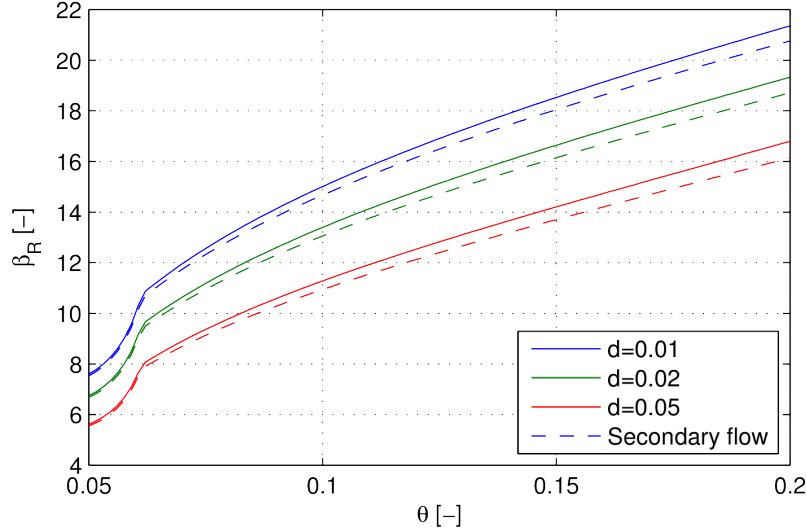


Figure 7.12: Resonant aspect ratio as a function of the relative roughness and the Shields stress (for $r = 0.5$) with and without secondary currents (dashed and continuous lines respectively). The Parker (1990) transport formula has been adopted.

The coefficients k_i are graphically reported, as a function of the relative roughness d_s , in Zolezzi and Seminara (2001) or can be determined by solving few integrals as indicated by the same paper.

The solution of the linear system Eq. 7.21 for a straight channel for a single Fourier mode can again be written as in Eq. 7.23. However including the terms h_C, m_C, n_C we obtain two more eigenvalues arise; this is because the ordinary differential system in x , which is obtained after substituting the transverse structure (see Zolezzi and Seminara, 2001), can be written as a first order linear system of six equations (7.21 plus 7.93 and 7.94) in the six dependent variables $\eta_1, U_1, V_1, D_1, C_1, C_1'$.

The effect of such a closure on the resonance point can be seen in figure 7.12, where we can notice that the spiral flow induce only a minor impact (of the order of -5%) on the resonant point. We can therefore conclude that, in terms of direction of dominant morphodynamic influence, the secondary effects are relatively small, thus producing weak impact on the bifurcation instability.

This result provide a support of the theory of Zolezzi and Seminara (2001) which does not include in the formulation any effect related on the streamline curvature so that does not consider, in a straight channel, any secondary effect.

The weak impact observed on the capability of the channel to propagate upstream the morphological influence, does not imply that the three-dimensional circulations do not play any role in the bifurcation morphodynamics; indeed the local solution, near the bifurcation node, can be significantly affected, especially if an angle between the main channel and the distributaries occurs.

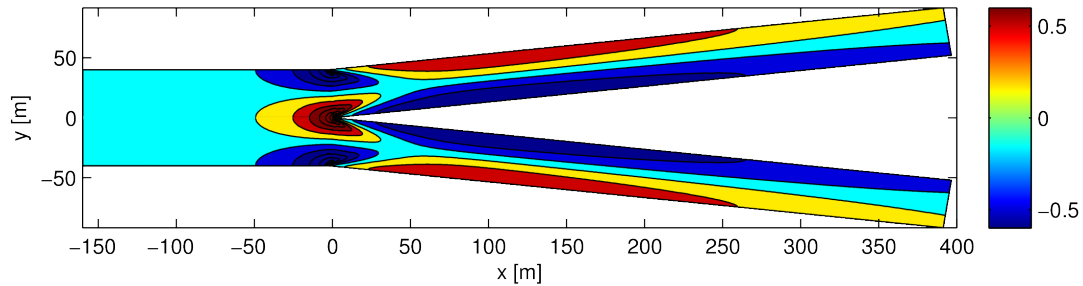


Figure 7.13: Bottom elevation $\eta_1\alpha$ of a diverging bifurcation similar to figure 7.9 but taking into account the secondary current. The colour scale is in [m] and the contours interval is 0.33 m.

A further simplification in modelling the secondary flow can be obtained by neglecting the non-local (convection and shoaling) effects, namely the terms dependent on the spatial derivatives (Kalkwijk and de Vriend, 1980; Kalkwijk and Booij, 1986), as often assumed in several both numerical and analytical 2D models (e.g. Crosato et al., 2011). In this way we obtain a differential system in which the terms depending on the curvature derivatives disappear ($k_0 = k_1 = k_4 = 0$) and only the terms proportional to k_3 remains. This linear system does not need the definition of the new dependent variables \mathcal{C}_1 and \mathcal{C}'_1 ; therefore as in the original (without secondary currents) model, there are only four eigenvalues, so that an identical procedure can be found to develop the analytical solution for the bifurcation.

Once again no significant impact on the instability (resonant) point can be found. However, if compute the forced solution in a diverging bifurcation (figure 7.13), we can find a relevant different of the solution in the distributaries with respect to the original 2D result reported in figure 7.9b.

7.9. *Appendixes*

Chapter 8

Conclusions

The present section summarises the conclusions presented in each chapter, in order to give the reader a general overview of the main results of the research with reference to the research questions formulated at the beginning of the manuscript.

Chapter 2 provides the first insight into the morphodynamical changes observed in a natural gravel bed river, the Rees (New Zealand), and their connection with sediment transport.

Specifically, we have firstly seen that the reach-scale erosion and deposition volumes depend on both magnitude and duration of the flood. Scour and fill volumes displaced during different floods appear to be mainly related to an increase of the active area rather than of the average depth of the scour or deposition sites. Similarly the frequency distribution of elevation changes appears to be largely independent of the flow magnitude.

Quantitative analysis of the size of the deposition and scour patches, based on an automated algorithm, reveals a strong dependence of the reach-averaged length on the intensity of the driving event. In particular, the small flow pulses produce much smaller areas of scour and fill than those associated with much large floods.

On the basis of the analysis above, we have proposed a new method to estimate the transport rate once the erosion and deposition volumes are known. Observations suggest that the average size of these patches may be representative of the path length, namely the average travel distance of the displaced particles as defined by Ashmore and Church (1998). When tested against the result of numerical simulations, such a method seems able to capture the variations of the reach-averaged bedload between the different flood events.

The transport rate estimate, based on the above method, is also relatively robust with respect to the compensation effect due to subsequent scour and refill, which causes underestimation of the scour/deposition volumes.

Within the subsequent *Chapter 3*, we tackle the problem of the regime morphodynamics attained by a braided network at the laboratory scale subject

to constant water and sediment supply.

Quantification of the morphological state requires the definition of suitable metrics; for this reason we have introduced an indicator of the reach-averaged braided morphology which represents the portion of braidplain lying below a given elevation, where the elevation is calculated with respect to the deepest point of each individual cross-section. This indicator is expressed as a curve which can be taken as representative of the reach-averaged geometry; we therefore named *Average section* an equivalent compact section having exactly the same width-depth curve.

The reach-scale geometry of a braided network is expected to respond to the external controlling conditions, identified through dimensional analysis. Specifically, if the bed material is well-sorted and the effect of vegetation is not accounted for, the regime morphology depends only on slope, discharge and confinement width. The role of these parameters is assessed through flume experiment, which enable to study the simplest case of constant (through time) and homogeneous (along the flume) conditions. Specifically, we have analysed an existing dataset of 58 experiments carried out at the hydraulic laboratory of the Trento's University and we have complemented the data with morphological data from three natural braided rivers: the Rees (New Zealand), the Sunwapta (Canada) and the Tagliamento (Italy).

Correlation between the channels depth and the flume slope occurs in the laboratory experiments, whereas the shape of the *Average section*, represented by the exponent α of the fitting power-law, is significantly impacted by the degree of confinement and ranges from $\alpha > 2$ (indicating the *Y-shape* typical of braided morphology) to $\alpha < 0.5$ (representative of the *U-shape* characteristics of single-thread channels).

The reach-scale indicator can be adopted in order to account for the spatial distribution of the Shields stress, which is recognised to be a crucial ingredient for the estimation of the solid discharge in a braided network. Numerical hydrodynamic simulations suggest that the proposed procedure is able to capture the shear stress variability; furthermore a comparison based on the set of laboratory experiments with different discharges, sediment size, slope and confinement width confirms the capability of the simple method to approximately predict the average sediment transport rate within a wide range of morphological conditions, from the nearly single-thread alternate bars pattern to fully-developed braided networks.

This method allows for a very simple investigation of the at-a-station response of the network to varying discharge. Indeed, assuming a power-law interpolation of the width-depth curves we can compute analytically the bed-load and active width and analyse the connection between average geometry the at-a-station response.

The first step to understand the response to changing discharge is developed in *Chapter 4*. Within this part we tackle, for the first time, the question of

understanding the effect of the discharge unsteadiness on sediment transport rate in braided networks. We have studied the problem using a laboratory-scale physical model, which enables to control the water discharge and to measure the sediment transport at the flume outlet.

It is well-known that in a braided network the transport rate at a given section (as the flume outlet) shows a great variability even in experiments with constant controlling conditions. If the discharge is varying, an additional problem arises as we need to distinguish between the response of the mean bedload and the stochastic component. This is because the timescale of the hydrologically-driven flow variations is short if compared with the timescale of the internally generated fluctuations, so that a simple filter does not allow to remove this “noise” without hiding the effect of the unsteady flow.

In order to overcome this issue we have adopted a novel methodology in the analysis of braided networks at the laboratory scale, based on a statistical approach; specifically, we have repeated several time the same simple hydrograph in order to determine a mean response of the system. The ensemble mean contains much less variability and, if the number of repetitions is sufficiently large, is expected to depend on the external controls, namely the shape, the intensity and the duration of the flow hydrograph.

The flume observations reveal a different response depending on the degree of confinement of the braided network. In the experiments where the flow is confined, the instantaneous response to increasing discharge exceeds the equilibrium transport rate (overshooting), whereas a decrease of the flow is associated with a strong decrease of the transport, which falls below the long-term equilibrium (undershooting). This short-term response is followed by a phase of gradual adaptation towards the long-term equilibrium conditions.

The response to changing flow is significantly different for the experiments with wider, relatively unconfined braided networks, when the transport rate due to the flow unsteadiness seems to rapidly adapt to the new equilibrium conditions.

A possible interpretation of this behaviour comes from the analysis of the morphological network response to the varying flow, measured through distributions of elevation at the reach scale. For relatively confined braided networks, such a distribution changes significantly with the discharge. Since these changes are not instantaneous but needs time to fully develop, there is a transitory phase when transport rate is different from the long-term equilibrium value.

This is not the case for relatively free braided networks, which does not show any significant variation of bed elevation distributions throughout the run; this suggest the absence of relevant morphological adjustment to the new flow conditions. Consequently the effect of unsteadiness on the transport is weak and not detectable in our observations, and therefore do not undergo any significant morphological adjustment to the new conditions.

Within the present work the limited number of experiments does not en-

able to quantify how the magnitude of the overshooting effect and the temporal scale of the adaptation to equilibrium conditions depend on the discharge and the confinement rate. In addition our analysis is limited to well-sorted sediment and to very simplified, artificial hydrographs. For these reasons further investigations is needed.

The following *Chapter 5* investigates the response of a braided network to changes of the sediment supply.

The laboratory experiments we performed reveal that after changes in the sediment feed rate a disequilibrium of the morphology occurs in the upper part of the flume. This is evident, for instance, after a reduction of the sand supply, which leads to the transition from the braided pattern to single-single thread in the upstream part of the flume. However, this is only a temporary effect and, in the long term, a fully braided pattern is recovered.

Experimental observations suggest that the sediment transport rate can be assumed to be in instantaneous equilibrium with the reach-scale slope (and discharge) provided the incision/aggradation rate is sufficiently slow. If this is the case the evolution of the one-dimensional, longitudinal bed level profile can be modelled as a simple diffusive process.

Such simple formulation, which was extensively adopted, with variable success, in previous studies of single-thread rivers, seems to be more appropriate for steep and shallow channels typical of gravel-bed braided networks than for deep, low gradient currents.

The introduction of a more complete formulation enables to investigate the potential effect of the local non-equilibrium of the braided morphology on the evolution of the bed profiles; our analysis shows that the diffusive model is valid in the limit of slow variation of the bed level elevation.

A direct outcome of this simple model is that, as common to all the diffusive processes (for example heat or mass diffusion), the temporal scale of the evolution of bed level profiles, T , is proportional to the square of the length scale L and therefore differs from the temporal scale of the local morphological evolution T_E .

The last part of the manuscript focus on the morphodynamic influence exerted by a localised obstacle and the connection of such theory with the stability of bifurcations, which are fundamental processes in the braided river morphodynamics.

In *Chapter 6* we derive an analytical solution of the steady shallow water morphodynamic model for a local, sinusoidal obstacle placed in a straight channel with rectangular cross-section. This solution, expressed in terms of Fourier series, is formally exact in the limit of small amplitude obstacle.

The analytical approach allows for studying the long-term morphological response of a gravel-bed channel in different conditions; indeed it enables to determine both the local effect near the obstacle region and the morphological influence exerted on the upstream and downstream branches.

The resonant aspect ratio β_R (Blondeaux and Seminara, 1985), which depends on the relative roughness and on the Shield stress, has revealed to be crucial for determining the dominant (upstream or downstream) direction of morphodynamic influence (Zolezzi and Seminara, 2001).

Our result confirms the importance of the resonance point for the case of a localised obstacle. Specifically, as also predicted by numerical experiments (Siviglia et al., 2013), an upstream propagation of two-dimensional disturbances occurs only under super-resonant conditions (i.e. $\beta > \beta_R$), whereas only downstream influence can be observed in the narrower, sub-resonant, case.

We have also seen that, including the secondary effects of the spiral flow causes a minor impact on the results in terms of the direction of morphodynamic influence. However, if the length of the obstacle is relatively small, the secondary currents produce a significant variation of the morphology in the region near the obstacle.

The analytical model also enables to explore the role of the boundary conditions, showing that an unique steady solution can be found once three upstream and one downstream conditions are specified.

The above results are the starting point for understanding the analysis presented in *Chapter 7* where we tackle the problem of bifurcation stability.

We have solved analytically the shallow-water, mobile-bed 2D model for the case of a geometrically symmetrical bifurcation. Under the hypothesis of small variations with respect to the basic configuration, we have found a solution which is valid within each of the three branches which joins at the bifurcation, but also satisfies suitable matching conditions which ensure the continuity of all the variables across the three channels.

The analytical model shows that non-trivial steady solution can be found if, and only if, the main channel belongs to super-resonant conditions. This result provides a rigorous theoretical explanation to the observations of Bertoldi and Tubino (2007), who noticed, on the basis of laboratory outcomes, a connection between the bifurcation dynamics and the theory of the morphodynamic influence proposed by Zolezzi and Seminara (2001).

An additional support to this theory comes from the numerical results of Siviglia et al. (2013), whose observations about bifurcation stability can be correctly interpreted in term of morphodynamic influence.

The solution we have derived by refers to a simple, non-diverging bifurcation formed by a thin barrier which separates the two distributaries. However, the introduction of an angle between the secondary branches does not change the result in terms of bifurcation stability. Indeed, for relatively small angles we can derive again an analytical solution, which enables to reproduce the scour/deposition pattern predicted by fully-nonlinear numerical models and frequently observed in natural bifurcations. Such an analytical approach provides a deeper understanding of the fundamental mechanisms which drive the morphodynamic response of the diffluence.



Figure 8.1: Braided reach of the River Rakaia (New Zealand, $43^{\circ}34' S$, $171^{\circ}45' E$); from *Google Earth, Digital Globe (2014)*. Flow is from left to right.

The present model enables to clearly distinguish between the instability due to the free morphodynamic response and the effect driven by "external" forcing effects, such as the presence of a slope advantage between the distributaries or a curvature of the main channel, which both may result in an unbalanced bifurcation.

Overall, our work provides a comprehensive analysis the physical processes involved in the bifurcation morphodynamics with respect to the pre-existing quasi-2D models. Specifically, it also provides a prediction of the threshold for the occurrence of unbalanced configuration which does not require an empirical estimate of the model coefficients.

Acknowledgements

Developing a PhD thesis is a complex and demanding process, whose final scientific quality is highly dependent upon people who are directly or indirectly involved in the research activity. It is therefore needed to acknowledge who helped me during this journey through the world of research.

First of all I would like to thank my busy supervisor prof. *Marco Tubino*. Working with “the big boss” means on the one hand being free to develop your ideas and having the opportunity to discuss about deep concepts, on the other hand implies having not much support about how to plan and organise your work, how to solve the daily problems, how to improve your technical and writing skills. Albeit this represented a limitation, especially at the beginning of my research activity, I hope it helped me in the longer term to develop my ability to afford complex tasks in a more autonomous, independent and original way.

I can not forget my second supervisor prof. *James Brasington*, not only for the the amazing dataset of the Rees River but also for the punctual corrections of my chapter and for the motivation he transmitted to me.

A great thank to *Walter Bertoldi* is needed because of his contagious passion for research, for the support in the laboratory and for the precious suggestions coming from his experience and vision.

A special mention is needed for prof. *Guido Zolezzi* who, besides the valuable help, ranging from the bothering administrative practices to the more fascinating scientific questions, often transmitting to me positiveness and encouragements, limiting factors needed to overtake the unavoidable difficulties arising during the research activity.

For the laboratory work it was fundamental the both practical and conceptual contribution of *Matilde Welber*, as well as the competence of *Martino Salvaro* and of the technician in the laboratory *Lorenzo Forti* and *Andrea Bampi*. In addition I have also to thank our secretaries *Marina Rogato* for here politeness and *Laura Martuscelli* for the important support.

Acknowledging colleagues is more delicate because it is often impossible to clearly distinguish between the contribution of each person to my personal and professional growth. For this reason, among a number of lovely people I met during these three years, I only mention *Umesh Singh* and *Simone Zen* because of the direct impact of the scientific discussions often taken place at the Trento’s office.



Bibliography

- M.B. Abbott. *Computational Hydraulics, Elements of the theory of free surface flows*. Pitman, London, 1979.
- K. Ashida and M. Michiue. Study on hydraulic resistance and bedload transport rate in alluvial streams. *Transactions, Japan Society of Civil Engineering*, (206):59–64, 1972.
- P. Ashmore. Laboratory modeling of gravel braided-stream morphology. *Earth Surface Processes and Landforms*, 7:201–225, 1982.
- P. Ashmore. Bed load transport in braided gravel-bed stream models. *Earth Surface Processes and Landforms*, 13:677–695, 1988.
- P. Ashmore. Channel morphology and bed load pulses in braided, gravel-bed streams. *Geografiska Annaler*, 73 (A):37–52, 1991.
- P. Ashmore. Braiding phenomena: statics and kinetics. In *Gravel-Bed Rivers 5*, pages 95–114. New Zealand Hydrological Society, 2001.
- P. Ashmore. Morphology and dynamics of braided rivers. In J. Shroder and E. Wohl, editors, *Treatise on Geomorphology*, volume 9, Fluvial Geomorphology, pages 289–312. Academic Press, San Diego, CA, 2013.
- P. Ashmore and E. Sauks. Prediction of discharge from water surface width in a braided river with implications for at-a-station hydraulic geometry. *Water Resources Research*, 42:1–11, 1996.
- P. Ashmore, R.I. Ferguson, K.L. Prestegard, P.L. Ashworth, and C. Paola. Gravel transport and morphological change in braided sunwapta river, alberta, canada. *Earth Surface Processes and Landforms*, 17:299–311, 1992.
- P. Ashmore, W. Bertoldi, and J.T. Gardner. Active width of gravel-bed braided rivers. *Earth Surface Processes and Landforms*, 36:1510–1521, 2011.
- P.E. Ashmore and M.A. Church. Sediment transport and river morphology: a paradigm for study. In P.C. Klingeman, R.L. Beschta, P.D. Komar, and J.B. Bradely, editors, *Gravel-Bed Rivers in the Environment*, page 115–149. Water Resources Publications, LLC, 1998.
- P.E. Ashmore and G. Parker. Confluence scour in coarse braided streams. *Water Resources Research*, 19:392–402, 1983.

Bibliography

- J. Beavan, P. Denys, M. Denham, B. Hager, T. Herring, and P. Molnar. Distribution of present-day vertical deformation across the southern alps, new zealand, from 10 years of gps data. *Geophysical Research Letters*, 37, 2010.
- R.G. Bell and A.J. Sutherland. Nonequilibrium bedload transport by steady flows. *Journal of Hydraulic Engineering*, 109:351–367, 1983.
- W. Bertoldi. *River Bifurcations*. PhD thesis, Faculty of Engineering, University of Trento, 2005.
- W. Bertoldi. Life of a bifurcation in a gravel-bed braided river. *Earth Surface Processes and Landforms*, 37:1327–1336, 2012.
- W. Bertoldi and M. Tubino. Bed and bank evolution of bifurcating channels. *Water Resources Research*, 41, 2005.
- W. Bertoldi and M. Tubino. River bifurcations: Experimental observations on equilibrium configurations. *Water Resources Research*, 43, 2007.
- W. Bertoldi, P. Ashmore, and M. Tubino. A method for estimating the mean bed load flux in braided rivers. *Geomorphology*, 103:330–340, 2009a.
- W. Bertoldi, A. Gurnell, N. Surian, K. Tockner, L. Zanoni, L. Ziliani, and G. Zolezzi. Understanding reference processes: linkages between river flows, sediment dynamics and vegetated landforms along the tagliamento river, italy. *River Research and Applications*, 25:501–516, 2009b.
- W. Bertoldi, L. Zanoni, S. Miori, and M. Tubino. Interaction between migrating bars and bifurcations in gravel bed rivers. *Water Resources Research*, 44, 2009c.
- W. Bertoldi, L. Zanoni, and M. Tubino. Planform dynamics of braided rivers. *Earth Surface processes and Landforms*, 34:547–557, 2009d.
- W. Bertoldi, L. Zanoni, and M. Tubino. Assessment of morphological changes induced by flow and flood pulses in a gravel bed braided river: The tagliamento river (italy). *Geomorphology*, 114:348–360, 2010.
- W. Bertoldi, N.A. Drake, and A.M. Gurnell. Interactions between river flows and colonizing vegetation on a braided river: exploring spatial and temporal dynamics in riparian vegetation cover using satellite data. *Earth Surface Processes and Landforms*, 36:1474–1486, 2011a.
- W. Bertoldi, A.M. Gurnell, and N.A. Drake. The topographic signature of vegetation development along a braided river : Results of a combined analysis of airborne lidar, color air photographs, and ground measurements. *Water Resources Research*, 47, 2011b.
- J.L. Best. The morphology of river channel confluences. *Progress in Physical Geography*, 10:157–174, 1986.
- J.L. Best and B.L. Rhoads. Sediment transport, bed morphology and the sedimentology of river channel, confluences. In S. Rice, A. Roy, and B.L. Rhoads, editors, *River Confluences, Tributaries and the Fluvial Network*, pages 45–72. Wiley, Chichester, 2008.

Bibliography

- P. Blondeaux and G. Seminara. A unified bar-bend theory of river meanders. *Journal of Fluid Mechanics*, 157:449–470, 1985.
- M. Bolla Pittaluga, R. Repetto, and M. Tubino. Channel bifurcation in braided rivers: Equilibrium configurations and stability. *Water Resources Research*, 39(3), 2003.
- J. Brasington. From grain to floodplain: Hyperscale models of braided rivers. *Journal of Hydraulic Research*, 45, 2010.
- J. Brasington, B.T. Rumsby, and R.A. Mcvey. Monitoring and modelling morphological change in a braided gravel-bed river using high resolution gps-based survey. *Earth Surface Processes and Landforms*, 25:973–990, 2000.
- J. Brasington, J. Langham, and B. Rumsby. Methodological sensitivity of morphometric estimates of coarse fluvial sediment transport. *Geomorphology*, 53(3-4), 2003.
- J. Brasington, D. Vericat, and I. Rychkov. Modeling river bed morphology, roughness, and surface sedimentology using high resolution terrestrial laser scanning. *Water Resources Research*, 48, 2012.
- H. Bulle. Untersuchungen über die geschiebeableitung bei der spaltung von wasserläufen. *Forschungsarbeiten auf dem Gebiete des Ingenieurwesens (in German)*, 282:57–84, 1926.
- L.M. Burge. Stability, morphology and surface grain size patterns of channel bifurcation in gravel-cobble bedded anabranching rivers. *Earth Surface Processes and Landforms*, 31:1211–1226, 2006.
- M.A. Carson and G.A. Griffith. Bedload transport gravel channels. *Journal of Hydrology*, 151, 1987.
- M. Church. Geomorphic thresholds in riverine landscapes. *Freshwater Biology*, 47, 2002.
- M. Colombini, G. Seminara, and M. Tubino. Finite amplitude alternate bars. *J. Fluid Mech.*, 181:213–232, 1987.
- S. Cordier, M.H. Le, and T. Morales de Luna. Bedload transport in shallow water models: Why splitting (may) fail, how hyperbolicity (can) help. *Advances in Water Resources*, 34:980–989, 2011.
- T.J. Coulthard. Effects of vegetation on braided stream pattern and dynamics. *Water Resources Research*, 41, 2005.
- A. Crosato and E. Mosselmann. Simple physics-based predictor for the number of river bars and the transition between meandering and braiding. *Water Resources Research*, 45, 2009.
- A. Crosato, E. Mosselman, F. Beidmariaam Desta, and W.S.J. Uijttewaal. The relation between channel instability and sediment transport. *Water Resources Research*, 47, 2011.

Bibliography

- A. Crosato, F. Beidmariam Desta, J. Cornelisse, F. Schuurman, and W.S.J. Uijtewaal. Experimental and numerical findings on the long-term evolution of migrating alternate bars in alluvial channels. *Water Resources Research*, 48, 2012.
- T.R.H. Davies. Problems of bedload transport in braided gravel-bed rivers. In C.R. Thorne, J.S. Bathurst, and R.D. Hey, editors, *Sediment Transport in Gravel-Bed Rivers*, page 793–811. Wiley, Chichester, 1987.
- M. de Vries. Considerations about non-steady bed-load transport in open channels. *Proceedings IAHR Congress*, 1965.
- J.R. Desloges and M.A. Church. Wandering gravel-bed rivers. *The Canadian Geographer*, 33(4):360–364, 1989.
- M. Doering, R.I. Ferguson, U. Uehlinger, and K. Tockner. Vertical hydrological exchange, and ecosystem properties and processes at two spatial scales along a floodplain river (tagliamento, italy). *Freshwater Science*, 32(1):12–25, 2013.
- B.C. Eaton and M.F. Lapointe. Effects of large floods on sediment transport and reach morphology in the cobble-bed sainte-marguerite river. *Geomorphology*, 40:291–309, 2001.
- D.A. Edmonds and R.L. Slingerland. Stability of delta distributary networks and their bifurcations. *Water Resources Research*, 44, 2008.
- R. Egozi and P. Ashmore. Defining and measuring braiding intensity. *Earth surface processes and landforms*, 114, 2008.
- R. Egozi and P. Ashmore. Experimental analysis of braided channel pattern response to increased discharge. *Journal of Geophysical Research*, 114, 2009.
- H.A. Einstein. *Bedload transport as a probability problem*. PhD thesis, 1937.
- F. Engelund and J. Fredsoe. Sediment ripples and dunes. *Annual Review of Fluid Mechanics*, 14:13–37, 1982.
- B. Federici and C. Paola. Dynamics of channel bifurcations in noncohesive sediments. *Water Resources Research*, 39(6), 2003.
- R. Ferguson, P. Ashmore, P. Ashworth, C. Paola, and K. Prestegard. Measurements in a braided river chute and lobe. 1. flow pattern, sediment transport and channel change,. *Water Resources Research*., 28(7):1877–1885, 1992.
- R.I. Ferguson. The missing dimension: effects of lateral variation on 1-d calculations of fluvial bedload transport. *Geomorphology*, 56:1–14, 2003.
- S. Francalanci, L. Solari, M. Toffolon, and G. Parker. Do alternate bars affect sediment transport and flow resistance in gravel-bed rivers? *Earth Surface Processes and Landforms*, 37:866–875, 2012.
- A. Frascati and S. Lanzoni. Morphodynamic regime and long-term evolution of meandering rivers. *Journal of Geophysical Research*, 114, 2009.

- J. Fredsoe. Meandering and braiding of rivers. *Journal of Fluid Mechanics*, 84(4): 609–624, 1978.
- J. Gao. Bathymetric mapping by means of remote sensing: methods, accuracy and limitations. *Progress Phys. Geogr.*, 33:103–116, 2009.
- G.A. Garcia Lugo. *Braided rivers: an exploratory study combining flume experiments and the analysis of remotely-sensed data*. PhD thesis, Queen Mary University of London, 2014.
- G.A. Garcia Lugo, W. Bertoldi, A. Gurnell, and A. Henshaw. Flume experiments to investigate multi-thread channel development under varying discharge and channel confinement, 2013.
- D. Germanoski and S.A. Schumm. Changes in braided river morphology resulting from aggradation and degradation. *The Journal of Geology*, 101:451–466, 1993.
- M. A. Gill. Hyperbolic model for aggrading channels. *Journal of Engineering Mechanics*, 114:1245–1255, 1988.
- J.R. Goff and P. Ashmore. Gravel transport and morphological change in braided sunwapta river, alberta, canada. *Earth Surface Processes and Landforms*, 19:195–212, 1994.
- G.A. Griffith. Conversion of braided gravel-bed rivers to single-thread channels of equivalent transport capacity. *Journal of Hydrology New Zealand*, 28:63–75, 1989.
- G.A. Griffith and A.J. Sutherland. Bedload transport by translation waves. *J. Hydraul. Div. Am. Soc. Civ. Eng.*, 103:1279–1291, 1977.
- A. Gurnell, N. Surian, and L. Zanoni. Multi-thread river channels: A perspective on changing european alpine river systems. *Aquatic science*, 71:253–265, 2009.
- D.G. Ham and M. Church. Bed-material transport estimate from channel morphodynamics: Chilliwack river, british columbia. *Earth Surface Processes and Landforms*, 25:1123–1142, 2000.
- R.J. Hardy, S.N. Lane, and D. Yu. Flow structures at an idealized bifurcation: a numerical experiment. *Earth Surface Processes and Landforms*, 36:2083–2096, 2011.
- J.K. Haschenburger and M. Church. Bed material transport estimated from the virtual velocity of sediment. *Earth Surface Processes and Landforms*, 23:791–808, 1998.
- M.A. Hassan, R. Egozi, and G. Parker. Experiments on the effect of hydrograph characteristics on vertical grain sorting in gravel bed rivers. *Water Resources Research*, 42(W09408), 2006.
- R.D. Henderson and S.M. Thompson. Extreme rainfalls in the southern alps of new zealand. *Journal of Hydrology (New Zealand)*, 38:309–330, 1999.
- T.B. Hoey and A.J. Sutherland. Channel morphology and bedload pulses in a braided river. *Earth Surface Processes and Landforms*, 16:447–462, 1991.

Bibliography

- L.B. Hong and T.R.H. Davies. A study of stream braiding. *Geological Society of America Bulletin*, 90:1839–1859, 1979.
- R. Humphries, J.G. Venditti, L.S. Sklar, and J.K. Wooster. evidence for the effect of hydrographs on sediment pulse dynamics in gravel-bedded rivers. water resources research. *Water Resources Research*, 48, 2012.
- E.J. Hundey and P.E. Ashmore. Length scale of braided river morphology. *Water Resources Research*, 25:501–516, 2009.
- S. Ikeda. Bend theory of river meanders. part 1. linear development. *Journal of Fluid Mechanics*, 112:363–377, 1981.
- S. Ikeda. Prediction of alternate bar wavelength and height. *Journal of Hydraulic Engineering*, 110:371–386, 1984.
- S. Ikeda, G. Parker, and K. Sawai. Incipient motion of sand particles on side slopes. *Journal of the Hydraulics Division, ASCE*, 108(1), 1982.
- M.N.R. Jaeggi. Formation and effects of alternate bars. *Journal of Hydraulic Engineering*, 110(2), 1984.
- S.C. Jain. Note on lag in bedload discharge. *Journal of Hydraulic Engineering*, 118(6): 904–917, 1992.
- C.L. Jang and Y. Shimizu. Bed and bank evolution of bifurcating channels. *ASCE Journal of Hydraulic Engineering*, 131(7), 2005.
- W.F. Jaramillo and S.C. Jain. Aggradation and degradation of alluvial-channel beds. *Journal of Hydraulic Engineering*, 106:1072–1085, 1984.
- J.P. Kalkwijk and j.H. de Vriend. Computation of the flow in shallow river bends. *Journal of Hydraulic Research*, 18:327–342, 1980.
- J.P.T. Kalkwijk and R. Booij. Adaptation of secondary flow in nearly horizontal flow. *Journal of Hydraulic Research*, 24:19–37, 1986.
- G.J. Klaassen, K. Douben, and M. van der Waal. Novel approaches in river engineering. *Proceedings of RiverFlow 2002, Lovain la Neuve, Belgium*, pages 27–43, 2002.
- M.G. Kleinhans, H.R.A. Jagers, E. Mosselman, and C.J. Sloff. Bifurcation dynamics and avulsion duration in meandering rivers by one-dimensional and three-dimensional models. *Water Resources Research*, 44, 2008.
- M.G. Kleinhans, R.I. Ferguson, S.N. Lane, and R.J. Hardy. Splitting rivers at their seams: bifurcations and avulsion. *Earth Surface Processes and Landforms*, 38:47–61, 2013.
- R.A. Kuhnle. Bed load transport during rising and falling stages streams. *Earth Surface Processes and Landforms*, 17:191–197, 1992.
- E.W. Lane. A study of the shape of channels formed by natural streams flowing in erodible material. *U.S. Army Corps of Engineers, Missouri River Division, Sediment Series*, 9:106, 1957.

- J.R. Lane, J.H. Chandler, and K.S. Richards. Developments in monitoring and terrain modelling of small-scale river bed topography. *Earth Surface Processes and Landforms*, 19:349–368, 1994.
- S. Lane. Approaching the system-scale understanding of braided river behaviour. In G.H. Sambrook Smith, J.L. Best, C.S. Bristow, and G.E. Petts, editors, *Braided Rivers: Process, Deposits, Ecology and Management. Association of Sedimentologists Special Publication*, volume 36, pages 339–359. Blackwell, Oxford, 2006.
- S.N. Lane, R.M. Westaway, and M. Hicks. Estimation of erosion and deposition volumes in a large, gravel-bed, beaded river using synoptic remote sensing. *Earth Surface Processes and Landforms*, 28:249–271, 2003.
- S. Lanzoni. Experiments on bar formation in a straight flume 1. uniform sediment. *Water Resources Research*, 36(11):3337–3349, 2000.
- S. Lanzoni and G. Seminara. On the nature of meander instability. *Journal of Geophysical Research*, 111, 2006.
- K.T. Lee, Y.L. Liu, and K.H. Cheng. Experimental investigation of bedload transport processes under unsteady flow conditions. *Earth Surface Processes and Landforms*, 18:2439–2454, 2004.
- L.B. Leopold and M.G. Wolman. River channel patterns: braided, meandering and straight. *Geological Survey Professional Paper*, 282B, 1957.
- F. Liebault, S. Lallias-Tacon, and N. Talaska. Long profile responses of alpine braided rivers in se france. *River Research Applications*, 29(10):1253–1266, 2012.
- J.B. Lindsay and P.E. Ashmore. The effect of survey frequency on estimates of scour and fill in a braided river model. *Earth Surface Processes and Landforms*, 27:27–43, 2002.
- T.E. Lisle and M. Church. Sediment transport-storage relations for degrading, gravel bed channels. *Water Resources Research*, 38, 2002.
- T.E. Lisle, J.E. Pizzuto, H. Ikeda, and F. Iseya. Evolution of a sediment wave in an experimental channel. *Water Resources Research*, 33:1971–1981, 1997.
- R. Luchi, G. Zolezzi, and M. Tubino. Bend theory of river meanders with spatial width variations. *Journal of Fluid Mechanics*, pages 311–339, 2011.
- M.A. Madey, D.G. Sutherland, T.E. Lisle, and B. Pryor. Channel responses to varying sediment input: A flume experiment modeled after redwood creek, california. *Geomorphology*, 103:507–519, 2009.
- L. Mao, A. Dell’Agnese, C. Huincache, D. Penna, M. Engel, and G. Niedrist. Bedload hysteresis in a glacier-fed mountain river. *Earth Surface Processes and Landforms*, 39:964–976, 2014.
- W.A. Marcus and M.A. Fonstad. Optical remote mapping of rivers at sub-meter resolutions and watershed extents. *Earth surface processes and landforms*, 33:4–24, 2008.

Bibliography

- W.A. Marcus and M.A. Fonstad. Remote sensing of rivers: The emergence of a subdiscipline in the river sciences. *Earth Surface Processes and Landforms*, 35:1867–1872, 2010.
- C. Marti and G.R. Bezzola. Bed load transport in braided gravel-bed rivers. In G.H. Best, J.L. Bristow, and C.S. Petts, editors, *Braided Rivers: Process, Deposits, Ecology and Management. Special Publication*, volume 36, pages 199–215. Blackwell, 2006.
- D.G. McLean. *The relation between channel instability and sediment transport on lower Fraser River*. PhD thesis, University of B.C., Vancouver, 1990.
- D.G. McLean and M. Church. Sediment transport along lower fraser river 2. estimates based on the long-term gravel budget. *Water Resources Research*, 35(8):2549–2559, 1999.
- E. Meyer-Peter and R. Müller. Formulas for bed load transport. *Proceedings of the 2nd IAHR Congress*, 2:39–64, 1948.
- S. Miori, R. Repetto, and M. Tubino. A one-dimensional model of bifurcations in gravel bed channels with erodible banks. *Water Resources Research*, 42, 2006.
- M.P. Mosley. An experimental study of channel confluences. *Journal of Geology*, 84: 535–562, 1976.
- M.P. Mosley. Analysis of the effect of changing discharge on channel morphology and instream uses in a braided river, ohau river, new zealand. *Water Resources Research*, 18(4), 1982.
- M.P. Mosley. Response of braided rivers to changing discharge. *Journal of Hydrology New Zeland*, 22:18–67, 1983.
- E. Mosselman, M. Tubino, and G. Zolezzi. The overdeepening theory in river morphodynamics: Two decades of shifting interpretations. *Proceedings of River Flow 2006, London*, pages 1175–1181, 2006.
- A.B. Murray. Contrasting the goals, strategies, and predictions associated with simplified numerical models and detailed simulations. In P.R. Wilcock and R.M. Iverson, editors, *Prediction in geomorphology. Geophysical Monograph*, volume 135, pages 151–165. American Geophysical Union, 2003.
- A.B. Murray and C. Paola. A cellular model of braided rivers. *Nature*, 371:54–57, 1994.
- G.B. Nagy, O.E. Ortiz, and O.A. Reula. The behavior of hyperbolic near their parabolic limits heat equations' solutions. *J. of Mathematical Physics*, 35(8):4334–4356, 1994.
- C.R. Neill. Bed forms of the lower red deer river, alberta. *J. of Hydrology*, (7), 1957.
- C.R. Neill. River bed transport related to meander migration rates. *J. of Waterways, Harbors Coastal Engineer division, ASCE*, 95:783–786, 1971.

- C.R Neill. Sediment balance considerations linking long-term transport and channel processes. In C.R Thorne, J.S. Bathurst, and R.D Hey, editors, *Sediment Transport in Gravel-Bed Rivers*, pages 225–239. Wiley, Chichester, 1987.
- A.P. Nicholas. Modeling bedload yield in braided gravel bed rivers. *Geomorphology*, 36:89–106, 2000.
- C. Paola. Turbulence as a metaphor for stream braiding. volume 65, pages 11–46. John Wiley and Sons, Blackwell: Oxford, 1996.
- C. Paola. Modelling stream braiding over a range of scales. In M.P. Mosley, editor, *Gravel bed rivers V*, pages 11–46. New Zealand Hydrologic Society, Christchurch, 2001.
- C. Paola and E. Fofoula-Georgiou. Statistical geometry and dynamics of braided rivers. In M.P. Mosley, editor, *Gravel bed rivers V*, pages 47–69. New Zealand Hydrologic Society, Christchurch, 2001.
- C. Paola, K. Straub, D. Mohrig, and L. Reinhardt. The “unreasonable effectiveness” of stratigraphic and geomorphic experiments. *Earth-Science Reviews*, 97:1–43, 2009.
- G. Parker. On the cause and characteristic scales of meandering and braiding in rivers. *Journal of Fluid Mechanics*, 76(3):457–479, 1976.
- G. Parker. Surface-based bedload transport relation for gravel rivers. *Journal of Hydraulic Research*, 28:417–436, 1990.
- E.J. Plate. The need to consider non-stationary sediment transport. *Int. J. Sediment Res.*, 9:117–123, 1994.
- B.S. Pryor, D.S. Montoya, T. Lisle, and S. Hilton. Transport and storage of bed material in a gravel-bed channel during episodes of aggradation and degradation: a field and flume study. *Earth Surface Processes and Landforms*, 36:2028–2041, 2011.
- R.S. Pyrcie and P.E. Ashmore. The relation between particle path length distributions and channel morphology in gravel-bed streams. *Geomorphology*, 56:167–187, 2003a.
- R.S. Pyrcie and P.E. Ashmore. Particle path length distributions in meandering gravel-bed stream: results from physical models. *Earth Surface Processes and Landforms*, 28:951–966, 2003b.
- M. Redolfi and M. Tubino. A diffusive 1d model for the evolution of a braided network subject to varying sediment supply. *Proceedings of River Flow 2014, Lausanne, SUI*, pages 983–991, 2014.
- I. Reid, L.E. Frostick, and J.T. Layman. The incidence and nature of bedload transport during flood flows in coarse-grained alluvial channels. *Earth Surface Processes and Landforms*, 10:33–44, 1985.
- R. Repetto, M. Tubino, and C. Paola. Planimetric instability of channels with variable width. *Journal of Fluid Mechanics*, 457:79–209, 2002.

Bibliography

- B.L. Rhoads and A.N. Sukhodolov. Lateral momentum flux and the spatial evolution of flow within a confluence mixing interface. *Water resources research*, 44, 2008.
- J.S. Ribberink and J.T.M. Van der Sande. Aggradation in rivers due to overloading — analytical approaches. *Journal of Hydraulic Engineering*, 110:1072–1085, 1984.
- M. Rinaldi, B. Wyzga, and N. Surian. Sediment mining in alluvional channels: physical effects and management perspectives. *River research and applications*, 21:805–828, 2005.
- V. Sapozhnikov and E. Foufoula-Georgiou. Self-affinity in braided rivers. *Water Resources Research*, 32:1429–1439, 1996.
- V. Sapozhnikov and E. Foufoula-Georgiou. Experimental evidence of dynamic scaling and indications of self organized criticality in braided rivers. *Water Resources Research*, 33:1983–1991, 1997.
- V. Sapozhnikov and E. Foufoula-Georgiou. Experimental evidence of dynamic scaling and indications of self organized criticality in braided rivers. *Water Resources Research*, 34(4), 1998.
- G. Seminara. Effect of grain sorting on the formation of bedforms. In R.D. Rajaona, editor, *Sediment Transport Mechanisms in Coastal Environments and Rivers*, volume 244, pages 549–563. Appl. Mech. Rev., 1995.
- G. Seminara and M. Tubino. Alternate bars and meandering: Free, forced and mixed interactions. In S. Ikeda and G. Parker, editors, *River Meandering, Water Resour. Monogr.*, volume 12, pages 267–320. AGU, Washington, D.C., 1989.
- G. Seminara and M. Tubino. Weakly nonlinear theory for regular meanders. *Journal of Fluid Mechanics*, 244:257–288, 1992.
- G. Seminara, G. Zolezzi, M. Tubino, and D. Zardi. Downstream and upstream influence in river meandering. part 2. planimetric development. *Journal of Fluid Mechanics*, 438:213–230, 2001.
- Y. Shimizu and T. Itakura. Calculation of bed variation in alluvial channels. *Journal of Hydrological Engineering*, 115(3), 1989.
- A.B. Shvidchenko and Z.D. Kopalani. Hydraulic modeling of bed load transport in gravel-bed laba river. *Journal of Hydrology*, 124, 1998.
- J. Sieben. *Modelling of hydraulics and morphology in mountain rivers*. PhD thesis, T.U. Delft, 1997.
- A. Siviglia, G. Stecca, D. Vanzo, G. Zolezzi, E.F. Toro, and M. Tubino. Numerical modelling of two-dimensional morphodynamics with applications to river bars and bifurcations. *Advances in Water Resources*, 52:243–260, 2013.
- L.C. Smith, B. Isacks, and A Bloom. Estimation of discharge from threebraided rivers using synthetic aperture radar satellite imagery: Potential application to ungauged basins. *Water Resources Research*, 32:2021–2034, 1996.

- J.P. Soni, R.J. Garde, and K.G. Ranga Raju. Aggradation in streams due to overloading. *J. Hydraul. Div, Am. Soc. Civ. Eng.*, 106:117–132, 1980.
- A. Strickler. Beiträge zur frage der geschwindigkeitsformel und der rauhgigszahlen für ströme, kanäle un geschlossene leitungen. *Mitt. des Am. für Wasserwirtschaft (in German)*, (16), 1923.
- N. Struiksma and A. Crosato. Analysis of a 2-d model for rivers. *Water Resources Monograph*, 12(3), 1989.
- N. Struiksma, K.W. Olesen, C. Flokstr, and J.H. De Vriend. Bed deformation in curved alluvial channels. *Journal of Hydraulic Research*, 23(1), 1985.
- N. Surian. Channel changes due to river regulation: the case of the piave river, italy. *Earth Surface Processes and Landforms*, 24:1135–1151, 1999.
- N. Surian, L. Mao, M. Giacomini, and L. Ziliani. Morphological effects of different channel-forming discharges in a gravel-bed river. *Earth Surface Processes and Landforms*, 34(8), 2009a.
- N. Surian, L. Ziliani, F. Comiti, M.A. Lenzi, and L. Mao. Channel adjustment and alteration of sediment fluxes in gravel-bed rivers of the north-eastern italy: potential and limitations for channel recovery. *River research and applications*, 25:551–567, 2009b.
- M. Tal and C. Paola. Effects of vegetation on channel morphodynamics: results and insights from laboratory experiments. *Earth Surface Processes and Landforms*, 35: 1014–1028, 2010.
- A. Talmon, C.L.M. Van Mierlo, and N. Struiskma. Laboratory measurements of direction of sediment transport on transverse alluvial-bed slopes. *Journal of Hydraulic Research*, 33(4):519–543, 1995.
- R.E. Thomas, D.R. Parsons, S.D. Sandbach G.M. Keevil, W.A. Marra, R.J. Hardy, J.L. Best S.N. Lane, and J.A. Ross. An experimental study of discharge partitioning and flow structure at symmetrical bifurcations. *Earth Surface Processes and Landforms*, 36:2069–2082, 2011.
- A.B. Thompson. Transport of gravel by flows up to $500\text{ m}^3\text{ s}^{-1}$, ohau river, otago, new zealand. *Journal of Hydraulic Engineering*, 23:285–303, 1985.
- K. Tockner, J. Ward, D. Arscott, P. Edwards, J. Kollmann, A. Gurnell, G. Petts, and B. Maiolini. The tagliamento river: a model ecosystem of european importance. *Acquatic science*, 65:239–253, 2003.
- K. Tockner, A. Paetzold, U. Karaus, C. Claret, and J. Zettel. In International Association of Sedimentologists, editor, *Ecology of Braided rivers*, pages 339–359. Blackwell, Oxford, 2006.
- M. Toffolon and A. Crosato. Developing macroscale indicators for estuarine morphology: The case of the scheldt estuary. *Journal of Coastal Research*, 23(1):195–212, 2007.

Bibliography

- D. Tonolla, V. Acuna, U. Uehlinger, T. Frank, and K. Tockner. Thermal heterogeneity in river floodplains. *Ecosystems*, 13:727–740, 2010.
- M. Tubino. Growth of alternate bars in unsteady flow. *Water resources research*, 27, 1991.
- M. Tubino and G. Seminara. Free-forced interactions in developing meanders and suppression of free bars. *Journal of Fluid Mechanics*, 214:131–159, 1990.
- M. Tubino, R. Repetto, and G. Zolezzi. Free bars in rivers. *Journal of Hydraulic Research*, 37(6):759–775, 1999.
- I.M. Turnbull. Geology of the wakatipu area. *Institute of Geological and Nuclear Sciences Limited: Lower Hutt, New Zealand*, 2000.
- C. Van der Meer, E. Mosselman, K. Sloff, B. Jager, G. Zolezzi, and M. Tubino. Numerical simulations of upstream and downstream overdeepening. *River, Coastal and Estuarine Morphodynamics*, pages 1721–1729, 2011.
- D. Van der Nat, A.P. Schmidt, K. Tockner, P.J. Edwards, and J.V. Ward. Inudation dynamics in braided floodplains: Tagliamento river, northeast italy. *Ecosystems*, 5: 636–647, 2002.
- M. Van der Nat, K. Tockner, P.J. Edwards, J.V. Ward, and A.M. Gurnell. Geomorphic thresholds in riverine landscapes. *Freshwater Biology*, 48, 2003.
- C.B. Vreugdenhil and M. de Vries. Analytical approaches to non-steady bed load transport. *Delft Hydraulics Laboratory Report*, 87(IV), 1973.
- H.J. De Vriend. Analysis of horizontally two-dimensional morphological evolutions in shallow water. *Journal of Geophysical Research*, 92(C4), 1987.
- J. Walsh and D.M. Hicks. Braided channels: Self-similar or self-affine? *Water Resources Research*, 38, 2002.
- M.G. Wang, R.J. Fokkink, and M. De Vries. Stability of river bifurcations in 1d morphodynamics models. *Journal of Hydraulic Research*, 33(6):739–750, 1995.
- J. Warburton. A brief review of hydraulic modelling of braided rivers in new zeland. *Journal of Hydrology*, 35:157–173, 1996.
- J. Warburton and T. Davies. Variability of bedload transport and channel morphology in a braided river hydraulic model. *Earth Surface Processes and Landforms*, 19: 403–421, 1994.
- M. Welber. *Morphodynamics and driftwood dispersal in braided rivers*. PhD thesis, Faculty of Engineering, University of Trento, 2013.
- M. Welber, W. Bertoldi, and M. Tubino. The response of braided planform configuration to flow variations, bed reworking and vegetation: the case of the tagliamento river, italy. *Earth Surface Processes and Landforms*, 37:572–582, 2012.
- P. Wesseling. *Principles of Computational Fluid Dynamics*. Springer, 2001.

Bibliography

- J.M. Wheaton, J. Brasington, S.E. Darby, and D.A. Sear. Accounting for uncertainty in dems from repeat topographic surveys: improved sediment budgets. *Earth Surface Processes and Landforms*, 35:136–156, 2010.
- M. Wild, T. Cochrane, T.R. Davies, D.M. Hicks, D. Painter, and G. Palmer. Recent sedimentation rates for the rees-dart braided river delta. In J. Schmidt, T. Cochrane, C. Phillips, S. Elliot, T. R. Davies, and L. Basher, editors, *Sediment Dynamics in Changing Environments*, pages 312–315. IAHS Press, 2008.
- M.A. Wild. *Growth dynamics of braided gravel-bed river deltas in New Zealand*. PhD thesis, University of Canterbury, 2012.
- G. Willgoose and G. Hancock. Bed load transport in braided gravel-bed stream models. *Earth Surface Processes and Landforms*, 23:611–623, 1988.
- R.D. Williams, J. Brasington, D. Vericat, D.M. Hicks, F. Labrosse, and M. Neal. Monitoring braided river change using terrestrial laser scanning and optical bathymetric mapping. In M. Smith, P. Paron, and J. Griffiths, editors, *Geomorphological Mapping: Methods and Applications*. 2011.
- R.D. Williams, J. Brasington, M. Hicks, C.D. Rennie, and D. Vericat. Hydraulic validation of two-dimensional simulations of braided river flow with spatially continuous adcp data. *Water Resources Research*, pages 1–23, 2013a.
- R.D. Williams, J. Brasington, D. Vericat, and D.M. Hicks. Hyperscale terrain modelling of braided rivers: fusing mobile terrestrial laser scanning and optical bathymetric mapping. *Earth Surface Processes and Landforms*, 2013b.
- M. Wong and G. Parker. Reanalysis and correction of bed-load relation of meyer-peter and muller using their own database. *Journal of Hydraulic Engineering*, 132(11), 2006a.
- M. Wong and G. Parker. One-dimensional modeling of bed evolution in a gravel bed river subject to a cycled flood hydrograph. *Journal of Geophysical Research*, 111: 1–20, 2006b.
- M. Wong and G. Parker. Reanalysis and correction of bed-load relation of meyer-peter and muller using their own database. *Journal of Hydraulic Engineering*, 132(11): 1159–1168, 2006c.
- W.J. Young and T.R.H. Davies. Prediction of bedload transport rates in braided rivers: A hydraulic model study. *Journal of hydrology*, 29, 1990.
- W.J. Young and T.R.H. Davies. Bed load transport processes in a braided gravel-bed. *Earth Surface Processes and Landforms*, 16:499–511, 1991.
- W.J. Young and W. Warburton. Principles and practice of hydraulic modelling of braided gravel-bed rivers. *Journal of Hydrology*, 35:175–198, 1996.
- H. Zhang and R. Kahawita. A nonlinear model for alluvional channels. *Journal of Hydraulic Engineering*, 113:353–368, 1987.

Bibliography

- H. Zhang and R. Kahawita. Linear hyperbolic model for alluvional channels. *Journal of Hydraulic Engineering*, 4:478–493, 1990.
- G. Zolezzi and G. Seminara. Downstream and upstream influence in river meandering. Part 1. general theory and application to overdeepening. *Journal of Fluid Mechanics*, 438:183–211, 2001.
- G. Zolezzi, M. Guala, D. Termini, and G. Seminara. Experimental observations of upstream overdeepening. *Water Resources Research*, 531:191–219, 2005.
- G. Zolezzi, W. Bertoldi, and M. Tubino. Morphological analysis and prediction of channel bifurcations. In G.H. Best, J.L Bristow, and C.S. Petts, editors, *Braided Rivers: Process, Deposits, Ecology and Management. Special Publication*, volume 36, pages 227–250. Blackwell, 2006.
- G. Zolezzi, R. Luchi, and M. Tubino. Morphodynamics regime of gravel bed, single-thread meandering rivers. *Geomorphology*, 14, 2009.